

THESIS FOR THE DEGREE OF DOCTOR OF PHILOSOPHY IN GEOTECHNICAL  
ENGINEERING

On the long-term behaviour of tension loaded piles in natural  
soft soils

A field study and numerical modelling

JORGE YANNIE

Civil and Environmental Engineering

Division of Geo-Engineering

CHALMERS UNIVERSITY OF TECHNOLOGY

Göteborg, Sweden 2016

On the long-term behaviour of tension loaded piles in natural soft soils  
A field study and numerical modelling  
JORGE YANNIE  
ISBN 978-91-7597-485-9

© JORGE YANNIE, 2016

Doktorsavhandlingar vid Chalmers tekniska högskola  
Ny serie nr. 4166  
ISSN 0346-718X  
Civil and Environmental Engineering  
Division of Geo-Engineering  
Chalmers University of Technology  
SE-412 96 Göteborg  
Sweden  
Telephone: +46 (0)31-772 1000

Chalmers Reproservice  
Göteborg, Sweden 2016

On the long-term behaviour of tension loaded piles in natural soft soils  
A field study and numerical modelling  
Thesis for the degree of Doctor of Philosophy in Geotechnical Engineering  
JORGE YANNIE  
Civil and Environmental Engineering  
Division of Geo-Engineering  
Chalmers University of Technology

## ABSTRACT

The complexity and scale of new infrastructure projects have challenged the current geotechnical design practice. Urban areas are growing at a fast pace in the horizontal and vertical direction, with taller buildings and deeper underground constructions in already densely populated areas. The West Link project in Gothenburg city is a good example of the latter. The geotechnical challenges in this project include deep excavations and deep foundations in soft sensitive natural clays. An important aspect in this case is the large buoyancy load arising from the ground water pressure, the stability of the soil mass in the excavation vicinity and the unloading heave from the soil. Typically, these loads are counterbalanced by the superstructure self-weight and by bedrock anchors. The very deep clay deposits in Gothenburg, however, require traditional floating piles to sustain the permanent tension loads from these processes. Little is known about the long-term behaviour of pile foundations in deep soft soil deposits under permanent tension loads. The need for a reliable foundation system for the West Link tunnel and the limited data available on permanently loaded tension piles in soft clays motivates further theoretical and experimental investigation of this pile type in natural soft structured clays.

As a result this Thesis presents new findings on the long-term behaviour of tension loaded piles in natural soft structured clays. The unique results from the field tests on six pile elements incorporate all significant stages in the pile cycle, i.e. pile installation, set-up and long-term loading, yet are sufficiently short to link the pile response to the soil behaviour of one particular layer. Furthermore, a novel cost-effective loading rig using gas springs and remote logging based on open-source software and freely available cloud storage is developed for execution of the field tests. The results indicate that the measured long-term bearing capacity is smaller than the short-term reference capacity. The difference is in the order of 20 – 30 % smaller. This reduction is attributed to the on-going creep deformations in the soil surrounding the pile shaft. These deformations cause relaxation of the effective stresses due to the kinematic constrains at the pile-soil interface. In addition to an analytical system level interpretation of the measured pile head displacement that showed only benign maximum final pile head displacements after 100 years, an advanced numerical analysis that incorporates a state-of-the-art rate dependent soft soil model is performed. The measured data and simulation results are in good agreement and corroborate previous investigations, however, for the first time the physical mechanisms underpinning the measured response are generalised and tertiary creep failure is reproduced. The long-term pile response is directly related to the behaviour of the soil adjacent to the pile shaft. Further work should focus on the evolution of the stress field

and soil properties under long-term pile loading. Deviatoric creep deformations should be studied in more detail by means of element level laboratory test on natural and remoulded soft clays.

Keywords: soft clay, piles, tension load, uplift, installation, field test, creep of piles, creep rupture, long-term, numerical model, rate dependent

*to my lovely family, Lina and my friends. Love you all!*



# PREFACE

## ACKNOWLEDGEMENTS

The research presented in this Thesis has been funded by the Swedish Transport Administration (Trafikverket) under contracts TRV 2012/48805 & TRV 2012/759028 and for the final part by the Trafikverket research program BIG (Branschsamverkan I Grunden) contract TRV 2015/49674 and further contributions from PEAB AB and Chalmers University of Technology all of which is greatly acknowledged.

It has been a long journey full of very valuable experiences that you only get once in your life. There has been many intense periods of learning and personal development, and I have met a lot of people on the way which has contribute in one way or another to my work in this Thesis. Therefore, I first want to thank everyone that has supported and helped me under my PhD studies. If I do not mention you here please know that I am grateful for your help and that if I would name everyone I will not be able to fit my Thesis content.

I had the great opportunity to do my PhD studies at the Geo-Engineering division of Chalmers University of Technology. I would like to express my sincere gratitude to Gunnar Lanner and Professor Claes Alén, who believed in me and selected me as the best candidate for the position. Prof. Claes Alén was my main supervisor under the first part of my studies. His talent for solving problems in a simple, yet robust and theoretical sound way, inspired me under difficult moments. His genuine and elegant approach to work out problems has been named “à la Claes”–method among us as a sign of admiration. I must say he is one of the most ingenious and kind Professor I have had the pleasure to meet and work with.

My PhD initially focused on the long-term behaviour of deep excavations in soft soils. Anders Kullingsjö brought up the topic as a follow up of his own research, and together with Prof. Claes Alén they guided my first steps. I want to thank Anders for his support and for the opportunity to participate in a field investigation at one construction site from Skanska AB. However, after one and a half year, my PhD took a different path with a new research topic (this Thesis). The problem with tension loaded piles became relevant during the planning of the West Link railway tunnel project in Gothenburg city. The idea was developed by Professor Göran Sällfors together with Leif Jendeby and Anders Hansson. I am grateful for giving me the possibility to work with this project and for the great discussions that helped to define the project itself.

I want to thank PEAB AB for their great support with the field test, specially Anders Engström and his team at the test site, and Fredrik Larsson and his team with the planning and resource allocation. I also want to thank the technicians from Chalmers Geotechnical laboratory, especially Aaro Pirhonen and Peter Hedborg for the passion, dedication and enormous help during the preparation and execution of the field test. I would have not made without both of you. Thanks to Ingemar Forsgren and John Forsgren for their help with sample extraction and site characterisation.

My sincere gratitudes to the CREEP project (Creep of Geomaterials PIAPGA-2011-286397) and the Chalmersska forskningsfonden for my exchange time at the Norwegian Geotechnical Institute (NGI) in Oslo, Norway. Thanks to the Computational Geomechanics team at NGI and Hans-Petter Jostad for their wonderful collaboration and support during my stay. In particular, I want to thank Nallathamby Sivasithamparam, who provided me priceless support in the understanding of advanced soft soil models and guide in my Thesis.

I want to thank all my colleagues at the Geo-Engineering division of Chalmers University for all their support and help, particularly during the end of my PhD. Thank you for the amazing times we have spent together and all the “fika” breaks that helped me relax under stress periods. I am especially grateful for the support from Mats Karlsson, as he has significantly helped me in the academic and personal life. Mats is one of my best friends and for me he is my Swedish brother. I hope that one day I can support all my colleagues as they did with me.

I would like to express my sincere gratitude to Professor Minna Karstunen and Jelke Dijkstra for their great support, help and teaching under the last years of my studies. I have not seen two people with such a great passion and love for everything related to Geotechnical Engineering. Their arrival to Chalmers’ Geotechnical division marked the beginning of a new remarkable era in Geotechnical Engineering in Sweden. I particularly want to thank Jelke Dijkstra for his support and patience from the very beginning he started working at the division. He eventually became my main supervisor after Prof. Claes Alén retired from Chalmers. Jelke has been an extraordinary supervisor who has taught me a lot about Geotechnical Engineering and the scientific world as a whole. His passion for science is unmatched, and his knowledge and creativity is outstanding. We have had great discussions which have sparked many interesting ideas. I really enjoy those moments and wish we can continue to work together in the future. I would not have been able to finalise this Thesis without his supervision.

Finally, but not least, I want to thank my family, my girlfriend Lina and my friends for their love and patience during this intense study time. They have always been there when I needed it the most. I specially thank Lina, who has been at my side during my sleepless working nights and my terrible mood. I love you all and this work is dedicated to you.

## NOMENCLATURE

<b>Abbreviation</b>			method for pile capacity
<i>BAT</i>	Field pore pressure transducer	$\beta_s$	Ratio between the residual and peak unit friction ( $\tau_{sr}/\tau_{su}$ )
<i>CAUC</i>	Anisotropically-consolidated undrained triaxial compression	$\chi$	Amount of bonds
<i>CEM</i>	Cavity Expansion Method	$\chi_0$	Initial bonds
<i>CIUC</i>	Isotropically-consolidated undrained triaxial compression	$\Delta\varepsilon_v^c$	Volumetric creep strains
<i>CPT</i>	Cone Penetration test	$\Delta F$	Change in load
<i>CRP</i>	Constant rate of penetration	$\Delta u$	Excess pore water pressure
<i>CSS</i>	Current Stress Surface	$\Delta u^{creep}$	Creep generated excess pore water pressure
<i>DSS</i>	Direct simple shear	$\Delta u_i$	Pile installation excess pore water pressure
<i>ICS</i>	Intrinsic Compression Surface	$\delta'$	Soil effective friction angle at current effective stress
<i>MLT</i>	Maintained load test	$\Delta\delta$	Change in displacement
<i>NCS</i>	Normal Consolidation Surface	$\Delta_{10}$	Set-up factor (capacity increase per decade)
<i>NSF</i>	Negative skin friction	$\delta_{end}$	Final pile head displacement for a given stage during pile testing
<i>OCR</i>	Overconsolidation ratio	$\delta_{ij}$	Kronecker's delta
<i>PI</i>	Plasticity Index	$\delta_{ini}$	Initial pile head displacement for a given stage during pile testing
<i>QML</i>	Quick-maintained load test	$\delta_{ult}$	Pile head displacement at $Q_{ult}$
<i>RH</i>	Relative humidity	$\dot{\Lambda}$	Visco-plastic multiplier
<i>SPM</i>	Strain Path Method	$\eta$	stress ratio $q/p'$
<i>SPT</i>	Standard Penetration test	$\eta^*$	Factor of increase in $S_u$ per decade of strain rate
<i>ULS</i>	Ultimate Limit State	$\eta_{K_0^{nc}}$	Actual stress ratio $q/p'$ in the 1D normally consolidated stress path
<i>QML</i>	Quick Maintained Load	$\kappa^*$	Modified swelling index
<i>SLS</i>	Serviciability Limit State	$\lambda^*$	Slope of the post-yield compression line in $\varepsilon_v - \ln \sigma'_v$ for 1D compression
<b>Greek letters</b>		$\lambda_i^*$	Intrinsic modified compression index for reconstituted soil
$\alpha$	Inclination of the yield surfaces in respect to the $p'$ axis	$\mu^*$	Modified creep index for a given
$\alpha$	Factor for the total stress method for pile capacity		
$\alpha_0$	Initial inclination of the yield surface		
$\alpha_{K_0^{nc}}$	Inclination of the yield surface in the normally consolidated state		
$\beta$	Factor for the effective stress		

	stress and reference time	$\varepsilon_d$	Deviatoric strains
$\mu_d^*$	Deviatoric modified creep index	$\varepsilon_v$	Volumetric strains
$\mu_i^*$	Modified intrinsic creep index	$\varepsilon_v^c$	Volumetric creep strain
$\mu_v^*$	Volumetric modified creep index	$\varepsilon_d^c$	Deviatoric creep strains
$\omega$	Absolute effectiveness of rotational hardening	$\varepsilon_d^e$	Elastic deviatoric strains
		$\varepsilon_v^e$	Elastic volumetric strains
$\omega_d$	Relative effectiveness of rotational hardening in respect to $\varepsilon_d^p$	$\xi$	Absolute rate of destructuration
$\phi'$	Soil effective friction angle	$\xi_d$	Relative rate of destructuration in respect to $\varepsilon_d^p$
$\phi'_{cs}$	Effective critical state friction angle	$d\varepsilon_d^p$	Deviatoric plastic strains
$\phi'_r$	Remoulded soil effective friction angle	$d\varepsilon_v^p$	Volumetric plastic strains
$\Psi^{d,avg}$	Average creep index for pile head displacement (unitless)	$M(\theta_\alpha)$	Lode angle failure criterion
		$v'$	Drained Poisson's ratio
$\Psi^l$	Average creep index for pile head displacement (with length units)	<b>Roman letters</b>	
$\sigma'_{hc}$	Horizontal effective stress after pile set-up	<b>B</b>	Strain-displacement transformation matrix
$\sigma'_{pc}$	Apparent pre-consolidation pressure	<b>R</b>	Residual load matrix
$\sigma'_{v,nsf}$	Reduced vertical stress due to negative skin friction	$a$	Pile influence area
$\sigma'_{v0}$	In-situ vertical effective stress	$A_b$	Pile base area
$\sigma_r$	Radial stress	$A_s$	Pile shaft area
$\sigma_z$	Vertical stress (axisymmetric model)	$C_c$	Compression index
$\sigma_\theta$	Hoop or circumferential stress	$C_r$	Swelling index
$\sigma'_{ij}$	Stress tensor	$C_\alpha$	Secondary compression index
$\sigma_{v,b}$	Total vertical stress at the pile base level	$C_{ci}$	Intrinsic compression index
$\sigma_{v0}$	In-situ total vertical stress	$D_{eq}$	Pile equivalent diameter
$\tau$	Reference time for creep index	$e$	Void ratio
$\tau^{peak}$	Peak shear stress	$E_1$	Triaxial strain invariant
$\tau_s(z)$	Unit skin friction at depth $z$	$E_2$	Cylindrical cavity expansion strain invariant
$\tau_{ult}$	Ultimate unit shaft resistance	$E_3$	Simple shear strain invariant
$\varepsilon^c$	Creep strains	$f_y$	Yield surface function
$\varepsilon^p$	Plastic strains	$G$	Secant shear modulus
		$G(r)$	Shear stiffness function of distance $r$ from pile center line.
		$G_{50}$	Secant shear modulus at 50% of

	peak deviator stress from CAUC tri-axial	$Q_{avg}$	Average load for a given stage during pile testing
$J_{2\alpha}$	Second invariant of the modified deviatoric stress ( $q - \alpha p'$ )	$Q_{creep}^{ref}$	Reference pile creep load
		$Q_{crp}$	Pile creep load
$J_{3\alpha}$	Third invariant of the modified deviatoric stress ( $q - \alpha p'$ )	$Q_{end}$	Final load during for a given stage during pile testing
$k$	Spring constant	$Q_{ini}$	Initial applied load for a given stage during pile testing
$K_0$	Coefficient of at-rest earth pressure	$Q_{res}$	Pile residual load
$K_c$	Coefficient of horizontal stress as pile set-up in relation the the initial in-situ vertical effective stress.	$Q_{sls}$	Serviciability Limit state load
		$Q_{ult}$	Ultimate Limit State pile capacity
$K_f$	Coefficient of lateral pressure at failure during pile loading in relation to the initial in-situ effective stress	$Q_{ult}^{base}$	Ultimate Limit State base load
		$Q_{ult}^{est}$	Estimated Ultimate Limit State pile capacity
$L_{bag}$	The contact length of the bag	$Q_{ult}^{ref}$	Reference Ultimate Limit State capacity
$M$	Critical state line	$Q_{ult}^{shaft}$	Ultimate Limit State shaft load
$M_c$	Stress ratio at critical state in triaxial compression	$R$	Gas constant
		$R$	Sphere height
$M_e$	Stress ratio at critical state in triaxial extension.	$r_0$	Pile radius
$M_{DSS}$	Critical state line in DSS	$R_{pile}$	Pile radius
$M_{max}$	Peak measured torque	$S_s$	Relative movement at the pile shaft
$n$	Gas mass	$S_t$	Soil sensitivity
$n$	Pile influence area factor	$S_u$	Undrained shear strength
$N_c$	Base bearing capacity factor	$S_u^{creep}$	Undrained shear strength for pile creep load
$P$	Spring force	$S_u^{ref}$	Undrained shear strength for a given time or shear rate
$p'$	Mean effective stress	$S_{u,b}$	Undrained shear strength at the pile base level
$p'_f$	Mean stress at failure	$t_{ref}$	Reference time for the onset of pure creep strains
$p'_i$	Initial mean effective stress	$u$	Pore water pressure
$p'_m$	Mean effective stress tangent to the Natural Yield Surface or Normal Compression Surface	$u_0$	In-situ pore pressure
		$u_{hs}$	Hydrostatic pore pressure
$p'_{mi}$	Mean effective stress tangent to Intrinsic Surface	$V$	Shear load
$Q$	Pile load		
$q$	Deciatoric stress		
$q_t$	Cone tip pressure resistance		

$W'$  Effective pile weight  
 $w_L$  Clay liquid limit

$w_n$  Clay natural water content

# CONTENTS

<b>Abstract</b>	<b>i</b>
<b>Preface</b>	<b>v</b>
<b>Acknowledgements</b>	<b>v</b>
<b>Nomenclature</b>	<b>vii</b>
<b>Contents</b>	<b>xi</b>
<b>1 Background</b>	<b>7</b>
1.1 Pile foundations in soft soils . . . . .	9
1.2 Objectives and limitations . . . . .	10
<b>2 Pile foundations</b>	<b>11</b>
2.1 Installation . . . . .	11
2.2 Set-up period . . . . .	15
2.3 Pile loading . . . . .	19
2.3.1 Short-term pile loading . . . . .	22
2.3.2 Long-term pile loading . . . . .	24
2.4 Pile capacity and settlement analysis . . . . .	33
2.5 Swedish pile research . . . . .	35
<b>3 Soil behaviour</b>	<b>41</b>
3.1 Rate effects . . . . .	41
3.2 Deviatoric creep . . . . .	42
3.3 Creep rupture . . . . .	43
3.4 Creep modelling . . . . .	46
3.5 Constitutive models for soft soils . . . . .	47
3.5.1 SCLAY1S . . . . .	47
3.5.2 CREEP-SCLAY1S . . . . .	49
<b>4 Long-term field test</b>	<b>53</b>
4.1 The test site . . . . .	53
4.2 Soil characterisation . . . . .	54
4.2.1 In-situ tests . . . . .	55
4.2.2 Element testing . . . . .	56
4.2.3 Groundwater monitoring . . . . .	62
<b>5 Load test setup</b>	<b>63</b>
5.1 Selection of loading method . . . . .	64
5.1.1 Final solution: Lifting bag . . . . .	66
5.1.2 Adding load control . . . . .	68
5.2 Test piles . . . . .	69

5.3	Load frame . . . . .	70
5.4	Instrumentation . . . . .	71
5.5	Data logging - local and remote . . . . .	74
5.6	Calibration . . . . .	75
5.7	Protocols and execution of pile load tests . . . . .	78
5.7.1	Short-term (ST) pile load tests . . . . .	79
5.7.2	Long-term (LT) pile load tests . . . . .	80
<b>6</b>	<b>Results from field test</b>	<b>83</b>
6.1	Data acquisition and processing . . . . .	83
6.2	Installation and set-up measurements . . . . .	87
6.3	Short-term tension load test results (ULS) . . . . .	87
6.4	Long-term tension load test results (SLS) . . . . .	93
6.4.1	Stepwise manually-loaded . . . . .	93
6.4.2	Stepwise automatic-loaded . . . . .	104
6.4.3	All Piles . . . . .	109
6.5	Discussion . . . . .	109
6.5.1	Test Results . . . . .	109
6.5.2	Creep criterion . . . . .	110
<b>7</b>	<b>Result analysis</b>	<b>113</b>
7.1	Bearing Capacity . . . . .	113
7.1.1	Ultimate Limit State . . . . .	113
7.1.2	Load transfer method . . . . .	118
7.2	Long-term response: simple method . . . . .	122
7.3	Prediction of expected creep rate . . . . .	123
7.3.1	Modelling pile installation with SPM . . . . .	124
7.3.2	Results SPM . . . . .	130
7.3.3	Creep rates . . . . .	137
<b>8</b>	<b>Conclusions</b>	<b>147</b>
8.1	Recommendations . . . . .	149
<b>A</b>	<b>APPENDIX</b>	<b>151</b>
A.1	Test site . . . . .	151
A.2	Test piles . . . . .	155
A.3	Long-term measurement data . . . . .	158
	<b>References</b>	<b>169</b>

# List of Figures

1.1	The West Link railway tunnel route in Gothenburg (tunnel in berg=rock, jord/lera=soil/clay, trafikverket.se) . . . . .	7
1.2	Typical stages during deep excavations in soft soils and sources of tension load (adopted from Kempfert and Gebreselassie 2006). . . . .	8
2.1	Illustration of the pile cycle (adapted from Randolph and Gourvenec (2011)). 0 = initial conditions, i = installation, c = after equalisation, f = at failure. . . . .	11
2.2	(a) $S_u$ from fall cone test and $w_n$ from soil adjacent to pile shaft (Karlsrud and Haugen 1985), (b) shear strength after equalisation of installation pore water pressures from numerical analysis (Whittle 1987). . . . .	16
2.3	Illustration of shear strength after pile set-up and from pile loading (Karlsrud, Nadim, et al. 1990). Critical zone at a distance $r_2$ from shaft. . . . .	16
2.4	Percentage change of shear wave velocity ( $V_s$ ) from initial conditions during and after equalisation of installation $\Delta u$ . Closed-ended pile $D = 0.6$ m and $L = 35$ m. Equalisation after approximately 250 days (adopted from Hunt et al. 2002). . . . .	17
2.5	DSS at 7.3m for pre- and post-installation. Following cyclic = after 3 loading cycles; Transverse = rotated $90^\circ$ (adopted from Hunt et al. 2002). . . . .	18
2.6	Concentric cylinder model of soil stresses around the pile shaft. . . . .	19
2.7	Distribution of shear load from the pile shaft to the soil from the concentric cylinder model. . . . .	20
2.8	Principal stress rotation effect and Mohr's circle (in (b) the same applies for simple shear substituting $\tau_{z\theta}$ with $\tau_{rz}$ ). . . . .	21
2.9	Stress paths for soil at pile shaft and DSS of undisturbed samples from Bothkennar clay (Lehane and Jardine 1994.) . . . . .	22
2.10	Pile tests of short length concrete piles with different rates, $D = 152$ mm and $L = 100$ mm at 3.5–4.5 m depth (adopted from Torstensson 1973). . . . .	23
2.11	Variation of $S_u$ with time to failure (shearing rate). . . . .	24
2.12	Change of vertical effective stress due to NSF (adopted from Zeevaert (1983)). . . . .	25
2.13	Illustration of the deformation due to NSF in soil adjacent to the pile shaft. (a) Long-term soil settlements, (b) Short-term compression loading, (c) Short-term tension loading. . . . .	26
2.14	Rate versus time from tests in Table 2.4. Bound lines calculated using Equation (2.21). . . . .	30
2.15	Illustration of creep shear strains adjacent to the pile shaft. . . . .	32
2.16	Pile testing at Gothenburg's harbour circa 1910 using E. Wendel load frame (SGF Väst). . . . .	35
2.17	Tension loading of full-scale floating piles in soft clays (Bengtsson and Hansbo 1979; Bengtsson and Sällfors 1983). Hold period deformation subtracted in dotted curve. . . . .	38

2.18	Methods for determining the pile “creep” load; (a) data from Bäckebol clay, $S_u^{creep} = 0.72S_u^{ref}$ . Vane allowed to rest for one day before testing (adopted from Hansbo 1984), (b) the pile “creep” load is obtained at the minimum curvature radius. . . . .	39
3.1	U-shaped model illustrating the variation of soil strength with respect to drainage conditions and rate effects, e.g. for triaxial compression tests (adopted from Quinn and Brown 2011). . . . .	42
3.2	Creep phases in triaxial conditions with constant total stresses (adopted from Augustesen, Liingaard, et al. 2004) . . . . .	43
3.3	$K_0$ consolidated undrained triaxial creep tests (adopted from Campanella and Vaid 1974). . . . .	44
3.4	Illustration showing (a) the stress boundaries for stable and unstable creep (rupture) and (b) time-displacement curves for different shear loads at the pile shaft. . . . .	45
3.5	Incremental loading (IL) oedometer at 5m depth for Bothkennar clay, $\sigma'_{pc} \approx 81$ kPa (adopted from Nash et al. 1992). . . . .	47
3.6	SCLAY1S natural yield (NYS) and intrinsic (IS) surfaces in 2D triaxial space. . . . .	48
3.7	CREEP-SCLAY1S surfaces (adopted from Gras et al. (In press)) . . . . .	50
4.1	Site location at Marieholm, Gothenburg (Waterloogatan, coordinates 6402173, 321345 – SWEREF99 system). . . . .	53
4.2	Soil from test site at Marieholm, Gothenburg . . . . .	54
4.3	Undrained shear strength from vane, CPTu and DSS. . . . .	56
4.4	Marieholm clay properties. . . . .	57
4.5	DSS tests at depths similar to the test pile location. . . . .	58
4.6	Result from 1D compression tests . . . . .	59
4.7	Results from 1D Constant Rate of Strain compression tests . . . . .	59
4.8	Results from 1D Incremental Loading (IL) compression tests and creep parameter $\mu^*$ . . . . .	60
4.9	Results from undrained and drained triaxial compression tests. . . . .	61
4.10	Average pore water pressure with depth near and at the site for different years. . . . .	62
5.1	Ideal spring curve and constant spring design. . . . .	63
5.2	Disk springs. . . . .	65
5.3	Trelleborg AB lifting bags. . . . .	66
5.4	TBL32 load versus displacement curves for different pressure and loading conditions. . . . .	67
5.5	Bag control algorithm implemented in LabVIEW. . . . .	69
5.6	Pile elements. . . . .	71
5.7	Boundary conditions of a single pile in the field test. . . . .	72
5.8	Loading frame parts at ground level (left) and concrete pile head details (right). . . . .	73
5.9	Illustration of possible bag configurations. Four bags give a stable frame against eccentricity as compared to two bags. . . . .	73
5.10	Strain gauges glued to sister rebars. . . . .	74

5.11	Half-bridge strain gauges connection diagram to the NI 9237 module. . . .	74
5.12	Pore water pressure transducer mount design at pile shaft. . . . .	75
5.13	Compression of 1 meter model pile: (a) Load cycle 200 kN, (b) $E_{tan}$ as $f(\varepsilon)$ for 200 kN, (c) Load cycle 500 kN, (d) $E_{tan}$ as $f(\varepsilon)$ for 500 kN. . . .	77
5.14	Plan view of the pile field test and the in-situ test investigation. . . . .	78
5.15	Test protocol for short-term QML tests. . . . .	80
6.1	Loading frame details. . . . .	85
6.2	Picture illustrating the tilting of the load frame to the left with reference to the timber mat. . . . .	86
6.3	Levelling of steel extension piles (accuracy $\pm 1$ mm/km) . . . . .	87
6.4	Excess pore pressure after installation and equalization period at the pile shaft. Transducer at pile shaft and BAT (B; average) in the vicinity. . . .	88
6.5	Short-term loading of Piles 5 and 6 (TT is tell-tale, LP is linear potentiometer). . . .	89
6.6	Accumulated creep displacement for the last 6 minutes of each load step for Piles 5 and 6. . . . .	90
6.7	Load distribution from strain gauge measurements for test ST5A. . . . .	91
6.8	Load distribution from strain gauge measurements for test ST6B. . . . .	91
6.9	Load and displacement with time for all loading stages of test LT2A. . . .	94
6.10	Long-term load-displacement curve for test LT2A. . . . .	95
6.11	Time displacement for each stage of test LT2A. . . . .	96
6.12	Pile head displacement rate in linear (left) and log-log (right) scale for each load step and creep curves for $\Psi^l = 0.2$ and $0.7$ with $t_{ref} = 24h$ for test LT2A. . . . .	97
6.13	Normalized pile displacement for each stage of tests LT2A. . . . .	98
6.14	Pore pressure at LT2A shaft mid height. . . . .	99
6.15	Load and displacement with time for all loading stages of test LT4A. . . .	100
6.16	Long-term load-displacement curve for test LT4A. . . . .	101
6.17	Time displacement for each stage of test LT4A. . . . .	102
6.18	Displacement rate for each load step and creep curves for $\Psi^l = 0.2$ and $0.7$ with $t_{ref} = 24h$ for test LT4A. . . . .	102
6.19	Normalized pile displacement for each stage of tests LT4A. . . . .	103
6.20	Load and displacement with time for all loading stages of test LT5A. . . .	104
6.21	Long-term load-displacement curve for test LT5A. . . . .	105
6.22	Time displacement for each stage of test LT5A. . . . .	106
6.23	Displacement rate for each load step and creep curves for $\Psi^l = 0.2$ and $0.7$ with $t_{ref} = 24h$ for test LT5A. . . . .	107
6.24	Load and displacement with time for all loading stages of test LT5A. . . .	108
6.25	Average load and accumulated displacement with time for all Piles. . . .	109
6.26	Idealised creep failure criterion for long-term loaded piles. . . . .	111
6.27	Illustration of possible creep effects on the short-term pile capacity. . . .	112
6.28	Illustration of possible redistribution of load with time. . . . .	112
7.1	Radial stress measurements around full displacement piles from Chow (1997) (adopted from Fleming 2008). . . . .	116
7.2	DSS failure modes (adopted from Randolph and Wroth 1981). . . . .	117
7.3	Zhang's t-z curve (Zhang 2012) . . . . .	118

7.4	Effects of $S_{su}$ and $\beta_s$ on Zhang's t-z curve. . . . .	119
7.5	Back calculation of test ST5A. . . . .	120
7.6	Back calculation of test ST5A. . . . .	120
7.7	Effective radial stresses after equalisation of installation pore pressures (adopted from Lehane and Jardine 1994). . . . .	121
7.8	Creep parameter $\Psi_{d,avg}$ from long-term sustained load tests. . . . .	123
7.9	Extrapolation of creep settlements for maximum $\Psi_{d,avg}$ . . . . .	124
7.10	Trapezoidal integration for installation pore pressures in SPM. . . . .	129
7.11	Strain invariants from SPM for some soil elements at depth $z = 3$ m. . . . .	132
7.12	Strain components for node at (0.15,3) from SPM, pile radius 0.15 m. . . . .	133
7.13	Predicted installation stresses and pore water pressure with SPM and SCLAY1S. . . . .	134
7.14	Predicted installation stresses and pore water pressure with SPM and SCLAY1S compared to MIT-E3 for BBC (Whittle 1987). . . . .	134
7.15	Predicted installation stresses and pore water pressure with SPM and SCLAY1S compared to MCC for BBC (Whittle 1987). . . . .	135
7.16	Predicted destructuration with SPM and SCLAY1S. . . . .	135
7.17	Predicted anisotropy with SPM and SCLAY1S. . . . .	136
7.18	Different boundary conditions for DSS test. . . . .	138
7.19	Initialisation of set-up stresses for DSS test with $\Delta t = 90$ days. . . . .	139
7.20	Short-term loading of single element under DSS conditions. . . . .	141
7.21	Deviatoric creep from simulated DSS tests for Undrained boundary conditions (bc1). . . . .	142
7.22	Deviatoric creep from simulated DSS tests for Drained boundary conditions (bc2). . . . .	144
7.23	Deviatoric creep from simulated DSS tests for Drained boundary conditions (bc3). . . . .	145
7.24	Deviatoric creep parameter from simulated DSS tests compared to field measurements. . . . .	146
A.1	Aerial view of test site. Located next to Waterloo street 100 m north-east of the Partihalls connection road. . . . .	151
A.2	Site blueprints illustrating new roads and previous soil investigations done in connection to the Marieholm tunnel project. . . . .	152
A.3	Test site after installation of the 6 test piles. . . . .	153
A.4	Steel extension pile and timber mat on top of fill material. . . . .	153
A.5	Settlement measurements at the test site and from previous investigations. . . . .	154
A.6	Average air temperature at test site. . . . .	154
A.7	Model pile used to calibrate the strain gauges (1 m long). . . . .	155
A.8	Equipment used for the load rig (without HEB beams). Load cell, lifting bags (white box) and portable air compressor. . . . .	156
A.9	Concrete piles, steel extension piles, tell-tales and tension loading rod. . . . .	156
A.10	Load frame. . . . .	157
A.11	Load frame and manual pressure regulation panel. . . . .	157
A.12	Load-displacement data for test LT1A. . . . .	159
A.13	Pore water pressure measurements at pile shaft for test LT1A. . . . .	160

A.14 Load-displacement data for test LT3A. . . . .	162
A.15 Detailed data for Test LT2A, stage 1 and 2. . . . .	163
A.16 Detailed data for Test LT2A, stage 3. . . . .	164
A.17 Detailed data for Test LT2A, stage 4. . . . .	165
A.18 Detailed data for Test LT2A, stage 5. . . . .	166
A.19 Detailed data for Test LT2A, stage 6. . . . .	167

# List of Tables

2.1	Analytical and numerical methods for approximation of pile installation. . . . .	12
2.2	Normalized excess pore water pressure directly after installation . . . . .	14
2.3	Change in radial effective stress after consolidation . . . . .	17
2.4	Overview of investigations on long-term behaviour of piles. . . . .	31
2.5	Estimation methods for pile bearing capacity . . . . .	34
2.6	Overview of main pile research in Swedish soft clays. . . . .	36
3.1	Parameter description for SCLAY1S and CREEP-SCLAY1S. . . . .	52
4.1	Laboratory tests from the test site soil. . . . .	58
5.1	Springs studied for loading the piles in tension . . . . .	64
5.2	Instrumentation of field test . . . . .	76
5.3	Short-term pile tests . . . . .	80
5.4	Long-term loading ratio $Q/Q_{ult}$ (%) . . . . .	81
6.1	Configuration of data logger NI-cDAQ9178 . . . . .	83
6.2	Instrumentation stability . . . . .	84
6.3	Short-term test results. . . . .	92
6.4	Data from test LT2A. . . . .	95
6.5	Data from test LT4A. . . . .	101
6.6	Data from test LT5A. . . . .	105
7.1	Parameters for SCLAY1S at 15m depth, Marieholm. . . . .	127
7.2	Effective stresses after set-up period from numerical models. . . . .	137
7.3	Parameters for CREEP-SCLAY1S at the pile shaft following pile installation (15m depth, Marieholm). . . . .	138
7.4	Short-term DSS loading rates. . . . .	139
A.1	Data from test LT1A. . . . .	158
A.2	Data from test LT3A. . . . .	161

# 1 Background

The complexity and scale of new infrastructure projects have challenged the current geotechnical design practices. Urban areas are growing at a fast pace in the horizontal and vertical direction, with taller buildings and deeper underground constructions in already densely populated areas. The City of Gothenburg is a good example of the latter, especially with the West Link underground railway project; construction starting already in 2017.

Part of the West Link tunnel will be built in very deep deposits of soft clay in the heart of Gothenburg city. Figure 1.1 shows the tunnel track and the different construction types along its planned route. The project is very challenging as the tunnel is surrounded by many building types, from new residential areas to historic churches and major roads. This in turn translates into low displacement tolerances for the foundation and retaining structures for the tunnel. Therefore, a good understanding of the long-term soil-structure interaction is necessary to reduce uncertainties in the design and avoid damage to existing structures.

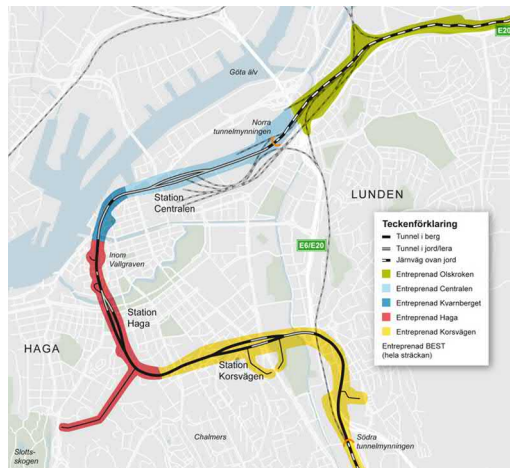


Figure 1.1: *The West Link railway tunnel route in Gothenburg (tunnel in berg=rock, jord/lera=soil/clay, trafikverket.se)*

The geotechnical challenges of the West Link tunnel include deep excavations and deep foundations in soft sensitive natural clays as illustrated in Figure 1.2. An important aspect in this case is the large buoyancy load arising from the ground water pressure, the stability of the soil mass in the excavation vicinity and the unloading heave from the soil. Typically, these loads are counterbalanced by the superstructure self-weight or filling material on top of it. When the latter is not sufficient, the foundation is in general anchored to the bedrock. However, the very deep clay deposits in Gothenburg city make the use of anchors very complicated and not economically feasible. Instead, traditional

floating piles are necessary to sustain the permanent heaving loads.

Recent investigations in Sweden have addressed part of the above problems, with research on deep excavations (Persson 2004; Kullingsjö 2007) and the long-term behaviour of soft soils (Olsson 2010; Olsson 2013). However, deep foundations under the West Link conditions have not been investigated, with most of the pile research focusing on pile capacity (B.H. Fellenius 1972; Torstensson 1973; Bengtsson and Sällfors 1983) and the foundation settlement as a whole (Jendeby 1986; Claesson et al. 2007). Similar trend is observed in international pile research (Randolph 2003). Little is known about the long-term behaviour of pile foundations in deep soft soil deposits under permanent tension loads.

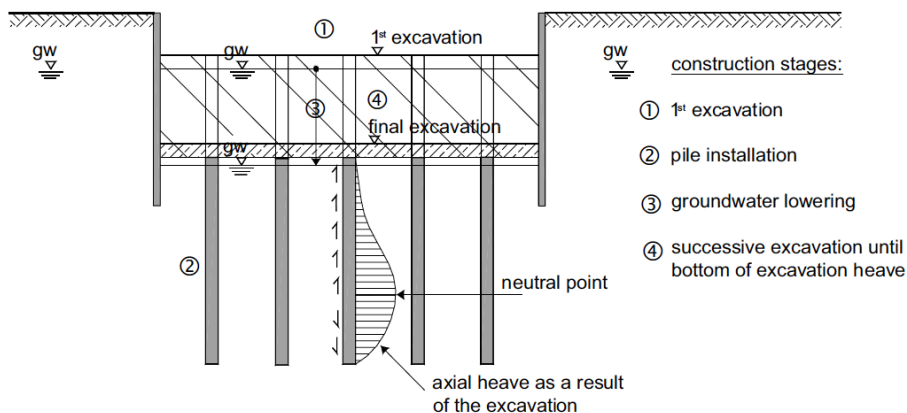


Figure 1.2: *Typical stages during deep excavations in soft soils and sources of tension load (adopted from Kempfert and Gebreselassie 2006).*

Pile foundations are used to minimize settlements, transferring the superstructure loads to a deeper bearing stratum. Therefore, piles are commonly subjected to compression loads, but can also provide capacity for tension loads. The latter loads are less common in the urban environment (for permanent loads). Instead, most knowledge about tension piles stems from the offshore industry, where platforms located in deep water require an anchoring system to sustain hydrodynamic loads. Tension piles became important in the 1980s with the newly developed Tension-Leg platforms (Bradshaw et al. 1984; Jardine and Potts 1988). This early work demonstrated the importance of the visco-plastic behaviour of soft soils for piles under sustained loading and rapid short-term loads (St.John et al. 1983; Ramalho Ortigao and Randolph 1983). Nevertheless, tension piles are less common onshore where only a few cases can be found in the literature (Karlsrud 2012).

## 1.1 Pile foundations in soft soils

Pile foundations have been studied intensively since most urban areas have developed on soft soils with poor bearing capacity which are susceptible to large settlements. Engineers have adopted simplified methods to study and design pile foundations due to the complex pile-soil interaction. These methods indirectly account for the complexities involved by using correlations derived from pile testing databases and model pile tests in the laboratory. These simplified methods proved to be reasonably successful in practice as long as local empirical data is available. If this information is not correct or a new foundation type is required, these methods fail to accurately predict the pile response. This will increase the costs resulting from larger safety factors and mitigation measures in order to incorporate larger uncertainties. In Sweden, the latter is particular an issue for the design and construction of pile foundations in soft clays under sustained tension loads.

Most studies in soft clays have focused on the short-term response of displacement piles loaded in compression, with very few cases under tension and long-term sustained loads. These studies have shown that the pile capacity is directly proportional to the effective stress, soil properties and loading rate at the pile-soil interface. Furthermore, results from various investigations point out that, for soft clays, there is no difference in the loading direction when evaluating the bearing capacity of single piles under short-term loading (Torstensson 1973; Bengtsson and Sällfors 1983; Lehane and Jardine 1994). On the other hand, long-term effects are mainly considered when studying the combined behaviour of the foundation raft and piles. In this case focus has been given on the long-term consolidation settlements and the load (re-)distribution below the raft and along the pile shaft, with little or no consideration for creep settlements (B.H. Fellenius 2015). The magnitude of this long-term deformation is considered rather small under working loads (Poulos et al. 2002). However, long-term pile displacements (creep of piles) is important for tension loaded piles, i.e. the additional load from creep deformations in the soil cannot be redistributed to the raft.

The need for a reliable foundation system for the West Link tunnel and the limited data available on permanently loaded tension piles in soft clays motivates further experimental investigation of this pile type in soft soils. By performing a field test all stages from installation to pile set-up are properly accounted for including the natural soft structured clay that is difficult to replicate in the laboratory. Details on the experimental set-up and information about the site characterisation is reported in Chapter 4 and 5. The results presented in Chapter 6 elaborate the importance of considering the visco-plastic properties of soft clays for the long-term bearing capacity and settlement profiles. Failure by creep displacement (i.e. tertiary creep) was observed for load levels below those obtained from short-term loading. Chapter 7 present numerical analysis using a rational framework, i.e. incorporating installation effects and set-up period together with more advanced constitutive models for predicting the behaviour of soft clays.

## 1.2 Objectives and limitations

The aim of the Thesis is to obtain new quantitative experimental data on the long-term response of displacement piles under sustained tension loads in natural soft clays. A field test program will be developed in order to faithfully capture pile installation and subsequent ageing and creep in natural clay. Furthermore, these new findings will be interpreted in the framework of contemporary soft soil modelling, and thus generalised for other conditions using a rate-dependent constitutive soil model.

This work is limited to the study of short length displacement piles in normally to slightly over-consolidated clays under static loading conditions. Similar to all field tests, external variables, such as temperature and vibrations from nearby construction, could have influenced the field results.

## 2 Pile foundations

In order to understand the long-term response of pile foundations, the complete loading history needs to be considered using a rational framework. In addition to the soil geological and stress history, the behaviour of the pile-soil system is directly related to the installation methods, set-up period and loading conditions. Multiple stages from installation to loading can be summarised in a *pile cycle* (Figure 2.1) discussed in the following. Proper understanding of the underlying soil behaviour during the pile cycle will potentially improve the design methods (Randolph and Gourvenec 2011; Karlsrud 2012). Details for this cycle are presented in subsequent Sections with focus on pre-fabricated full displacement piles in soft clays.

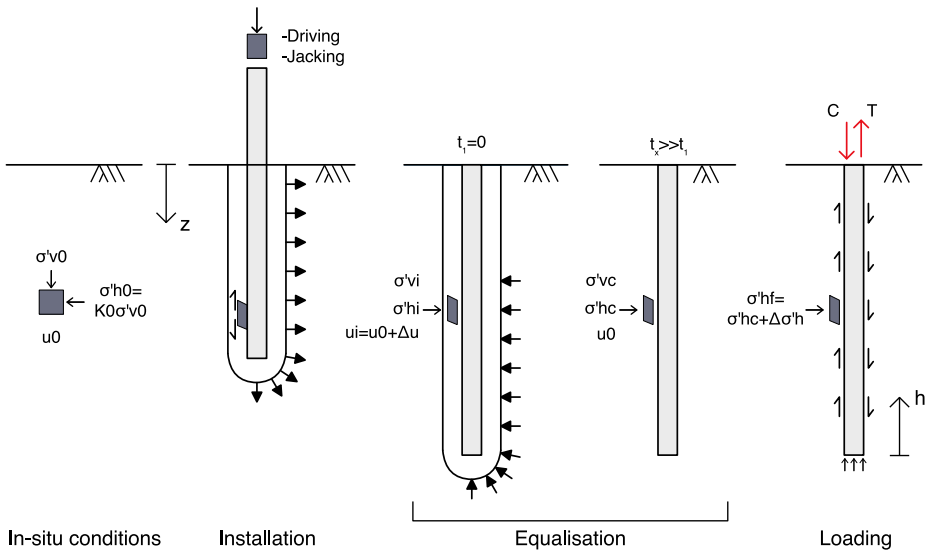


Figure 2.1: *Illustration of the pile cycle (adapted from Randolph and Gourvenec (2011)).*  $0$  = initial conditions,  $i$  = installation,  $c$  = after equalisation,  $f$  = at failure.

### 2.1 Installation

The first step in the pile cycle is the *installation* of the pile elements in the soil. Installation of displacement piles in soft clays results in a complex kinematic process that generates large distortions in the soil around the pile. Consequently, the soil properties and stress conditions adjacent to the pile shaft will change significantly. This new state will govern the future response of the pile (Lehane and Jardine 1994). Numerous experimental investigations have been reported on pile installation in soft soils, as summarised for example by Jardine and Potts (1988), Hunt (2000), Pestana et al. (2002) and Karlsrud

(2012).

Based on these and many other investigations, analytical and numerical models have been developed to capture the kinematics of pile installation; some of these are listed in Table 2.1. The most popular analytical approaches are the cavity expansion method CEM (Randolph, Carter, et al. 1979; Carter et al. 1979; Yu 2013) and the strain path method SPM (Baligh 1985; Whittle 1987; Sagaseta et al. 1997). On the other hand, several numerical techniques has been employed, as for example the Eulerean (Dijkstra et al. 2011) or the Material Point Method (MPM) (Beuth 2012). These numerical frameworks are then combined with soil constitutive models to obtain the pile-soil system behaviour. Despite the many advances in modelling the installation effects and the soil response, these methods are currently seldomly used in engineering practice.

Table 2.1: Analytical and numerical methods for approximation of pile installation.

Method	Description	Reference
Cavity Expansion Method (CEM)	Expansion of a cylindrical cavity.	Randolph, Carter, et al. 1979; Carter et al. 1979; Castro and Karstunen 2010; Yu 2013
CEM + Shear shaft	CEM together with an applied vertical displacement at the pile shaft boundary.	Pham et al. 2010; Basu et al. 2013 Sheil et al. 2015
Strain Path Method (SPM)	Steady flow around a penetrating element.	Baligh 1985; Whittle 1987; Aubeny 1992; Sagaseta et al. 1997; Yu et al. 2000; Liu et al. 2014
Eulerian	Mesh independent numerical analysis. Flow of soil around the pile.	Dijkstra et al. 2011
Press-replace method (PRM)	Stepwise pile penetration by pushing a small increment $\Delta\delta$ and replace soil for pile material. No change in reference geometry.	Engin et al. 2015 Tehrani et al. 2016
Updated Lagrangean (UL-FEM)	Modification/update of the finite element mesh after each calculation.	Sheng et al. 2009
Arbitrary Lagrangean Eulerean (ALE)	Material particles move through a fixed finite element mesh. Use of convected coordinate system.	Berg 1994, Sheng et al. 2009, Sabetamal et al. 2016
Material Point Method (MPM)	From the same family as ALE with an additional cloud of material points.	Beuth 2012; Ceccato et al. 2016

Displacement piles can be installed by either pile jacking or pile driving. In the latter case, the degree and extend of disturbance will be larger than the former due to the cyclic

loading/unloading from the stress wave propagation in the pile and soil from each hammer blow. Another issue with pile driving is that the stress wave in the pile (reflected from the pile base) generates tension loads that can crack the concrete. This can lead to a reduction in the cross section stiffness, corrosion of the steel reinforcement and spalling of the concrete (Kempfert and Gebreselassie 2006). More details of possible driving methods are given in Fleming et al. (2008) and Tomlinson and Woodward (2014).

As the pile penetrates in the ground, the soil at the toe is distorted, pushed downward and then displaced laterally. These processes destroy the initial soil structure and stress history. For very low permeability clays, there is nearly no volume change during installation (i.e. undrained conditions). The kinematics for deep penetration can be analytically approximated with the steady flow approach applied in the Strain Path Method (SPM) (Baligh 1985). The steady-state penetration assumption has been observed by field test with fully instrumented piles in soft clay (Lehane and Jardine 1994). Sagaseta et al. (1997) further developed the SPM and incorporated the ground surface effects in the Shallow Strain Path Method (SSPM). In both the SPM and SSPM, the large strain zone concentrates within  $1D$  from the pile shaft. Field measurements show similar vertical and radial strains that are confined within  $0.5D$  and  $1.5D$ , respectively, from the pile shaft (Zeevaert 1983; Pestana et al. 2002).

Total stresses in the soil increase during installation as the soil is displaced to accommodate the pile volume. This change in total stresses is directly related to the changes in pore water pressure during undrained penetration, as the soft clay is restricted to contract with no volume change (Randolph and Gourvenec 2011). These changes are relatively independent of the pile diameter (Pestana et al. 2002). Field observations have shown changes in  $\Delta\sigma_h$  of the same magnitude as  $\Delta u$  during single and pile group installation, as for example in Onsøy clay (Karlsrud 2012) and north-west Stockholm clay (Johansson and Jendebý 1998) respectively. Randolph and Gourvenec (2011) suggest that the magnitude of  $\Delta\sigma_h$  can be related to the undrained shear strength  $S_u$  of the clay and is typically in the range of  $4 - 6 S_u$ .

Table 2.2 shows some findings from studies where excess pore water pressure was measured at the shaft or adjacent to the pile directly after installation for normally to slightly overconsolidated soft clays. Some authors correlate the installation excess pore water pressure ( $\Delta u_i$ ) to the undrained shear strength ( $S_u$ ) of the clay. This correlation could be influenced by sample disturbance, testing techniques and site specifics as  $S_u$  profiles vary. Therefore, it is better to use the in-situ vertical effective stress for normalisation.

Roy et al. (1981) proposed Equation 2.1 as a modified version of the analytical expression given by Lo and Stermac (1965) to estimate the installation excess pore water pressure at the pile shaft. In their expression, the soil stress history is considered (OCR).

$$\frac{\Delta u_i^{max}}{\sigma'_{v0}} = (1 - K_0) + OCR \left( \frac{\Delta u}{p'} \right)_{max} \quad (2.1)$$

Table 2.2: Normalized excess pore water pressure directly after installation

Reference	Site	$\Delta u_i / \sigma'_{v0}$	Note
B.H. Fellenius (1972)	Bäckebo	0.4	$\approx 1.5D$ from shaft <sup>1</sup>
Torstensson (1973)	Bäckebo	1.6 – 2.5	At shaft
Roy et al. (1981)	Saint-Alban	2.0 – 2.1	At shaft
Lehane and Jardine (1994)	Bothkennar	1.9 – 2.1	At shaft
Johansson and Jendeby (1998)	Tibble	0.3 – 0.4	$\approx 4.2D$ from shaft
Pestana et al. (2002)	S.F. Bay Mud	0.9 – 1.1	$\approx 1D$ from shaft
Karlsru	Onsøy	1.5 – 1.6	At shaft

<sup>1</sup> It is possible that the piezometer deviated away from the pile during installation.

where  $\sigma'_{v0}$  is the initial vertical effective stress,  $K_0$  is the coefficient of earth pressure at-rest,  $p'$  is the consolidated mean effective stress in a triaxial test before shearing,  $\Delta u/p'$  is the ratio of maximum excess pore water pressure in undrained triaxial compression at large strains and  $OCR$  is the vertical overconsolidation ratio. Theoretical studies by Randolph, Carter, et al. (1979) using the cavity expansion method (CEM) and an elastic perfectly-plastic model suggested an increase in the mean total stress next to and on the pile shaft given by Equation 2.2 and 2.3:

$$\Delta p(r) = \Delta u_i(r) = 2S_u \ln(R/r) \quad \text{for } r_0 \leq r \leq R \quad (2.2)$$

with  $R^2 = (G_{50}/S_u)r_0^2$

$$\Delta p = \Delta u_i^{max} = S_u \ln(G_{50}/S_u) \quad (2.3)$$

where  $G$  is selected as  $G_{50}$ , the secant shear modulus at 50% of peak deviator stress from CAUC triaxial (Karlsru 2012),  $r_0$  is the pile radius and  $S_u$  the undrained shear strength of the clay. In their calculations for normally and slightly overconsolidated clays,  $\Delta u_i^{max}$  is approximately  $3.4 - 4.4 S_u$ . These equations were corrected to account for the change of mean effective stress during shearing (contraction or dilation effect), resulting in Equation 2.4:

$$\Delta u_i = (p'_i - p'_f) + S_u \ln(R/r) \quad (2.4)$$

where  $p'_i$  is the initial mean effective stress and  $p'_f$  mean effective stress at failure. For Bäckebo clay, Torstensson (1973) proposed a  $G_{50} = 100 - 150 S_u$ , with  $S_u$  from the uncorrected shear vane test. This  $G_{50}$  range is similar to that proposed by Karlsru

(2012) for Onsøy clay, with  $G_{50} = 100 - 200 S_u$ , using the  $S_u$  from DSS and triaxial tests. As an example, a  $G_{50} = 150S_u$  in Equation 2.3 gives a  $\Delta u_i^{max} = 5S_u$ , which, by assuming that  $\Delta\sigma_h = \Delta u_i^{max}$ , is equivalent to the average of the range reported in Randolph and Gourvenec (2011).

As the pile continues to penetrate further, total stresses and excess pore water pressure far above from the pile toe tend to reduce until they reach a steady state, where the pile slides on the pile-soil interface (quasi-static penetration). For Bothkennar clay, Lehane and Jardine (1994) found this limit to be around  $15D$  from the pile toe and for Saint-Alban clay, Roy et al. (1981) observed this threshold at approximately  $8.5D$ . Similar behaviour was observed in the Onsøy tests described by Karlsrud (2012). When the pile reaches its final depth, unloading and relaxation can take place with additional reduction of total horizontal stress, with small or no change in excess pore water pressure (i.e. decrease in effective stress). This was observed by Johansson and Jendebý (1998) and Pestana et al. (2002).

Installation of long piles differs from the short ones. The long piles can deviate from the vertical alignment and experience bending or “beating”<sup>1</sup>(B.H. Fellenius 2015). As a consequence, the bearing capacity can vary from pile to pile as the stress conditions along the pile shaft are not uniform (Karlsrud 2012). However, the possibility for the pile to buckle under these conditions is minimal (Alén 2015).

## 2.2 Set-up period

The *set-up* period is the time when the bearing capacity recovers due to the equalization of excess pore water pressures (increase of effective stresses) and ageing in the clay. The latter effect is related to creep and thixotropy (Augustesen, Andersen, et al. 2006).

Recovery in clay shear strength and stiffness has been observed during a rest period without change in water content or effective stress after intense distortion (Seng and Tanaka 2012). In colloid science this is known as thixotropy. Mewis and Wagner (2009) define this phenomenon in terms of the colloid micro-structure (i.e. fabric in soils), where the latter will break down into separated flocs when flowing, decreasing in size as the strain rate increases. The micro-structure will return when the strain rate decreases and recovers during rest conditions. Therefore, after some time during the pile set-up stage, the clay micro-structure will reach a new equilibrium state after which thixotropic effects will be minimal compared to other processes, such as creep (Seng and Tanaka 2012).

As the clay consolidates, the excess pore water pressure dissipates and the initial void ratio decreases. The preferred flow path for the water will be in the radial direction (Randolph, Carter, et al. 1979). The equalisation time depends on the hydraulic conductivity and stiffness of the clay. Remoulded high sensitive clays can have consolidation coefficients

---

<sup>1</sup>Strong shake/movement of the piles, specially in the lateral directions.

on the order of 0.1 to 0.01 of that from natural undisturbed conditions (Zeevaert 1983). Experience in Gothenburg clay show equalisation times from 3 to 6 months (B.H. Fellenius 1972). The reduction in void ratio will translate into an increase in the undrained shear strength of the clay next to the shaft. The latter has been observed in the field (Roy et al. 1981; Zeevaert 1983; Karlsrud and Haugen 1985) and by numerical approximations (Whittle 1987) (see Figure 2.2 and 2.3).

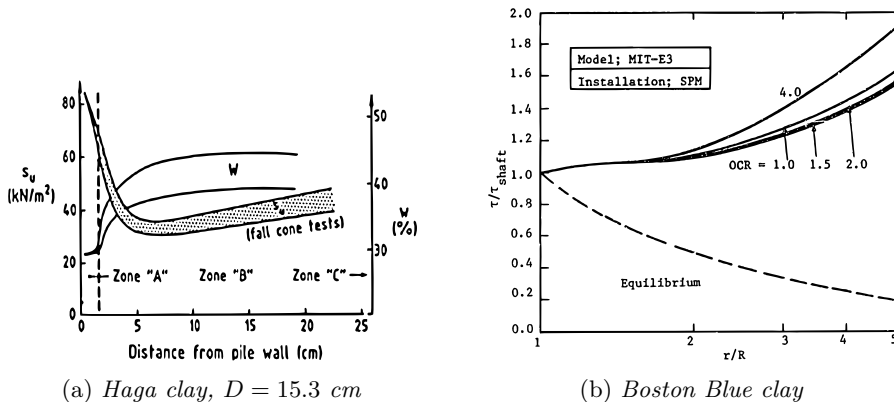


Figure 2.2: (a)  $S_u$  from fall cone test and  $w_n$  from soil adjacent to pile shaft (Karlsrud and Haugen 1985), (b) shear strength after equalisation of installation pore water pressures from numerical analysis (Whittle 1987).

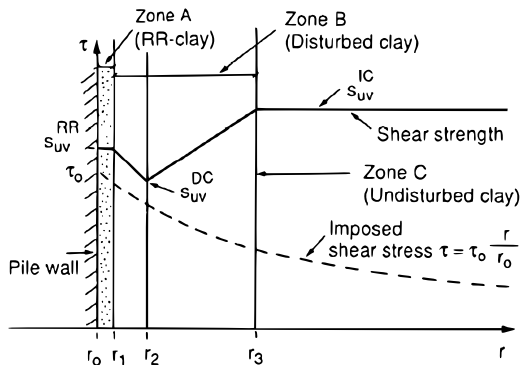


Figure 2.3: Illustration of shear strength after pile set-up and from pile loading (Karlsrud, Nadim, et al. 1990). Critical zone at a distance  $r_2$  from shaft.

The effective stresses will increase to a new equilibrium state after all the excess pore water pressure is dissipated. Previous studies found that soil stresses change significantly within  $10D$  from the shaft surface (Randolph, Carter, et al. 1979). Lehane and Jardine (1994) observed that changes in radial effective stress depend on the clay OCR and stiffness (directly proportional), and sensitivity (inversely proportional). In addition, Karlsrud (2012) observed a trend for the plasticity index, with higher values showing

a larger recovery of the horizontal effective stress after installation. Table 2.3 shows some examples of the final ratio between the initial  $K_0$  and the final  $K_c$  ( $\sigma'_{hc}/\sigma'_{v0}$ ) after equalisation of  $\Delta u_i$  (see also Jardine and Potts 1988 and Karlsrud 2012). It is important to note that measurements of total normal stress at the shaft can be affected by: (1) non-uniform stress distribution around the sensing membrane (Torstensson 1973) and (2) soil heterogeneity at the sensor depth.

Table 2.3: Change in radial effective stress after consolidation

Site	$S_t$	OCR	PI(%)	$K_c^1$	$K_c/K_0$
Drammen	4 – 8	1	10 – 20	0.50 <sup>2</sup>	n.a.
Onsøy	4 – 8	1.3	40	0.4 – 0.5	0.75
Bothkennar	10 – 13	1.8	30	0.8	1.14

<sup>1</sup> Far above the toe;  $K_c = \sigma'_{hc}/\sigma'_{v0}$ .

<sup>2</sup> Back-calculated from the test results. Can be up to 15 – 20% higher before loading, see stress path in Lehane and Jardine (1994).

Hunt et al. (2002) carried out advanced field tests before and after installation of an instrumented pile in San Francisco Bay Mud. They observed that the soil around the pile was significantly remoulded, had lower water content and higher density. Measurements of shear wave velocities showed a decrease from the initial conditions near the pile shaft although higher density values. Far field measurements showed the opposite effect (i.e. increase in shear wave velocities, see Figure 2.4). They considered the reduction to be caused by remoulding and destructuration of the soil.

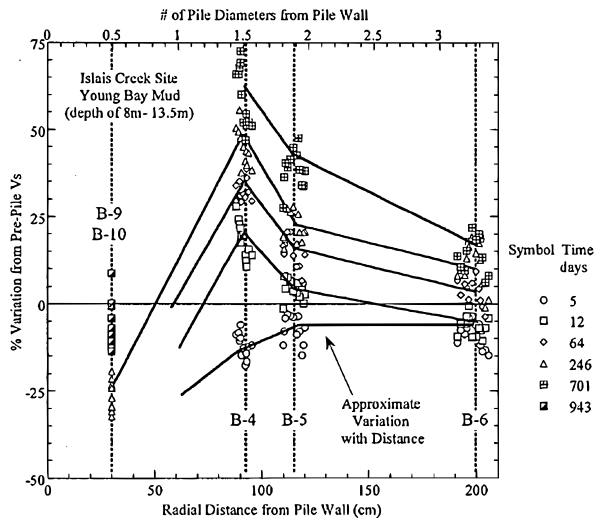


Figure 2.4: Percentage change of shear wave velocity ( $V_s$ ) from initial conditions during and after equalisation of installation  $\Delta u$ . Closed-ended pile  $D = 0.6$  m and  $L = 35$  m. Equalisation after approximately 250 days (adopted from Hunt et al. 2002).

In addition to the field test, Hunt et al. (2002) performed advanced laboratory tests on disturbed soil sampled taken adjacent to the pile shaft after the equalisation of installation pore pressures. One dimensional compression tests showed a small reduction in the re-compression index  $C_r$ , followed by a smooth transition to the virgin compression line, with the compression index  $C_c$  approaching the intrinsic value  $C_{ci}$ . The samples did not show a clear pre-consolidation pressure (Casagrande's method) and appeared to be normally consolidated. This indicates that the soil history, fabric and structure was destroyed during pile installation and the soil was consolidated to stresses similar or slightly larger than in-situ conditions. Anisotropically consolidated triaxial tests (CAUC) consolidated to in-situ stresses showed no peak nor softening as for the initial undisturbed samples. Instead, the soil hardened and reached critical state at very large strains ( $>10\%$ ). The effective stress path on all samples showed a contractive response. Direct simple shear tests consolidated to in-situ stresses showed larger strength than the samples taken before installation. Hunt et al. (2002) attribute this difference to the change in layer orientation due to installation.

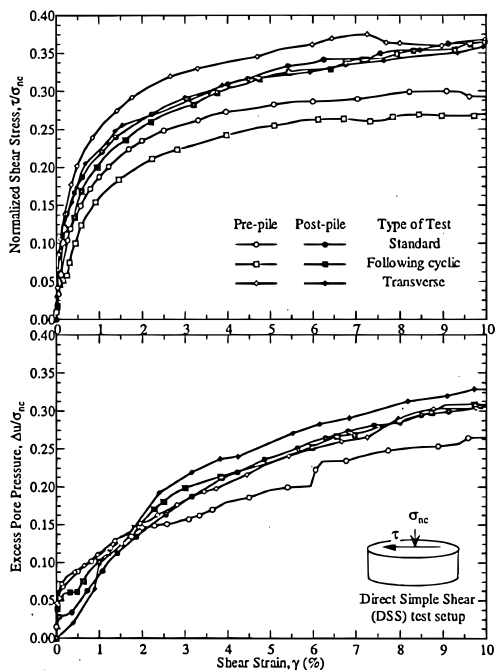


Figure 2.5: DSS at 7.3m for pre- and post-installation. Following cyclic = after 3 loading cycles; Transverse = rotated  $90^\circ$  (adopted from Hunt et al. 2002).

## 2.3 Pile loading

It is well known from experimental and theoretical considerations that the bearing capacity of a pile is directly proportional to the normal effective stress and interface friction angle at the pile-soil interface (i.e. Coulomb friction) (Randolph and Gourvenec 2011; Lehane and Jardine 1994). During pile loading, the observed response is a combination of soil and pile element behaviour. The pile bearing capacity and settlement are a function of the effective stresses and soil properties at the pile shaft, with the load distribution along the pile length depending on the pile stiffness, shaft area and end-bearing capacity.

The load applied at the pile head will transfer as shear to the surrounding soil. Randolph and Wroth (1978) described this transfer mechanism as concentric cylinders in shear around the pile shaft, as illustrated in Figure 2.6. This approximation assumes that the main displacement component happens in the vertical direction, with negligible radial displacement. Using linear elasticity and assuming vertical equilibrium in these cylinders, the distribution of shear stress in the radial direction is approximated by Equation (2.5):

$$\tau(r) \approx \frac{\tau_0 r_0}{r} \quad (2.5)$$

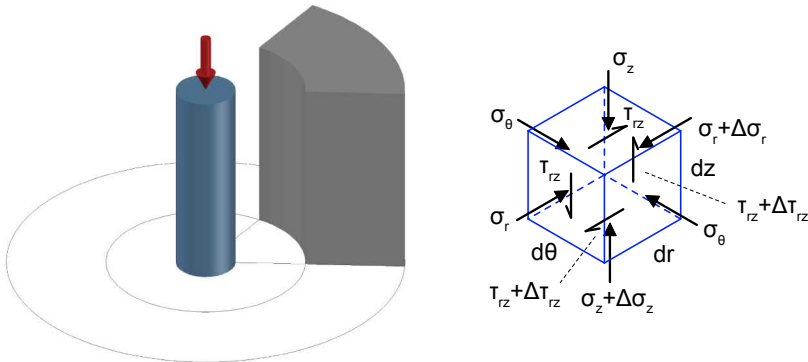


Figure 2.6: *Concentric cylinder model of soil stresses around the pile shaft.*

where  $\tau_0$  is the shear stress at the pile-soil interface at the pile radius  $r_0$ . The shear stress will decrease with increasing distance from the pile surface (see Figure 2.7). If the pile surface is rough enough, one can see from Equation (2.5) and in Figure 2.3 that failure will occur within the soil near the interface where the applied shear stress will be larger than the available shear strength (Zeevaert 1983).

In a similar manner, the shear strain is approximated by neglecting the radial displacements and assuming that simple shear conditions prevail. This can be calculated by Equation

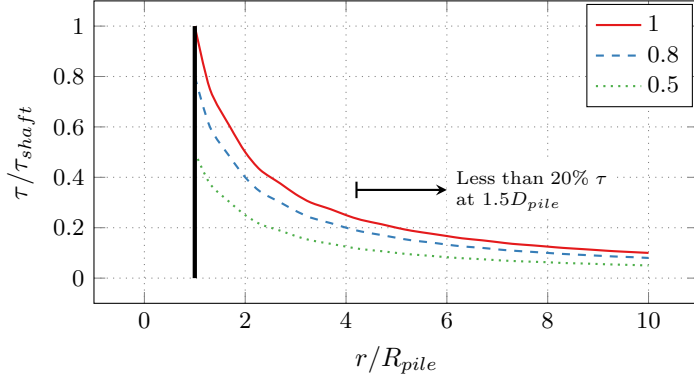


Figure 2.7: *Distribution of shear load from the pile shaft to the soil from the concentric cylinder model.*

(2.6). As observed, the pile settlement will depend on the shear stiffness of the surrounding clay.

$$\gamma(r) \approx \frac{\tau(r)}{G(r)} \approx \frac{\tau_0 r_0}{rG(r)} \quad (2.6)$$

where  $G(r)$  is the shear stiffness of the soil.

As the pile is loaded, the shear stress at the pile shaft increases, generating a principal stress rotation in the soil (Randolph and Wroth 1981). The latter will influence the shear strength of the soil adjacent to the pile, as the failure surface depends on the intermediate principal stress (Lode angle dependency) (Hicher and Lade 1987). Figure 2.8 illustrates the stress rotation for torsion of a soil element in cylindrical coordinates. The same effect will occur for the simple shear at the pile shaft (plane  $rz$  instead of  $z\theta$ ). This is representative for a soil element near the pile interface.

In clays, the loading stress path at the pile-soil interface is analogous to a constant volume direct simple shear test (DSS) and is relatively independent of loading direction. It is important to note that the DSS apparatus cannot impose true simple shear stress conditions due to its boundary conditions. Therefore, the strength obtained from this will slightly underestimate the ideal simple shear case (Doherty and Fahey 2011). This behaviour was observed by Lehane and Jardine (1994) for drained and undrained model pile field tests. In their tests, the resulting shear stress at the pile shaft caused a reduction of the radial effective stress of  $\approx 15\%$  at peak ( $0.85\sigma'_{hc}$ ) (see Figure 2.9). This reduction was smaller than in DSS tests on undisturbed samples. For the undrained pile tests the reduction was due to excess pore water pressure  $\Delta u$ , while for the drained case relaxation of the radial effective stress is observed. The friction angle from DSS tests was larger than

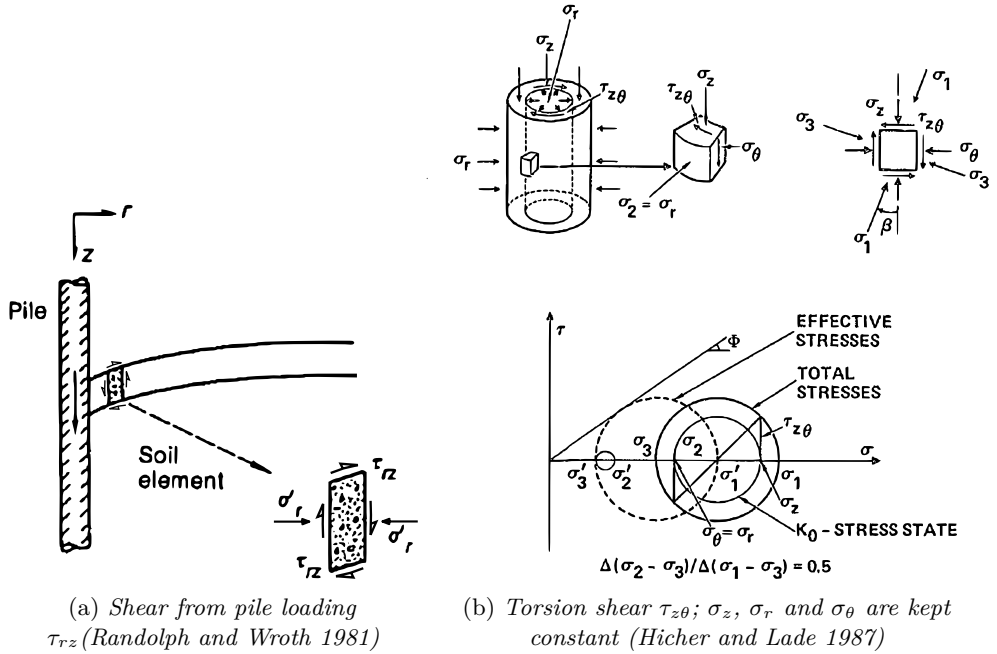


Figure 2.8: Principal stress rotation effect and Mohr's circle (in (b) the same applies for simple shear substituting  $\tau_{z\theta}$  with  $\tau_{rz}$ ).

those obtained in the pile tests. On the other hand, the friction angle from ring shear interface tests provided a better approximation for their pile tests (as expected due to the intense shearing from installation). Reloading of the failed piles showed no variation in the friction angle and the difference in bearing capacity was attributed to the changes of radial effective stresses at the onset of loading.

By using the effective principal stresses and ultimate Mohr circle, Zeevaert (1983) showed Equation (2.7) for the horizontal to vertical effective stress ratio at plastic failure.

$$\frac{\sigma'_h}{\sigma'_v} = \frac{1 - \sin^2 \phi'}{1 + \sin^2 \phi'} = K_f \quad (2.7)$$

where  $\phi'$  is the angle of internal friction of remoulded soil. Typical values of  $\phi'$  for soft soils range from  $25^\circ$  to  $35^\circ$ , which result in  $K_f$  ranging from 0.7 to 0.5. These values are in good agreement with those in Table 2.3.

For shaft bearing piles in tension, the ultimate bearing capacity is reached with very small pile-soil relative displacements. For soft clays, typical values range between  $(0.5 - 3\%)D_{pile}$  for field tests and  $(0.4 - 2\%)D_{pile}$  for laboratory tests (Mochtar and Edil 1988; Fleming

et al. 2008; Tomlinson and Woodward 2014). This displacement up to ultimate state is rather small and will depend on the soil response, independently of the pile diameter (B.H. Fellenius 2015). For compression loaded piles, the ultimate capacity is not always cleared defined as the pile base continues to provide additional bearing capacity with further penetration. A general rules is to define this capacity by a limit pile displacement, as for example  $\delta_{head} = 0.1D_{pile}$ . More details about different failure criteria can be found in Kempfert and Gebreselassie (2006).

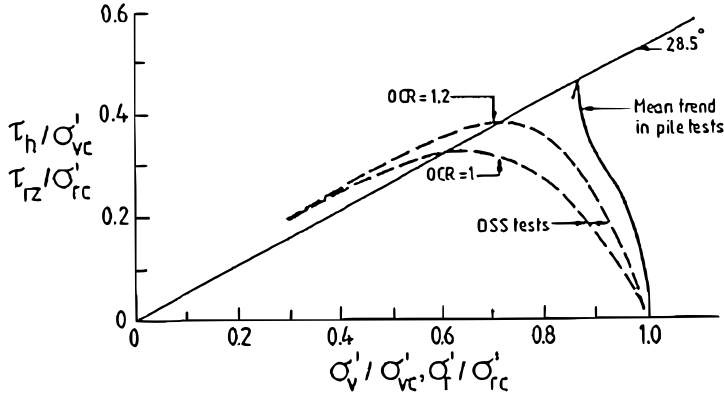


Figure 2.9: *Stress paths for soil at pile shaft and DSS of undisturbed samples from Bothkennar clay (Lehane and Jardine 1994.)*

### 2.3.1 Short-term pile loading

In general, pile research has focused on the short-term bearing capacity. This has been investigated by testing model and prototype piles with static (e.g maintained load test (MLT), quick-maintained load test (QML) and constant rate of penetration (CRP)), dynamic and statnamic methods (see Fleming et al. 2008 for more details). The results from these tests are often correlated to clay properties, as for example, the undrained shear strength, plasticity index, sensitivity and stress history (OCR) (Karlsrud 2014). The latter is done as the initial normal effective stress and soil properties at the pile shaft are difficult to estimate beforehand. With these correlations, piles are designed against failure in combination with safety factors.

For pile tests in soft clays, the soil rate effects are an important factor affecting all the above mentioned testing methods. Therefore, the measured pile capacity will be directly related to the type of test, i.e. the loading rate. Overall, pile tests are performed under fast loading rates where the soil response is undrained or partially drained. Depending on the stress path and boundary conditions, these fast rates can over-predict the bearing capacity. For example, Torstensson (1973) showed large differences in the ultimate bearing capacity between slow and fast loading rates for pile tests in Bäckebol clay (Gothenburg) as shown in Figure 2.10.

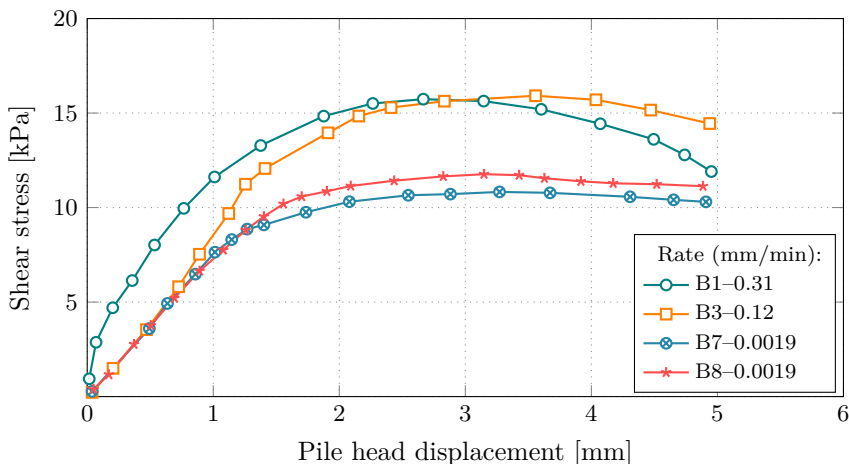


Figure 2.10: *Pile tests of short length concrete piles with different rates,  $D = 152$  mm and  $L = 100$  mm at 3.5–4.5 m depth (adopted from Torstensson 1973).*

Several authors have proposed corrections of the undrained shear strength of the clay for rate effects, for example by using the semi-logarithmic law in Equation (2.8)–(2.9) (Hansbo 1984) or the power law in Equation (2.10) (Torstensson 1973; Briaud and Garland 1985; Biscontin and Pestana 2001). The first model describes the change of  $S_u$  with respect to loading rate as a straight line in a semi-log plot, while the second model proposes a straight line in a log-log plot.

$$\frac{S_{u2}}{S_{u1}} = A + B \log(t_1/t_2 + C), \quad (2.8)$$

$$\frac{S_{u2}}{S_{u1}} = A + B \log(C) \quad \text{for } t = \infty \quad (2.9)$$

$$\frac{S_{u2}}{S_{u1}} = \alpha(t_1/t_2)^\beta \quad (2.10)$$

where  $A$ ,  $B$  and  $C$  for Equation (2.8)–(2.9), and  $\alpha$  and  $\beta$  for Equation (2.10) are empirical parameters obtained from curve fitting these equations to the undrained shear strength  $S_{u1}$ ,  $S_{u2}$  obtained from tests at various loading rates  $t_1$ ,  $t_2$ . These rate models are shown in Figure 2.11 using typical values for soft clays as for example  $A = 1$ ,  $B = 0.125$  and  $C = 0.15 \times 10^{-3}$ ;  $\alpha = 0.9 - 1.1$  and  $\beta = 0.02 - 0.10$  (Hansbo 1984; Briaud and Garland 1985; Lämsivaara 1999). The  $C$  parameter in Equation (2.8) and (2.9) establish a limit

decrease of  $S_u$  for very slow shearing rates.

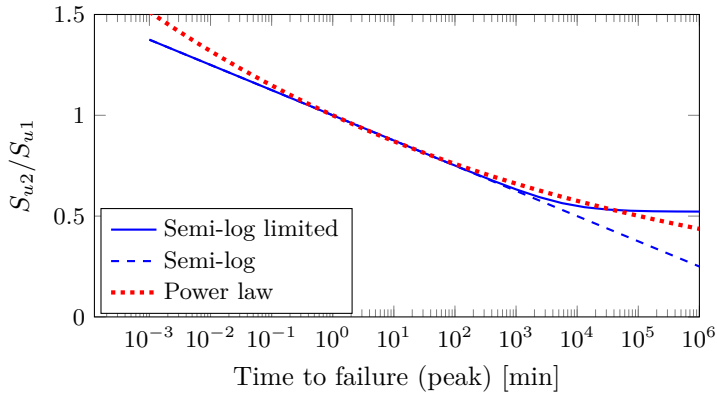


Figure 2.11: Variation of  $S_u$  with time to failure (shearing rate).

### 2.3.2 Long-term pile loading

Research on the long-term performance of piles is scarce. The majority of information available focuses on: (1) the load from negative skin friction due to subsidence of the surrounding soil and (2) on the increase of bearing capacity after installation. A third important, but less studied problem, is (3) the long-term settlement of the pile element under constant load. This settlement occurs due to the primary and secondary compression of the soil adjacent to the pile shaft under shear loading. Details for each point are given below.

#### Negative skin friction

Negative skin friction (NSF) acting on the shaft of a floating pile in soft soil arises from the relative displacement of the pile-soil interface. In this case, the soil settles faster relative to the shaft due to creep or effects that increase the effective stresses, e.g. on-going consolidation from surcharge loading or lowering of the groundwater table. As the pile is loaded for the first time, residual loads from NSF might develop following the installation and set-up period (B.H. Fellenius 1972). The NSF will give rise to an additional drag load on the pile and change the stress field around the shaft.

Part of the soil weight will be transferred to the pile by NSF, creating a relief on the effective vertical stress (opposite for positive skin friction) (Zeevaert 1983). This in turn could release horizontal effective stress, decreasing the available unit shaft resistance along the shaft affected by NSF. By assuming vertical force equilibrium in the pile influence zone,

the average decrease in effective vertical stress by depth can be obtained by numerically solving Equations (2.11) to (2.17) (see Figure 2.12). For practical purposes, the influence area factor  $n$  can be taken as 12 for isolated piles. However, in reality this factor depends on depth and pile spacing (see Zeevaert 1983).

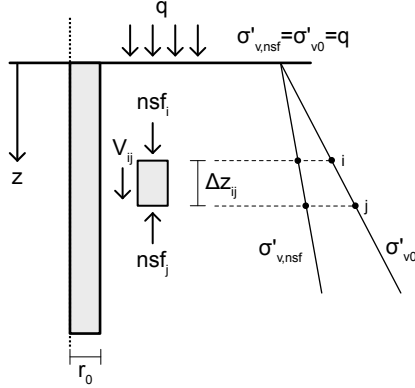


Figure 2.12: *Change of vertical effective stress due to NSF (adopted from Zeevaert (1983)).*

$$NSF_j - NSF_i = V_{ij} \quad (2.11)$$

$$NSF_i = (\sigma'_{v0,i} - \sigma'_{v,nsf,i}) a_i \quad (2.12)$$

$$NSF_j = (\sigma'_{v0,j} - \sigma'_{v,nsf,j}) a_j \quad (2.13)$$

$$V_{ij} = (2\pi r_0) \Delta z_{ij} \tau_{s,ij} \quad (2.14)$$

where for point  $i$  and  $j$ ,  $V$  is the shear load at the  $\Delta z$  shaft,  $NSF$  is the drag load,  $a$  is the pile influence area,  $\sigma'_{v0}$  is the in-situ vertical effective stress,  $\sigma'_{v,nsf}$  is the reduced vertical effective stress due to negative skin friction,  $\tau_s$  is the average shear stress from negative skin friction and  $r_0$  is the pile radius.

$$a_i = a_j = \pi(nr_0)^2 \quad (2.15)$$

$$\tau_{s,ij} = 0.5K_f(\sigma'_{v,nsf,j} + \sigma'_{v,nsf,i}) \tan(\phi') \quad (2.16)$$

where  $n$  is the influence area factor,  $K_f$  is the coefficient of lateral pressure at failure and  $\phi'$  is the effective friction angle of the soil. Solving for  $\sigma'_{v,nsf,j}$ ,

$$\sigma'_{vnsf,j} = \sigma'_{v0,j} - (V_{ij} + NSF_i) a_j \quad (2.17)$$

As the pile is loaded by the drag load, this will displace relative to the soil, developing positive skin friction. Therefore, the pile and soil will move relative to each other in order to have equilibrium. The point along the shaft where the pile and soil displacement are equal (zero relative movement) and where the forces are in equilibrium, is called the neutral plane (see Figure 1.2). This plane is located within a transition zone, whose length will depend on the gradient of the relative pile-soil displacement (B.H. Fellenius 2006). The NSF phenomenon is always present for piles, since extremely small soil settlements are sufficient for it to emerge (B.H. Fellenius 2015).

During compression loading, part or all of the downdrag load will be eliminated where the pile displacement is larger than that caused by the soil settlement. After the pile-soil system reaches new equilibrium conditions, the NSF will increase again as the soil continues to settle relative to the pile (B.H. Fellenius 1972). The opposite is for tension loading, as the relative movement of the pile is similar to that from the negative skin friction (see Figure 2.13). In this case, the tension load will be counterbalanced by the pile weight, the drag load and the not yet mobilised negative shaft resistance. In both cases the pile bearing capacity will not be affected by negative skin friction. However, the stiffness will be different for the tension loading as part of the tension shaft resistance is initially mobilised.

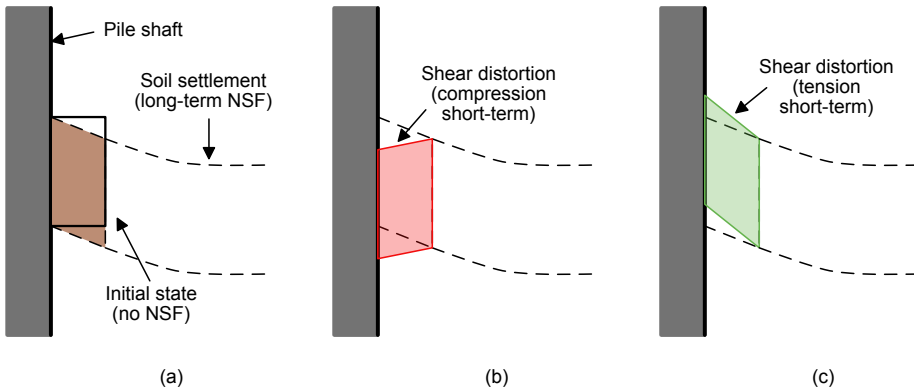


Figure 2.13: *Illustration of the deformation due to NSF in soil adjacent to the pile shaft. (a) Long-term soil settlements, (b) Short-term compression loading, (c) Short-term tension loading.*

## Evolution of bearing capacity over time

The set-up effects in soft soils can be divided into three components in time: (1) the equalisation of excess pore water pressure, (2) ageing effects and (3) creep. Note that this separation is assuming that one process is dominant over the other during a certain time, but not completely independent (i.e. they occur simultaneously).

During the equalisation of excess pore water pressures there is a regain in effective stresses in the soil. At the same time, ageing and creep effects occur. It is not yet clear which mechanisms take place during the ageing of piles in clay. A plausible hypothesis is that circumferential arching develops during installation, relaxing with time due to creep (Augustesen 2006). Other possible explanations are the creation of new bonds and rearrangement of the fabric due to thixotropy effects. All these effects push the failure zone further out in the soil-soil interface. However, these hypotheses have been proven hard to verify from experimental investigations. Instead, empirical relations (often called *time functions*) are used to quantify the increase in bearing capacity with time due to these ageing effects. These are derived from pile tests where the same pile is loaded several times within a certain time period (staged testing) or different piles are loaded once after certain time (unstaged testing). Augustesen, Andersen, et al. (2006) validated the time function in Equation 2.18 proposed by Skov and Denver (1988) by using a large pile test database.

$$Q = Q_0 \left\{ 1 + \Delta_{10} \log_{10} \left( \frac{t}{t_0} \right) \right\} \quad (2.18)$$

where  $Q$  is the axial bearing capacity at time  $t$  after installation,  $Q_0$  the reference axial bearing capacity at the reference time  $t_0$  and  $\Delta_{10}$  is the set-up factor (capacity increase per decade). Based on statistical studies of a large database of pile load tests, Augustesen (2006) recommends  $\Delta_{10} = 0.24$  for staged and  $\Delta_{10} = 0.13$  for unstaged loading with a  $t_0$  of 100 days. Karlsrud, Jensen, et al. (2014) proposed Equation 2.19 correlating  $\Delta_{10}$  with OCR and PI for first time loading and  $t_0 = 100$  days. For a pile in soft clay, a reference time of 100 days will in general be sufficient for complete consolidation, with just ageing effects taking place (Karlsrud, Jensen, et al. 2014).

$$\Delta_{10} = 0.05 + 1.3 \left( 1 - \frac{PI}{50} \right)^2 OCR^{-0.5} \quad (2.19)$$

Recently, Karlsrud, Jensen, et al. (2014) investigated the effects of sustained loading in the increase of bearing capacity with time. In their study, piles were loaded 6 months after installation with a sustained load ratio of  $Q/Q_{ult} = 0.6$ . The piles were loaded to failure

18 months after pre-loading. The sustained load enhanced the shaft resistance compared to first time load test of non-loaded piles with the same set-up time. An additional increase of 10 to 20% was measured for slightly over-consolidated medium to high plasticity clays. Karlsrud, Jensen, et al. (2014) stated that the results support the plausible theory of increase of effective stresses at the shaft due to creep relaxation of arching effects.

## Creep of piles

Creep<sup>2</sup>behaviour in soils is defined as the ongoing deformations in time under constant effective stress. In pile foundations, the term is used in mixed conditions, and two main scenarios are identified.

The first case is related to the long-term static bearing capacity. For piles in soft clays this capacity corresponds to the maximum load that the pile can sustain under serviceability state without excessive displacements. This limiting load is called the *creep load* and represents the threshold for creep failure under long-term static loading. The concept received greater attention around the 1970s and 1980s, from soft soils rate effects studies and observations made on the rate of deformation in pile field tests (Bjerrum 1973; Torstensson 1973; Gallagher and St John 1980; Hansbo 1984). Several studies have shown this threshold to be between 0.7 to 0.8  $Q_{ult}$  from short-term loading tests (Gallagher and St John 1980; Bengtsson and Sällfors 1983). However, this creep load is obtained from looking at the deformation rates under constant total stresses and not effective stresses. Therefore, pure creep does not take place under this condition and the term is inaccurate.

The second area focuses on the long-term settlements of the pile foundation as a whole. For service loads, these settlements are considered small relative to the initial deformation after loading (Poulos et al. 2002). However, these settlements can be beneficial for pile-raft foundations if properly designed (Jendebý 1986; Randolph 2003).

The long-term displacement components are due to (1) primary and (2) secondary compression, i.e. creep. At the pile-soil interface the main creep displacement component results from deviatoric creep. The creep rate will be directly proportional to the amount of mobilized shear  $\tau/\tau_{ult}$ , as a result of the remoulded and partially remoulded soil behaviour adjacent to the pile. In the remoulded zone, the creep rate for a given load will be smaller compared to further away from the pile shaft. This is due to the destructuration process caused during pile installation (i.e. intrinsic creep rate). The significance of the partially remoulded soil is a function of the pile load influence area, as this zone will extend with increasing load. The creep rate will decrease with time as the soil fabric reaches equilibrium under the applied load (Bjerrum 1973).

Table 2.4 summarizes results from experimental studies of pile creep in soft soils. Figure 2.14 shows some of the data extracted from Table 2.4 (tests 1 to 5). The pile head displacement is normalized with the pile diameter  $D$  or equivalent diameter  $D_{eq}$  for

---

<sup>2</sup>See Section 3.2 for the complete description of creep in soils.

non-circular piles (e.g. for square piles  $D_{eq} = 4l/\pi$ ). This normalisation is adopted assuming that for a constant load, the creep shear strains can be obtained from the analogy of DSS loading as shown in Figure 2.15. In this case, it is believed the strains will concentrate within  $1D$  and that these are uniform along the complete pile length. In addition, it is assumed that the pile and soil deform as a continuum up to peak (St. John et al. 1983). In all studied cases the creep rate decreased with time. A logarithmic model as that given in Equations (2.20) and (2.21) for oedometer conditions fit well this decrease in creep rate.

$$\varepsilon_v^c = \mu^* \ln \frac{t_{ref} + t}{t_{ref}} \quad (2.20)$$

$$\dot{\varepsilon}_v^c = \frac{\mu^*}{t_{ref} + t} \quad (2.21)$$

where  $\varepsilon_v^c$  is the volumetric creep strains,  $\mu^*$  is the modified creep parameter obtained from 1D compression,  $t_{ref}$  is the reference time for the onset of pure creep strains and  $t$  is the increase in time to extrapolate the creep strains.

From previous research it can be summarised that:

- Long-term accumulated pile head displacements are larger than those from short-term pile loading tests.
- The creep rate is a function of the applied load  $Q/Q_{ult}$ .
- The creep rate gradually decreases with time for loads below a certain threshold governed by creep.
- Creep rupture<sup>3</sup> can take place if the pile is loaded above the threshold where perhaps relaxation take place and/or creep generated pore pressure accumulate in the critical strain zone, reducing the normal effective stress.

For long piles, the creep of the pile material (e.g. concrete or steel) is an important component in the long-term deformation measured at the pile head. However, no information was available about the creep of the pile material in the previous summarised investigations.

---

<sup>3</sup>See Section 3.3 for a complete definition of creep rupture.

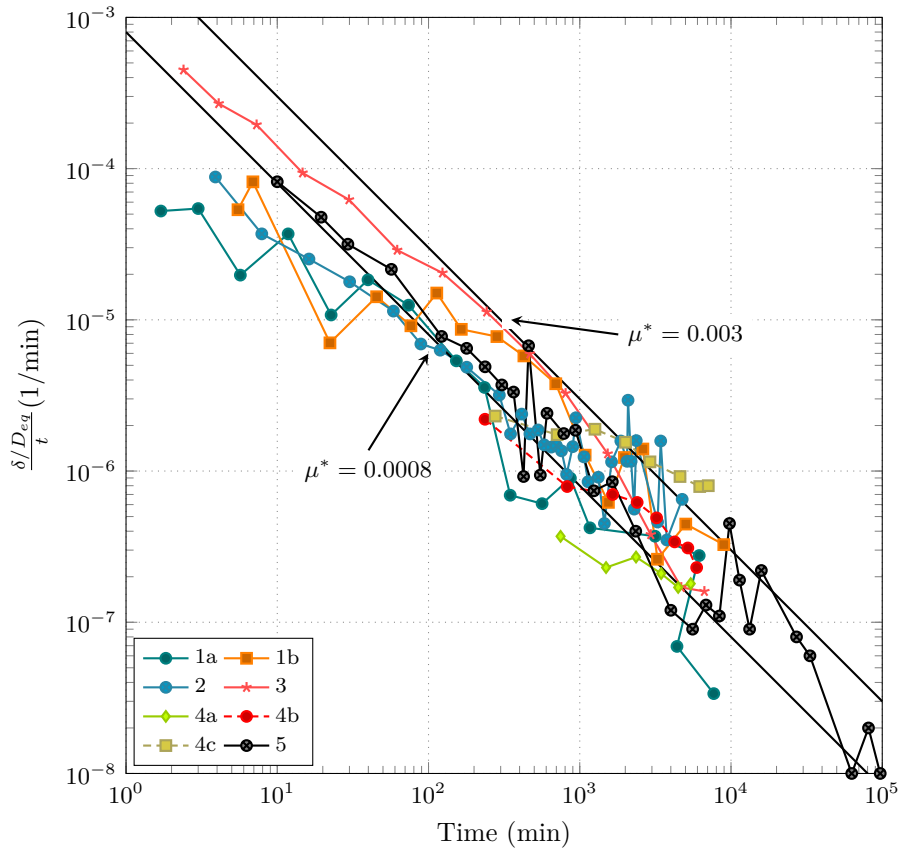


Figure 2.14: Rate versus time from tests in Table 2.4. Bound lines calculated using Equation (2.21).

Table 2.4: Overview of investigations on long-term behaviour of piles.

Reference	Site	Soil	Time(d)	Observations	Parameters	
1	Ramalho Ortigao and Randolph 1983	Brazil	Highly OC stiff boulder clay <sup>2</sup>	41	Large primary consolidation settlements after $Q/Q_{ult} = 0.4$ .	$Q/Q_{ult}=(a)0.51$ and (b)0.62, $D=203\text{mm}$ , $L=9.5\text{m}$ , $S_u=120\text{ kPa}$
2	Bengtsson and Sällfors 1983	Sweden	Göteborg slightly OC soft clay	4	Second test on pre-failed pile with sustained load after 51 days set-up.	$Q/Q_{ult}=0.60-0.67$ , $D=340\text{mm}$ , $L=26\text{m}$ , $S_u=20-60\text{ kPa}$ , $S_t=10-20$ , $w_n=70\%$
3	Bengtsson and Sällfors 1983	Sweden	Göteborg slightly OC soft clay	4.5	Nordstan test for HEB180 anchor beam.	$Q/Q_{ult}=0.75-0.80$ , $D \approx 175\text{mm}$ , $L=23\text{m}$ , $S_u=30-50\text{ kPa}$ , $S_t=10$ , $w_n=60-75\%$
4	Edil and Mochtar 1988	Lab <sup>1</sup>	NC Kaolin clay	$\approx 7$	Tertiary creep at $Q/Q_{ult} = 0.95$ . Negligible volume change (pre-sheared sample).	$Q/Q_{ult}=(a)0.34$ , (b)0.69 and (c)0.91, $D=27\text{mm}$ , $L=143\text{mm}$
5	Kuwabara et al. 1993	Saitama, Japan	Satte NC clay	$\approx 120$	No pile failed by creep for $Q/Q_{ult} < 0.4$	$Q/Q_{ult}=0.31$ , $D=328\text{mm}$ , $L=4.5\text{m}$ , $S_u=20-30\text{ kPa}$ , $w_n=40-50\%$
6	Eide et al. 1961	Norway	Drammen NC silty marine clay	73-95	$\approx$ equal long- and short-term $Q_{ult}$ . Large primary consolidation settlements after $Q/Q_{ult} = 0.4$ . Only primary consolidation was measured.	
7	Karlsrud, Jensen, et al. 2014	Norway	Onsøy OC marine clay	540	Sustained load $Q/Q_{ult} = 0.6$ . Long-term $Q_{ult}$ 20% larger than short-term. No displacement data available.	

<sup>1</sup> Laboratory

<sup>2</sup> Not soft clay, but similar trend observed.

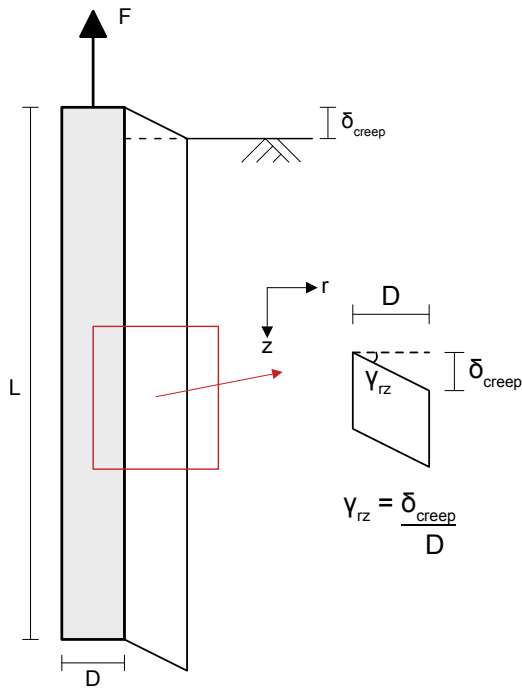


Figure 2.15: *Illustration of creep shear strains adjacent to the pile shaft.*

## 2.4 Pile capacity and settlement analysis

Most foundation design is based on empirical and semi-empirical methods calibrated with local field and laboratory tests (Randolph 2003). The empiricism originates from the complex kinematics in the soil during the pile installation, making it a challenge to assess post-installation conditions for subsequent loading. Augustesen (2006) listed many factors that potentially affect the bearing capacity and behaviour of piles in soft soils. However, no attempt is made to put these factors in a general framework of soft soil behaviour.

Commonly, the main concern in engineering of single piles is to estimate the maximum bearing capacity provided by the designed pile foundation and the soil. Other factors, such as the load distribution along the pile shaft and the long-term performance are usually neglected. This has led to design methods that are strongly based on empirical correlations that implicitly account for the uncertainties in the pile cycle (e.g. installation, set-up and stress state). The empirical component of each method is derived from local investigations under limited testing conditions. Therefore, there is an inherent uncertainty in the empirical factor related to (1) the sample quality and soil testing procedure, (2) the pile testing and measurement technique as well as (3) the interpretation of results. Table 2.5 gives an overview of these methods and detailed description can be found for example in Karlsrud (2014) and B.H. Fellenius (2015).

For soft clays the total stress  $\alpha$ -method is the most used approach to estimate the pile bearing capacity. Despite recognizing that the pile-soil interaction is effective stress based, this method remains rather popular due to the large amount of experience and its simplicity. Partial safety factors are combined with the empirical  $\alpha$  factor to calculate the design bearing capacity. Karlsrud (2014) recently proposed a new calibration for the  $\alpha$  factor. In his work, this parameter is related to the plasticity index and OCR of the clay. Comparison of a larger number of tests did not show any clear trend with respect to pile diameter, shape or length. In general, the  $\alpha$  correlation works well for estimating the short-term bearing capacity for relatively homogeneous soil deposits with nearly constant OCR and  $S_u/\sigma'_{v0}$  ratio with depth.

The long-term loading effects are considered in these methods using reduction factors. These can be applied to the soil properties, e.g. correction for rate effects, or directly to the calculated bearing capacity  $Q_{ult}$ . In Sweden, the characteristic undrained shear strength used in the  $\alpha$ -method is reduced by 30% to account for the long-term capacity (Eriksson et al. 2004).

Where more detailed analyses are required for estimating the load-displacement curve, the load-transfer methods have proven to be valuable tools. With this method the load distribution with depth can be estimated and rate effects can be incorporated (Randolph and Wroth 1978; Guo 2012; Q.-q. Zhang and Z.-m. Zhang 2012; B.H. Fellenius 2015).

Table 2.5: Estimation methods for pile bearing capacity

Method	Description	Equation
Total stress, $\alpha$	The undrained shear strength of the clay is correlated with the $\alpha$ factor to obtain the unit skin friction $\tau$ at the pile shaft. $S_u$ is generally obtained from laboratory DSS tests or in-situ vane shear tests.	$\tau = \alpha S_u$
Effective stress, $\beta$	The ratio between vertical and normal effective stress at the shaft and the effective friction angle of the pile-soil interface is correlated with the $\beta$ factor.	$\tau = \beta \sigma'_{v0}$ ; where $\beta = K_f \tan(\phi')$
Hybrid approach, $\lambda$	The mean vertical effective stress and the undrained shear strength are correlated with the $\lambda$ factor.	$\tau = \lambda (\sigma'_{v0,m} + 2S_{u,m})$
Standard Penetration test, SPT	The N-index from the SPT is correlated to the pile capacity. This method is very subjective and highly variable. Several equations are available.	
Cone Penetration test, CPT	Very site specific correlations. Two approaches exist: * Indirect method: use soil parameters with bearing capacity or cavity expansion theory to estimate the pile capacity. * Direct method: use of the cone resistance as the pile resistance. Some scaling factors are used.	
Load Transfer	Use of functions that describe the soil response from the unit skin friction transferred to the surroundings. Together with pile element response to the applied load, the complete load distribution along the pile length is obtained.	

## 2.5 Swedish pile research

In Sweden, and especially the West Coast, the use of piles for deep foundations has a long tradition dating back more than 100 years. The importance of understanding the performance of piles has been recognised in the early days of Civil Engineering. The Swedish initial investigations of pile behaviour in soft clays date to late 19<sup>th</sup> century and beginning of the 20<sup>th</sup>, by engineers at the Harbour Engineering Office in Gothenburg. By that time, Wendel (1900) developed the simplified loading frame shown in Figure 2.16, which was later used in many other investigations (e.g. B.G. Fellenius 1938; B.G. Fellenius 1955). Table 2.6 presents a time line with the main research findings of each decade until the present day.



Figure 2.16: *Pile testing at Gothenburg's harbour circa 1910 using E. Wendel load frame (SGF Väst).*

These previous researchers investigated mainly the short-term loading of compression piles using the quick maintained load method (QML) to study the pile bearing capacity in soft clays. Design methods were established by correlating the bearing capacity to the undrained shear strength of the clay. The later relation was initially based on the shear strength correlated from fall cone tests and later from the field vane test. One extensive investigation was done by B.G. Fellenius (1955), where he tested 40 full-scaled piles in Gothenburg central station area. His observations showed a gain in the bearing capacity with time and a resistance independent of loading direction. In addition, he found that the undrained shear strength of the clay correlated well with the measured bearing capacity (total stress method).

Torstensson (1973) corroborates the above findings in his model pile investigation. In his experiments he studied the pile installation effects, size and material, and the clay

Table 2.6: Overview of main pile research in Swedish soft clays.

Year	Reference	Test
1900	Wendel, Ernst	
1926	Petterson, Knut	QML tests
1928	Hultin, Torsten	
1934	Lidén, Gösta	Pile raft settlement
1955	Fellenius, Bror Gustaf	QML tests
1972	Fellenius, Bengt H	End-bearing – Downdrag
1977	Bjerin, L	End-bearing – Downdrag
1973	Torstensson, BA	
1979	Bengtsson, PE	QML tests
1986	Jendeby, Leif	
2007	Claesson, Peter et al.	Pile raft settlement

behaviour in relation to the shaft resistance. He observed large disturbance in the clay after installation with excess pore water pressure at the pile shaft equal or larger than the initial radial effective stress. Furthermore, the pile diameter, material and loading direction showed no difference in shaft resistance. For typical QML test, he found that the pile bearing capacity could be well estimated by using the uncorrected undrained shear strength of the clay from the field vane shear test. In addition, he found that the bearing capacity was related to the rate of loading (i.e. rate-dependency of clays). He derived an experimental rate function from vane shear tests with different rotation velocities.

Subsequently the long-term behaviour of piles was studied. The 7 years of measurements from B.H. Fellenius (1972) and Bjerin (1977) focused on the effects of negative skin friction on long piles installed to bearing soil layers. They observed that re-consolidation settlements from installation effects and on-going settlements in young slightly over-consolidated and normally consolidated clays generate relative displacements in the pile-soil interface which result in an additional load component on the pile shaft (i.e. dragload). As the piles were loaded, the mobilised load was equal to the applied load, and not the sum of this and the developed dragload. This indicates that the dragload was released after loading. However, the dragload increased again with time as the soil settlement continued, adding to the applied load.

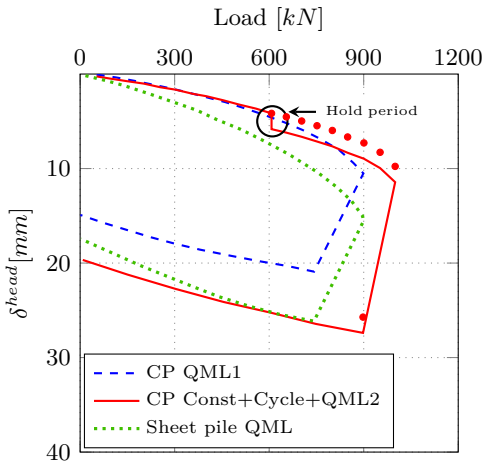
Bengtsson and Hansbo (1979) performed tension and compression QML tests on full-scale floating piles of different materials in highly plastic soft clay. The test site was located in the same clay deposit as B.H. Fellenius (1972) (i.e. Bäckebol). The experiment showed no loading direction or pile material dependence in relation to the shaft resistance. They also observed an increase in the shaft resistance with larger set-up times. Figure 2.17 shows some of these results for a pre-stressed concrete pile (CP) and a sheet pile type Larssen II (same surface area as CP). The first QML1 was carried out after a pile set-up time of 45 days. No difference in  $Q_{ult}$  was observed between the sheet pile and the concrete pile despite the difference in cross section stiffness. This indicates that little or no softening took place after the full mobilisation of the shaft friction. The QML1

test was followed by an additional pile set-up period of 51 days and a 4 days constant load test at 600 kN. During holding, the pile head displacements were small and the displacement rate decreased with time. After the hold period, the pile was subjected to 13 unloading-reloading cycles of 600-20-600 kN and then failed in QML2. The previous tests before QML2 did not seem to affect the pile-soil interface stiffness (see shifted dotted curve in Figure 2.17a and 2.17b) and the increase in bearing capacity is attributed to the additional set-up period.

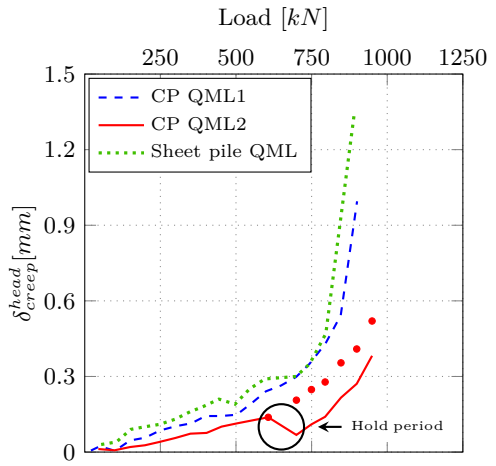
Hansbo (1984) and Jendebý (1986) looked at the long-term behaviour of pile raft foundations. They found that by utilising the “creep strength” of the clay, a more efficient foundation could be designed by sharing the structural load between the raft and the piles. This concept emerged from the study of the strain rate effects on the undrained shear strength of clays. The creep strength of a clay is defined as the limit where no shear failure will occur under low deformation rate (i.e. the maximum strength for long-term loading). This limit is empirically correlated by two methods, (1) by means of field vane shear tests and (2) by QML pile load testing. Both methods are illustrated in Figure 2.18 and described below.

For the first method, the vane shear test is rotated with different speeds, with very low speed giving the long-term shear strength. This shear strength is then used to calculate the pile bearing capacity with the  $\alpha$ -method using  $\alpha = 1$ . For the second method, the pile is loaded with 8 to 10 load increments with a hold time of 15 minutes each. For every step, the rate of pile head displacement for the last 6 minutes is calculated and plotted in a load versus rate plot. The part of the curve with the minimum curvature radius is selected as the pile *creep load* (i.e. the load that triggers high displacement rates). The pile capacity calculated using the first method has been found to approximate the creep load of QML test (Hansbo 1984).

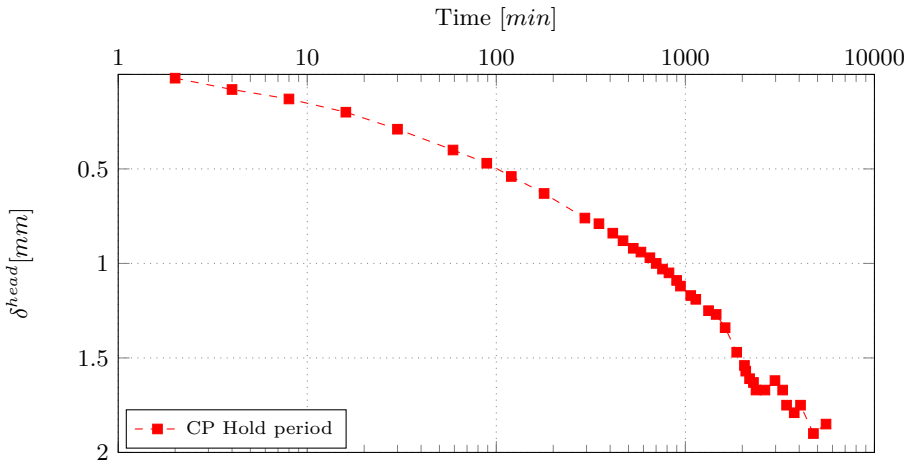
All in all, the pile shaft resistance in normally to slightly over-consolidated and high plasticity Gothenburg clay showed to be independent of pile size, length, material or loading direction. Semi-empirical methods were derived from QML tests, mainly from compression loading. This empiricism is restricted to local conditions and simplified loading scenarios. The latter represent a limitation for the current complex infrastructure projects in urban environments, and for the proper understanding of the long-term behaviour of floating piles in clays.



(a) Load-displacement curves

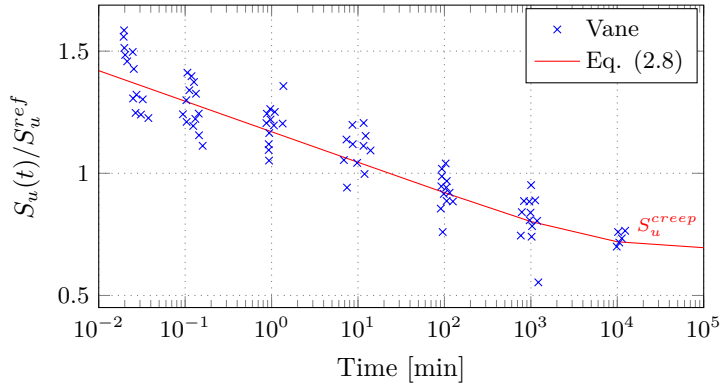


(b) Accumulated creep between minute 1 to 8 each load step

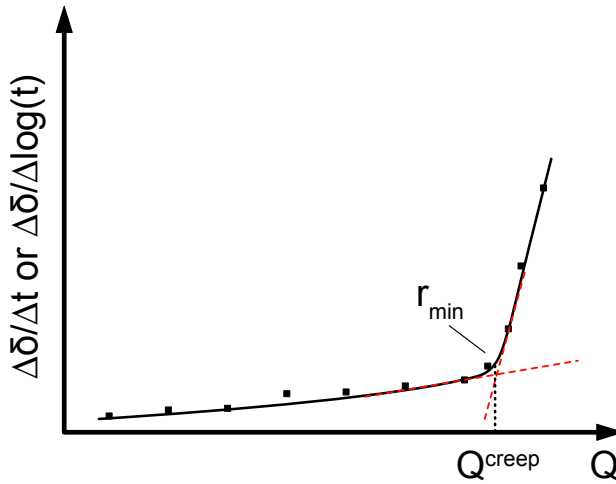


(c) Load-displacement curves

Figure 2.17: Tension loading of full-scale floating piles in soft clays (Bengtsson and Hansbo 1979; Bengtsson and Sällfors 1983). Hold period deformation subtracted in dotted curve.



(a) Vane shear tests with different rates



(b) Creep load concept

Figure 2.18: Methods for determining the pile “creep” load; (a) data from Bäckebol clay,  $S_u^{creep} = 0.72S_u^{ref}$ . Vane allowed to rest for one day before testing (adopted from Hansbo 1984), (b) the pile “creep” load is obtained at the minimum curvature radius.



## 3 Soil behaviour

As pointed out in Chapter 2, the pile response is directly related to the response of the adjacent soil. Therefore, a good understanding of the soil behaviour is required for a sound comprehension of pile foundations. Focus is given to the rate-dependent properties of soft clays.

### 3.1 Rate effects

Saturated normally and lightly over-consolidated soft clays present different mechanical behaviour dependent on the rate of shear strains applied. For example, triaxial tests with different shearing rates exhibit diverse peak shear strength or oedometer tests show different apparent pre-consolidation pressure (Graham et al. 1983; Länsivaara 1999). In other words, the strength and stiffness of the clay will depend on how fast the shear load is applied. The mechanical response observed in the measured engineering parameters due to rate effects can be related to three phenomena, (1) the free water viscosity in the porous media, (2) the viscosity of bounded water on the soil particles and (3) the water and soil structure interaction under shearing deformation and drainage (Briaud and Garland 1985).

Equation (3.1) is a general empirical model used to account for changes in the undrained shear strength with different strain rates. This relation only considered the change of the shear strength as a function of the shearing rate. As shown by Graham et al. (1983) for different clays, the change in  $S_u$  magnitude appears to be independent of test type and soil plasticity. Similar results were found by Länsivaara (1999). Nevertheless, other authors suggest that soil plasticity does influence the rate effects (Bjerrum 1973; Brown and Powell 2013). This latter aspect is still under investigation and is not yet clearly identified or generally accepted.

$$S_u = S_{u,ref} \left[ 1 + \eta^* \log\left(\frac{\dot{\gamma}}{\dot{\gamma}_{ref}}\right) \right] \quad (3.1)$$

where  $\eta^*$  is the increase per decade of strain rate and  $S_{u,ref}$  is the reference undrained shear strength with a rate  $\dot{\gamma}_{ref}$ . Values for  $\eta^*$  range between 0.05-0.20 (Graham et al. 1983). However, several authors found that the rate effects are also related to the strain level and therefore the  $\eta^*$  parameter is not always constant (Graham et al. 1983; Länsivaara 1999; Robinson and Brown 2013).

Quinn and Brown (2011) and Robinson and Brown (2013) explored the importance of considering the drainage conditions as illustrated in Figure 3.1. For very slow rates, the

excess pore water pressures can dissipate. As the rate increases, there is a transition from partial drained to totally undrained shear. During undrained conditions, viscous effects are dominant, with the shear strength increasing with the increase in shearing rate.

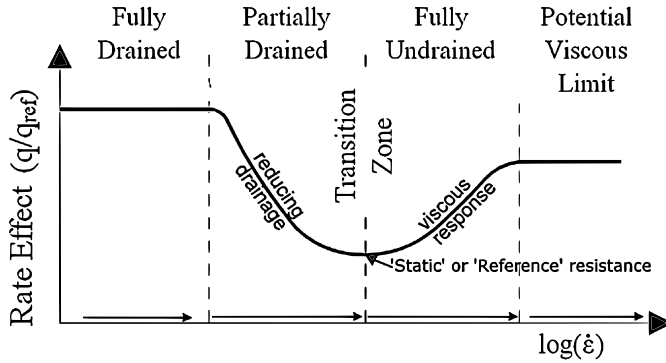


Figure 3.1: *U-shaped model illustrating the variation of soil strength with respect to drainage conditions and rate effects, e.g. for triaxial compression tests (adopted from Quinn and Brown 2011).*

For natural weakly bonded soft clay, the rate effects are mainly a function of the response of the soil’s micro-structure. Slow shear rates will result in lower peak shear strength as the soil will be allowed to deform and restructure (destruction) (Lefebvre and LeBoeuf 1987). On the other hand, for remoulded clays with little or no structure, the difference in shear strength due to rate effects is mainly caused by the generated excess pore water pressure resulting from the selected shearing stress path (Lefebvre and LeBoeuf 1987).

### 3.2 Deviatoric creep

According to the definition of creep in soils, pure creep processes only occur with constant effective stresses (Augustesen, Liingaard, et al. 2004). During undrained conditions, the effective stresses decrease with the build-up of creep induced excess pore water pressure, therefore the observed creep cannot be called pure creep. For the soil adjacent to the pile, the long-term response under sustained loading is considered to be under drained conditions and under constant effective stresses; thus fulfilling the condition for pure creep.

The measured displacement at the pile head can be divided into three different components. The first and second contribution are from the soil’s instantaneous elastic response and from the consolidation triggered by any shear-induced excess pore water pressure. The third arises from the deviatoric creep at the pile shaft. It is this creep behaviour that governs the long-term response of the piles (St.John et al. 1983; Ramalho Ortigao and Randolph 1983).

Deviatoric creep has been studied in laboratory conditions by several authors by means of drained and undrained triaxial and direct simple shear tests (Campanella and Vaid 1974; Tavenas et al. 1978; Tian et al. 1994; Havel 2004; Torpe 2014). Under the boundary conditions of DSS and triaxial tests, the soil can develop the three phases of creep, namely (1) primary or fading, (2) secondary or stationary and (3) tertiary or accelerating creep, as shown in Figure 3.2. On the other hand, under 1D oedometer tests the clay only can exhibit the primary phase. A soil that experience secondary and tertiary creep will ultimately fail by creep rupture.

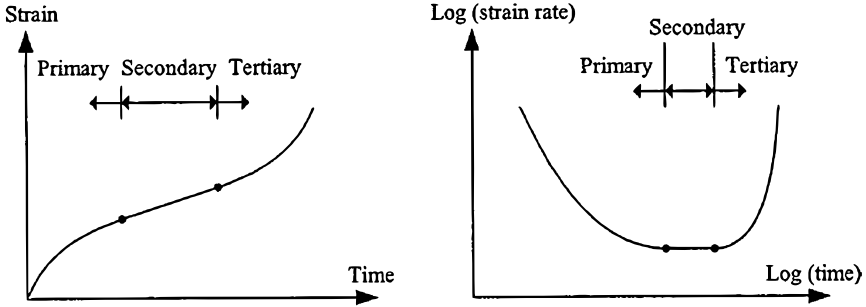


Figure 3.2: *Creep phases in triaxial conditions with constant total stresses (adopted from Augustesen, Liingard, et al. 2004)*

### 3.3 Creep rupture

Creep rupture is defined as the failure following the tertiary creep phase due to strength degradation in the clay. In clays, the loss of strength due to creep deformations can be caused by several factors. Mitchell and Soga (2005) presented some of these as:

- Creep deformation will contribute to the destructuration processes.
- If there are kinematic constraints and creep deformation cannot take place, then the effective stresses will decrease by relaxation.
- In undrained conditions, creep deformation can generate excess pore water pressure and therefore a reduction in effective stresses. On the other hand, for high creep rates in drained tests, the rate of increase in  $\Delta u_{creep}$  (if any) could be larger than the rate of dissipation. The latter can be aggravated with the reduction of permeability, as the soil compresses with time.

Campanella and Vaid (1974) studied the creep rupture phenomenon under undrained conditions for Haney normally consolidated natural soft clay (British Columbia, Canada). They assert that creep rupture might occur only under undrained conditions. In their test, the initial creep rate decreased to a minimum value and thereafter increased until

rupture. At all times, excess pore water pressure developed due to the creep strains. The magnitude of the creep strains up to failure depended on the stress path history of the soil element. For example, CIU triaxial tests accumulated approximately 4 times more strains to creep rupture compared to CAU test. However, for the same stress history, the accumulated strains at creep rupture were almost the same for the mobilisation ratios in their tests. The time to creep rupture was a function of the mobilised shear load. Figure 3.3 shows some of the results from their tests, with higher mobilisation degrees failing faster. As the degree of mobilisation decreased, the time to failure increased and tended to an asymptote value (creep rupture might not take place). The main cause of creep rupture appears to be the accumulation of excess pore water pressure, i.e. reduction of effective stresses. During the tertiary creep phase, no discontinuity was observed in the pore pressure measured at one end of the soil element in the triaxial apparatus due to the accelerating strain rates. Failure took place when the effective stress path reached the failure envelope obtained from standard tests (Coulomb failure line).

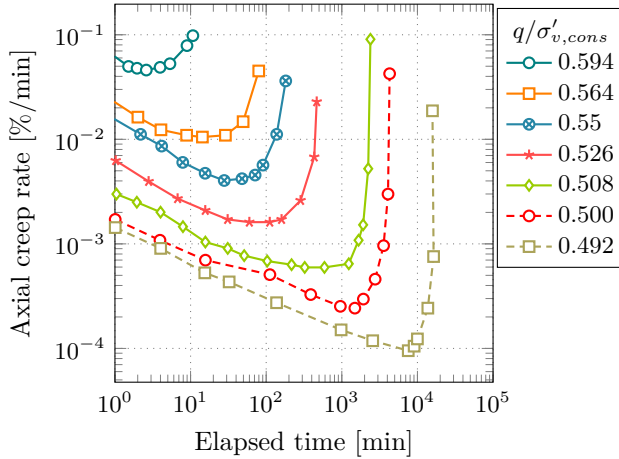


Figure 3.3:  $K_0$  consolidated undrained triaxial creep tests (adopted from Campanella and Vaid 1974).

Tavenas et al. (1978) studied in detail the creep behaviour of natural soft clays under triaxial and 1D oedometer tests. Their first important observation is that the soil limit state surface is rate and age dependent. They also observed that the creep strain rates  $\dot{\epsilon}^c$  form isotache surfaces with similar shape as the limit state surface in the stress space. This isotache surfaces showed to be homothetic to each other and the limit state surface. New constitutive models, such as the CREEP-SCLAY1S can capture this type of soil behaviour (Sivasithamparam et al. 2015). In their drained creep tests, rupture only took place for stress levels that were very close or above the soil failure envelope (Coulomb failure line). The failure mechanics resemble that of undrained creep rupture, first having an initial decrease in creep strain rates and then rapid increase up to failure. For their undrained tests, samples with mobilised stresses close to the limit state surface experienced rupture

within the observation time. The failure time was directly proportional to the mobilisation degree as in Campanella and Vaid (1974) investigations.

Drained triaxial and DSS creep tests performed by Tian et al. (1994) showed no creep rupture for stress levels below the failure envelope. The latter confirm the observations made by Tavenas et al. (1978). They observed that for stress levels with a degree of mobilisation  $\geq 70 - 75\%$  ( $mob = \tan \delta' / \tan \phi'$ ; where  $\delta'$  is the angle at current effective stress, and  $\phi'$  is the soil effective friction angle) large axial strains developed initially. They believe this deformations originate from large modifications of the clay structure after a certain mobilisation degree. In addition, they performed double step loaded tests in order to study the ageing effects of the samples under deviatoric creep. These tests showed a reduction of accumulated strain compared to single loaded tests for the same mobilised stress, and higher initial stiffness and undrained shear strength.

From these observations, it can be concluded that if the current stress is far from the failure envelope and the creep rate is sufficiently low to avoid accumulation of  $\Delta u^{creep}$ , creep rupture will not take place. Figure 3.4 illustrates this highlighting the stable and unstable creep zones in the stress space of an anisotropic structured soft soil model. For drained tests, the soil will creep stable if the stresses are mobilised just below the failure envelop ( $\approx 80-90\%$ , see Hunter and Khalili 2000). Whereas undrained tests will be stable if the stresses are within the intrinsic compression surface as little or no structural changes are expected to take place.

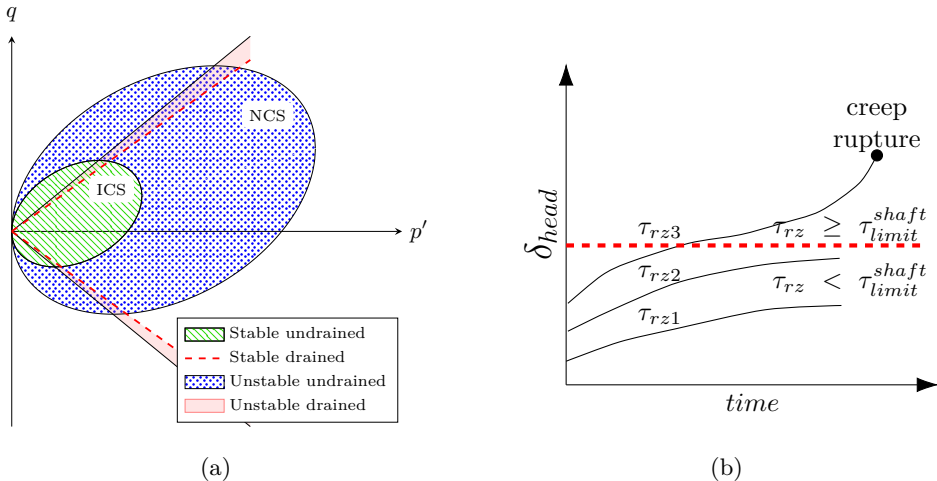


Figure 3.4: Illustration showing (a) the stress boundaries for stable and unstable creep (rupture) and (b) time-displacement curves for different shear loads at the pile shaft.

### 3.4 Creep modelling

Modelling of creep can be done in several ways, for example by empirical models, rheological models or general stress-strain-time constitutive laws. A good summary of the different approaches to model creep is given by Liingaard et al. (2004) and more details can be found in Mitchell and Soga (2005). The most common theoretical approach is to use an empirical logarithmic law, such as given in equation 3.2 (first presented by Buisman 1936). This type of model is based on 1D compression tests and can only predict primary creep, with the creep strains having a linear relation with the logarithm of time (note that  $\varepsilon =$  logarithmic strains).

$$\varepsilon_{axial}^c = \varepsilon_{vol}^c = \mu_v^* \cdot \ln \left( \frac{t_{ref} + t}{t_{ref}} \right) \quad (3.2)$$

where  $\mu_v^*$  is the modified coefficient of secondary compression for changes in volumetric strains ( $\Delta\varepsilon_v^c/\Delta \ln(t)$ ),  $t_{ref}$  is the time from where creep strains are assumed to start and  $t$  is the time following the onset of creep. The time reference in the above equations is usually taken as the time after primary consolidation, which can vary a lot. For incremental loading oedometer tests, this time is often taken equal to 1 day as each load step is held for the same duration due to practical convenience. Therefore, the stepwise incremental loading oedometer curve is called the 1 day reference stress-strain curve.

Not all clays exhibit this type of behaviour and non-linearity can be observed with time (Mitchell and Soga 2005). For example, if the applied load is close to the apparent pre-consolidation pressure, the soil might experience larger strains caused by destructuration. The latter will change the soil behaviour and therefore non-linearity can emerge. Furthermore, after a long creep period the deformation rate will decrease to a point where other processes will dominate, e.g. chemical bonding. If one incorporates these variations into the model, the non-linear behaviour can be captured (Liingaard et al. 2004) but for practical purposes, Equation (3.2) gives a good approximation.

The creep parameter in Equation 3.2 is the slope of the linear part of the measurement curve in a  $\varepsilon$ - $\ln(t)$  plot. This parameter is not constant and it is a function of the applied stress and accumulated strains. Figure 3.5 shows a typical curve of  $C_\alpha$  ( $\mu^* = C_\alpha/2.3(1 + e_0)$ ), where  $e$  is void ratio, as a function of stress for undisturbed natural soft clays from Bothkennar (Nash et al. 1992). For practical calculations,  $\mu^*$  is often selected based on the working stress range. Because of the remoulding process caused by pile installation, one will expect this parameter to be close to the intrinsic value at large strains and stresses (e.g.  $\varepsilon > 30\%$  and  $\sigma'_v > 3\sigma'_{pc}$ ). Therefore, the stress dependency is not that dominant as for undisturbed clays.

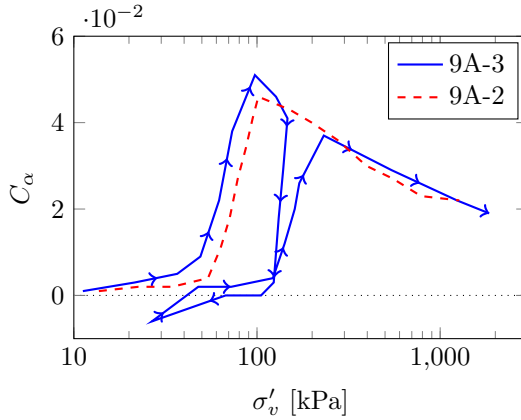


Figure 3.5: *Incremental loading (IL) oedometer at 5m depth for Bothkennar clay,  $\sigma'_{pc} \approx 81$  kPa (adopted from Nash et al. 1992).*

## 3.5 Constitutive models for soft soils

### 3.5.1 SCLAY1S

The SCLAY1S soft soil model is an extended critical state elasto-plastic constitutive model that captures important soil characteristics such as anisotropy and structure (Wheeler et al. 2003; Karstunen et al. 2005). The anisotropy is represented with an inclined yield surface having the shape of a distorted ellipse. Furthermore, the structure is introduced with an additional smaller intrinsic yield surface having the same shape and orientation as the natural yield surface. Finally, the SCLAY1S incorporates the Drucker-Prager failure criterion, which assumes a circular shape in the  $\pi$ -plane (later versions are Lode angle dependent where the strength in extension can be different from the strength in compression). Figure 3.6 illustrate the model intrinsic and natural yield surface for the special case of simplified triaxial stress space. These surfaces are obtained with Equation (3.3), where the fabric inclination is given by the scalar  $\alpha$  parameter for triaxial stress space. These two surface are linked with Equation (3.4).

$$f_y = (q - \alpha p')^2 - (M^2 - \alpha^2)(p'_m - p')p' = 0 \quad (3.3)$$

$$p'_m = (1 + \chi)p'_{mi} \quad (3.4)$$

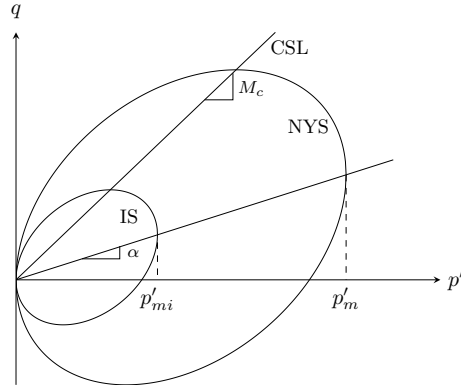


Figure 3.6: *SCLAY1S* natural yield (*NYS*) and intrinsic (*IS*) surfaces in 2D triaxial space.

where  $p'_m$  and  $p'_{mi}$  are the intersection of the vertical tangent of the natural and intrinsic ellipse with the effective mean pressure axis  $p'$  and  $\chi$  is the amount of bonding.

The model has three hardening laws and an associated flow rule. The first is an isotropic hardening law describing the change in size of the intrinsic yield surface as given by Equation (3.5). This law depends only on the plastic volumetric strains.

$$\Delta p'_{mi} = \frac{p'_{mi}}{\lambda_i^* - \kappa^*} \Delta \varepsilon_v^p \quad (3.5)$$

where  $\lambda_i^*$  is the intrinsic modified compression index for reconstituted soil and  $\kappa^*$  is the modified unload-reload index.

The second hardening rule characterises the changes in orientation of the natural and intrinsic yield surface with plastic volumetric and deviatoric strains as given in Equation (3.6) (kinematic hardening).

$$d\alpha = \omega \left( \left[ \frac{3\eta}{4} - \alpha \right] \langle d\varepsilon_v^p \rangle + \omega_d \left[ \frac{\eta}{3} - \alpha \right] |d\varepsilon_d^p| \right) \quad (3.6)$$

where  $d\varepsilon_v^p$  and  $d\varepsilon_d^p$  are the volumetric<sup>1</sup> and deviatoric plastic strains respectively,  $\omega$  controls the absolute rate of rotation,  $\omega_d$  regulate the rotation based on the norm of  $d\varepsilon_d^p$ ,  $\eta$  is the stress ratio  $q/p'$ ,  $\alpha$  is the inclination of the yield surfaces in respect to the  $p'$  axis (in the range of  $\frac{3\eta}{4}$  and  $\frac{\eta}{3}$ ).

<sup>1</sup>The volumetric plastic strains are regulated with Macaulay brackets  $\langle \rangle$  as  $\langle d\varepsilon_v^p \rangle = d\varepsilon_v^p$  for  $d\varepsilon_v^p > 0$  and

The last hardening rule gives the degradation of bonding  $\chi$  with plastic volumetric and deviatoric strains (see Equation (3.7)), and is closely linked to the first isotropic hardening rule. The relation exist as the state variable  $p'_{mi}$  is inversely proportional to the amount of bonding  $\chi$  (see Equation (3.4)). Therefore, the natural yield surface will shrink and the intrinsic surface will expand or shrink (depending on the flow rule) until there is no bonding left and they have the same size.

$$d\chi = -\xi \chi (|d\varepsilon_v^p| + \xi_d |d\varepsilon_d^p|) \quad (3.7)$$

where  $d\varepsilon_v^p$  and  $d\varepsilon_d^p$  are the volumetric and deviatoric plastic strains respectively,  $\xi$  is the parameter controlling the absolute rate of bond degradation and  $\xi_d$  is the parameter controlling the bond degradation in relation to  $d\varepsilon_d^p$ .

Taking  $\alpha = 0$  and  $\chi = 0$  the model transforms back to the modified Cam-clay isotropic model, with  $p'_{mi} = p'_m$ . A full description of the model is discussed in Sivasithamparam (2011).

### 3.5.2 CREEP-SCLAY1S

Apart from anisotropy and structure, soft clays also exhibit viscous behaviour (rate dependency and creep). This additional property incorporates the time dimension in the material description. CREEP-SCLAY1S is an elasto-viscoplastic constitutive model capable of modelling rate dependency (Sivasithamparam et al. 2015, Gras et al. In press). It is similar to the SCLAY1S in the manner anisotropy and structure are formulated. In addition, it is a special extended over-stress model that uses a generalised empirical formulation obtained from one dimensional observations (see Equation (3.2)) to model the rate dependent behaviour of the soil (Sivasithamparam et al. 2015). As a result the additional viscous parameters can be readily obtained from standard laboratory tests.

The model has three surfaces with the same shape and orientation describing the soil behaviour (see Figure 3.7) and an associated flow rule. The failure criterion is altered from the original version of SCLAY1S by introducing the modified Lode angle formulation of  $M(\theta_\alpha)$  in Equation (3.8), giving a shape similar to the Matsuoka and Nakai failure criterion in the  $\pi$ -plane. This modification predicts better the influence of the intermediate principal stress ( $\sigma_2$ ) in the soil behaviour.

$$M(\theta_\alpha) = M_c \left( \frac{2m^4}{1 + m^4 + (1 - m^4) \sin 3\theta_\alpha} \right)^{\frac{1}{4}} \quad (3.8)$$

---

$\langle d\varepsilon_v^p \rangle = 0$  for or  $d\varepsilon_v^p < 0$ .

where  $m$  is the ratio between the extension and compression critical state line  $M_e/M_c$  and  $\sin 3\theta_\alpha$  is given in Equation (3.9).

$$\sin 3\theta_\alpha = -\frac{3\sqrt{3}}{2} \frac{J_{3\alpha}}{(J_{2\alpha})^{\frac{3}{2}}} \quad (3.9)$$

where  $J_{2\alpha}$  and  $J_{3\alpha}$  are the second and third invariants of the modified deviatoric stress  $(q - \alpha p')$ .

As described by Sivasithamparam et al. (2015), the CREEP-SCLAY1S model differs from traditional elasto-plastic models, as it does not have a consistency condition to satisfy (i.e. there is no purely elastic domain and a fixed yield criterion for the onset of plastic strains). Therefore, elastic and viscoplastic strains take part at all time within a *reference surface* called the Normal Consolidation Surface (NCS). The stress path can overshoot the NCS depending on the rate of loading (over-stress type model). Within the Current Stress Surface (CSS) the soil will behave mainly elastic. During loading, with a stress path moving the CSS towards NCS, the viscoplastic strains will start to become significant and the Intrinsic Compression Surface (ICS) will expand or shrink depending on the flow rule (i.e. normal strain vector direction). As the stress path crosses through the NCS, large creep strains will develop. The critical state will be unique in the stress space and independent of stress path and strain rate.

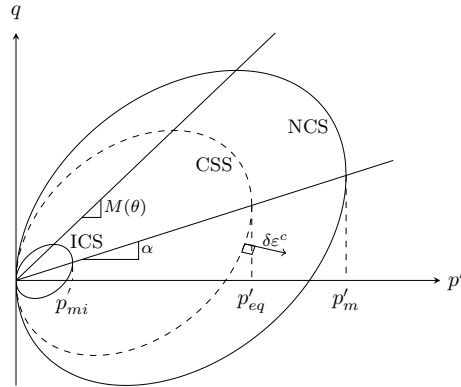


Figure 3.7: *CREEP-SCLAY1S surfaces (adopted from Gras et al. (In press))*

The viscoplastic strains are analogous to the plastic strains in traditional elasto-plastic models. The total strains rates are given by adding the elastic and viscoplastic (creep)

strains rates as given in Equation (3.10).

$$\begin{aligned}\dot{\varepsilon}_v &= \dot{\varepsilon}_v^e + \dot{\varepsilon}_v^c \\ \dot{\varepsilon}_d &= \dot{\varepsilon}_d^e + \dot{\varepsilon}_d^c\end{aligned}\tag{3.10}$$

where  $\dot{\varepsilon}_v$  and  $\dot{\varepsilon}_d$  are the volumetric and deviatoric elastic (superscript  $e$ ) and creep (superscript  $c$ ) strains.

The creep strains are calculated using the associated flow rule and the concept of constant rate visco-plastic multiplier  $\dot{\Lambda}$  as shown in Equations (3.11) and (3.12).

$$\dot{\varepsilon}_v^c = \dot{\Lambda} \frac{\partial p'_{eq}}{\partial p'} \quad \text{and} \quad \dot{\varepsilon}_d^c = \dot{\Lambda} \frac{\partial p'_{eq}}{\partial q}\tag{3.11}$$

$$\dot{\Lambda} = \frac{\mu_i^*}{\tau} \left( \frac{p'_{eq}}{p'_m} \right)^\beta \left( \frac{M_c^2 - \alpha_{K_0^{nc}}^2}{M_c^2 - \eta_{K_0^{nc}}^2} \right)\tag{3.12}$$

where  $\mu_i^*$  is modified intrinsic creep index measured in the  $\varepsilon_v$ - $\ln t$  plane or transformed with Equation (3.13),  $\tau$  is the reference time relating to the duration of the load steps in the 1D compression test used to obtain  $\mu_i^*$  and the apparent pre-consolidation pressure,  $\beta$  is the ratio in Equation (3.14),  $M(\theta_\alpha)$  is the Lode angle failure criterion,  $\alpha_{K_0^{nc}}$  is the inclination of the ellipses in the normally consolidated state, and  $\eta_{K_0^{nc}}$  is the actual stress ratio  $q/p'$  in the 1D normally consolidated stress path.

$$\mu^* = \frac{C_\alpha}{\ln 10(1 + e_0)}\tag{3.13}$$

$$\beta = \frac{\lambda_i^* - \kappa^*}{\mu_i^*}\tag{3.14}$$

The CREEP-SCLAY1S has three hardening rules similar to the SCLAY1S model. Their formulation is analogous, with the plastic strains  $\varepsilon^p$  replaced with the creep strains  $\varepsilon^c$ .

## Model parameters

The SCLAY1S and CREEP-SCLAY1S model parameters are listed in Table 3.1.

Table 3.1: Parameter description for SCLAY1S and CREEP-SCLAY1S.

### Isotropic parameters (MCC)

$\kappa^*$	Slope of the unload-reload line in $\varepsilon_v - \ln \sigma'_v$ space for 1D compression.
$\lambda^*$	Slope of the post-yield compression line in $\varepsilon_v - \ln \sigma'_v$ space for 1D compression.
$\lambda_i^*$	Same as $\lambda^*$ for remoulded soil.
$\nu'$	Drained Poisson's ratio (purely elastic).
$M_c$	Stress ratio at critical state in triaxial compression.
$M_e$	Stress ratio at critical state in triaxial extension.

### Anisotropic parameters (SCLAY1)

$\alpha_0$	Initial inclination of the yield surface.
$\omega$	Absolute effectiveness of rotational hardening.
$\omega_d$	Relative effectiveness of rotational hardening in respect to $\varepsilon_d^p$ .

### Destruction parameters (SCLAY1S)

$\chi_0$	Initial bond amount.
$\xi$	Absolute rate of destructuration.
$\xi_d$	Relative rate of destructuration in respect to $\varepsilon_d^p$ .

### Viscous parameters (CREEP-SCLAY1S)

$\mu^*$	modified creep index for a given working stress.
$\mu_i^*$	modified creep index for remoulded soil.
$\tau$	reference time.

### Initial conditions

$\sigma'_{pc}$	Pre-consolidation pressure corresponding to reference time $\tau$ .
OCR	Over-consolidation ratio.
POP	Pre-overburden pressure.
$e_0$	Initial void ratio (not affecting the model predictions).

## 4 Long-term field test

A field test was used to study the long-term behaviour of model piles under sustained tension loads. The field test was preferred as it incorporates all the stages of the pile cycle described in previous Chapters. Furthermore, the soil is in its natural state and under the proper stress conditions in relation to deep excavation projects. The first part of this Chapter describes the site and soil characterization. Subsequently the model piles and loading setup is presented.

### 4.1 The test site

The test site was located at Marieholm, Gothenburg, within the construction perimeter of the contractor PEAB AB for the Marieholm connection project (Figure 4.1). The available area for the test was circa 150 m<sup>2</sup>. The surrounding area has been an active construction site in the recent years (e.g. Partihall connection project). As a consequence, the soil has a complex loading history which is not completely known. However, most of the impact from previous works is expected to be close to the ground surface. On-going settlements in the area are low with rates below <1mm/year (Trafikverket 2014; see Appendix). Therefore negative skin friction should not affect the measurements within the period concerned here.



(a) The site was located north of the central station (red circle)



(b) Zoom of field test at the PEAB AB working site (red pentagon)

Figure 4.1: Site location at Marieholm, Gothenburg (Waterloogatan, coordinates 6402173, 321345 – SWEREF99 system).

The selected location is part of the extensive Göta river sedimentation basin, which extends all the way to Gothenburg's central train station where the West link tunnel will be built. Hence this site presented similar soil conditions to those of interest for future

construction. The ground level is at +11.4 m above sea level, with the first 1.9 – 2.0 meters of fill material (mix of gravel, sand, silt and clay), followed by a thin stiff clay layer of approximately 0.3 m. Thereafter, deep deposits of rather homogeneous and young (in geological time  $\approx$  11,000 years) post-glacial and glacial clays can be found up to 100 meters deep (Klingberg et al. 2006).

Based on previous soil investigations near the site, the boundary between the post-glacial and glacial clay is estimated to be around 10 m deep. Focus is given to the glacial clay, as excavations for the West link project will be generally 15 – 25 m deep. Therefore, the piles were installed to deep soil layers, with the pile head 13 m below the ground surface. At this depth the clay has high sulphide content, consequently it has a dark grey or black colour as shown in Figure 4.2. This can be attributed to the presence of organic matter during the sedimentation period and the anaerobic decomposition process that generated hydrogen sulphide. The latter reacted with the iron in the soil forming iron mono-sulphide ( $\text{FeS}$ ) and pyrite ( $\text{FeS}_2$ ) (Müller 2010).



(a) *Filling material*



(b) *Sulphide clay*

Figure 4.2: *Soil from test site at Marieholm, Gothenburg*

## 4.2 Soil characterisation

The Marieholm deposit has previously been characterised in relation to other construction projects. The clay in this area is rather homogeneous, slightly over-consolidated and with increasing shear strength with depth. Undrained shear strength data from field vane shear tests and DSS from these investigations were initially used in the preliminary design of the test piles considered here (Trafikverket 2014). The data was selected as close as possible to the test site, assuming an equal stress history for all levels below +11.4 m. All data is referred to +11.4 m, which was the ground surface level at the test site (i.e. 0 m depth). An overview with the selected in-situ tests and boreholes is given in the Appendix.

In addition to this desk study derived data, new in-situ and laboratory tests were performed to test the soil exactly where the piles were installed. A field vane shear test ( $Vt$ ), a piezo-cone penetration test ( $CPTu$ ) and extraction of natural soil samples using the Swedish piston sampler ST2 were conducted prior to the pile installation and after the pile set-up period. The first sample extraction and in-situ tests were executed between 2014-04-07 and 2014-04-08, and a second borehole taken in 2014-09-03. All new tests are coded as CTH-TP1 and CTH-TP2.

### 4.2.1 In-situ tests

The field vane shear test was done following the Swedish guideline SGF 2:93E (SGF 1993). The vane had blades of  $d=100$  mm and  $h=200$  mm, which were first pushed to the desired depth and left to rest for 5 minutes before applying torque. During shearing, the rate of rotation was controlled until the peak strength was reached within 2 to 4 min. Therefore, the shear rate was not constant as the shear strength increased with depth. After the peak was reached the vane was rotated further by  $20^\circ - 30^\circ$  to study the softening of the clay and evaluate the residual load. The undrained shear strength was calculated using equation (4.1) and corrected with  $\mu=0.8$  in equation (4.2)(SGF 1993).

$$\tau_v = \frac{6M_{max}}{7\pi D^3} \quad (4.1)$$

$$S_u = \mu \cdot \tau_v \quad (4.2)$$

where  $M_{max}$  is the peak measured torque,  $D$  is the vane diameter (blades),  $\tau_v$  is the calculated uncorrected undrained shear strength and  $S_u$  is the corrected undrained shear strength.

The  $CPTu$  test has been evaluated using the Swedish guideline SGI-INFO-15 (Larsson 2007). Equation (4.3) is used for the calculation of the undrained shear strength ( $S_u$ ) and Equation (4.4) for estimating the pre-consolidation pressure. An  $OCR=1.3$  and an average liquid limit of 75% was used to evaluate the results.

$$S_u \approx \frac{q_t - \sigma_{v0}}{13.4 + 6.65w_L} \left( \frac{OCR}{1} \right)^{-0.2} \quad (4.3)$$

$$\sigma'_{pc} \approx \frac{q_t - \sigma_{v0}}{1.21 + 4.4w_L} \quad (4.4)$$

where  $q_t$  is the cone tip pressure resistance,  $\sigma_{v0}$  is the in-situ total vertical stress,  $w_L$  is the clay liquid limit and  $OCR$  is the apparent pre-consolidation pressure ( $\sigma'_{pc}/\sigma'_{v0}$ ).

The measurements for the  $Vt$  and  $CPTu$  are presented in Figure 4.3. The uncorrected vane results approximate the laboratory DSS values. After an additional rotation of  $25^\circ$  following peak, the residual strength for the vane reduced to 50% of the peak value for the whole depth. The  $CPTu$  exhibit the same trend as the  $Vt$ , however the shear strength is much lower. This lower strength is closer to the residual strength in the vane test. An additional  $CPTu$  test from previous investigations is presented for comparison. Again the same trend is observed but lower shear strength compared to the uncorrected vane test. It is hard to explain this large difference between these in-situ testing methods. Most probably the  $CPTu$  interpretation methods used in Sweden are falling behind the international state-of-art.

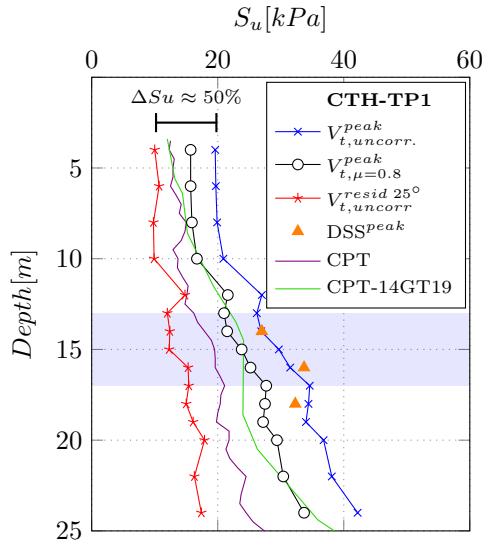


Figure 4.3: Undrained shear strength from vane,  $CPTu$  and  $DSS$ .

## 4.2.2 Element testing

The natural soil samples were obtained using the Swedish STII piston sampler, with diameter 50 mm and three sample tubes of length 170 mm. These were preserved in a relative humidity  $RH$  and temperature  $T$  controlled room ( $T=7^\circ\text{C}$  and  $RH > 90\%$ ). All advanced tests were performed at Chalmers Geotechnical laboratory under similar temperature controlled conditions. For all sampled levels, routine tests were performed, measuring density, water content, plasticity and undrained shear strength from the fall cone test. These results are shown in Figure 4.4. In addition, Table 4.1 shows the number

of laboratory tests performed with more advanced test procedures.

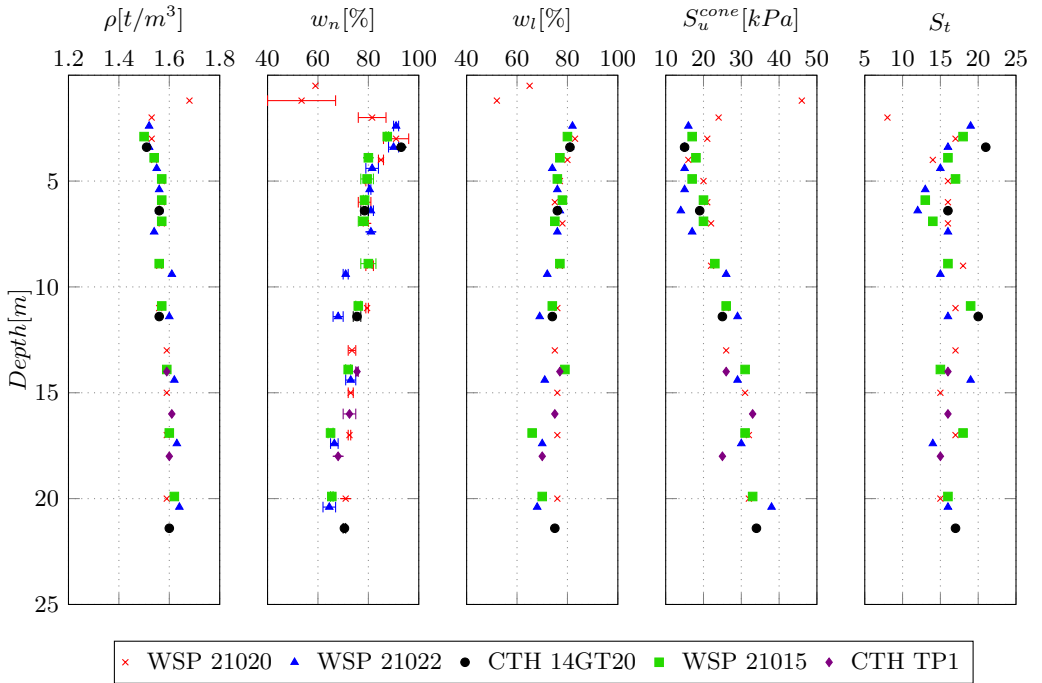


Figure 4.4: *Marieholm clay properties.*

The DSS test perhaps is most representative of the pile-soil interface shear strength (Randolph and Wroth 1981). However, laboratory tests on natural samples are not similar to conditions after pile installation (Hunt et al. 2002). Nevertheless, the results from these tests showed peak values that were in line with the uncorrected vane shear test results shown in Figures 4.3 and 4.5. These peaks took place at 5 to 8% shear strain and were followed by some limited softening.

The constant rate of strain (CRS) and incremental loading (IL) oedometer tests helped to identify the apparent pre-consolidation pressure ( $\sigma'_{pc}$ ) and the soil behaviour under one dimensional (1D) compression. All CRS tests had a displacement rate of 0.0024 mm/min and the IL stepwise loading used load steps of 24 h duration. The Sällfors and Casagrande methods (Sällfors and Andreasson 1985) were used to evaluate  $\sigma'_{pc}$  from the CRS tests. As shown in Figure 4.6a in linear scale, the samples have a clear transition from stiff to more compliant compression response, with the yield point at stresses larger than in-situ conditions. For the CRS test the apparent over-consolidation ratio (OCR) lies between 1.3 to 1.4 (see Figure 4.7b). For some of the IL tests in Figure 4.7a the  $\sigma'_{pc}$  was not clearly identified, indicating the clay to be normally consolidated. The latter can be attributed to rather large load steps before and after the apparent pre-consolidation pressure. This

Table 4.1: Laboratory tests from the test site soil.

Depth [m]	IL	CRS	DSS	CAUC	CAUE
13	1	1 (1)*	-	1	-
14	1	1 (1)*	1	1	-
16	1	1	1	1	-
17	1	-	-	-	1
18	-	1 (1)*	1	-	-
22	1	-	-	-	1

IL: stepwise oedometer, CRS: 1D constant rate of strain oedometer, DSS: direct simple shear, CAUC: anisotropically consolidated undrained triaxial test sheared in compression.

\* Numbers in parentheses are tests on disturbed samples.

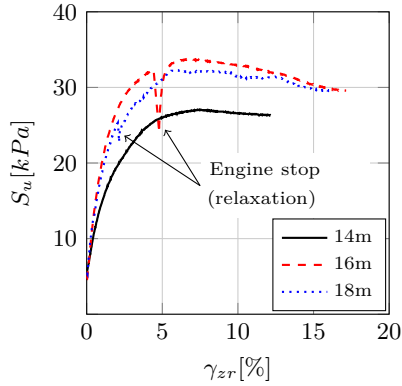
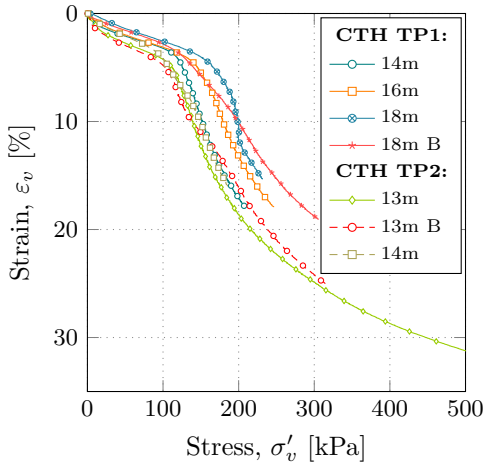


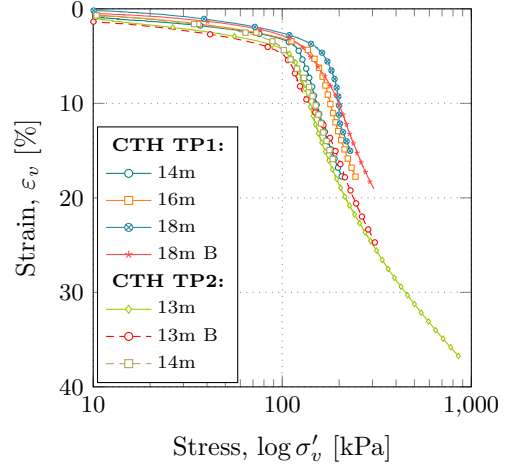
Figure 4.5: DSS tests at depths similar to the test pile location.

hampered the assessment of the yield point as illustrated in Figure 4.7a (for smaller steps). In addition to  $\sigma'_{pc}$ , the secondary compression coefficient was determined for each IL step and are presented in Figure 4.8. Additional results from previous 1D investigations are plotted in Figure 4.7b together with CTH-TP1.

Undrained triaxial compression tests showed a more significant softening behaviour compared to DSS after reaching a peak at 1.6-1.8% axial strain. From drained and undrained triaxial compression tests, an effective critical state friction angle  $\phi'_{cs,Mc}$  between 38-41 degrees was found with  $c' = 0$  (evaluated from  $p'-q$  plot). For undrained triaxial extension tests, the effective critical state friction angle was approximately  $\phi'_{cs,Me}$  45 degrees with  $c' = 0$ . The results are presented in Figure 4.9. The clay is contractant, showing a reduction in volume under shear loading. Undrained conditions do not allow for volumetric deformations, resulting in an increase in pore water pressure.

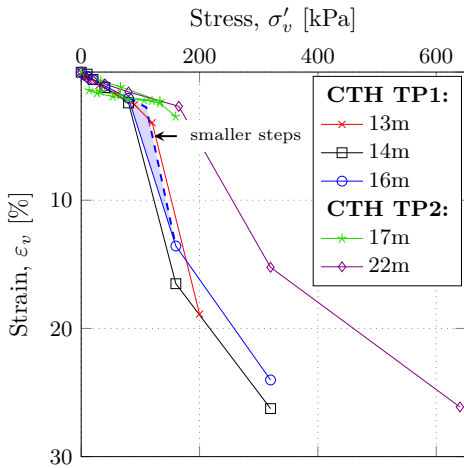


(a) CRS linear

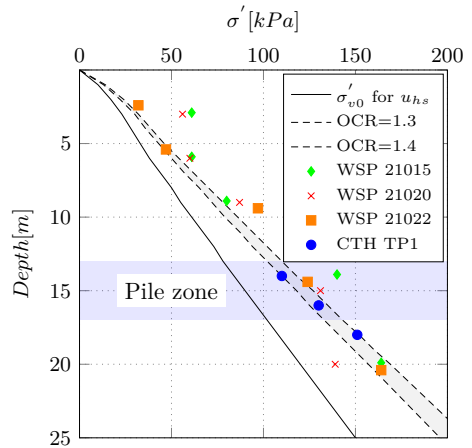


(b) CRS semilog

Figure 4.6: Result from 1D compression tests

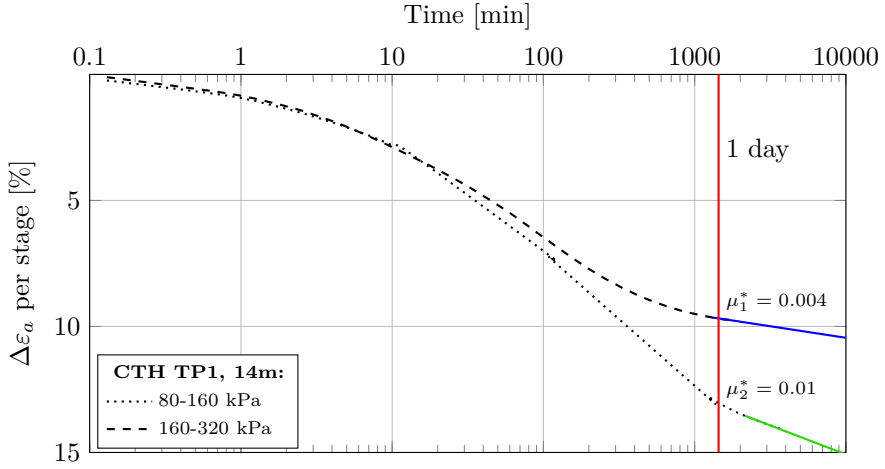


(a) IL test

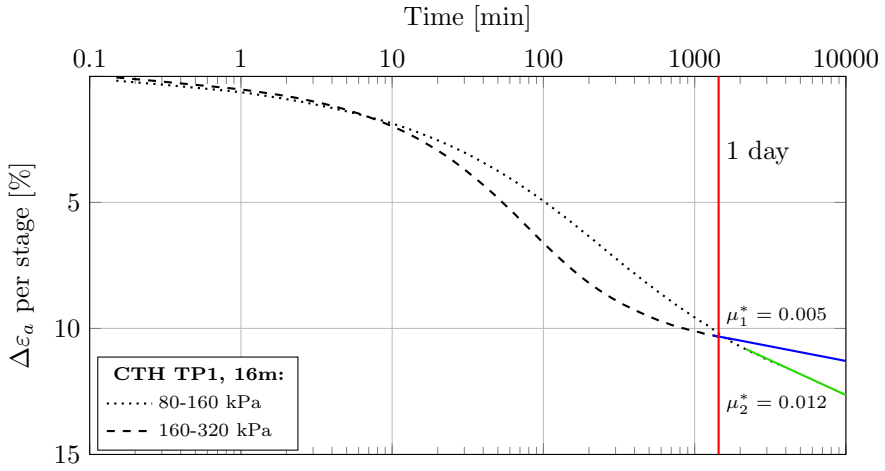


(b)  $\sigma'_{pc}$  from CRS (Sällfors method)

Figure 4.7: Results from 1D Constant Rate of Strain compression tests

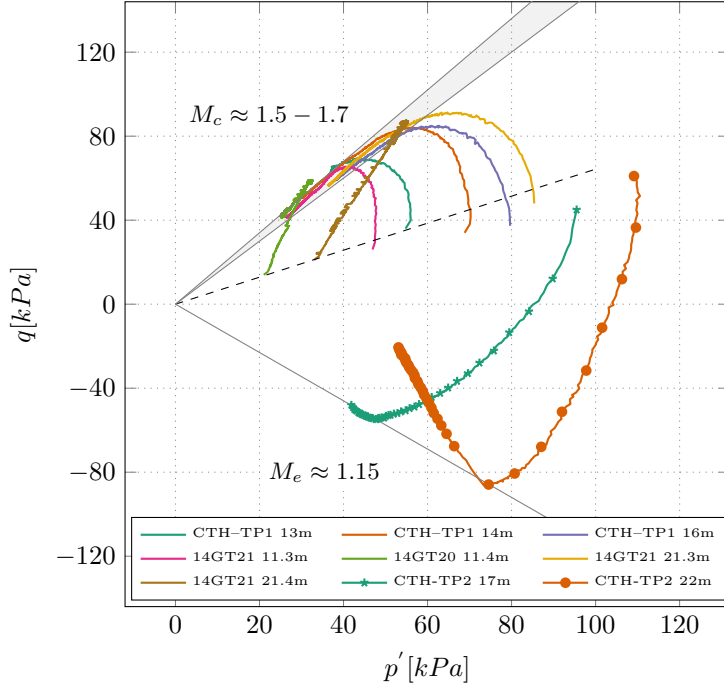


(a)

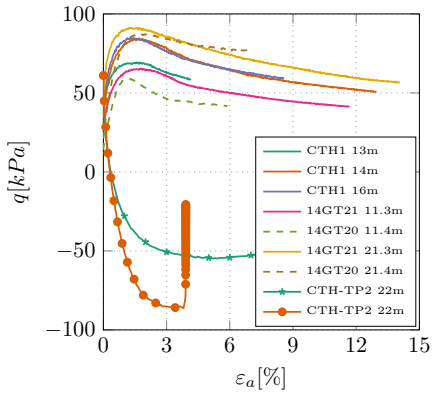


(b)

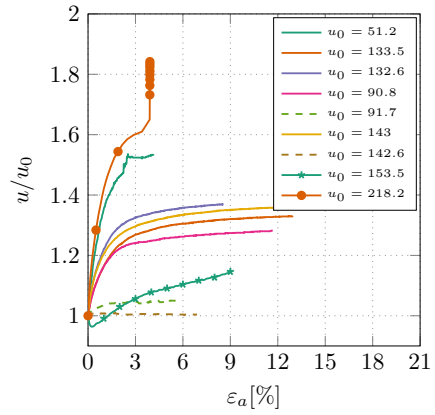
Figure 4.8: Results from 1D Incremental Loading (IL) compression tests and creep parameter  $\mu^*$ .



(a)



(b)



(c)

Figure 4.9: Results from undrained and drained triaxial compression tests.

### 4.2.3 Groundwater monitoring

In order to monitor the pore water pressure evolution during the test, four BAT piezometers were installed at depths of 11 m, 15 m (two units) and 19 m. Unfortunately, one of the 15 m sensors stopped working after 1 month. Measurement of pore water pressures are shown in Figure 4.10, together with previous nearby measurements. On average, the groundwater table is at  $\approx 0.30$  m below the surface level and the pore water pressure is not completely hydrostatic (some excess pore water pressure can still be noticed in the plots). The excess pore water pressure could be due to (i) remaining excess pore water pressure from the old filling or a new road embankment next to the site, and/or (ii) artesian pore water pressure from a possible deep permeable layer. For the depth where the test pile was located, the ratio between the in-situ and hydrostatic pore pressure  $u_0/u_{h,s}$  was approximately 1.10.

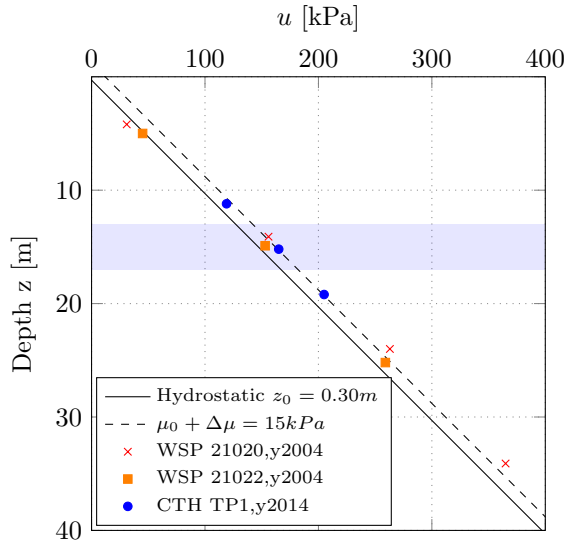


Figure 4.10: Average pore water pressure with depth near and at the site for different years.

# 5 Load test setup

Long-term pile load tests are rarely performed due to the considerable amount of time, work and costs. Another issue is that in-situ pile load tests cannot be easily generalised as the results depend on the site, pile type, testing procedures and experimenter (e.g. pile characteristics, installation method, loading regime). Generally, long-term tests of piles are performed using kentledge (dead weight) or complex hydraulic loading systems, e.g. Eide et al. (1961), B.H. Fellenius (1972), Ramalho Ortigao and Randolph (1983), and Karlsrud, Jensen, et al. (2014). Dead weights require strict safety measures and large bearing structures. Furthermore, hydraulic systems are costly and prone to control failure, as the  $\Delta\text{load}/\Delta\text{displacement}$  ratio is very large, requiring continuous work from the hydraulic pumps to maintain a constant load for small pile head displacements. Therefore, a new method was developed to overcome the difficulties of traditional approaches.

In the current research a new loading method was developed to overcome some of aforementioned limitations. This new approach is designed to apply long-term moderate loads in a robust and simple manner, while being cost-effective and safe. It is based on utilising the potential energy of a (gas) spring system and Hooke’s law (Equation (5.1)). Here  $k$  is the spring constant related to the spring behaviour that includes the material and geometry of the spring (Elert 2015). The ideal spring should have a small  $k$  in the working range, such that any additional displacement will only result in a small load variation (Figure 5.1a with  $k_c$ ). This type of load-control system is commonly used in piping systems, where changes in fluid flow and temperature can generate large stresses at the supporting structures.

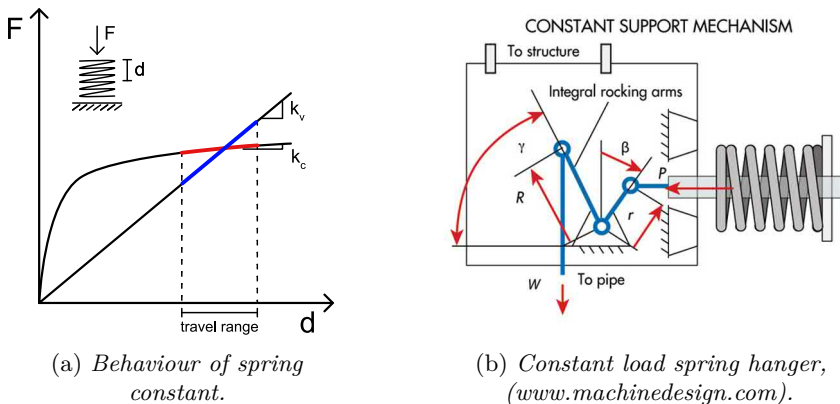


Figure 5.1: Ideal spring curve and constant spring design.

$$\Delta F = -k\Delta x \tag{5.1}$$

where the change in load  $\Delta F$  depends on the displacement  $\Delta x$  by a spring constant  $k$ .

## 5.1 Selection of loading method

Many solutions exist for conventional spring elements with several geometries and made of different materials. Typical spring types are: compression/tension/torsion coils, flat-rolled (clock spring), flat-stacked (leaf) and disc springs made out of steel, but other materials are used as well. A somewhat unconventional solution considered here is the gas (air) spring which are available in multiple geometries and materials. The three most promising types were studied in the design phase: (1) compression coil springs, (2) disc springs and (3) pneumatic lifting bags (gas springs). In addition to the load mobilisation, the main selection criterion for long-term testing is to have a relatively constant load with time by providing a sufficiently small spring constant in the displacement range of interest. The advantage and disadvantages of the selected devices are summarised in Table 5.1.

Table 5.1: Springs studied for loading the piles in tension

Spring type	Advantage	Disadvantage
Compression coil	One single spring	Heavy and big Safety Complex load frame
Disk	Versatility in stiffness and capacity Small and light	Safety Complex load frame Stress concentration cracks
Lifting bag	Versatility in stiffness and capacity Small and light	Requires auxiliary equipment

Coil springs are widely used today in many mechanical systems. These springs can control the load in a variable manner or keep it nearly constant. A variable load spring-hanger is preloaded in compression to a certain level and can take additional load until they are fully compressed. Within this range the load will change according to the spring constant. A more suitable coil spring solution is the constant stiffness spring mechanism that keeps an approximately constant load within a pre-defined displacement range (e.g. in industry the allowed load deviation is usually within 6%). This is illustrated in Figure 5.1b, where the principle is to make moment equilibrium between the external force  $W$  and the spring force  $P$  ( $W(R \cos \gamma) = P(r \cos \beta)$ ).

Both types of springs can be a good solution to the current problem, however, they increase in size for the desired capacity and a more elaborate reaction frame is required. For example, to mobilise a 200 kN load, a single steel compression coil spring with dimensions of 351 mm in diameter, 460 mm in height and coil diameter of 65 mm. The travel distance

in this spring would be about 360 mm with a load capacity of  $196 \text{ kN} \pm 25 \text{ kN}$ , giving  $k=0.55 \text{ kN/mm}$ .

Disc springs are more versatile than compression coil springs as it is possible to configure a desired non-linear spring stiffness by combining different types of disc springs (geometry). As a result the load-displacement curve can be nearly linear or highly non-linear (degressive). Furthermore, these discs can be stacked in different arrangements to give the desired loading capacity and travel distance as illustrated in Figure 5.2. For example, compressing the spring model #190008 from Mubea ([www.mubea.com](http://www.mubea.com)) to 70% of its initial height gives a travel distance of 3.6 mm per spring and a loading capacity of 70.5 kN. Using two stacks of 25 springs each will give 90 mm travel and 141 kN in loading capacity. Note that the springs cannot be fully loaded in static loading, since cracks can develop with time due to stress concentrations. In the current application the disc and coil springs, while technically feasible, if additional load frames are employed to ensure safety, proved to be too expensive.

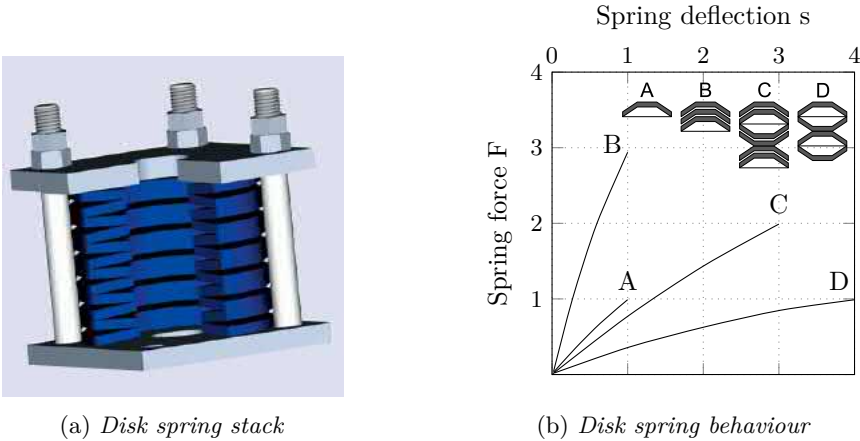
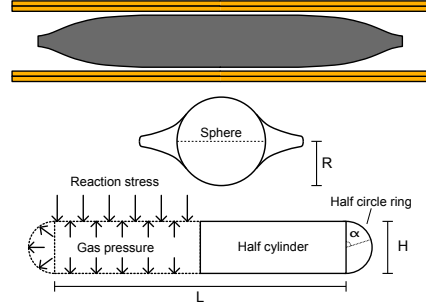


Figure 5.2: *Disk springs.*

Finally, a non-conventional air spring was studied. In this case, a pneumatic lifting bag from Trelleborg AB was selected (see Figure 5.3). These bags are made of high-quality rubber reinforced with layers of aramid fibre, making them robust and safe to work in the field. The bags are designed for a maximum of 800 kPa (8 bars) gas pressure and provide different load capacities depending on their size (contact area). The bags were found to be the best solution for the long-term test based on their simplicity, versatility and low cost. Two bags model TLB32 were used in the current application, with a maximum capacity of 32 tons for the largest contact area.



(a) Real bag shape



(b) Free form and squeezed bag model

Figure 5.3: Trelleborg AB lifting bags.

### 5.1.1 Final solution: Lifting bag

The reaction load from the bags is a function of the lifting height (hence the contact area), the applied gas pressure and the temperature. Three possible loading scenarios for these bags are considered:

1. *Constant pressure*: using a constant pressure source, e.g. an electrical air compressor.
2. *Constant gas mass*: the bags are pre-loaded with a pressure until the target load and subsequently sealed to keep the same air mass.
3. *Constant load*: using a regulated pressure source that is adjusted as function of the pile head load (stepwise/regulated), e.g. solenoid valves and electrical air compressor.

In the first case, temperature effects will not play any role since the pressure is regulated. Therefore, the bags can be model by simple equilibrium equations (Equation (5.2)) that are solely based on volume changes. However, in the second case, the load capacity becomes more complex since changes in volume and temperature could take place simultaneously. The effect of temperature is limited (e.g. for  $\Delta T = 20^\circ C$  the load change is 3.4 kN). The last option will keep the load constant, so changes in temperature or volume will be compensated by the control equipment (when properly designed). These different scenarios are elaborated in Figure 5.4 for an initial load of 50 kN with a 200 kPa gas pressure. The constant mass curve only presents the variation from volume change as temperature effects are minimal.

$$Q = \frac{\pi(L_{bag})^2}{4}p \quad (5.2)$$

where  $Q$  is the load generated,  $L_{bag}$  is the contact length of the bag and  $p$  is the gas pressure.

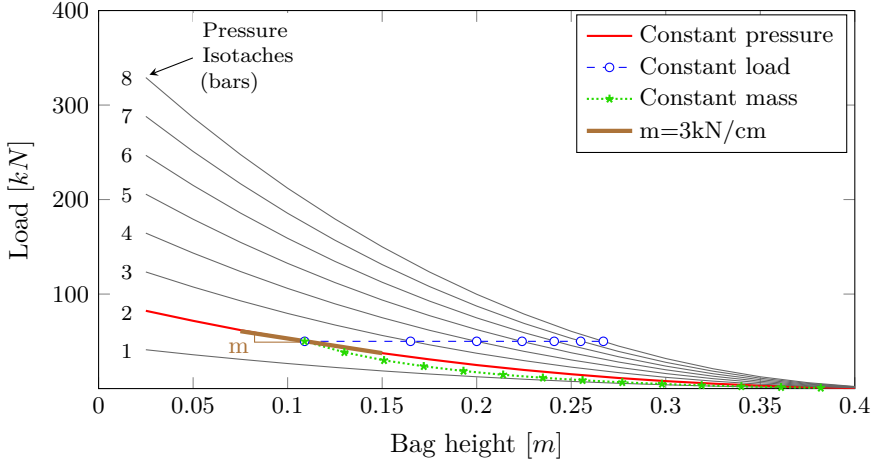


Figure 5.4: *TBL32 load versus displacement curves for different pressure and loading conditions.*

The sealed case (constant gas mass) can be modelled using Boyle's law for ideal gases (5.3):

$$p = \frac{nRT}{V} \quad (5.3)$$

$$p = \frac{kT}{V} \quad (5.4)$$

where  $p$  is the gas pressure,  $n$  is the gas mass,  $R$  the gas constant,  $T$  the gas temperature and  $V$  the volume occupied. For a fixed mass of gas with constant temperature  $T$ , the volume  $V$  occupied by the gas is inversely proportional to the pressure. The gas mass  $n$  and the gas constant  $R$  can be combined in a single constant  $k$  as shown in Equation (5.4).

In all cases the equilibrium equations are required to calculate the load. For the latter it is necessary to obtain the contact area between the bags and the reaction points. This area was approximated by modelling the bag geometry in three components as illustrated in Figure 5.3b. First, the bags have a complex shape when fully inflated under free conditions at very low air pressure ( $\ll 1$  bar), with a maximum lifting height based on the bag model. This complex form was approximated using a sphere, with a modified maximum height to account for the difference in volume from the true shape. Secondly, the bags were compressed between two plywood sheets for which a cylinder and a half-circle ring

are combined in one shape. Thirdly, the assumption of a rigid membrane was required to impose that both geometrical models have the same surface area. The contact area diameter  $L_{bag}$  is derived by equalising equation (5.5) and (5.6). The latter was corrected since the true contact is not fully circular.

The factors for the sphere height  $R = \chi R$  and the contact area radius  $L = \eta L$  were calibrated using the loading curves provided by the manufacture. For the TLB32 bag, the  $\chi$  and  $\eta$  factors were equal to 1.15 and 1.25, respectively. Based on this model, the bag behaviour could be estimated for changes in temperature and height.

$$A_{sphere} = 4\pi R^2 \quad (5.5)$$

$$A_{sphere}^{squeezed} = 2\pi \int_0^\pi \left( \frac{L}{2} + \frac{H}{2} \sin \alpha \right) \frac{H}{2} d\alpha + 2\frac{\pi}{4} L^2 \quad (5.6)$$

$$L_{bag} = \sqrt{\frac{\pi^2 H^2}{4} - 2H^2 + 8R^2} - \frac{\pi H}{2} \quad (5.7)$$

$$V_{bag} = \int_{\frac{L}{2}}^{\frac{L+H}{2}} 2\sqrt{\left(\frac{H}{2}\right)^2 - \left(r - \frac{L}{2}\right)^2} 2\pi r dr + \pi \frac{L^2}{4} H \quad (5.8)$$

The basic characteristics of the model pile and relevant soil conditions need to be known in advance in order to design the most appropriate loading system. For the field test in this study, two bags were used per pile in order to have more flexibility in the maximum load and travel distance (i.e. spring constant  $k$ ).

### 5.1.2 Adding load control

The initial load regulation was based on the criterion that a maximum deviation of  $\pm 10\%$  of the current applied load could be allowed. In that respect, a nearly constant load was obtained by just closing the valves of the bag, i.e. constant air mass was applied at the beginning of each load step. Manual adjustment of the load was required in case the deviation was close to or at the stated limit.

In order to investigate the difference between non-regulated ( $\pm 10\%$  variation) and fully regulated load, a simple control system using solenoid valves, an electrical air compressor and a control computer was developed. The air compressor and accumulator tank was mechanically regulated to a constant target pressure. Based on the load cell measurements the control loop running in LabView sent a digital signal to a relay that controlled

the valves to the lifting bag. The system was designed to adjust any arbitrary load variation resulting from the pile head displacement or changes in ambient temperature. Furthermore, it was safe against power loss problems since the solenoid valves were of the normally-closed type, with zero differential pressure and low internal leakage. A schematic design of the valve operation scheme is shown in Figure 5.5.

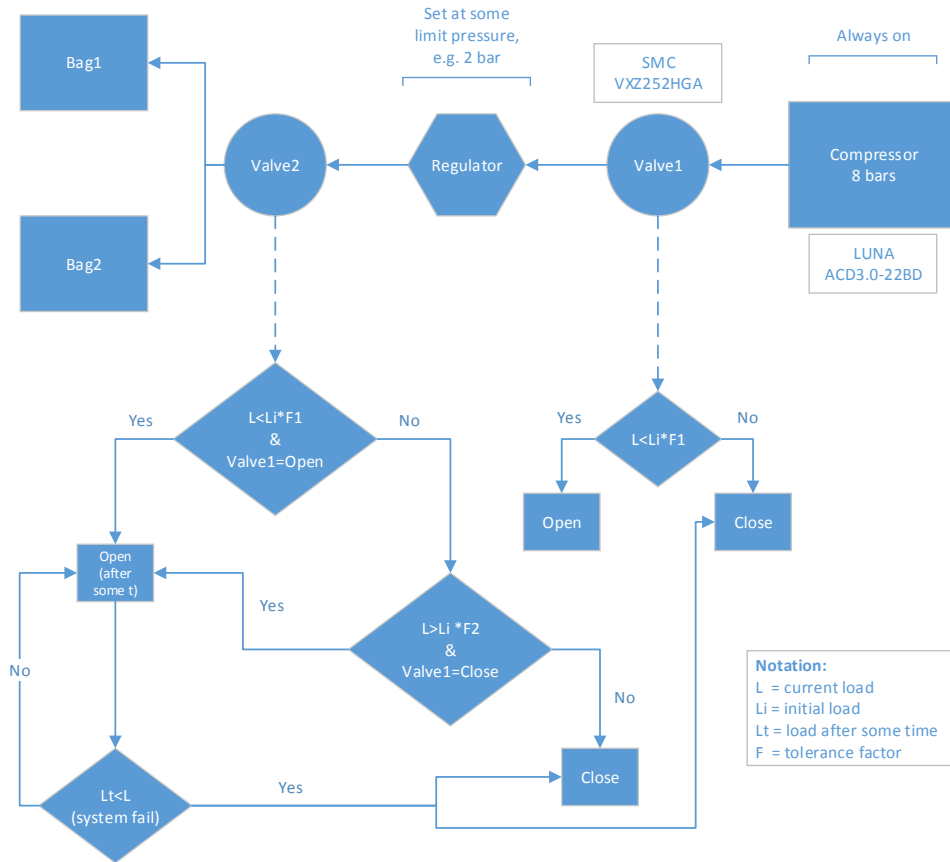


Figure 5.5: Bag control algorithm implemented in LabVIEW.

## 5.2 Test piles

The dominant long-term mechanism on the pile interface of floating piles in natural soft clays is the evolution of the relative displacement between the pile and the soil. Therefore, short test piles were used to only simulate the pile-soil interaction at the shaft within a limited length. Longer piles add additional variables that would complicate the test

interpretation, such as progressive failure, negative skin friction or non-uniform shaft friction distribution due to soil heterogeneities along the pile length. Furthermore, by embedding this element in deeper soil layers, surface effects (e.g. from the reaction frame) are minimised.

The pile elements consisted of six pre-cast reinforced concrete piles of 4.20 m length (1/3 of Swedish standard size) and 0.235 m x 0.235 m cross section. The concrete used for the piles had a mix designation C50/60. Apart from the steel reinforcement, the pile had a inspection pipe of 50 mm diameter for the tension loading rod all the way through, and two tell-tales of 20 mm diameter. One tell-tale pipe reached to the pile middle section and the other was fixed 0.25 m below the head (see Figure 5.6, 5.7 and 5.8). The bearing capacity for this short pile was initially estimated using the total stress method with  $\alpha = 1$ . For a natural soft clay with shear strength around 30–40 kPa, the estimated capacity was in the range of 100–150 kN.

The first 0.2 m (head) of the concrete pile was made of a steel square profile with a smaller cross section of 0.225 m x 0.225 m. This steel part at the pile head worked as a joint for the extension element required to penetrate the piles to deep soil layers. For the latter, an open-end steel pile of 13.5 m length (two 6 m and one 1.5 m section) with outer diameter of 0.220 m was used. At the same time, this pile served as a casing for the instrumentation cables, tell-tales and tension loading rod coming from the concrete piles. By joining the concrete and steel piles as a single element during installation, it was possible to achieve the proper installation effects and kept the clay from intruding into the open-end steel pile. After the target depth was reached, the extension pile was pulled back, detaching both piles with a gap remaining of 0.10 to 0.15 m.

A steel tension loading rod (GWS type made by Skanska AB) with diameter  $\varnothing = 32$  mm applied the tension load at the toe of the element and was guided to the surface level through the inspection pipe. In this way the concrete is compressed and tension cracks are avoided, keeping the material as a continuum without strain localisation. The weight of one pile element including the tension loading rod was approximately 6.45 kN.

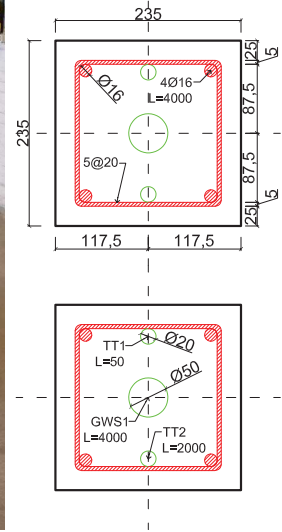
### 5.3 Load frame

The load frame consisted of two HEB260 steel beams resting on top of the bags and connected to the tension loading rod as shown in Figure 5.8. The bags were located between two double-layered waterproof plywood sheets and rested on top of a 0.30 m height timber mat. Pressurising the bags pushed the beams upwards, pulling the pile and creating a reaction load against the ground surface below the bags. Care was taken in centering the rod together with the frame in order to avoid eccentricity during loading.

The loading capacity of the frame is proportional to the number of bags and the configuration of the bag (pressure and contact area) and can be scaled as desired. The actual



(a) Concrete+steel fit for extension pile



(b) Cross-section (mm)

Figure 5.6: Pile elements.

and one ideal configuration are shown in Figure 5.9 with their respective capacity based on a selected pressure and initial lifting height of the bags. Two bags can balance in the vertical y-direction, keeping the frame straight. However, if the rod is not centred, the frame can tilt. The latter is not a problem in case of four bags, as these balance in both directions. Finally, it is important that the bags can redistribute the load on the ground level without inducing excessive settlement. Simple 1D calculations for a load of 50 kN under each bag with 1 m<sup>2</sup> contact area resulted in approximately 5 cm of ground surface settlement, distributed within the first 5 meters below.

## 5.4 Instrumentation

The piles were instrumented with strain gauges, pore pressure transducers and tell-tale rods. The tension load was measured using ring load cells and the displacement with linear potentiometers (LP) and mechanical dials. All instrumentation is listed in Table 5.2.

The strain gauges were used for estimating the load distribution along the pile length by measuring the strains in the reinforcement steel bars (assuming plane sections remain plane). In house sister bars of 0.50 m length and  $\varnothing = 16$  mm diameter, were tied to the main rebar as shown in Figure 5.10. First, the bars were polished in the centre area using a lathe, then the strain gauges were glued and then sealed with a silicon coating (SG250 HBM). A final coat of 3 mm thick kneading compound and 0.05 mm

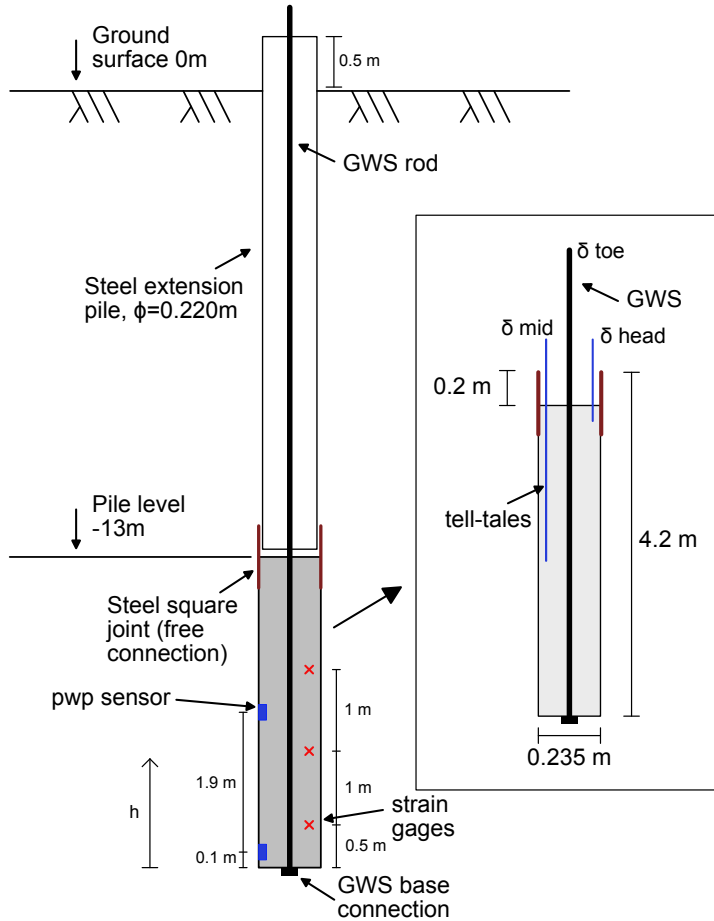


Figure 5.7: *Boundary conditions of a single pile in the field test.*

thick aluminum foil (ABM75 HBM) was applied to ensure the full sealing of the strain gauges. The sister bars length was selected based on the development/embedment length of reinforcement according to the American Concrete Institute (ACI) 318 code. Each pile had three measurement points along the shaft, located at  $h = 0.5$  m, 1.5 m and 2.5 m from the pile toe. At each level two sister bars were attached opposite to each other in order to have redundancy in the system. The gauges were configured as half-bridge, with one gauge in the axial direction and the other horizontal, to compensate for Poisson's ratio and temperature effects. A connection diagram of a half-bridge strain gauge and the data logger is shown in Figure 5.11.

Pore pressure transducers were installed at the pile shaft as shown in Figure 5.12. These measured the excess pore water pressure after installation, under the set-up period and during loading of the pile. The transducers were inside a small sealed canister fixed at

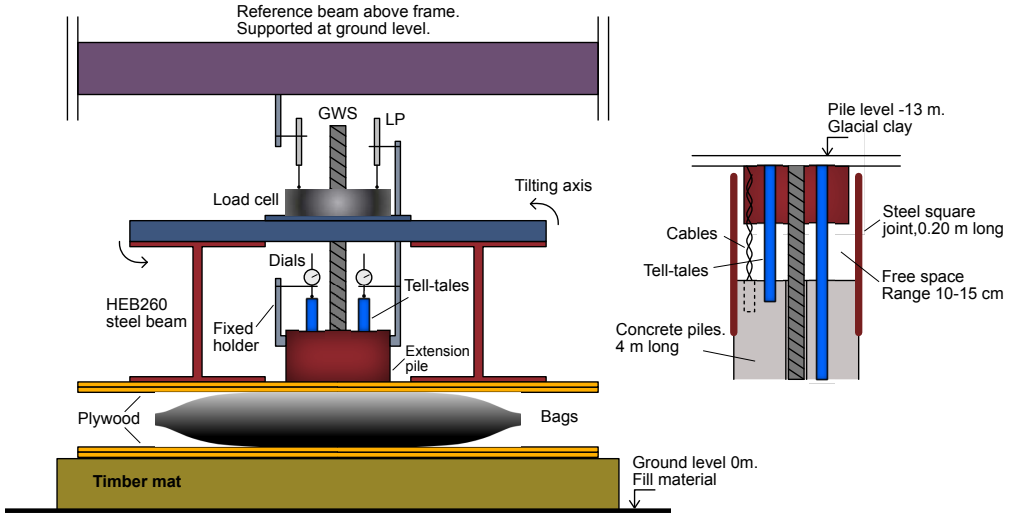


Figure 5.8: Loading frame parts at ground level (left) and concrete pile head details (right).

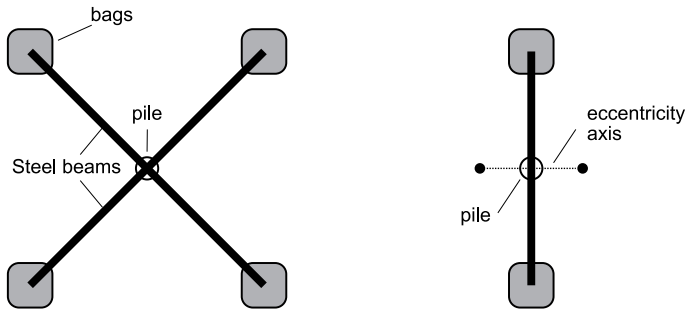


Figure 5.9: Illustration of possible bag configurations. Four bags give a stable frame against eccentricity as compared to two bags.

the pile shaft, and were located at the mid and/or bottom of the piles ( $h = 2$  m and/or 0.1 m above the pile toe). The transducer and stainless steel sintered filter stone were saturated with glycerine oil before the installation. This viscous liquid maintained the saturation during the lifting and installation of the piles.

The pile displacement was monitored using the LPs, dial gauges and tell-tales. The LPs were placed on top of the plate that connected the tension loading rod with the H-beams. At this measuring point, an additional elastic displacement component from the tension loading rod was indirectly incorporated in the measurements (to be corrected in the results).

The mechanical dial measured directly the tell-tales. The tell-tales were steel pipes of  $\varnothing = 20$  mm going from the ground level to two selected levels, namely the pile head and



(a) (b)

Figure 5.10: *Strain gauges glued to sister rebars.*

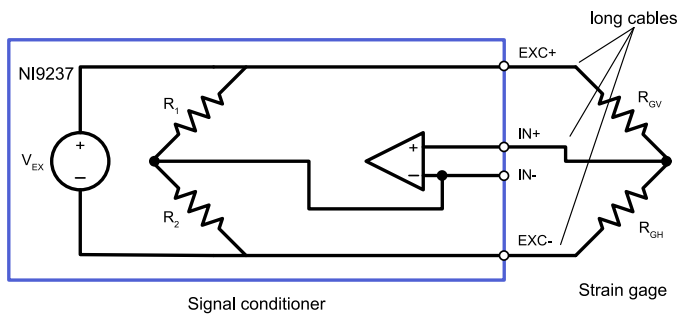


Figure 5.11: *Half-bridge strain gauges connection diagram to the NI 9237 module.*

the pile mid-section. A special mounting was designed to fix the dial gauges to the steel extension pile. This allowed removal of the dials after each measurement while keeping the same fix for subsequent measurements. The accuracy of this method was approximately  $\pm 0.10$  mm.

The fixed points used for measuring the relative displacement between the pile-soil interface were the steel extension piles and an aluminium beam going above the loading frame, resting on two steel holders supported at ground level. These points were considered stable and relatively fixed in space and with time. Levelling was done to control these fixed points using a digital level instrument and a reference point located on a nearby bridge foundation.

## 5.5 Data logging - local and remote

All instruments were connected to a National Instrument Data Acquisition (DAQ) system model NI-cDAQ9178 equipped with two NI9219 and two NI9237 modules. Both modules had four differential channels with 24-bit resolution that convert analogue input signals to digital. The DAQ chassis was grounded to one of the steel extension piles at the site.

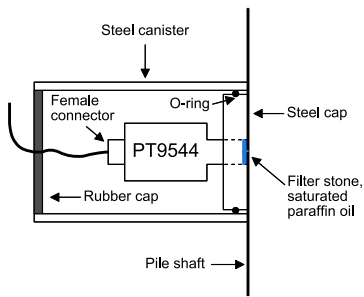


Figure 5.12: Pore water pressure transducer mount design at pile shaft.

The data was processed with a custom made LabView application before storage and visualisation. The data was stored in the field computer and a manually back-up every month. In addition, the computer was connected to the internet with a 4G USB modem. The latter gave the possibility to check the data live using a remote desktop viewer called *join.me* and to back up the measurements in the cloud using *Dropbox*. Furthermore, the computer was controlled remotely with *Google Remote Desktop* and a script was made using *Autoit* to automatically restart the measurements in case of a power loss.

## 5.6 Calibration

All the equipment was calibrated before the start of the experiment. The linear potentiometers, load cells and pore pressure transducers were calibrated at the Geotechnical and Concrete laboratories of Chalmers University of Technology. All devices performed within the specifications.

A model pile of 1 meter long was used to evaluate the strain gauges performance, and the stiffness of the concrete cross section. The strain gauges were glued directly to the main reinforcement steel at the mid level. The test was performed at the Concrete laboratory of the SP Technical Research Institute 156 days after casting. The pile was compressed axially without lateral support. The results are shown in Figure 5.13 for two loading cycles up to 500 kN. Non-linearity was found in the elastic modulus of the reinforced concrete specially under the expected working range. As observed,  $E$  ranged from 28–33 GPa for the 200 kN load cycle. The modulus was related to the strains following the same procedure as suggested by B.H. Fellenius (2001). The two strain gauges show different  $E_{tan}$ , this can be due to bending moments or that the reinforcement was not vertically aligned during casting and after curing.

Table 5.2: Instrumentation of field test

Measurement	Instrument	Manufacture	Specifications
Pile displacement	Linear Potentiometer HLP190 25mm	Penny & Giles	Independent linearity $\pm 0.3\%$ , Resolution $\infty$ , Hysteresis $< 0.01$ mm, Temperature $-30$ to $+85$ C $^\circ$
	Linear Potentiometer HLP190 75mm	Penny & Giles	Independent linearity $\pm 0.2\%$ , Resolution $\infty$ , Hysteresis $< 0.01$ mm, Temperature $-30$ to $+85$ C $^\circ$
	Dial gauges 20mm	Mitutoyo	Accuracy $\pm 0.01$ mm
Loads	Ring load cell 363YH 30ton	ANYLOAD	Sensitivity 2 mV/V, Nonlinearity $< 0.3$ %FS <sup>1</sup> , Hysteresis $< 0.3$ %FS, Repeatability $< 0.2$ %FS, Creep (30 min) $< 0.5$ %FS, Temperature $-10$ to $+50$ C $^\circ$
Pore pressure	PT9544 0 to 10 bars, IP67/69K, Relative pressure	IFM	Accuracy $\pm 1$ %FS, Linearity $< \pm 0.25$ %FS, Hysteresis $< \pm 0.2$ %FS, Temperature $-25$ to $+90$ C $^\circ$
Strains	Strain gauges HBM 1-XY11-6 / 350 $\Omega$	HBM	Maximum elongation 5e4 $\mu$ m/m, Gage factor $2.04 \pm 1$ %, Transverse sensitivity 0.2 %
Levelling	DNA03	Leica	Accuracy $\pm 1$ mm/km
Temperature (Air)	USB TH10	EXTECH	–

<sup>1</sup> FS= Full scale

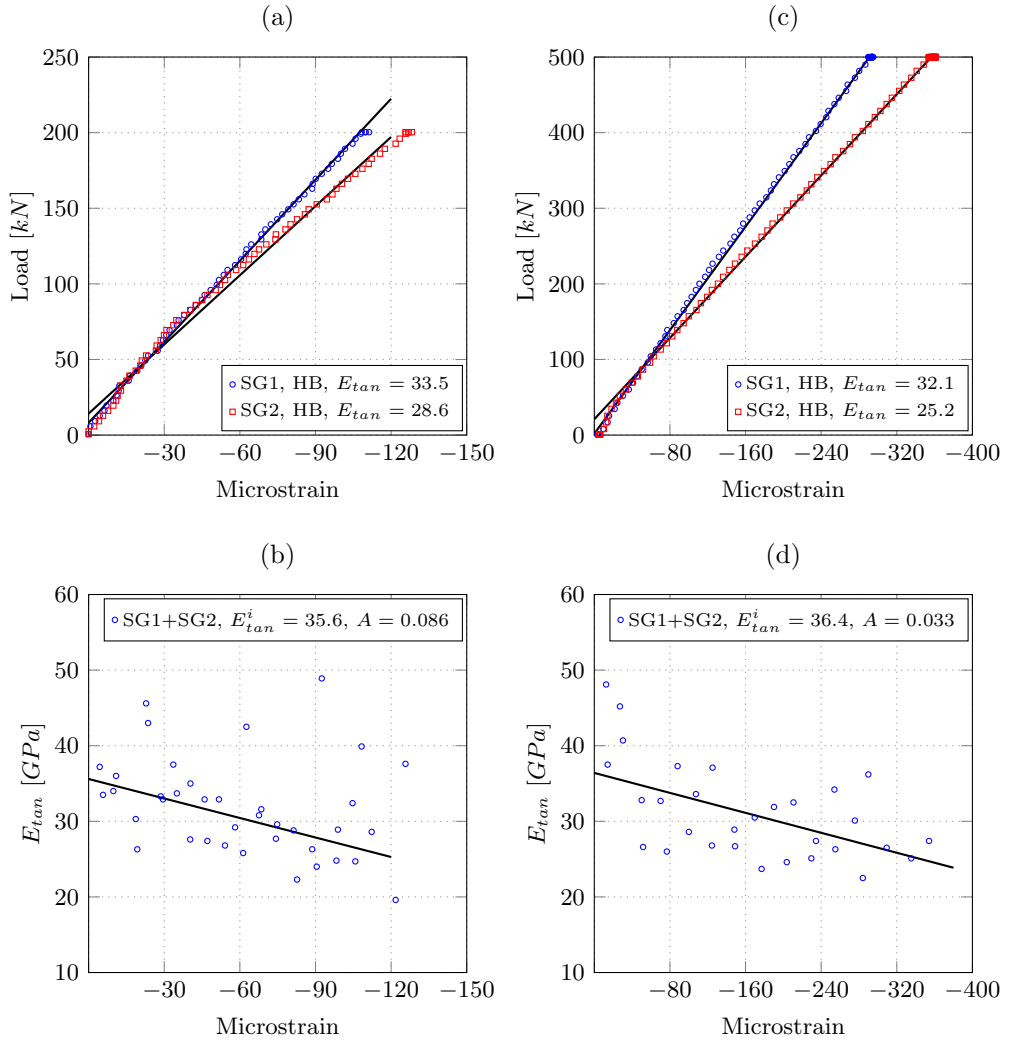


Figure 5.13: Compression of 1 meter model pile: (a) Load cycle 200 kN, (b)  $E_{tan}$  as  $f(\varepsilon)$  for 200 kN, (c) Load cycle 500 kN, (d)  $E_{tan}$  as  $f(\varepsilon)$  for 500 kN.

## 5.7 Protocols and execution of pile load tests

Piles 1 to 5 were installed at the site between 2014-04-10 and 2014-04-14, and Pile 6 on 2014-04-30. First, a hole through the filling material was created using a 2 meter long close-ended steel pile. This cleared any material from the fill that could hamper the installation of the concrete piles. Subsequently the extension steel pile and concrete pile were driven through the clay with a Junttan PM23lc pile driving rig that had a ram weight of 4 tons. The clay was very soft and the pile could sink just with the ram weight. The clay was very soft and the pile could sink just with the ram weight. Just a few blows were required when approaching the final depth. The extension pile was penetrated until 50 cm remained above the ground surface and immediately pulled back another 10 – 15 cm in order to detach it from the concrete test pile (but still keeping the sections inside the 20 cm high steel square joint). A steel plate was welded around the extension pile at ground level in order to avoid the pile sinking back directly after the pull-back. The plan view of the field arrangement is illustrated in Figure 5.14.

A fill layer of 0.30 – 0.40 m was laid on the ground to level the area and to form a base for the loading frame. This was done in two stages, one at 2014-09-01 and other 2014-09-30, equivalent to 4.5–5 months after installation of the piles. On top of the fill, a timber mat was installed for the lifting bags and to help redistribute the reaction loads into the ground.

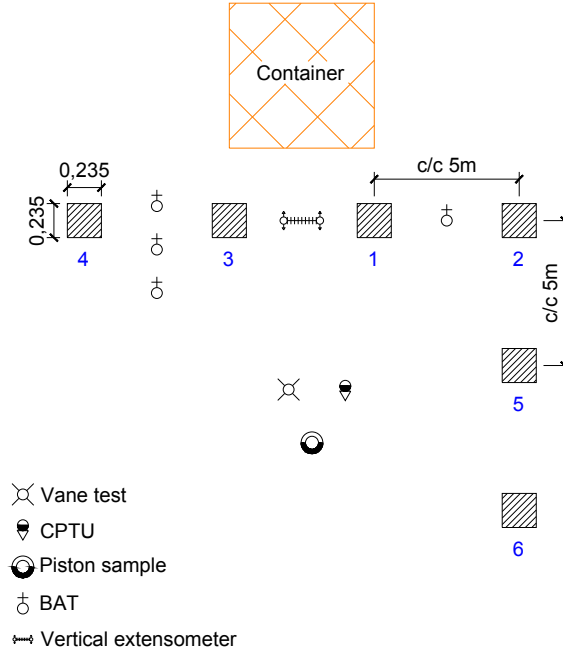


Figure 5.14: Plan view of the pile field test and the in-situ test investigation.

### 5.7.1 Short-term (ST) pile load tests

Knowledge on the short-term behaviour is required as a reference for the long-term loading. In this case, an estimate of the ultimate bearing capacity ( $Q_{ult}$ ) prior to loading was calculated using the  $\alpha$ -method. Characteristic values from DSS and vane shear test for  $S_u$  were used, with an average  $S_u$  value of 30 kPa along the pile shaft and  $\alpha=0.9$ . This resulted in  $Q_{ult}^{est}$  equal to 106.5 kN. A safety factor of 1.1 was used, giving a possible maximum  $Q_{ult}^{est}$  equal to 117 kN. The short-term tests were planned following this approximation.

In Sweden there is no specific standard for static load testing of piles neither in tension or compression. The pile commission report number 59 for static load testing (PK-R59, *Anvisningar för provpålning med efterföljande provbelastning*) is a guideline that mainly refers to static load testing of piles loaded in compression (PK-R59 1980). Looking at the international literature, it seems that there is not yet a defined standard for tension loaded piles. For example, the ISO is still working on a specific standard for tension loaded piles, under the TC182 committee, subcommittee SC1, project 224777. Therefore, it was decided to follow the Swedish guidelines even for tension loads as previous local experience showed reasonable results (Bengtsson and Sällfors 1983).

PK-R59 recommends a pile set-up period of 4 to 6 months before the test. Thereafter, the pile can be loaded using the quick maintained load method (QML). This approach loads the pile with small increments (5-10% of  $Q_{ult}^{est}$ ), holding the load for a short period of 15 minutes. After each load step, the measured pile displacement is mainly a result of the elasto-plastic response (in shear) of the soil and the pile elastic deformation. Therefore, very little consolidation and negligible creep takes place at this loading rate. The ultimate bearing capacity for a tension pile is reached when its shaft friction is fully mobilised. It is known from experience that small pile head displacements of 2 – 4 mm (or 1 to 2% of the pile equivalent diameter) are sufficient to reach this maximum, followed by a softening effect and/or slip at the pile shaft (Tomlinson and Woodward 2014).

The above procedure gives the load-displacement curve for the tested pile. Using the accumulated displacement of the last 3 to 6 minutes of each load step, a curve is obtained for the rate of displacement as a function of applied load. From this curve the “creep load” is evaluated as the point with the smallest radius of curvature.

A preliminary test was performed to test the functionality of the bags and the loading system. The maximum load applied in this test was 60 kN, which did not show any significant pile displacement. Based on this test, it was decided to start loading the piles from a first step of 20 to 50% of  $Q_{ult}^{est}$  and then with load steps of 10-15%. All short-term tests are listed in Table 5.3 and the test protocol for each pile is shown in Figure 5.15.

Two piles were used for short-term testing and a total of three tests were carried out to determine  $Q_{ult}$ . The first test (ST6A) presented problems with the measurement system. Therefore, a second test was conducted to validate the results (ST5A). The third test (ST6B) was aimed at studying the recovery of the bearing capacity of a previously tested

(failed) pile (ST6A).

Table 5.3: Short-term pile tests

Pile #	Test	Note	$t_{setup}$ (days)
5	ST5A	After set-up	207
6	ST6A	After set-up	165
	ST6B	After ST6A+new set-up period	206

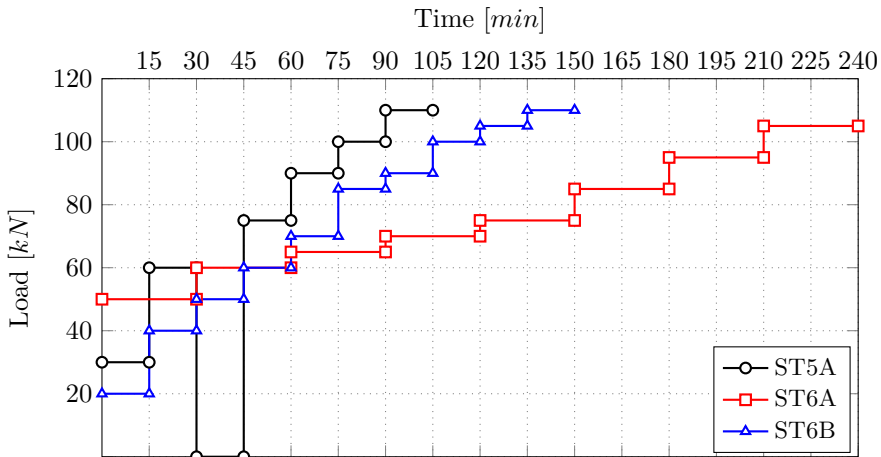


Figure 5.15: Test protocol for short-term QML tests.

## 5.7.2 Long-term (LT) pile load tests

The long-term tests are the main focus of this Thesis. These tests were designed to capture the creep displacements of the tension loaded pile section as a function of the applied load and holding time. In addition, the long-term bearing capacity is studied after a period of sustained load by loading the pile to failure.

The four remaining piles were used for the long-term tests. These piles had a pile setup period of 215 days. Based on the ultimate bearing capacity obtained from the short-term tests, the bags were initially configured to start with a lifting height around 125 mm and an air pressure in the range of 100–200 kPa (1 – 2 bars). This configuration gave a spring constant between 0.15–0.30 kN/mm and 0.08 kN/C°, which is rather small. Therefore, the loads were manually regulated instead of having a constant-load control system as the set-up was sufficiently compliant. The maximum allowed change in load was  $\pm 10\%$  of the current load level.

An additional pile was tested with a fully controlled load in order to compare the manual regulated results. Pile 5 was reused after resting for 184 days following its short-term test (391 days after installation). The load was kept constant in time using the system described in Section 5.1.2. LPs measurements were performed directly on the tell-tales since these were more stable reading points.

All piles were pre-loaded with 8-10 kN in order to remove the slack in all the joints of the loading frame. After that, the LPs and dials were zeroed and the piles were loaded to the target load levels given in Table 5.4. Different mobilisation ratios were selected to evaluate the creep rate as function of  $Q_{ult}$ . The hold time for each load step was evaluated according to two criteria:

- the displacement rate was lower than 0.01 mm/h, which is thirty times lower than the recommended rate of 0.30 mm/hour in the ISO 22477-1 standard (Standards 2016) for static maintained load test (ML);
- until the displacement-time curve showed a tendency to reach an asymptote (in a linear plot).

Table 5.4: Long-term loading ratio  $Q/Q_{ult}$  (%)

Step	Piles <sup>a</sup>				
	1	2	3	4	5 <sup>1</sup>
1	65	50	70	45	50
2	80	60	80	80*	60
3	95	80	85*	90	70
4	-	90	-	-	80
5	-	-	-	-	90

<sup>a</sup> After each load step in Pile 1 – 4, the load changed with time and was adjusted manually at irregular intervals.

<sup>1</sup> Pile 5 was pre-failed in ST and set-up for 184 days. For LT test the load was regulated at all time with solenoid vales.

\* First unloaded to 0 kN and then reloaded to new step.



## 6 Results from field test

### 6.1 Data acquisition and processing

The experimental data obtained from the field tests consisted of displacement, strain, load and pore water pressure measurements. A total of 16 channels were available at the field for logging the data. This number of channels was sufficient for the single piles during short-term tests. However, for the four simultaneously loaded piles with sustained loads, not all devices could be logged due to the limited channel quota. Therefore, the channels were distributed as follows: 4 load cells and 4 LPs (one per pile), 2 pore water pressure transducers and 3 strain gauges for Pile 1, and 1 pore water pressure transducer for Pile 2.

The configurations for the data logger for both the short- and long-term tests are given in Table 6.1. These configurations were based on the observations from a preliminary test (see Section 5.7.1) and in order to measure slowly varying processes under sustained loading. Each sample stored at every time  $t_{sample}$  corresponds to the arithmetic mean of  $f$  samples that were first smoothed using a moving average filter with a window of 20% of  $f$ .

Table 6.1: Configuration of data logger NI-cDAQ9178

Parameters	Short-term	Long-term
Sampling rate [Hz], $f$	50	50
Logging steps [s], $t_{sample}$	30	30 and 600–900 <sup>1</sup>

<sup>1</sup> the first time step is valid for the first 24 hours of each stage.

Most instrumentation was stable during the short- and long-term tests. However, unforeseen variables affected the measurements, for example tilting of the steel frame due to load eccentricity and condensation in the electronic enclosures for the strain gauges and load cells. In addition, the piles were loaded at the beginning of the winter season and the temperature fluctuations only started to become more noticeable in the following months. This variation affected the experiment by changing the pile load (air pressure in the bags) and by creating some noise/drift in some of the electronic devices. The stability of each instrument is shown in Table 6.2 and details of the unforeseen variables given in the following Section.

Table 6.2: Instrumentation stability

Pile #	Long-term					Short-term		
	1	2	3	4	5B	5A	6A	6B
LP	D/E	S	E	S	S	S	E	S
Load cell	S	S	S	S	D	S	S	S
Pore water <sup>1</sup>	S/D	S/D	-	-	-	-	-	-
Strain gauges	D	-	-	-	S	S	F	S
Tell-tales	S	S	S	S	S	S	-	-

S: stable, F: failed, D: drift, E: erroneous reference, -:N/A

<sup>1</sup> The PWP were located at the middle (m) or bottom (b) of the pile shaft.

## Displacements measurements

The linear potentiometers measured against the top plate of the loading frame as illustrated in Figure 6.1a. At this point the measured displacement corresponds to the toe, and was the result of (1) the elastic extension of the steel pulling rod, (2) the pile element elastic compression (concrete), (3) the relative movement of the pile against the soil due to the soil elasto-viscoplastic response (elasticity, consolidation and creep), and/or (4) the tilting of the steel frame due to load eccentricity. On the other hand, the tell-tale measurements only captured components (2) and (3) as the dials/LPs were fixed to the extension steel pile (see Figure 6.1b). Therefore, the latter are considered the “real” displacement since these are isolated from the frame or pulling rod. As result, measurements at the loading frame top plate were corrected using the tell-tale measurements as reference (average of mid and head). For this process, the trend was preserved while the magnitude was corrected according to the manual dial measurements. The procedures are described below keeping in mind that there is some inherent uncertainties in the continuous data even after this correction.

1. *Elastic displacement component from the pulling rod.* The pile load was applied at the toe of the concrete pile using a GWS steel rod, which had a length of  $\approx 18.5$  meters for all piles. Based on the steel elastic modulus of 210 GPa, for each kN applied the elongation of the rod was  $\approx 0.11$  mm. This additional component was subtracted from the LPs raw data as a function of the applied load.
2. *Load frame tilting.* In some occasions, the loading frame tilted along its short axis (see Figure 6.2). The tilting was observed directly after load application and remained nearly constant thereafter. The amount of tilting was identified by differentiating the LP and the dial (tell-tale) measurements at the beginning of each stage. This difference was subtracted from the data series for each stage.

Two mechanical dials were used to measure the tell-tale displacements. A fixed mount for the dials was built for each pile in order to reuse the same dials for manually monitoring



(a) *LP at top plate*



(b) *Fix for dial gauges*

Figure 6.1: *Loading frame details.*

all piles (see Figure 6.1b). The difference in magnitude between the middle and top tell-tale was in a range of 0.30–0.60 mm. This difference is considered too large, since it will be equivalent to a change in load from the pile middle to head equal to  $\approx 225\text{--}450$  kN ( $F = \sigma A = \varepsilon EA = \Delta\delta EA/(0.5L)$ ). Hence, the latter is clearly an inaccuracy in the measurements. This difference is the result of the accumulated error from using a non-fixed dial. The average of the tell-tales is presented herein and is considered as the stable pile head displacement. For such a short pile element, the difference between the toe and head displacement is minimal based on the concrete compression.

Levelling was done to control the fixed points used to measure the pile-soil relative movements. The far field fixed point was a nearby bridge abutment founded on long piles. This point was assumed to be locked in space during the experiment time. The fixed points near the piles were the shallow supports for the crossing aluminium beam and the steel extension piles in the soil. From these points, the latter were the most reliable ones, with recorded movements varying with  $\pm 1$  mm on average as shown in Figure 6.3. On the other hand, the shallow supports showed large movements and differential settlements. Therefore, only measurements relative to the extension pile are presented.

### Load and pore water pressure

The ring load cells were very stable during the short- and long-term tests, with little noise and negligible drift. However, during the first short-term test (ST6A), condensation in the electrical enclosure (cable joint connections) influenced the load measurements. This was avoided in all subsequent tests by properly sealing these enclosures.



Figure 6.2: *Picture illustrating the tilting of the load frame to the left with reference to the timber mat.*

All pore pressure transducers were functional during the pile installation and set-up period. During the long-term loading, only three pore pressure transducers were used. In some occasions, these did not give any measurements.

### **Strains in pile element**

Measurement of the strains in the concrete pile can be a complicated and resource demanding. For each measurement level it is recommended to have at least three full-bridge gauges separated by  $120^\circ$  (compensating for temperature, Poisson's ratio and bending moments). These strain gauges should be aligned in the vertical axis and positioned at the exact same level in the three positions. The latter is difficult to achieve since the strain gauges are glued to the main or sister rebars which are not 100% vertically and horizontally aligned.

In the tests presented herein a simplified set-up was used, consisting of half-bridge strain gauges glued to sister rebars and connected to the logger by cables of 15 to 20 meters long. Two sister rebars were used at each measuring level, with only one being recorded at a time due to the limited channel quota (the second was for redundancy). As consequence of the selected configuration, the measurement presented could be affected by bending moments and temperature effects.

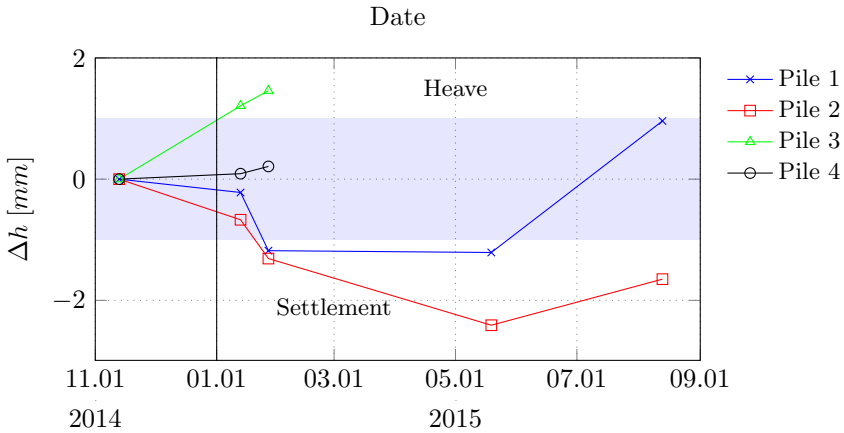


Figure 6.3: *Levelling of steel extension piles (accuracy  $\pm 1$  mm/km)*

## 6.2 Installation and set-up measurements

The excess pore water pressure was measured directly after installation and at irregular intervals during the equalisation time as shown in Figure 6.4. It can be seen that the excess pore pressure  $\Delta u$  is approximately double that of the initial in-situ conditions  $u_0$ . In relation to the in-situ effective vertical stress,  $\Delta u/\sigma'_{v0} \approx 1.4$  at the pile mid section (15 m below the ground surface) and  $\Delta u/\sigma'_{v0} \approx 1.5$  at the pile toe (17 m below the ground surface). This is in good agreement with the results from previous investigation presented in Table 2.2.

The equalisation time was approximately two months after the pile installation. This time was compared to the analytical charts given by Randolph, Carter, et al. (1979) for a linear elastic soil under consolidation with a ratio  $G/S_u = 150$ , permeability  $k = 1e - 9$  m/s, Poisson's ratio 0.2 and  $S_u = 30$  kPa. The latter resulted in an equalisation time of approximately 44 days, which is in good agreement with the measurements. For the long-term tests there were some periods where the transducers stopped working (temporarily). The reason for such problem in the measurement is not yet clear. One possible explanation can be the infiltration of water inside the canister.

## 6.3 Short-term tension load test results (ULS)

The short-term tests studied the ultimate tension bearing capacity of the piles after the set-up period using the test procedure described in Chapter 5. These tests served as a base reference for comparing the long-term tests. Two tests were performed using first-time

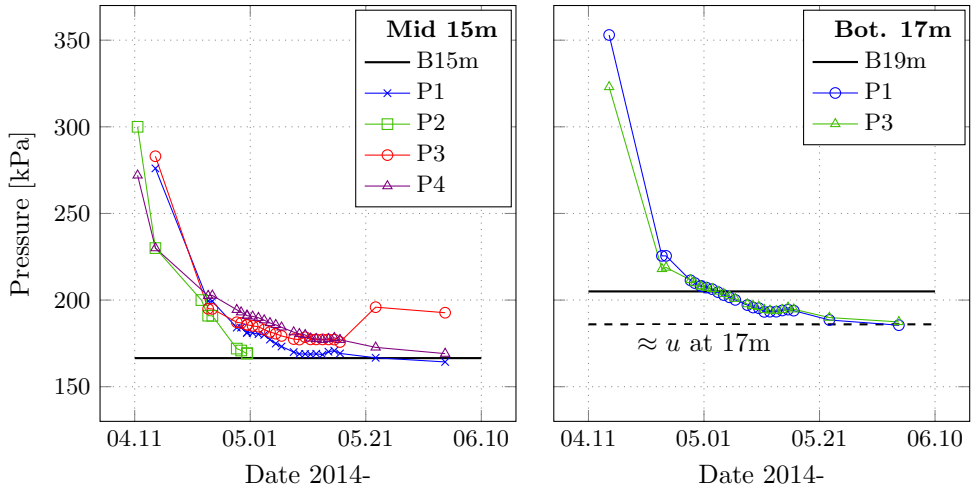


Figure 6.4: *Excess pore pressure after installation and equalization period at the pile shaft. Transducer at pile shaft and BAT (B; average) in the vicinity.*

loaded piles, while a third test was repeated using an already loaded (failed) pile. The set-up period was comparable for all tests. The results for the three piles are shown in Figure 6.5.

### Pile 6 - test A

Test ST6A was the first pile load test. For this pile no tell-tales were available and all measurements were performed at the top plate of the loading frame (equivalent to the toe displacements). Note that for these short pile elements, the difference between the toe and head displacement is less than 0.2 mm (concrete compression). During testing, the frame tilted significantly and condensation built up in the electrical enclosure. These problems affected the displacement and strain gauge measurements to a large extent, with smaller effects on the load. Therefore, the complete load-displacement curve was considered unreliable, and only the final failure load and the average accumulated displacement given by manual levelling and dial measurements is presented. The net ultimate tension bearing capacity for ST6A was  $Q_{ult} = 100.8$  kN, with an accumulated average toe movement at the onset of failure of  $\approx 4.5$  mm  $\pm$  2 mm. During the last load step, it took approximately 4 minutes before the pile showed a rapid increase in the displacement rate where the applied load no longer could be sustained.

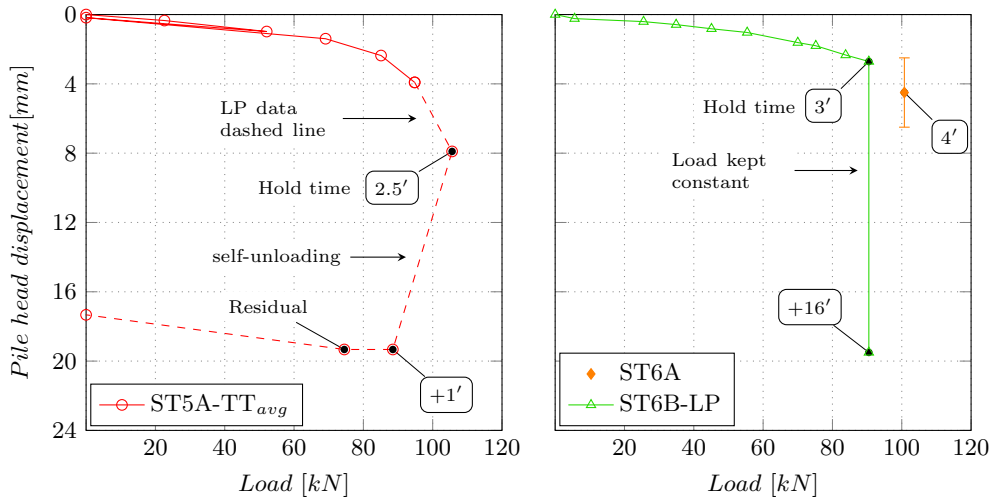


Figure 6.5: Short-term loading of Piles 5 and 6 (*TT* is tell-tale, *LP* is linear potentiometer).

### Pile 5 - test A

As a result of the difficulties with test ST6A, a second test was done, namely ST5A. This pile was equipped with tell-tales and strain gauges. Particular care was taken to seal all connections from humidity and to centre the loading frame. No problems were encountered and the result for  $Q_{ult}$  was in line with that obtained in ST6A, together with better data on the displacement. First, an unloading-reloading stage was performed at 60 kN, showing a recovery of the accumulated displacement up to that load. Thereafter, the pile was loaded to failure resulting in a net ultimate tension bearing capacity of  $Q_{ult}=105.6$  kN, with an average tell-tale displacement of  $\approx 8$  mm at failure. However, in the previous load step of 94.8 kN, the pile displacement rate was already very large at  $\approx 4$  mm of accumulated displacement. It is believed that the pile could have failed if the holding period was taken longer than 15 minutes. Nevertheless, the last load step was held for approximately 2.5 minutes, thereafter the pile started to slip. As the pile slipped during failure, the lifting height of the bags increased, decreasing the applied load. The slipping halted 1 minute after the pile was self-unloaded to 74.5 kN. The latter load represents the residual resistance at the shaft ( $Q_{res}$ ). The ratio between  $Q_{res}/Q_{ult}$  is 0.71 or 0.79 for  $Q_{ult} = 95$  kN.

The head and mid element tell-tales showed some difference in their magnitudes as a function of applied load. For the last load step, this difference was 0.15 mm for the top half of the pile (or in average 75 micro-strains with  $\delta/0.5L$ ), which in turn is equivalent to  $\approx 120$  kN. This load is larger than the applied load and can be attributed to the accuracy of the measurements. As a result, the average of the tell-tales was used for the pile head displacement. The creep load was evaluated following the Swedish pile testing guidelines

as described in Section 5.7.1. In this case, a bi-linear curve was fitted in the scatter plot of the accumulated creep displacement for the last 6 minutes of each load step as shown in Figure 6.6. The creep load range between 80 to 85 kN, with the intersection point at 83 kN.

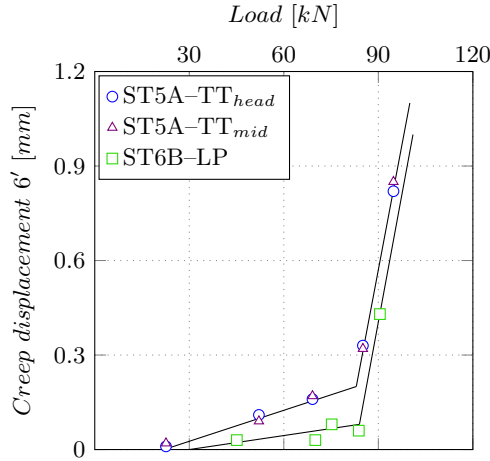


Figure 6.6: Accumulated creep displacement for the last 6 minutes of each load step for Piles 5 and 6.

Test ST5A was equipped with strain gauges. Their measurements are shown in Figure 6.7 corresponding to the two half-bridge arrays along the pile shaft. The load distribution is different in both sides, indicating that (1) the pile experience some bending or (2) some of the strain gauges are faulty or aligned with the load resultant. One side had an approximately linear decrease in load with increasing distance  $h$  from the toe up to the pile head. However, the other side showed a decrease in load just above the toe, followed by an increase of load above the pile mid height. Note that the load evaluated from the strain measurements is very sensitive for the selected concrete elastic modulus  $E_{conc}$  (B.H. Fellenius 2001). At the small strain levels in these tests, the  $E_{conc}$  is highly non-linear (see Section 5.6).

## Pile 6 - test B

A third test, experiment ST6B, was performed on the pre-failed Pile 6 after a second set-up period of 206 days. For this case, the frame was fixed in its short plane direction to avoid the tilting problem. The loading was fully controlled using the automatic and regulated system for constant load. The obtained ultimate tension bearing capacity was  $Q_{ult} = 90.5$  kN with displacement failure of  $\approx 3$  mm. This load could be held for 3 minutes before the onset of large displacement rates. The load was kept constant for another 16 minutes, as the slip mode did not occur immediately after the start of failure.

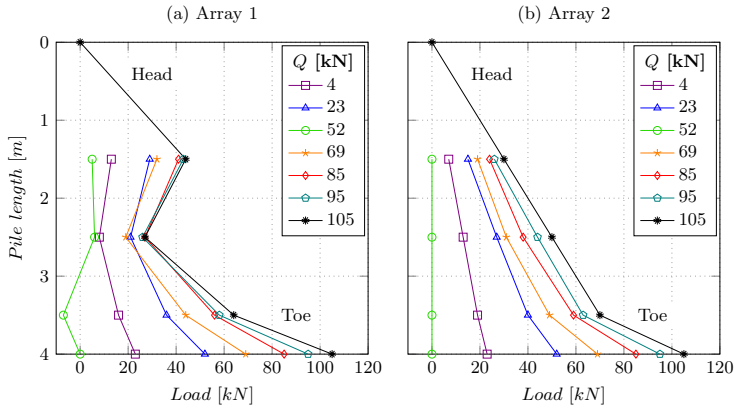


Figure 6.7: Load distribution from strain gauge measurements for test ST5A.

The evaluated creep load was  $\approx 84$  kN, which is almost identical to test ST5A (see Figure 6.6). However, test ST6B showed less accumulated displacements in each load stage and a lower  $Q_{ult}$  ( $\lesssim 10\%$ ) compared to ST5A. This indicates that the soil adjacent to the pile shaft has stiffened and the stress conditions varied following the shearing and subsequent set-up period from the first load test ST6A.

One of the strain gauge arrays was measured and the results shown in Figure 6.8. The load distribution pattern resembles that of array 1 of test ST5A, indicating that the pile might experienced some bending during loading.

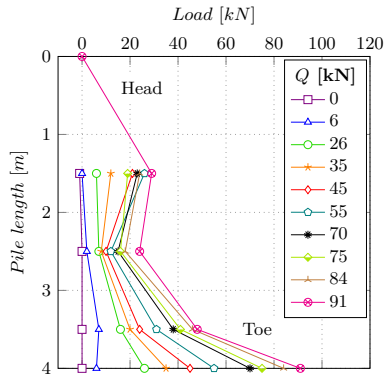


Figure 6.8: Load distribution from strain gauge measurements for test ST6B.

## Summary

The short-term results are summarized in Table 6.3. The virgin loaded piles show a similar ultimate tension bearing capacity and pile head displacement to failure. The second-time loaded pile shows a reduction in bearing capacity with lower accumulated displacement. In order to compare the long-term tests, a reference ultimate tension bearing capacity of  $Q_{ult}^{ref} = 100$  kN, a creep load of  $Q_{creep}^{ref} = 80$  kN and a pile head displacement of  $\delta_{head}^{ref} = 4$  mm was selected.

Table 6.3: Short-term test results.

Test	$Q_{ult}$ [kN]	$Q_{crp}$ [kN]	$Q_{res}$ [kN]	$\delta_{ult}$ [mm]	$\delta_{ult}/D_{eq}$ [%]
ST6A	100.8	–	–	4.5	1.5
ST5A	95/105.6	83	74.5	3.9/8	1.3/2.6
ST6B	90.5	84	–	3	1.2

## 6.4 Long-term tension load test results (SLS)

The long-term tests are the main objective in this research, aiming to explain the pile behaviour under the service load range ( $< 0.8Q_{ult}$ ). These tests studied the displacement and resistance evolution of the pile-soil system as a function of time and applied load magnitude. A total of 5 piles sustained loads for substantially longer periods than the short-term static QML tests. Four of these piles were stepwise adjusted, keeping the same air mass during each loading stage as describe in Chapter 5. The change in load was controlled to be within  $\pm 10\%$  of the current applied load and each load stage was held until the displacement rate was  $\leq 0.01$  mm/h. The fifth pile was loaded using the automatic regulated system, holding the load constant.

From all tests, Pile 2, 4 and 5 gave the best measurement data. Pile 1 and 3 yielded poor continuous displacement measurements due to tilting and reference problems (see Section 6.1). The results for these two piles can be found in the Appendix. First, the data from the manually regulated tests for Pile 2 and 4 is presented, followed by the automatic regulated test for Pile 5. The latter test was used to compare the load variation effects present in the unregulated piles. Finally, the measurement data is discussed before proceeding to detail analysis in the next Chapter (note that some gaps are present in the measurement data caused by power outage in the field). Additional details of these tests are found in the Appendix.

### 6.4.1 Stepwise manually-loaded

As described in Section 5.1.1, the lifting bags had a slight sensitivity to changes in height and temperature. Therefore it was decided to manually adjust the load with time for tests LT1A to LT4A. From these tests, LT2A and LT4A were the most stable during the complete loading period, with no signs of significant tilting from the load frame. Unfortunately, continuous displacement measurements for LT1A and LT3A were affected by tilting and changes in the fixed space reference (aluminium beam). Therefore the dial gauges measurements are the most reliable data for these two piles.

#### Pile 2 – LT2A

LT2A was instrumented with one LP, two tell-tales and one pore water pressure transducer at the middle height. The LP was located at the top plate of the load frame and fixed against the extension steel pile. At this point, the toe displacement was measured with an additional component from the pulling rod and tilting (if any). The latter factors were corrected as described in Section 6.1, resulting in an average displacement between toe and head. Displacement measurements were also carried out using the dial gauges on the tell-tales.

LT2A was loaded for a total of 149 days distributed under different load levels as shown in Figure 6.9. Each load increment was applied within 2 to 5 minutes. The load was not held constant and the pile self-unloaded with time as result of the pile element displacements, which changed the lifting bag volume. The displacement curve is not fully smooth and tends to an asymptotic value for load levels below 80 kN. The non-smoothness can be explained by the slight load variations and the soil properties along the pile shaft that are not fully uniform. The same has been observed for displacement curves in the laboratory (Ter-Stepanian 1992 as cited in Mitchell and Soga 2005). Furthermore, the measured data is a mix of pile creep and unloading displacements, with the latter being very small for the little load variation per load stage.

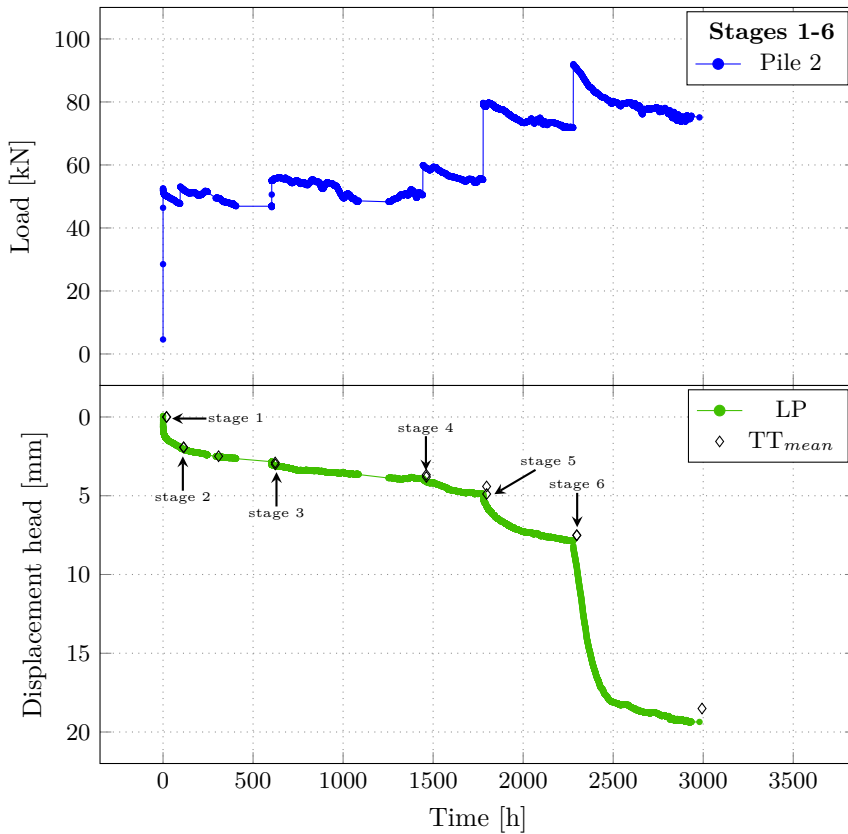


Figure 6.9: Load and displacement with time for all loading stages of test LT2A.

The applied load, accumulated displacement and hold time for each stage is given in Table 6.4 and plotted in Figure 6.10. The accumulated displacement for each load step consisted of (1) an instantaneous elasto-plastic component and (2) time dependent consolidation and creep. For the first hour, the accumulated displacements in each stage followed

closely the short-term loading curve. The magnitude of these displacements were larger than in the short-term tests for the same applied load level during the hold period. The displacements (and displacement rate) increased as the pile was loaded closer to its failure limit.

Table 6.4: Data from test LT2A.

Stage	t (d)	$Q_{ini}$	$Q_{end}$	$Q_{avg}$	$\delta_{ini}$	$\delta_{end}$	$\Delta\delta$	$\Delta\delta/t$
1	3.94	52.5	47.7	50.3	0.00	1.92	1.92	0.487
2	21.20	52.9	46.6	49.9	1.93	2.90	0.97	0.046
3	34.95	55.1	50.6	52.6	2.90	3.91	1.01	0.029
4	13.95	59.4	55.3	56.7	3.90	4.91	1.01	0.072
5	20.85	79.6	71.8	76.7	4.90	7.87	2.97	0.142
6	27.37	91.5	75.5	79.9	7.87	19.36	11.49	0.420
7	25.76	93.6	70.3	75.1	19.36	34.89	15.53	0.603

$Q_{ini}$ : load applied at the beginning of each stage.

$Q_{end}$ : load at the end of each stage (decrease due to lifting bags self-unloading.)

$Q_{avg}$ : average load for each stage.

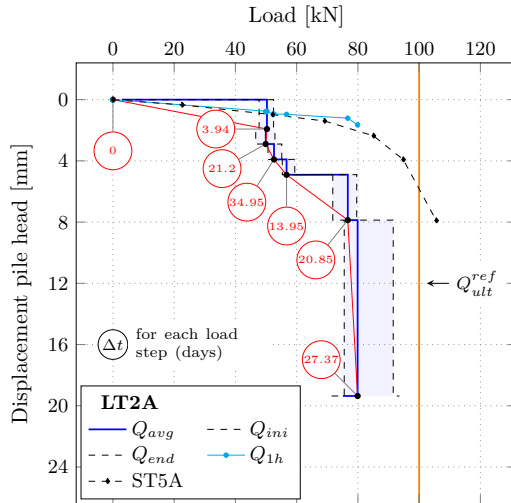


Figure 6.10: Long-term load-displacement curve for test LT2A.

Load steps 1 to 5 did not show any signs of failure that would be picked up by a sudden increase of the displacement rate. Therefore, these steps are considered “stable”. The test failed, however, during step 6 when loaded to 91.5 kN. Large instantaneous and time dependent displacements developed at this load, with no tendency to reach an asymptotic value after several days although the load reduction by self-unloading. The large displacement rate stabilized after the pile self-unloaded below 80 kN, which is

equivalent to a load ratio of  $Q_{sls}/Q_{ult}^{ref} = 0.80$  in relation to the short-term tests and equal to the reference creep load  $Q_{sls} = Q_{creep}^{ref}$  and average load for that stage ( $Q_{avg}$ ). At the onset of failure, the accumulated displacement was approximately that observed during the slip failure of the short-term tests, approximately 8 mm.

After failure, LT2A remained loaded with an average load of 80 kN for  $\approx 19$  days until it was loaded again to 93.6 kN. This time, failure occurred immediately (within 10 minutes) and the pile reached a lower residual load of 75 kN. This shows that the soil around the pile did not have enough time to heal and/or a shear band from the previous failure is re-activated.

Figure 6.11 presents a semi-log plot of the accumulated pile head displacement for each load step. It can be observed that these curves present a semi-log linear trend after some time (secondary compression). A linear regression is fitted at the region close to the end of each curve, with the slope of these lines as  $\Psi^l$  (the  $l$  superscript is for length units). Stages 5 and 6 exhibit a much larger creep rate than previous stages, with stage 6 failing after the first 24 hours. The  $\Psi^l$  parameter increased directly proportional to the applied load and it was bounded between  $\Psi^l$  0.2 to 0.7 mm before failure (tending to infinity for slip failure  $\Psi^l \rightarrow \infty$ ).

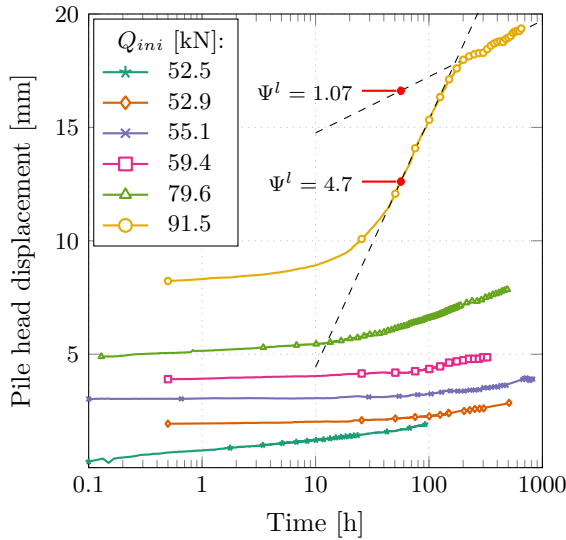


Figure 6.11: Time displacement for each stage of test LT2A.

Figure 6.12 shows the displacement rate with time for each stage. These rates were calculated for changes every 24 hours or every 6 hours for the failure stage. In general, the displacement rate decreased with time and was below 0.01 mm/h within the first 3 to 5 days after load step application. On the other hand, for stage 6 the rate remained constant at 0.1 mm/h for approximately 4 days and thereafter started to decrease. The

reduction was caused by the lifting bags self-unloading as the applied load could not be held constant. The decrease in pile creep rate is well approximated by using the logarithmic Equation (2.20) from Section 2.3.2, with the parameter  $\Psi^l$  and displacement  $\delta$  instead of the parameter  $\mu^*$  and strains  $\varepsilon$ .

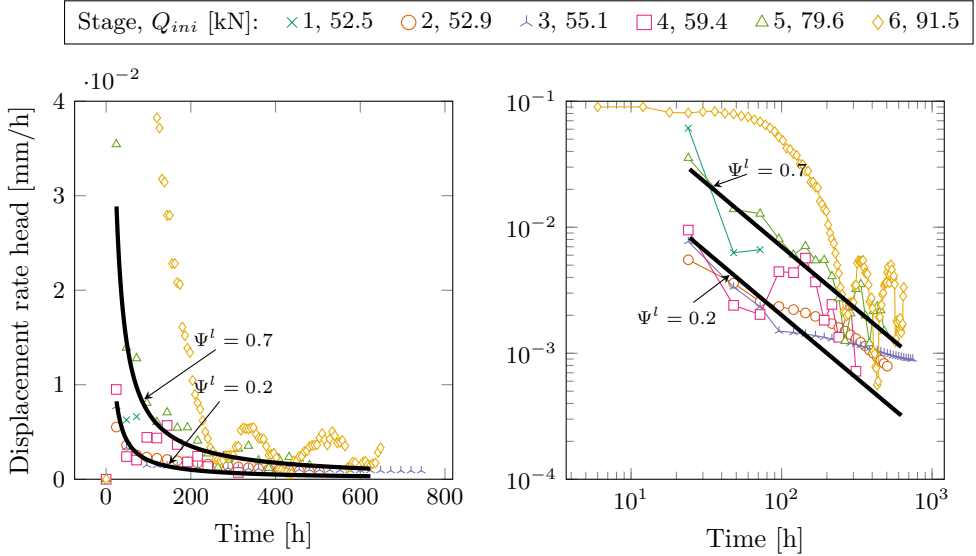


Figure 6.12: Pile head displacement rate in linear (left) and log-log (right) scale for each load step and creep curves for  $\Psi^l = 0.2$  and  $0.7$  with  $t_{ref} = 24h$  for test LT2A.

Another approach to plot the data is to normalize the pile displacements with the pile equivalent diameter  $D_{eq}$  (see Section 2.3.2). In this way a non-dimensional creep parameter is obtained analogous to that in Equation (2.20), representing the average deviatoric creep at the pile shaft ( $\Psi_{d,avg} = \Psi^l / D_{eq}$ ). Figure 6.13 shows the normalized pile displacement for all stages. The value of  $\Psi_{d,avg}$  is very similar to that obtained at large strains in 1D-oedometer tests (see Section 4.2).

For completeness Figure 6.14 shows the pore pressure measurements at the pile shaft at mid height. The data presents some scatter compared to the stable BAT measurements, with the initial pore pressure before any loading  $\approx 10$  kPa higher than the BAT. The latter increase in pore pressure can not be explained. The pore pressure fluctuated in time independently of the applied load. Changes in pore pressure due to new load steps were not always observed. For example, at stage 6 the pile failed by creep rupture, but the sensor did not measure any variation in pore pressure. However, some increase in pressure was observed upon reloading to failure in stage 7, approximately 5 kPa. However, those changes are more likely to be coincidental.

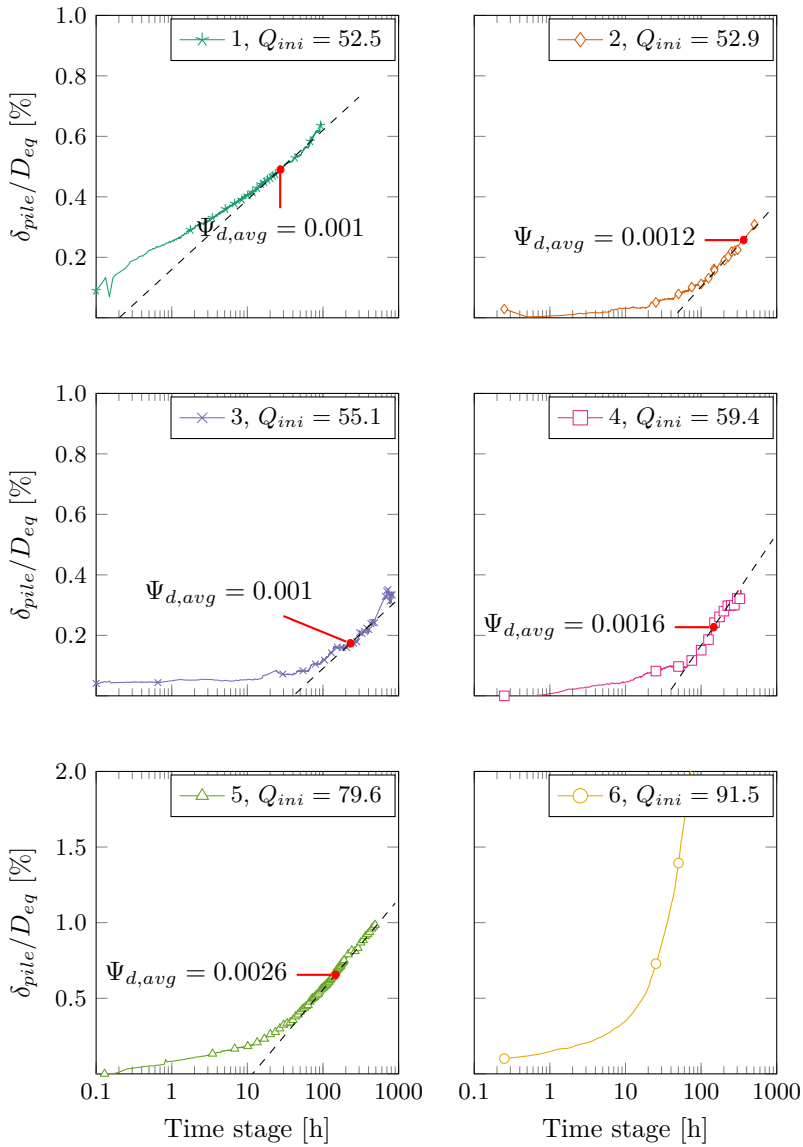


Figure 6.13: Normalized pile displacement for each stage of tests LT2A.

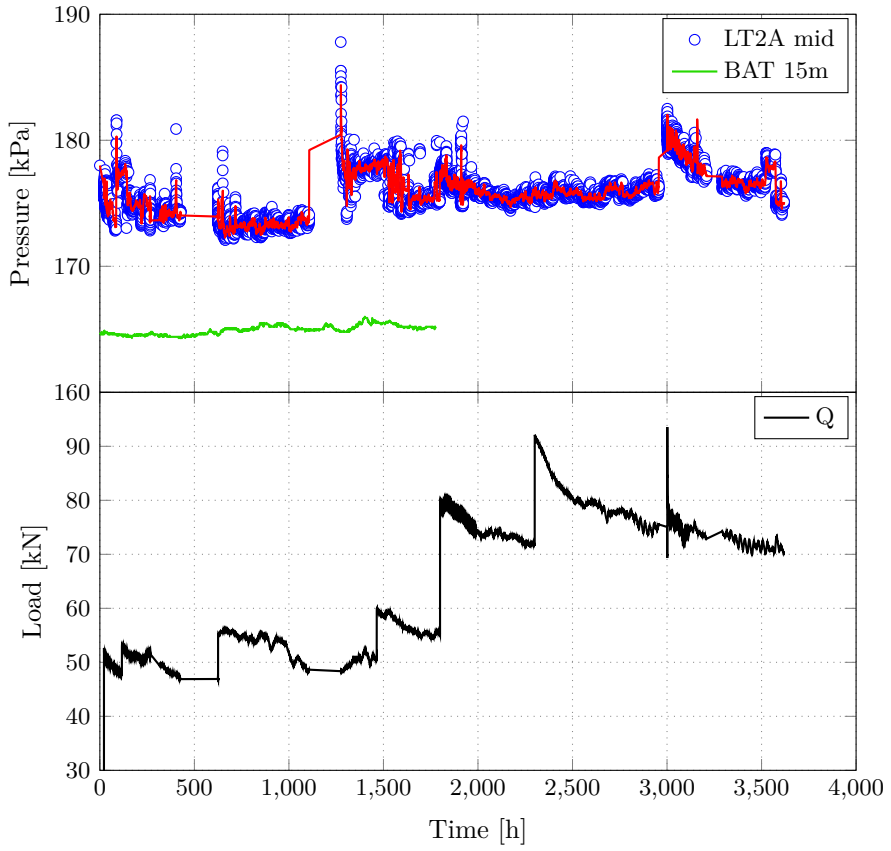


Figure 6.14: *Pore pressure at LT2A shaft mid height.*

## Pile 4 – LT4A

LT4A was only instrumented with one LP and two tell-tales. This test was configured similar to test LT2A, with the LP located at the top plate of the load frame and fixed against the extension steel pile. The displacement measurements were corrected for the additional elastic component from the pulling steel rod and tilting (if any). The load was manually regulated and kept within the variation limits of  $\pm 10\%$ . Initially, one of the lifting bag valves was leaking due to dirt intrusion inside the joint thread. It took some time to find the source of the problem, and therefore the pile had a smaller load for a longer period. The complete loading curve and pile head displacement data is presented in Figure 6.15.

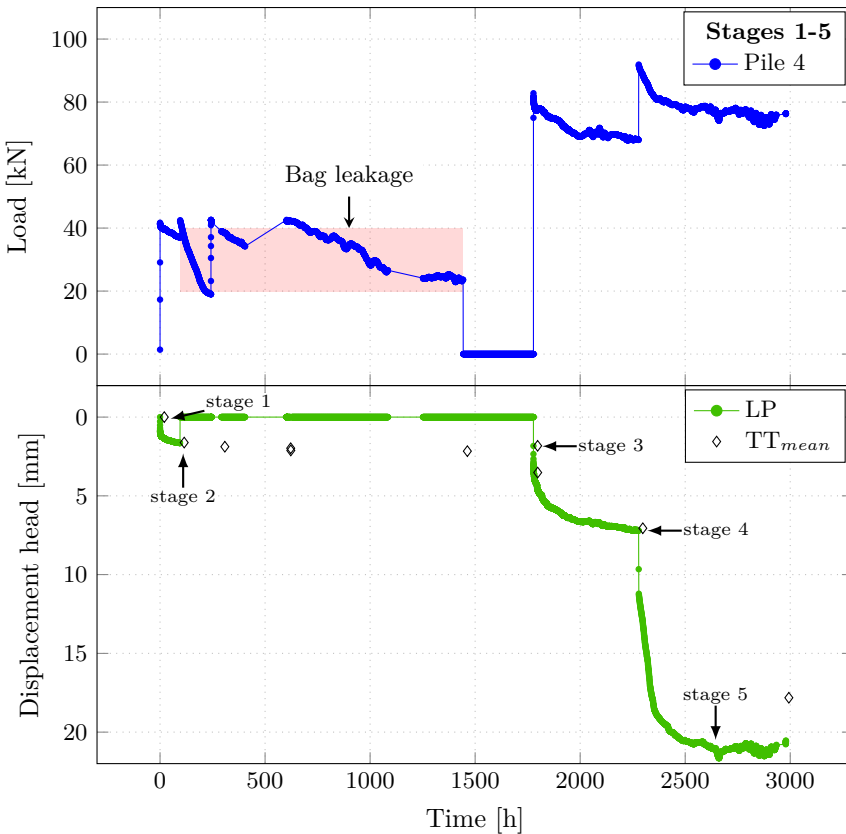


Figure 6.15: Load and displacement with time for all loading stages of test LT4A.

LT4A was loaded for a total of 116 days under three main load levels (Stage 1, 3 and 4). Each load increment was applied within 2 to 5 minutes. After each load step, the pile self-unloaded with time as result of the viscoplastic displacements (i.e. change of

lifting bag volume). The applied load, accumulated displacement and hold time for each stage is given in Table 6.5 and plotted in Figure 6.16. Similar to LT2A, the accumulated displacement for the first 15 minutes after each load step follows the same curve as in the short-term test. However, the magnitude of the accumulated displacement for each hold period is larger than the short-term tests for the same applied load; increasing as the pile was loaded closer to its failure limit. At stage 3, the pile failed by creep rupture with an initial load of 91.3 kN. The large displacement rate stabilized after the pile self-unloaded below 76 kN, which is equivalent to a load ratio of  $Q_{sls}^{ref}/Q_{ult}^{ref} = 0.76$  in relation to the short-term tests and  $Q_{sls}^{ref}/Q_{creep}^{ref} = 0.95$  in respect to the reference creep load. At the onset of failure, the accumulated displacement was approximately that observed during the slip failure of the short-term tests, approximately 7.2 mm.

Table 6.5: Data from test LT4A.

Stage	t (d)	$Q_{ini}$	$Q_{end}$	$Q_{avg}$	$\delta_{ini}$	$\delta_{end}$	$\Delta\delta$	$\Delta\delta/t$
1	3.95	41.8	37.0	39.7	0.00	1.65	1.65	0.419
2	61.88	42.0	0.0	–	1.65	1.83	0.18	0.003
3	20.85	83.8	68.1	73.7	1.83	7.21	5.38	0.258
4	15.27	91.3	77.5	80.3	7.21	21.03	13.83	0.905
5	13.93	77.5	76.3	75.8	21.03	20.54	-0.50	-0.036

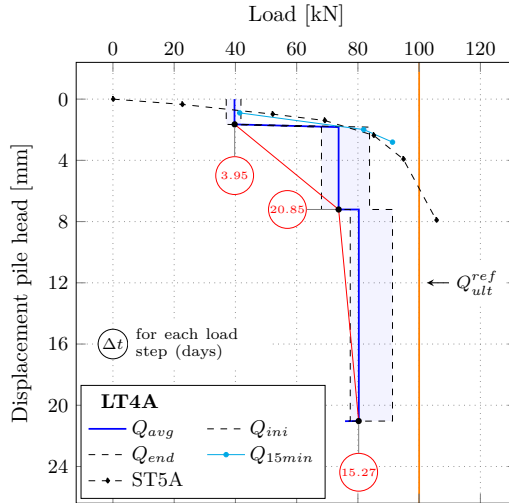


Figure 6.16: Long-term load-displacement curve for test LT4A.

Figure 6.17 presents a semi-log plot of the accumulated pile head displacement for each load step. It can be observed that these curves present a semi-log linear trend after certain time (secondary compression). The pile creep rate tend to decrease with time and as in test LT2A and seems to be bounded between the parameter  $\Psi^t$  0.2 to 0.7 mm

before failure (see Figure 6.18). Another approach to present the data is to normalize the pile head displacements with the pile equivalent diameter  $D_{eq}$ . The value for the non-dimensional creep parameters obtained in this way are in line to those in test LT2A as shown in Figure 6.19.

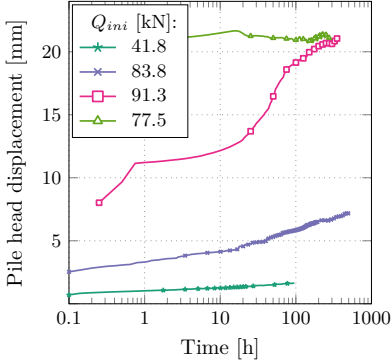


Figure 6.17: Time displacement for each stage of test LT4A.

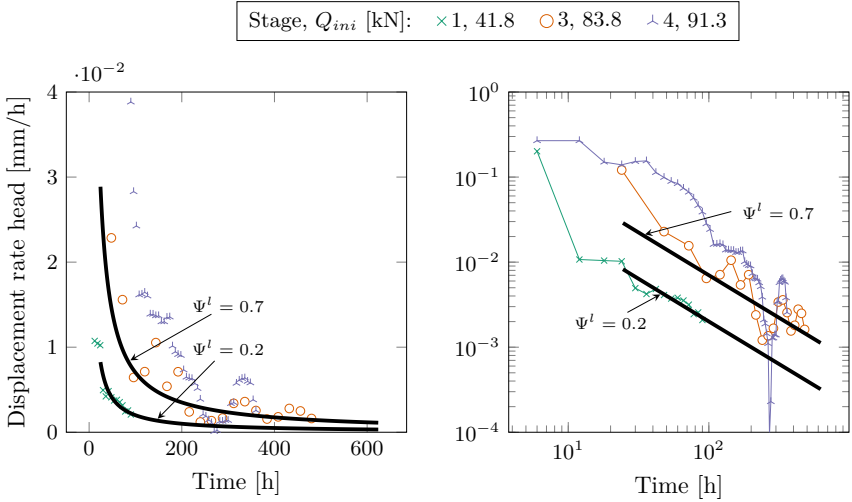


Figure 6.18: Displacement rate for each load step and creep curves for  $\Psi^l = 0.2$  and  $0.7$  with  $t_{ref} = 24h$  for test LT4A.

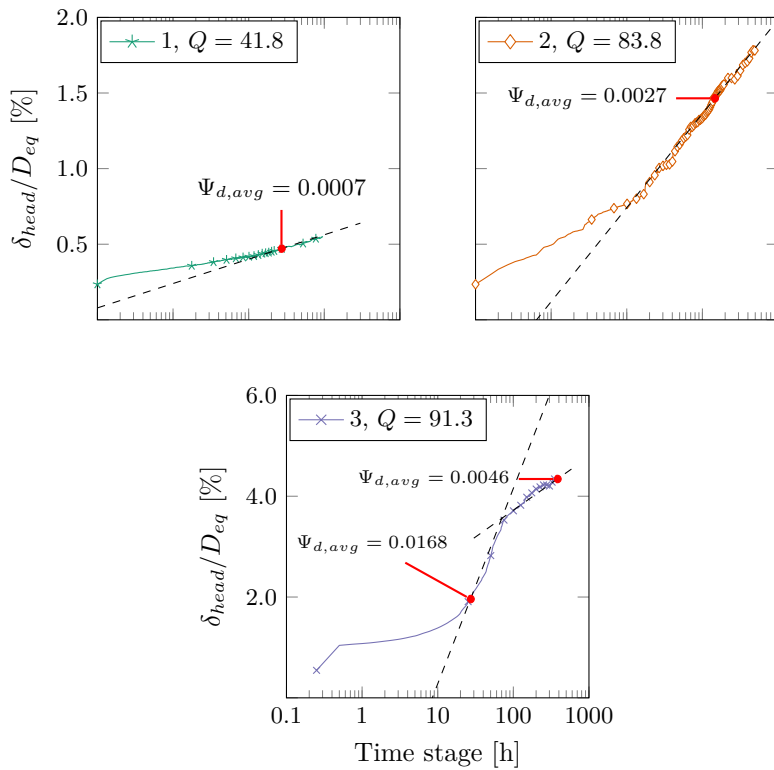


Figure 6.19: Normalized pile displacement for each stage of tests *LT4A*.

## 6.4.2 Stepwise automatic-loaded

### Pile 5 – LT5A

Pile 5 was reused for an additional long-term test following a setup period of 184 days after the short-term experiment ST5A. The purpose of this test was to observe if there was any difference in the pile creep by having constant versus varying load. LT5A used the automatic control system described in Section 5.1.2, keeping the load constant. Two LPs were placed on the tell-tales as these were not affected by the problems described in Section 6.1 (e.g. tests LT2A and LT4A). Therefore, the measured displacement was mainly from the pile creep at the pile shaft. The complete load and displacement curve versus time is presented in Figure 6.20. Each load increment was applied within 2 to 5 minutes. The load was kept constant in each stage and the displacement approached an asymptote with time for loads below 80 kN; similar to the manually regulated tests.

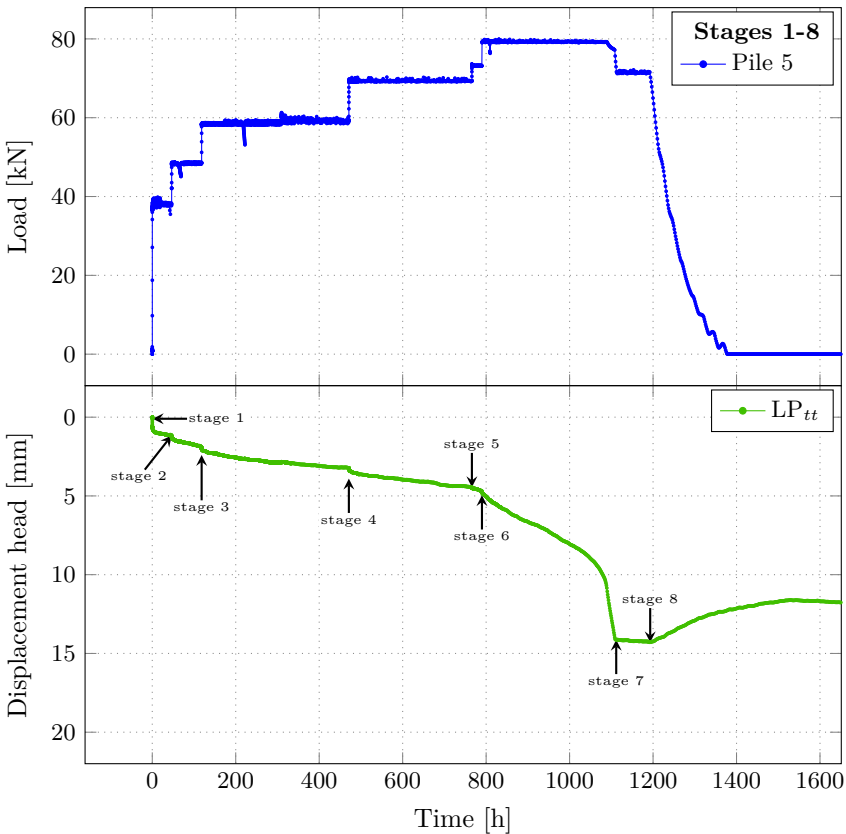


Figure 6.20: Load and displacement with time for all loading stages of test LT5A.

The applied load, accumulated displacement and holding period for each stage is given in Table 6.6 and plotted in Figure 6.21. From stage 1 to 6, the pile creep rate decreased with time. Failure occurred in stage 7 with an average load of 79 kN, which is equivalent to a load ratio of  $Q_{sls}/Q_{ult}^{ref} = 0.79$  in relation to the short-term tests and equal to the reference creep load  $Q_{creep}^{ref}$ . The pile displacement and failure load is similar to that of the manually-loaded piles, corroborating the pile creep behaviour and failure limit.

Table 6.6: Data from test LT5A.

Stage	t (d)	$Q_{ini}$	$Q_{end}$	$Q_{avg}$	$\delta_{ini}$	$\delta_{end}$	$\Delta\delta$	$\Delta\delta/t$
1	0.00	2.1	0.8	0.9	0.00	0.05	0.05	–
2	1.93	38.6	38.1	38.0	0.05	1.16	1.11	0.572
3	2.99	48.2	48.5	48.2	1.16	1.90	0.75	0.250
4	14.70	58.4	59.2	58.7	1.90	3.23	1.33	0.090
5	12.28	69.8	69.3	69.4	3.23	4.45	1.22	0.100
6	1.00	73.3	73.3	73.2	4.45	4.69	0.24	0.242
7	13.40	79.0	72.5	79.2	4.69	14.13	9.43	0.704
8	3.39	72.0	70.8	71.5	14.13	14.29	0.16	0.047
9	13.49	70.4	0.0	11.4	14.30	11.64	-2.66	-0.197

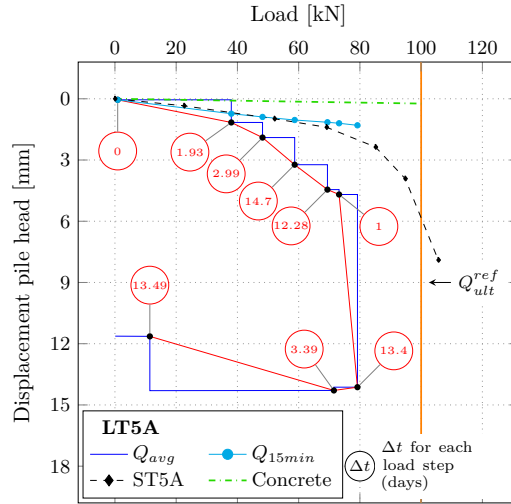


Figure 6.21: Long-term load-displacement curve for test LT5A.

Figure 6.22 presents a semi-log plot of the accumulated pile head displacement for each load step. It can be observed that these curves present a semi-log linear trend after certain time (secondary compression). The pile creep rate tend to decrease with time as in the manually regulated tests and is also bounded between the parameter  $\Psi^l$  0.2 to 0.7 mm before failure (see Figure 6.23). For stage 7, one can clearly observe the development

of secondary and tertiary creep, with the creep rate decreasing slightly within the first  $\approx 10$  days and then increasing towards infinity. The failure mechanism emerged more clearly than in the manually-loaded tests as the load was held constant. After failure, the pile stabilized again when unloaded to 72 kN. This load is equivalent a ratio of  $Q_{sls}/Q_{ult}^{ref} = 0.72$  in relation to the short-term tests and  $Q_{sls}/Q_{creep}^{ref} = 0.9$  in respect to the reference creep load. At the onset of failure, the accumulated displacement was approximately that observed during the slip failure of the short-term tests, approximately 7.1 mm.

Another approach to present the data is to normalize the pile head displacements with the pile equivalent diameter  $D_{eq}$ . The value for the non-dimensional creep parameters obtained in this way are in line with previous results as shown in Figure 6.19. The last stage in the plot shows how the pile creep rate initially reduces (following a linear semi-log trend) and then increases rapidly towards infinity.

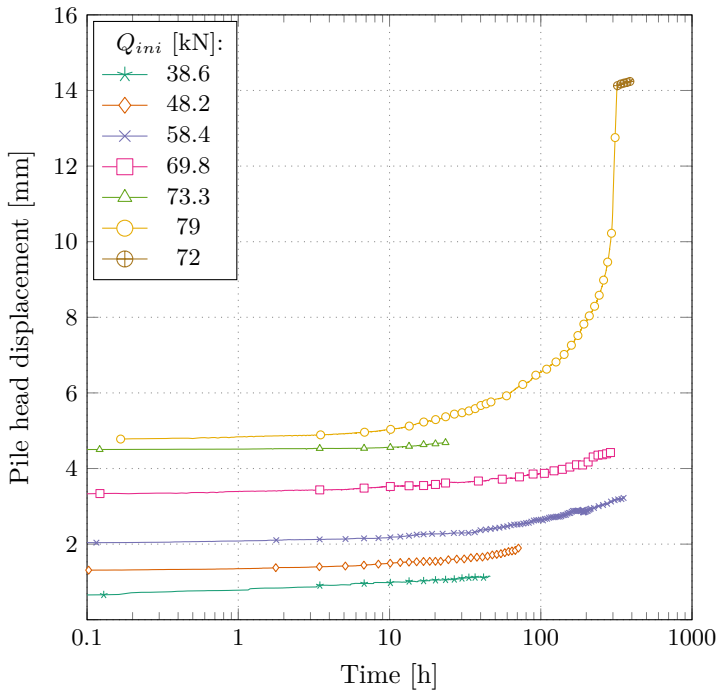


Figure 6.22: *Time displacement for each stage of test LT5A.*

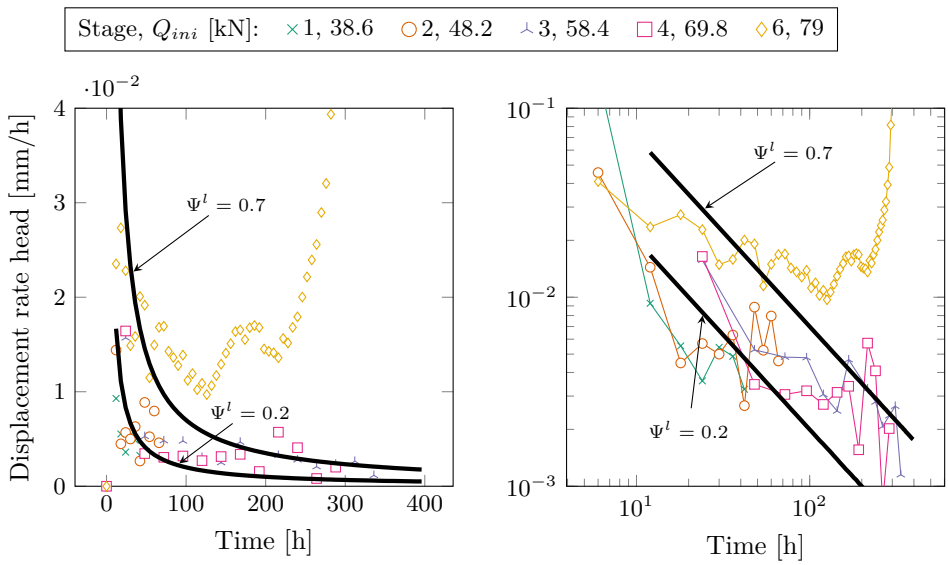


Figure 6.23: Displacement rate for each load step and creep curves for  $\Psi^l = 0.2$  and  $0.7$  with  $t_{ref} = 24h$  for test *LT5A*.

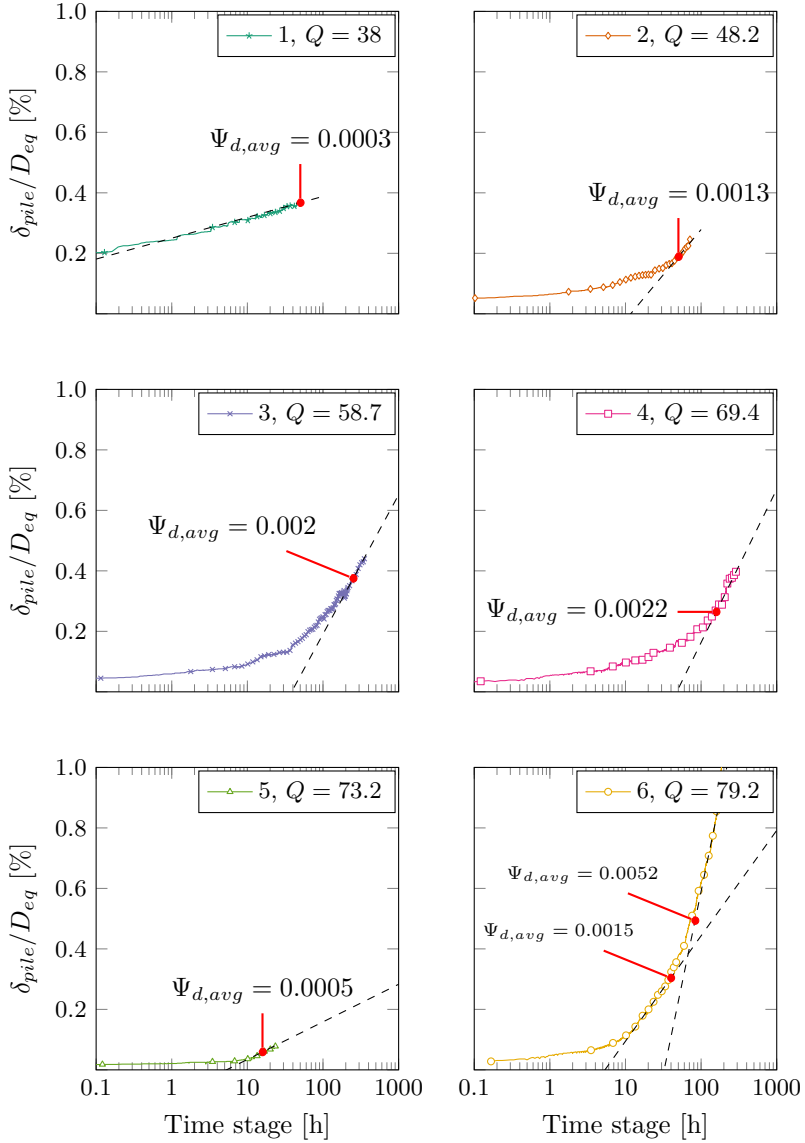


Figure 6.24: Load and displacement with time for all loading stages of test LT5A.

### 6.4.3 All Piles

The average load and accumulated displacement for all piles is presented in Figure 6.25. The maximum stable load is approximately 80 kN and with an accumulated displacement of approximately 7 mm. Pass this limit large pile head displacements developed and the piles experienced tertiary creep.

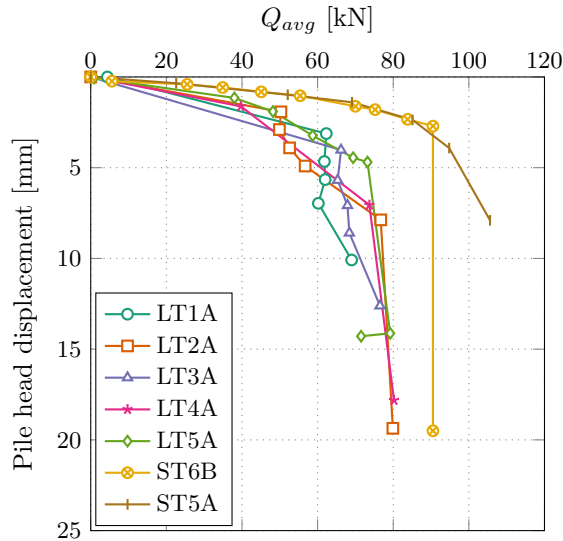


Figure 6.25: Average load and accumulated displacement with time for all Piles.

## 6.5 Discussion

### 6.5.1 Test Results

Differences between the short- and long-term loading results are mainly attributed to the soil rate effects (viscous behaviour). For example, as shown by Torstensson (1973) for scale field piles and field vane shear tests, fast loading rates gave larger pile bearing capacity and undrained shear strength compared to slow ones. During slow shearing, any rate effect in the soil will be insignificant, but instead the shear strains in the soil can lead to stress relaxation in kinematic-constrained boundary conditions (Randolph and Wroth 1981; St.John et al. 1983; Lehane and Jardine 1994). Therefore, any possible lock-in stress from the pile installation could be released with time.

The long-term tests show similar results as previously reported in the literature (see

Section 2.3.2). The pile head displacements are larger than those from short-term tests for the same load magnitude under the longer hold period. The pile displacement rate tend to increase with increasing load and subsequently decreases with time as the pile-soil system finds a new equilibrium. It is important to note that the clay properties are changing with time too (ageing). Therefore time-dependent ageing processes during the holding time in each load step could influence the next one. However, for the time frame of this investigation, these changes are considered sufficiently small.

All long-term loaded piles failed by creep rupture. Failure took place for  $Q_{sls}$  loads approximately 20% smaller than  $Q_{ult}$  and for accumulated displacements in the same order of magnitude of the short-term tests under slip failure ( $\approx 4-8$  mm). Here, the failure criterion is only considered based on the applied load as the accumulated displacements could be larger for much longer holding periods (under stable  $Q$ ). It is difficult to point out exactly the trigger of the creep rupture failure mechanism, as there were no measurements of the effective radial stresses and it was hard to assess any increase in pore water pressure at the pile shaft from test LT2A. Possible problems in the pore pressure measurements could be (1) the filter stone was not fully saturated or that its permeability reduced significantly relative to the surrounding soil, (2) excess pore water pressure will develop in the critical shear zone some distance away from the shaft, and (3) the sampling frequency was too low.

### 6.5.2 Creep criterion

The long-term tests clearly indicate creep rupture above a certain load threshold. This threshold falls approximately between 0.7 to 0.8  $Q_{ult}$ . Below this threshold, the piles showed very small creep displacements. This is slightly below the limit stated by St. John et al. (1983), where they state that loading the pile more than 80% of their short-term capacity will create significant plastic deformations in the soil. One possible explanation for this difference is that under the long-term hold period, the effective stresses around the pile decrease due to relaxation. Then, as the shear load increases and approaches the failure envelope, the clay becomes unstable and the creep rate increases. In this state, excess pore water pressures can develop in a non-uniform pattern in the radial direction (Kimura and Saitoh 1983) and accumulate in the critical strain zone (Bjerrum and Landva 1966), further reducing the effective stresses and leading to failure (creep rupture).

Based on the current work and previous investigations, a creep failure criterion is established for normally to slightly overconsolidated clays. This criterion is inspired by ideas from St. John et al. (1983), Ramalho Ortigao and Randolph (1983), Hunter and Khalili (2000), and experimental observations from the field reported here and in literature (Torstensson 1973; Lehane and Jardine 1994) and laboratory tests (Campanella and Vaid 1974; Tavenas et al. 1978; Bhat et al. 2013). The main components are summarized below:

- For shear stresses below the residual shear strength of the clay, the soil will only experience primary creep.

- For shear stresses larger than the residual shear strength of the clay, the soil will experience creep rupture. The transition from primary, to secondary and tertiary creep will be a function of the accumulated strain upon load application and the amount of mobilised shear.
- The soil structure will degrade significantly during creep (i.e. softening) for shear stresses larger than the residual strength and strains below the peak strain.
- Thereafter, the shear strains will localise and the material will fail (bifurcation).

Figure 6.26 illustrate these components. A shear-displacement curve is given for different loading rates, where  $\dot{\epsilon}_1$  represent a standard short-term undrained test and  $\dot{\epsilon}_4$  a standard long-term drained test. If the soil is loaded to point *A*, it will initially exhibit a larger strength. As the creep displacement develops with time, the soil structure evolves and the stress conditions change. It is important to note that the soil very close to the pile shaft is considered to be already fully remoulded during the installation process, i.e. there is little or no bonding left. However, some structure could be left just within the main influence area of the shear load. Beyond the peak strain, the soil enters an unstable softening phase that eventually will lead to creep rupture. If the soil is loaded to point *B* instead, creep rupture will not take place, as the mobilised load falls below the residual strength resulting from any changes in the soil properties and stresses with time.

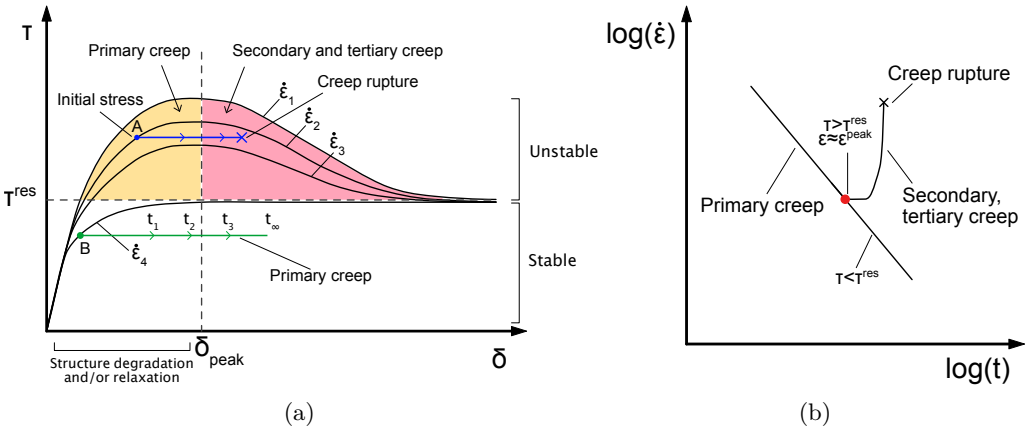


Figure 6.26: *Idealised creep failure criterion for long-term loaded piles.*

Figure 6.27 illustrates a soil element mobilised up to point *B* and then reloaded after some creep with a high loading rate  $\dot{\epsilon}_1$ . In this case, the available short-term strength might have degraded, be the same or increased due to holding period (Karlsrud, Jensen, et al. 2014). For the case of long piles, the mobilised load will be different along the pile shaft as illustrated in Figure 6.28. With time, the parts with higher mobilised loads will want to creep more than sections with a lower mobilised load. Therefore, the load will slowly be redistributed in order to find a new equilibrium along the complete pile shaft.

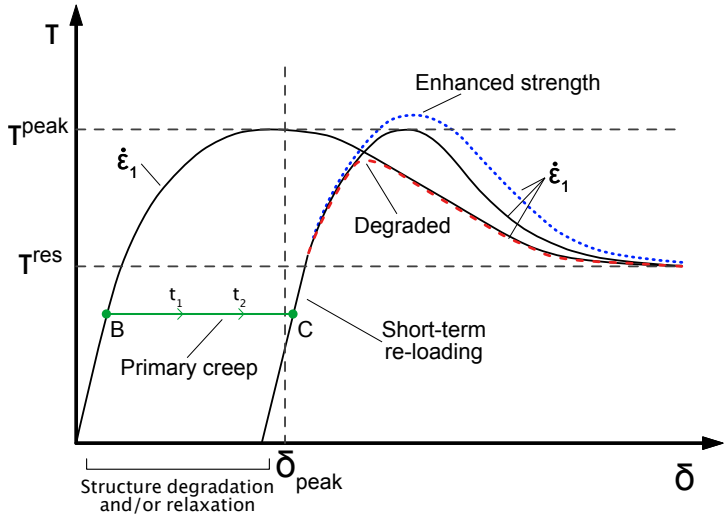


Figure 6.27: Illustration of possible creep effects on the short-term pile capacity.

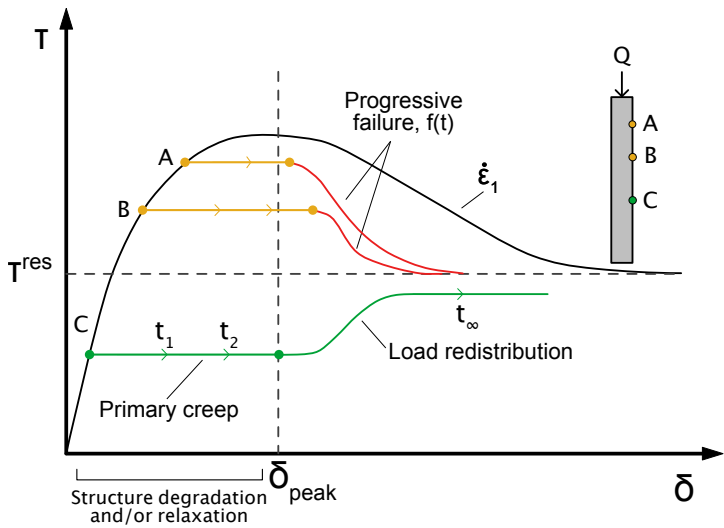


Figure 6.28: Illustration of possible redistribution of load with time.

# 7 Result analysis

## 7.1 Bearing Capacity

### 7.1.1 Ultimate Limit State

The short-term test results are interpreted using three analytical methods. The first two methods are only applicable to estimate the ultimate pile capacity without precise knowledge of the ultimate pile head displacement. Therefore, these methods can only estimate the final state of the pile at failure, disregarding effects as the pile load distribution with depth, principal stress rotation, pile-soil relative movement, among others (B.H. Fellenius 2015). The third method provides more detailed analysis of the ultimate state and the load distribution along the pile shaft. This method incorporates the non-linearity and softening behaviour observed for soft clays during shear loading.

The total bearing capacity for floating piles in clays is calculated using Equation (7.1). The base contribution for these piles is very small, with  $N_c$  values ranging from 6 to 9, where the lowest is for soft bearing layers and 9 for the tip embedded more than  $3D_{pile}$  in stiff layers (Skempton 1951). The unit shaft friction  $\tau_{ult}$  is calculated either using the total stress  $\alpha$ -method or the effective stress  $\beta$ -method.

$$Q_{ult} = Q_{ult}^{base} + Q_{ult}^{shaft} + W' \quad (7.1)$$

$$Q_{ult}^{base} = N_c S_{u,b} A_b \quad (7.2)$$

$$Q_{ult}^{shaft} = \tau_{ult} A_s \quad (7.3)$$

where  $W'$  is the effective weight of the pile,  $S_{u,b}$  is the undrained shear strength at the pile base level,  $N_c$  is the base bearing capacity factor,  $A_b$  is the base area of the pile,  $A_s$  is the area of the pile shaft and  $\tau_{ult}$  ultimate unit shaft resistance.

For tension piles, the base contribution is modified to account for the suction and uplift failure at the pile base, as given in Equation (7.4) (St.John et al. 1983). If  $Q_{ult}^{base}$  is negative, the soil will collapse, having negligible contribution for the tension capacity.

$$Q_{ult}^{base} = (N_c S_{u,b} - \sigma_{v,b}) A_b \quad (7.4)$$

where  $\sigma_{v,b}$  is the total vertical stress at the pile base level.

## The $\alpha$ —method

The total stress  $\alpha$ —method correlates the undrained shear strength of the clay with an  $\alpha$  factor in order to obtain the ultimate unit shaft resistance  $\tau_{ult}$  at a given depth (Equation (7.5)). This method implicitly accounts for the pile element characteristics, installation effects, changes in effective stress and the clay behaviour during loading (softening and rate effects). Therefore, the back-analysed  $\alpha$  factor from field tests frequently shows a large scatter in the literature (see Fleming et al. 2008). For the normally to slightly over-consolidated clays encountered in the Gothenburg area, this factor has been found to be relatively constant within the range of 0.8–1 (Torstensson 1973; Bengtsson and Sällfors 1983; Hansbo 1984).

$$\tau_{ult}(z) = \alpha(z)S_u(z) \quad (7.5)$$

where  $S_u$  is the undrained shear strength and  $\alpha$  is the correlation factor at a given depth  $z$ .

For long floating piles in soft clays, the base capacity is often neglected. However, for short piles as the one used in this Thesis, it can be significant. For the case of tension loading, Equation (7.4) is used to estimate the available suction capacity at the base. Using  $N_c = 9$  and  $S_u = 35$ , the maximum available load is approximately 2.2 kN, which is equivalent to 2.2% of the reference  $Q_{ult}^{ref}$ . The latter value is very small and can be neglected for the long-term (drained) loading conditions where no suction takes place.

The input shear strength in Equation (7.5) is generally obtained from the uncorrected in-situ vane shear test (Eriksson et al. 2004) or laboratory DSS tests on high quality samples (Karlsrud 2014). The selection of the shear strength value is not unique and will have a direct impact on the  $\alpha$  factor as these are directly proportional. The latter contributes to the scatter observed in the  $\alpha$  factor, as soil samples can be disturbed and the shearing rates vary while performing the vane test.

For the field tests in this Thesis the value for  $\alpha$  was back-calculated using the shear strength profile from the vane shear test and DSS test results presented in Figure 4.3. In this case, the vane shear test profile and DSS results were almost identical. Therefore, it was decided to average both test results. Equation (7.6) gives the average  $S_u$  profile used in the calculations of  $\tau_{ult}$ . The  $\alpha$  was assumed to be constant along the complete pile length (short pile). For first time loaded tests ST6A and ST5A, this factor is respectively 0.8 and 0.85. However, for the re-loaded test ST6B the factor is ca. 0.73, equivalent to a reduction of 9% compared to virgin loading. This reduction indicates a change in soil properties and stress conditions adjacent to the pile shaft. Nevertheless, it is difficult to support this conclusion with only one test. In general, the back-calculated  $\alpha$  values are in

good agreement to typical values obtained for pile foundations in Gothenburg.

$$S_u(z) = 27 + 2z \quad \text{for} \quad 13m \leq z \leq 17m \quad (7.6)$$

## The $\beta$ -method

The  $\beta$ -method is based on a more realistic interpretation of soil behaviour, where the soil-structure interaction is based on frictional contact and effective stress. This method relates the normal effective stress at the pile shaft with the pile-soil interface friction angle as given by Equation (7.7) and (7.8), and is in its simplest form independent of pile characteristics or loading direction (B.H. Fellenius 2015). The failure plane around a pile with rough shaft is considered to occur in the soil close to the interface (critical zone at lowest  $S_u$ , see Section 2.2)(Karlsrud and Haugen 1985). Therefore, determination of the friction angle of the soil and the radial effective stress after the setup period is necessary for estimating the pile capacity. On the other hand, measurement of the normal (radial) effective stress and friction angle at the pile-soil interface is rather difficult and costly. Therefore, the  $\beta$  factor is in general an average value obtained from field scale pile load tests based on local site experience. Typical  $\beta$  values for soft clays with medium to high plasticity are in the range of 0.27-0.35 (Karlsrud 2014).

$$\beta = K_c \tan(\phi'_r) \quad (7.7)$$

$$\tau_{ult}(z) = \beta(z)\sigma'_{v0}(z) \quad (7.8)$$

where  $K_c$  is the lateral earth pressure coefficient after the pile set-up period (dissipation of pore pressures),  $\phi'_r$  is the remoulded soil effective friction angle,  $\sigma'_{v0}$  is the in-situ vertical effective stress and  $\beta$  is the correlation factor at a given depth  $z$ .

For full displacement piles, the soil undergoes large distortions during installation, and is often considered to be fully remoulded. Therefore, the friction angle should be based on that from remoulded clay samples. Wood (2016) published triaxial tests on remoulded Gothenburg clay. The effective critical state friction angle for these clays is close to the natural samples. Allman and Atkinson (1992) observed similar results for Bothkennar clay, stating that it is difficult to reach the “real” critical state in standard triaxial tests. Lehane and Jardine (1992) performed ring shear tests to study the residual friction angle for remoulded Bothkennar clay. Their results showed a larger decrease in the friction angle compared to those from Allman and Atkinson. The residual friction angle for soil-soil and soil-interface (sand blasted stainless steel) was approximately  $\phi'_r = 33^\circ$  and  $\phi'_r = 31^\circ$  respectively. However, they stated that these values depend on the interpretation method used. If one assumes that the principal axes of stress and strain increments are coincident

and zero dilation, then  $\phi'_r = \sin^{-1}(\tau_{ult}/\sigma'_{nc})$  is used instead of  $\phi'_r = \tan^{-1}(\tau_{ult}/\sigma'_{nc})$  for calculating the friction angle. The former equation gives  $\phi'_r \approx 35^\circ$ , which agrees well with that found by Allman and Atkinson (1992).

Larsson (1981) presented a series of drained triaxial and direct simple shear tests for Bäckebol clay in Gothenburg. He found that the critical state angle was in the range of 30 to 40°, with the best conservative fit taken at 30° and cohesion  $c' = 2$  kPa. The latter friction angle is typically used in calculations of pile capacity. However, close examination of Larsson's data and results from new investigation show that the critical state angle for normally to slightly overconsolidated Gothenburg clays is closer to the upper bound mentioned before, with an average value of 37°, assuming  $c' = 0$  kPa.

In order to back calculate the tests in this Thesis with the  $\beta$ -method, it is necessary to assume a  $K_c$  or  $\phi'_r$  value. The soil remoulded friction angle  $\phi'_r$  was first chosen as 37° as discussed above. Hence, back calculation of tests ST6A and ST5A resulted in  $K_c$  values of 0.29 and 0.305 respectively, and  $\beta \approx 0.23$ . The obtained  $K_c$  values appeared to be rather low. Chow (1997) (as cited in Fleming et al. 2008) gathered data for  $K_c$  values from well instrumented pile load tests after full dissipation of the installation excess pore water pressures (see Figure 7.1). For clays with  $OCR < 2$ , the  $K_c$  range is approximately 0.5 to 0.9. Lehane and Jardine (1994) showed that at failure, the radial effective stress at the shaft reduces up to 20%. Correcting the horizontal coefficient with  $0.8K_c$ , results in a coefficient at failure  $K_f$  in the range of 0.4 – 0.7.

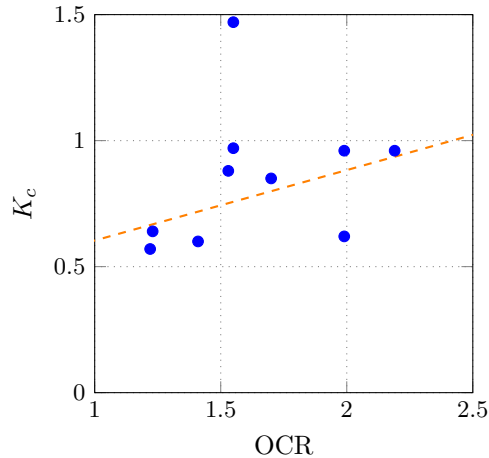


Figure 7.1: Radial stress measurements around full displacement piles from Chow (1997) (adopted from Fleming 2008).

It seems that the adopted friction angle is too high based on the back-calculated  $K_f$ . This can be possibly explained by looking at the shearing mode next to the pile shaft, which is analogous to a DSS test. Randolph and Wroth (1981) examined the stress path

and failure envelope of previous investigations in DSS tests. They observed that failure does not necessarily occur at the horizontal plane where the shear and normal stress is applied. Instead rupture planes will initially develop parallel to the major principal stress axis (i.e. vertical) as illustrated in Figure 7.2. Increments of strains will generate rotation of the principal stresses, resulting in additional reduction of the shear at failure  $\tau_f$  (apart from sensitivity and Lode angle effect) and changes in the failure plane direction (towards the horizontal). For the case where failure occurs at the vertical plane, the mobilised friction angle at the horizontal plane is given by Equation (7.9).

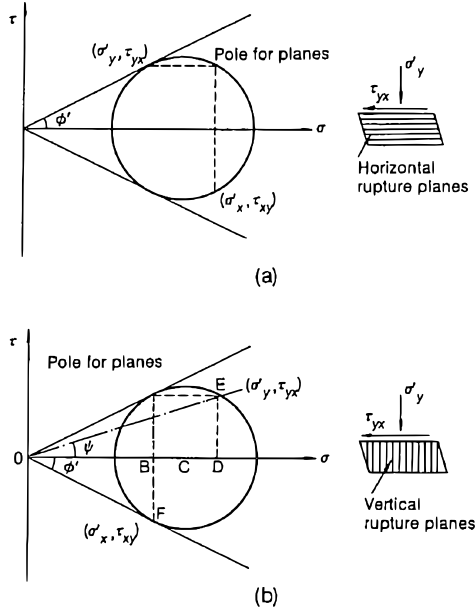


Figure 7.2: *DSS failure modes (adopted from Randolph and Wroth 1981).*

$$\Psi' = \tan^{-1} \left( \frac{\sin \phi' \cos \phi'}{1 + \sin^2 \phi'} \right) \quad (7.9)$$

Based on Equation (7.9), the friction angle will be between  $\Psi'$  and  $\phi'$  at planes parallel to the pile shaft during failure. Pile tests from Lehane and Jardine (1994) resulted in lower friction angles in comparison to the critical state angle of Bothkennar clay. Taking  $\phi'_{cs} = 37^\circ$ , then  $\Psi' = 19.5^\circ$  and the average of this two is  $\approx 28^\circ$ , which is in good agreement to that observed by Lehane and Jardine. Therefore, a lower friction angle in the  $\beta$  method can be justified. Using  $\phi' = 28^\circ$  for tests ST6A and ST5A gives  $K_f$  of 0.41 and 0.43 respectively.

Again, as observed for the  $\alpha$ -method, the effective stress  $\beta$  factor is in agreement with

values previously reported in the literature. Note that the governing parameters in Equation (7.3) and (7.7) are the shaft area, the effective friction angle of the soil and the effective horizontal stress ratio. The effective friction angle will be constant in time, therefore changes in the effective horizontal stress or the failure plane location (i.e. effective shaft area) will give the largest changes in the short-term bearing capacity.

### 7.1.2 Load transfer method

The load transfer method incorporates a more detailed description of the pile-soil relative movement and load distribution along the pile shaft (Q.-q. Zhang and Z.-m. Zhang 2012). B.H. Fellenius (2013) and B.H. Fellenius (2015) present a summary of different load-transfer functions available. Here, the non-linear softening function proposed by Q.-q. Zhang and Z.-m. Zhang (2012) together with their bisection algorithm was implemented in the general purpose numerical code MATLAB. This t-z curve is shown in Figure 7.3 using Equations (7.10) – (7.13).

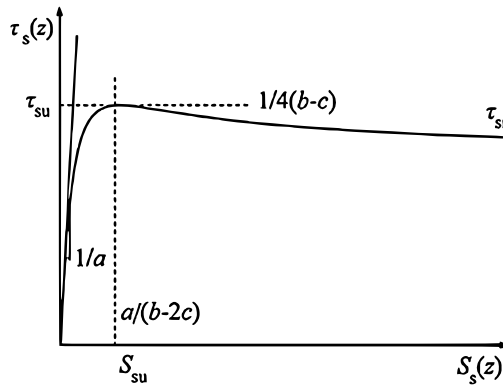


Figure 7.3: Zhang's t-z curve (Zhang 2012)

$$\tau_s(z) = \frac{S_s(z)[a + cS_s(z)]}{[a + bS_s(z)]^2} \quad (7.10)$$

$$a = (b - 2c)S_{su} \quad (7.11)$$

$$b = \frac{1 - \sqrt{1 - \beta_s}}{2\beta_s} \frac{1}{\tau_{su}} \quad (7.12)$$

$$c = \frac{2 - \beta_s - 2\sqrt{1 - \beta_s}}{4\beta_s} \frac{1}{\tau_{su}} \quad (7.13)$$

where  $\tau_s(z)$  is the unit skin friction at depth  $z$ ,  $S_s$  is the relative movement at the pile shaft,  $\tau_{su}$  is the peak shear stress at  $S_{su}$  displacement and  $\beta_s$  is the ratio between the residual and peak unit friction ( $\tau_{sr}/\tau_{su}$ ).

Zhang's function is flexible and can adopt several shapes by only modifying two parameters, namely  $S_{su}$  and  $\beta_s$ . Values for  $\tau_{su}$  can be obtained from vane shear test or DSS test corrected with the  $\alpha$  or  $\beta$  factor from Section 7.1.1.  $S_{su}$  and  $\beta_s$  are calibrated using data from pile load tests. The effect of these two parameters are presented in Figure 7.4. Depending on the displacement up to peak  $S_{su}$ ,  $\beta_s$  will regulate both the initial stiffness and the softening at large strain magnitudes. Softening will have a larger impact for smaller  $S_{su}$  and take place with small  $S_s$  values.

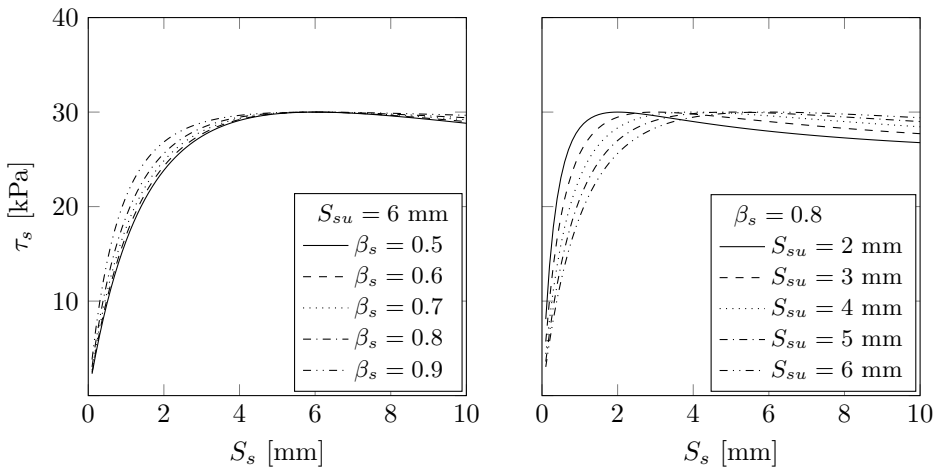


Figure 7.4: *Effects of  $S_{su}$  and  $\beta_s$  on Zhang's  $t$ - $z$  curve.*

Test ST5A was back calculated using this method. The parameters used to describe the pile segment in the field test were an elastic modulus of 33 GPa, length of 4.2 m and an equivalent diameter of 0.3 m. The soil shear strength profile with depth (Equation (7.6)) was corrected using an  $\alpha$  factor of 0.8, and combined with  $S_{su} = 6$  mm and  $\beta_s = 0.75$  to obtain the  $t$ - $z$  curve. The base resistance was neglected in the calculations. The numerical simulation is in good agreement with the measurement results for the load-displacement curve in Figure 7.5 and the load distribution along the pile shaft with data from the strain gauges (SG) in Figure 7.6a. Compared to the simulation results, the SG gauge data is somewhat lower along the shaft and higher near the toe. One could possibly relate this to the radial stress distribution before loading. Lehane and Jardine (1994) observed an increasing radial stress with depth, with much larger values near the toe (see Figure 7.7).

Similar to what is observed in element level tests on natural clays, just a few millimetres of relative pile-soil displacement is required to develop the ultimate shaft resistance.

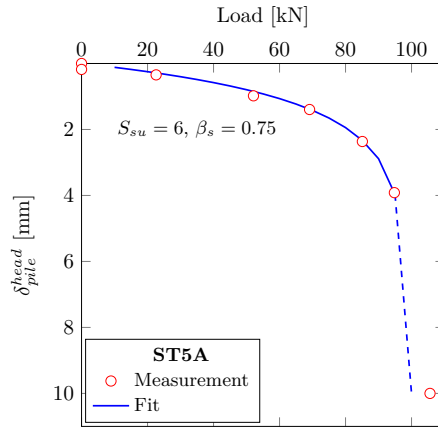


Figure 7.5: Back calculation of test ST5A.

For the short relatively stiff pile element considered here the behaviour will be rigid body movement. Therefore, the shaft resistance is mobilised along the complete shaft approximately at the same time and proportional to the pile-soil relative displacement as shown in Figure 7.6b.

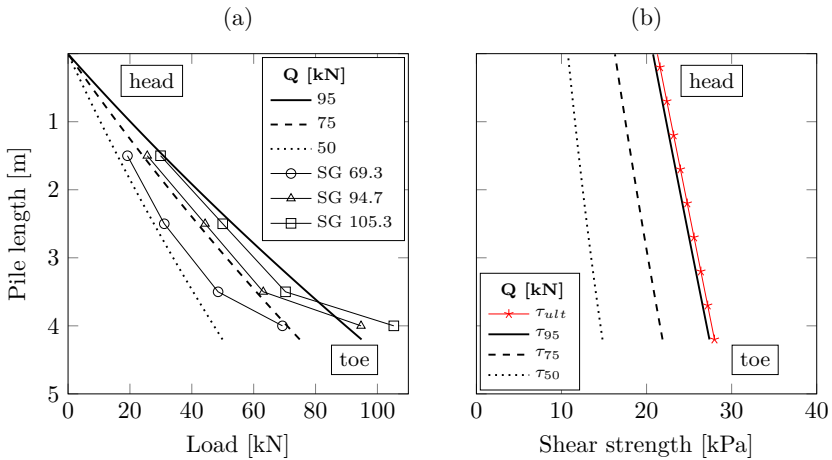


Figure 7.6: Back calculation of test ST5A.

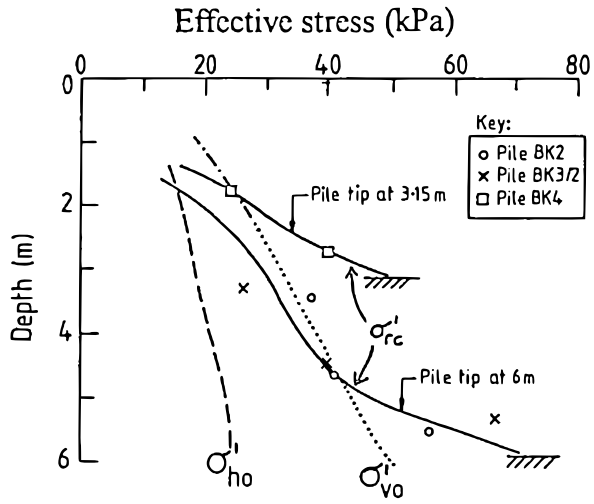


Figure 7.7: *Effective radial stresses after equalisation of installation pore pressures (adopted from Lehane and Jardine 1994).*

## 7.2 Long-term response: simple method

The long-term pile head displacements due to creep are important for the service life of the superstructure. At the pile shaft, the main creep component is deviatoric. In the simplified approach suggested here the equation for deviatoric creep is based on the traditional 1D volumetric formulation by introducing a deviatoric creep parameter, as shown in Equation (7.14). The  $\mu_d^*$  parameter might be obtained from triaxial or DSS creep tests by measuring the deviatoric creep strains under sustained shear loading.

The average pseudo deviatoric creep parameter  $\Psi_{d,avg}$  at the pile shaft can be obtained in a similar fashion by measuring the pile head displacement under long-term sustained loading and subsequently extrapolating the final pile head displacements after the service life of the piles using a non-linear relation (Equation (7.15)). It is important to note that this approach does not predict secondary or tertiary creep, i.e. creep rupture.

$$\varepsilon_d^c = \mu_d^* \ln \left( \frac{t_{ref} + t}{t_{ref}} \right) \quad (7.14)$$

$$\varepsilon_d^c = \Psi_{d,avg} \ln \left( \frac{t_{ref} + t}{t_{ref}} \right) \quad (7.15)$$

where  $\varepsilon_d^c$  are the viscoplastic (creep) deviatoric strains at the pile shaft,  $t_{ref}$  is the reference time for the creep parameter and  $t$  is the current time to extrapolate.

The  $\Psi_{d,avg}$  parameter for each pile are plotted in Figure 7.8 for the different initial loads  $Q_{ini}$  in each stage for each pile. For comparison the intrinsic creep parameter  $\mu_i^*$  obtained from incremental loading oedometer tests (IL) at large stress levels and strain magnitudes ( $> 20\%$ ) is added. An interesting finding is that  $\Psi_{d,avg}$  increases linearly with the applied load until the intrinsic value from the laboratory results is obtained. Load stages above 80 kN led to creep rupture, therefore no relevant creep parameter is obtained beyond this limit.

The creep displacements are extrapolated using the largest measured  $\Psi_{d,avg}$  to remain conservative. The reference time in each loading stage varied from a few hours to several days. For the extrapolation,  $t_{ref} = 3$  days and the total creep time of  $t = 100$  years (typical service life of the superstructure in Gothenburg) have been used. The results are plotted in Figure 7.9. In general, the total accumulated creep displacements are relatively small, with 80% developing within the first 20 years.

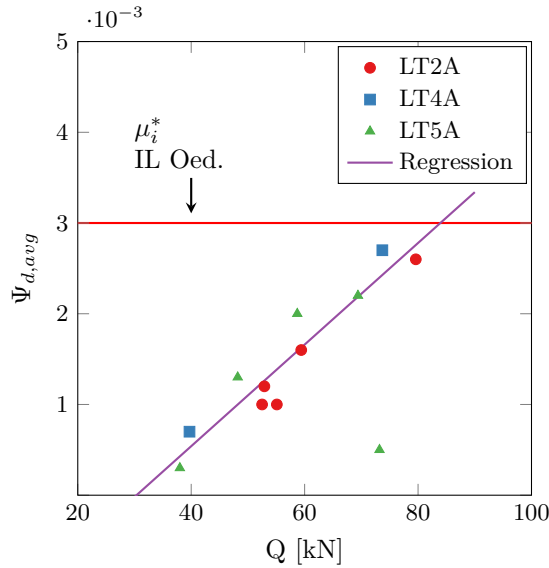


Figure 7.8: Creep parameter  $\Psi_{d,avg}$  from long-term sustained load tests.

### 7.3 Prediction of expected creep rate

In order to capture the long-term pile head displacement rates, it is necessary to use more advanced methods that incorporate the effect of loading history on the creep rate. The loading history is summarised in the pile cycle in Chapter 2. Hence, the largest impact on the creep rate is expected to be the pile installation stage where the soil will be distorted to a certain degree. In natural clays the initial bonds will be gradually destroyed. Furthermore, the stress rotations during shearing will affect the anisotropy. Here an unconventional approach will be adopted to investigate the effects of pile installation on the creep rate by combining the Strain Path Method (SPM) (Baligh 1985; Sagaseta et al. 1997) with an universal strain driver (Gras et al. In press) and an advanced soft soil model that incorporates anisotropy and destructuration (SCLAY1S, Karstunen et al. 2005) and its extension for creep (CREEP-SCLAY1S, Sivasithamparam et al. 2015). Employing a strain driver will circumvent issues with large deformation analyses in Finite Element codes, i.e. mesh distortions in traditional Updated Lagrangian formulations and numerical diffusion and convection of the state variables on the stability of advanced constitutive models in large deformation codes.

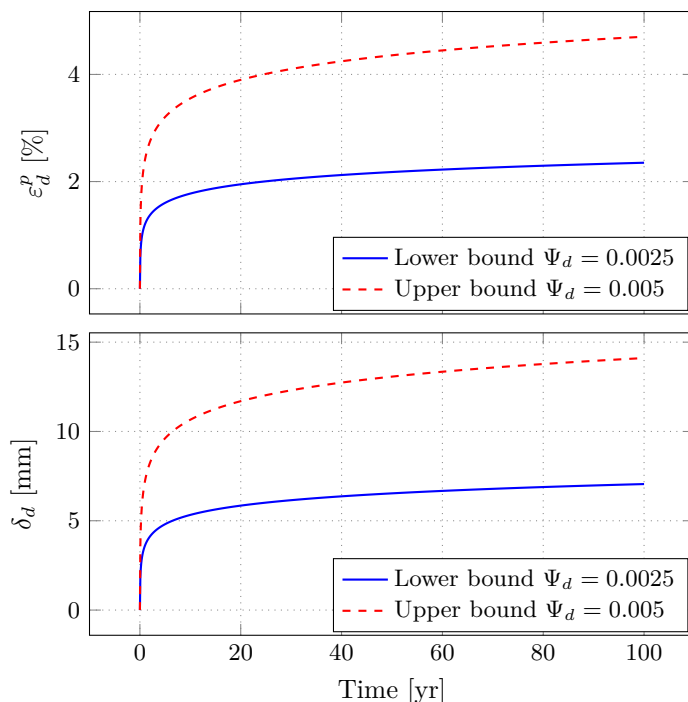


Figure 7.9: *Extrapolation of creep settlements for maximum  $\Psi_{d,avg}$ .*

### 7.3.1 Modelling pile installation with SPM

The Strain Path Method (SPM) was developed based on many field and laboratory observations of installation of rigid objects in soils (Baligh 1985). This method provides an analytical approximation of the installation effects of displacement piles in soft clays. The advantages of this method compared to other analytical approaches (e.g. Cavity Expansion Method) is that vertical soil displacements are considered and the pile penetration is approximated under steady state. Baligh (1985) presented a full description of the method and its application to piles, soil samplers and in-situ testing devices. The assumption behind SPM is that the deformations and strains for deep penetration problems are independent of the soil behaviour due to the dominating kinematic constraints in this process. The method assumes that penetration occurs under quasi-static steady state conditions, in incompressible, isotropic, homogeneous, non-viscous and rate independent soil under isotropic stress conditions and with no roughness at the pile-soil interface. Therefore, the penetration process reduces to a flow problem where the soil particles flow around a rigid penetrating object.

The strains around the pile are obtained by numerical integration of a velocity field resulting from combining sources and sinks together with a uniform flow field in a given

space domain (this is known as Potential Flow Theory in fluid dynamics). This velocity field has the properties of being irrotational and incompressible (conservation of volume). Having these strain paths, the effective stresses in each discrete point can be obtained by using any effective stress based soil constitutive model. In this way, the SPM separates the kinematic process and the mechanical response of the soil. Furthermore, strain paths are independent of the mesh (Eulerian approach). Due to the simplified assumption of isotropic state, the calculated effective stresses will not satisfy all the equilibrium conditions and therefore some small errors will remain (Baligh 1985).

## Installation

Sagaseta et al. (1997) incorporated the ground surface effects together with the deep penetration solutions presented by Baligh (1985), resulting in the Shallow Strain Path Method (SSPM). As opposed to the SPM, the SSPM does not have a reference system fixed to the penetrating object, but instead considers a transient source moving from the free surface into deep layers. Therefore, the penetration process is no longer a steady state process. As the source penetrates into deeper layers, the solution approximates that from the SPM. In other words, the surface effects are not longer dominant. Therefore, the sink and shear traction in their approach can be neglected. By numerical integration of Sagaseta et al. (1997) velocity and strain rate field given by the moving source, the soil deformations and strain paths can be obtained in time (or equivalent penetration depth). The position of a soil particle in Cartesian coordinates is given by Equation (7.16).

$$\begin{aligned} x(h) &= x_0 + \int_0^h v_x(x, z, h) \frac{1}{U} dh \\ z(h) &= z_0 + \int_0^h v_z(x, z, h) \frac{1}{U} dh \end{aligned} \tag{7.16}$$

where  $x_0$  and  $z_0$  are the initial soil particle coordinates,  $v_x$  and  $v_z$  are the velocities in the  $x$  and  $z$  direction induced by the penetrating source from 0 to  $h$  and  $U$  is the moving speed of the source. The  $x$  and  $z$  coordinates in the integrant part change as the source moves from 0 to  $h$ , corresponding to a large strains solution (updated geometry). If  $x$  and  $z$  are not updated and taken as  $x_0$  and  $z_0$ , the problem is solved assuming small strains.

Here, the velocity field of interest is that of the simple pile case. In this approach a cylindrical coordinate system is used, with  $x = r$  and  $z = z$ . The velocities and strain rates in each direction are given in Equation (7.17) and (7.18).

$$\begin{aligned}
v_r(r, z, h) &= \frac{UR^2}{4} \frac{r}{r_1^3} \\
v_z(r, z, h) &= \frac{UR^2}{4} \frac{z - h}{r_1^3}
\end{aligned}
\tag{7.17}$$

$$\begin{aligned}
\dot{\epsilon}_{rr} &= -\frac{UR^2}{4} \frac{1}{r_1^3} \left( 1 - 3 \frac{r^2}{r_1^2} \right) \\
\dot{\epsilon}_{\theta\theta} &= -\frac{UR^2}{4} \frac{1}{r_1^3} \\
\dot{\epsilon}_{zz} &= -(\dot{\epsilon}_{rr} + \dot{\epsilon}_{\theta\theta}) \\
\dot{\epsilon}_{rz} &= \frac{UR^2}{4} \frac{1}{r_1^3} \frac{3r(z - h)}{r_1^2}
\end{aligned}
\tag{7.18}$$

where  $r_1$  is the distance from a point in the space  $P(r, z)$  to the current location of the source  $S(0, h)$ , as calculated in Equation (7.19).

$$r_1 = \sqrt{r^2 + (z - h)^2} \tag{7.19}$$

## Strains and stresses

Equations (7.17) and (7.18) were numerically integrated in a 2D domain by using the equation-based modelling in the commercial software COMSOL Multiphysics. The displacements and strains were obtained from a radial cross section far below the free surface and far above the pile base. For deep penetration, all soil elements in the radial direction will experience the same strain paths (steady state). In this way, the strain paths can be determined for a given depth and all other variables can be normalised with the initial effective vertical stress at that point. A total of 201 discrete nodes were used to extract the strain paths. These were located at a spacing of 0.05:0.01:1.5 – 1.6:0.1:5 – 5.5:0.5:15 meters from the centre line of penetration. The solution precision for the strain path in each node depends on the mesh size and time step in the numerical integration of the velocity field in COMSOL.

The effective stresses for each discrete node were calculated using the strain paths obtained in COMSOL Multiphysics and the SCLAY1S soil constitutive model implemented in the

single element strain driver called VAMP (graphical interface, sensitivity and optimisation software for incrementalDRIVER) (Gudehus et al. 2008; Gras et al. In press). A MATLAB script was used to communicate with VAMP and loop all 201 nodes. The elastoplastic SCLAY1S model proved to be more stable than the CREEP-SCLAY1S model to simulate the installation processes in the single element strain driver.

The initial stress conditions are taken for the middle section of the pile, 15 meters below the ground surface. At this point  $\sigma'_{v0} = 90$  kPa and  $\sigma'_{h0} = 54$  kPa (assuming  $K_0 = 0.6$ ). The soil model parameters are given in Table 7.1. Details of the parameter determination procedures can be found in Wheeler et al. (2003), Karstunen et al. (2005) and Gras et al. (In press).

Table 7.1: Parameters for SCLAY1S at 15m depth, Marieholm.

$\kappa^*$	$\lambda_i^*$	$\lambda^{*1}$	$v'$	$M_c$	$\alpha_0$	$\omega$	$\omega_d$	$\chi_0$	$\xi$	$\xi_d$	OCR	$e_0$
0.015	0.1	0.25	0.2	1.64	0.5	150	1	14	9	0.4	1.3	2

<sup>1</sup> Used instead of  $\lambda_i^*$  when the bondings  $\chi$  are not considered.

### SPM excess pore water pressure

Given the effective stresses obtained from the strain paths and the soil constitutive model at the discrete soil nodes, the excess pore water pressure is calculated from the equilibrium conditions of total stresses. According to Baligh (1985) during undrained penetration, the change in total stress is governed by the equilibrium Equation (7.20) (in a cartesian frame and  $i, j = 1$  to 3). Here  $x_i$  are the coordinates of a material point and repeated indices imply summation over 1, 2 and 3.

$$\frac{\partial \sigma_{ij}}{\partial x_i} = 0 \tag{7.20}$$

$$x_i = (x_1, x_2, x_3)$$

The total stress is the sum of effective stress and pore water pressure as stated in Equation (7.21) ( $\delta_{ij} =$  Kronecker's delta). Hence, the pore water pressure is obtained from the equilibrium Equation (7.22).

$$\sigma_{ij} = \sigma'_{ij} + u\delta_{ij} \tag{7.21}$$

$$\frac{\partial u}{\partial x_i} = -\frac{\partial \sigma'_{ij}}{\partial x_i}$$

$$g = -\frac{\partial \sigma'_{ij}}{\partial x_i}$$
(7.22)

In a 2D axisymmetric problem,  $g$  in the above equation (multiplied by -1) is given by the equilibrium Equation (7.23), for the radial and vertical direction respectively. However, the solution for  $\Delta u$  will depend on the integration path as the constitutive model does not correspond to the assumptions made for the strain paths and the pore pressure field is not in equilibrium in all directions. Aubeny (1992) showed that at the shaft (far above the base),  $\Delta u$  is best approximated by radial integration. Below the base level the vertical integration works best. The integration path dependency is improved by taking the divergence of Equation (7.22) and solving numerically the resulting Poisson's Equation (7.24) (Baligh 1985; Aubeny 1992).

$$-\frac{\partial u}{\partial r} = -g_r = \frac{\partial \sigma'_{rr}}{\partial r} + \frac{\partial \sigma'_{rz}}{\partial z} + \frac{\sigma'_{rr} - \sigma'_{\theta\theta}}{r}$$

$$-\frac{\partial u}{\partial z} = -g_z = \frac{\partial \sigma'_{zz}}{\partial z} + \frac{\partial \sigma'_{rz}}{\partial r} + \frac{\sigma'_{rz}}{r}$$
(7.23)

$$\nabla^2 u = -\nabla g = -q$$
(7.24)

For deep penetration problems, strains along the pile shaft far above the tip tend to reach a steady-state (with every element in the radial direction experiencing the same strain and stress path at all depths). Therefore, the problem is reduced to solve Equation (7.22) in 1D (i.e. radial direction). For this condition Equation (7.22) and (7.23) become:

$$g_r = -\left(\frac{\partial \sigma'_{rr}}{\partial r} + \frac{\sigma'_{rr} - \sigma'_{\theta\theta}}{r}\right)$$

$$u = \int g_r \, dr = \int -\left(\frac{\partial \sigma'_{rr}}{\partial r} + \frac{\sigma'_{rr} - \sigma'_{\theta\theta}}{r}\right) \, dr$$
(7.25)

In this 1D case, the radial integration is performed starting from the far field towards the pile shaft located at  $R$  from the pile centre line (Teh 1987; Aubeny 2016). The integration

can be solved numerically with a trapezoidal rule as given in Equation (7.26), starting with a node  $i$  in the far field and moving to the next node  $i + 1$  closer to the pile shaft in the same radial line  $j$  (see Figure 7.10). In this integration scheme, the cavity stress  $(\sigma'_{rr} - \sigma'_{\theta\theta})$  will be the most sensitive to numerical errors (Aubeny 2016).

$$u = \int_{\infty}^{R_{pile}} - \left( \frac{\partial \sigma'_{rr}}{\partial r} + \frac{\sigma'_{rr} - \sigma'_{\theta\theta}}{r} \right) dr \tag{7.26}$$

$$u_{i+1,j} = u_{i,j} - \left( \frac{du}{dr} \right)_M \Delta r_i$$

where  $u$  is the pore pressure at a node  $i$ ,  $(du/dr)_M$  is the pore pressure gradient at the middle point between node  $i$  and  $i + 1$  and  $\Delta r_i$  is the spacing between the integration nodes.

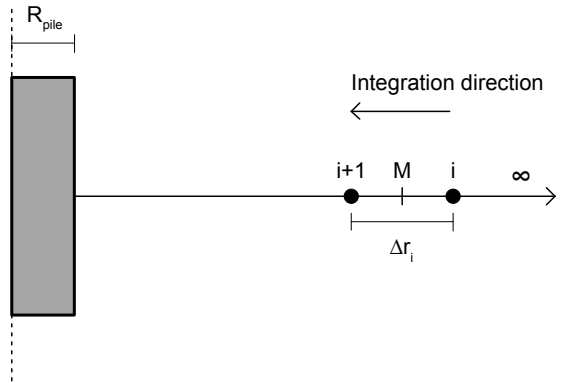


Figure 7.10: Trapezoidal integration for installation pore pressures in SPM.

The far field boundary is given by a Dirichlet condition where  $\Delta u = 0$ , the boundary at the pile shaft, however, is not known a priori. What is known is that at this latter location  $\Delta u \neq 0$  and the pore pressure gradient is not necessary  $\partial u / \partial n = 0$  (i.e. Neumann condition indicating no pore pressure gradients normal to the pile shaft). As the integration is performed from the far field side, the boundary at the pile shaft will emerge automatically and there is no need to specified it beforehand.

### SPM equalisation of $\Delta u$

Far above the pile base, the equalisation of the excess pore water pressures can be approximated by 1D radial consolidation (Whittle 1987). In this case, the effective stresses, installation pore water pressure and state variables from the SPM discrete elements must

be transferred to the 1D mesh. During pile installation, the shear component in the  $rz$  plane can be significant. However, Whittle (1987) stated that this do not affect the consolidation process and can be neglected. Whittle (1987) results from 1D numerical coupled consolidation (Biot's consolidation theory) using a non-linear soil model (MIT-E3) showed good agreement with field measurements (e.g. Piezo-Lateral Stress cell from Morrison 1984). His approximations agreed well with the equalisation effective stresses and pore water pressure dissipation times. Similar results were observed by Aubeny (1992) for 2D coupled consolidation with the same non-linear soil model.

Aubeny (1992) observed that for the 2D consolidation case, the installation total stress field do not necessarily satisfy internal equilibrium and might be incompatible with the 2D boundary conditions. The main incompatibility arises from the shear stress  $\sigma'_{rz}$  at the pile shaft and ground surface. He recommended two approaches to solve this problem:

- 1) Have an initial undrained step in order to allow the soil to equilibrate with the boundary conditions, or
- 2) Apply external corrective nodal forces  $\mathbf{R}$  in the 2D mesh at the beginning of the analysis and keep them constant throughout the consolidation (i.e. correction of the initial residual stresses). See Equation (7.27) (Nayak and Zienkiewicz 1972).

$$\mathbf{R} = - \int_V \mathbf{B}^T \boldsymbol{\sigma} dV \quad (7.27)$$

where  $\mathbf{B}$  is the strain-displacement transformation matrix,  $\boldsymbol{\sigma}$  is the total stress.

Far above the pile base, Aubeny (1992) calculations using the first approach did not show any significant changes in the initial radial effective stresses or installation pore water pressures. Therefore, this could be well used to estimate the consolidation problem at this location.

### 7.3.2 Results SPM

The resulting strains from the SPM are presented in Figure 7.11 for some soil elements adjacent to the pile shaft. The strains are calculated using the strain invariants given by Baligh (1985) (Equation (7.28)). The results compare exactly to that obtained by Baligh (1985) except for the soil elements very close to the pile centre line (still the difference is very small). As observed, the penetration process generates very large non monotonic strains in the soil (reversal of strain paths). Therefore, the post peak behaviour is very important for the constitutive relation adopted to estimate the effective stresses (Baligh 1985). Very large strains occur within one pile radius  $R$ . Therefore, the most uncertainties

will be in this zone.

$$\begin{aligned}
 E_1 &= \varepsilon_{zz} \\
 E_2 &= \frac{1}{\sqrt{3}}(\varepsilon_{rr} - \varepsilon_{\theta\theta}) \\
 E_3 &= \frac{2}{\sqrt{3}}\varepsilon_{rz}
 \end{aligned}
 \tag{7.28}$$

where these strain invariant represent  $E_1$  triaxial strains,  $E_2$  cylindrical cavity expansion and  $E_3$  simple shear.

Details of the individual strain components are presented in Figure 7.12 for a node located at (0.15,3). As the pile penetrates from above, the soil element is first loaded in compression. When the pile is approximately 1 pile radius above the initial location, the soil begins to experience extension loading (radial compression) and shear distortion. After the pile moves past the initial position, the shear distortion reverses in direction. The summation of the normal strain components is equal to 0, indicating no volume change during the penetration process.

The effective stresses and installation pore water pressure predicted using the SCLAY1S model and the strain driver are plotted as function of the pile radius,  $R_{pile}$ , normalised distance from the pile shaft  $r/R_{pile}$  in Figure 7.13. The effective stresses at the pile shaft reduced significantly from the initial in-situ conditions. At this point, the ratio between  $\sigma'_{r,i}/\sigma'_{v,i}$  is equal to 0.24 and the ratio between  $\sigma'_{r,i}/\sigma'_{v0} = K_i$  is equal to 0.03 from the initial value of 0.6 ( $K_0$ ). This results from the large distortion and excess pore water pressure at the shaft following the installation. The results agree well with previous investigations described in the literature which is summarised in Chapter 2.

In addition, the results are compared to previous simulations for the Boston Blue Clay (BBC) presented by Whittle (1987). These are plotted in Figure 7.14 and 7.14 for BBC with  $OCR = 1$  and for the Modified Cam-Clay (MCC) and MIT-E3 soil model. The simulation with the SCLAY1S are similar to the MIT-E3 model close to the pile shaft and in the far field. However, there is a significant difference between 3 to 10 pile radius. This can be attributed to the anisotropy effect in the SCLAY1S and the fact that the MIT-E3 can capture the small strain effects. On the other hand, the MCC results over estimate the simulation herein, predicting large radial effective stresses directly after installation.

The two most important state variables in the SCLAY1S model that relate to the degree of bonding and the anisotropy of the soil are  $\chi$  and  $\alpha$ . Large values for the first parameter  $\chi$  represent strong bonding in the soil. Figure 7.16 shows the variation of  $\chi$  following pile installation. It is clear from these results that the large strains totally remoulded the soil near the pile shaft, i.e.  $\chi$  reduced to zero. Further away from the pile shaft, at

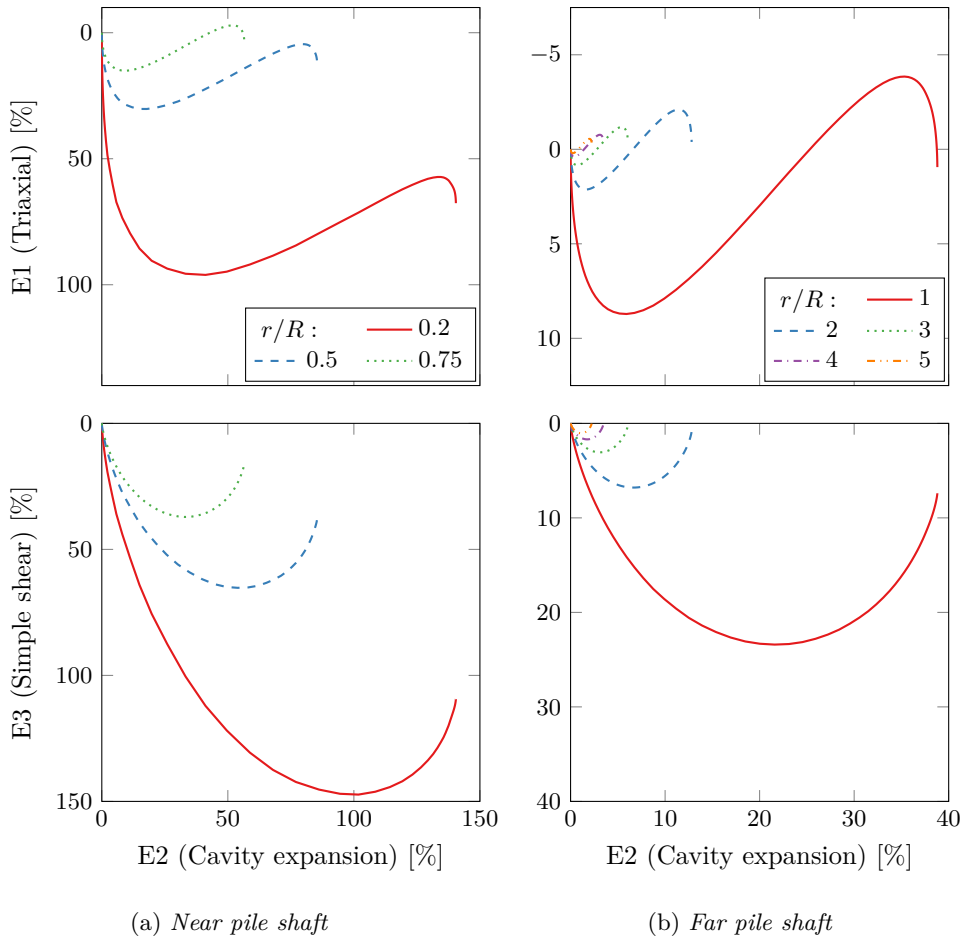
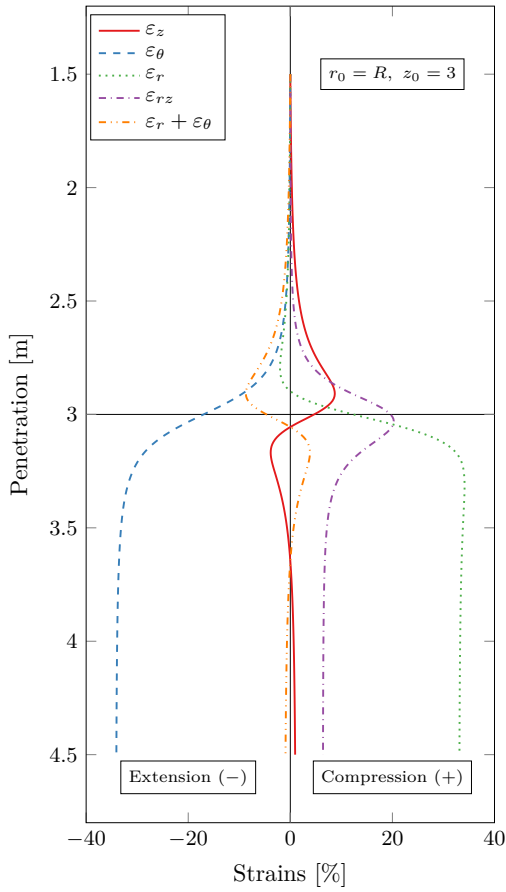


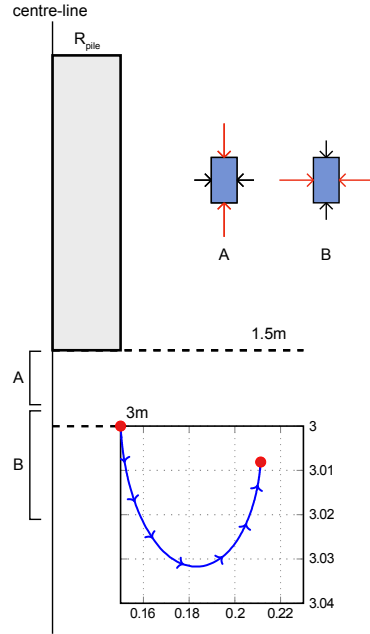
Figure 7.11: Strain invariants from SPM for some soil elements at depth  $z = 3$  m.

approximately  $1.5R_{pile}$ , the soil is partially remoulded and is nearly unaffected in the soil at a distance greater than  $10R_{pile}$ . The second important state variable  $\alpha$  represents the degree of anisotropy in the soil and is given by a tensor for all the space components. Of these  $\alpha$  in the  $r$ ,  $\theta$  and  $z$  direction, as well as the relevant off-diagonal components  $\alpha_{rz}$  and  $\alpha_{r\theta}$  (see Wheeler et al. 2003 for equations) are most illustrative.

Figure 7.17 plots the latter  $\alpha$  components as function of the normalised distance from the pile shaft. In case of an isotropic stress state, where the yield envelope is not initially rotated and similar to that of Modified Cam Clay, the diagonal components  $\alpha_r$ ,  $\alpha_\theta$ ,  $\alpha_z$  will be 1 and the off-diagonal components,  $\alpha_{rz}$ ,  $\alpha_{r\theta}$ , zero. Not surprisingly, small changes in the principal anisotropy components occur near the pile shaft. The off-diagonal  $\alpha_{rz}$ ,  $\alpha_{r\theta}$  show larger changes, as expected. Interestingly larger changes for  $\alpha_r$  and  $\alpha_z$  are observed



(a)



(b)

Figure 7.12: Strain components for node at  $(0.15,3)$  from SPM, pile radius  $0.15\text{ m}$ .

between 3 to 10 pile radius (at the partially remoulded zone). Here the anisotropy seems to reverse.

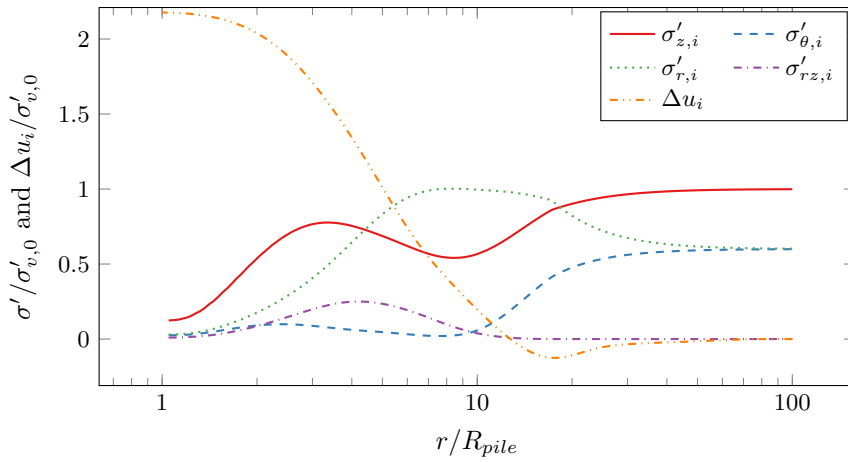


Figure 7.13: Predicted installation stresses and pore water pressure with SPM and SCLAY1S.

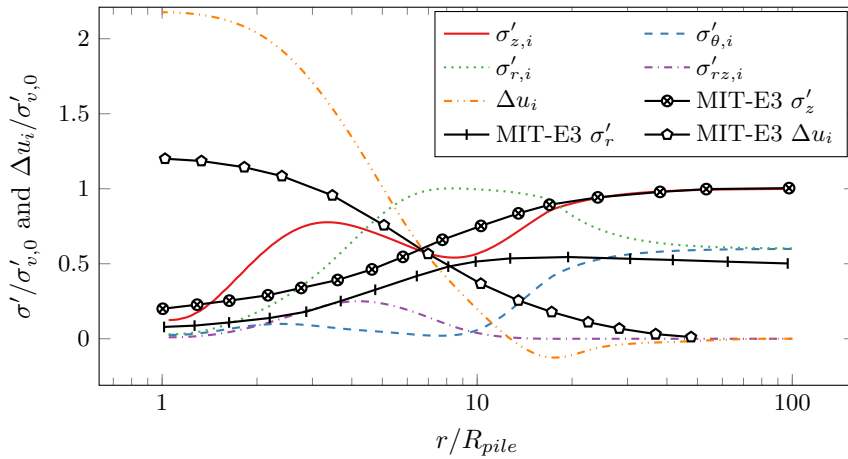


Figure 7.14: Predicted installation stresses and pore water pressure with SPM and SCLAY1S compared to MIT-E3 for BBC (Whittle 1987).

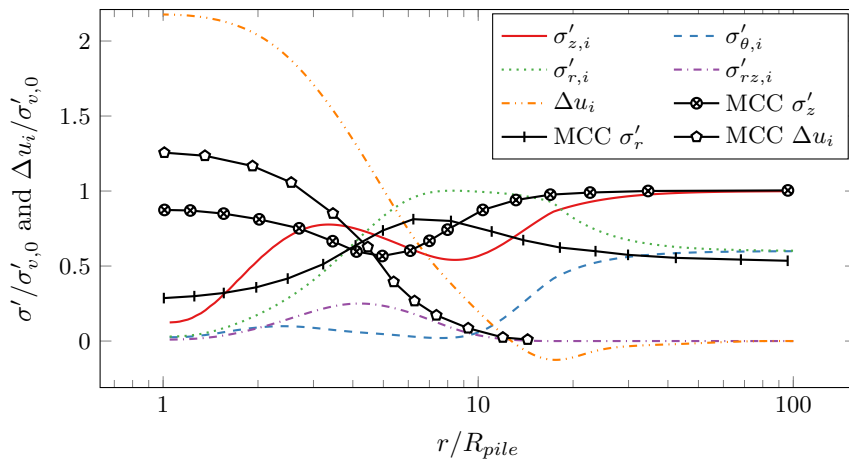


Figure 7.15: Predicted installation stresses and pore water pressure with SPM and SCLAY1S compared to MCC for BBC (Whittle 1987).

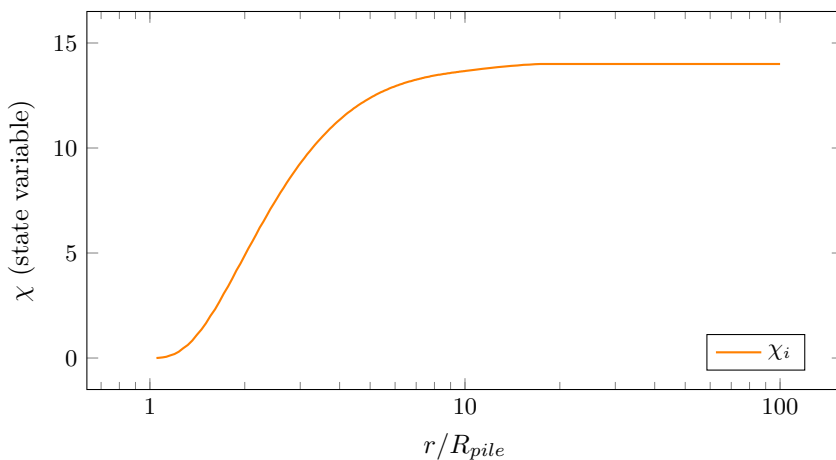


Figure 7.16: Predicted destructuration with SPM and SCLAY1S.

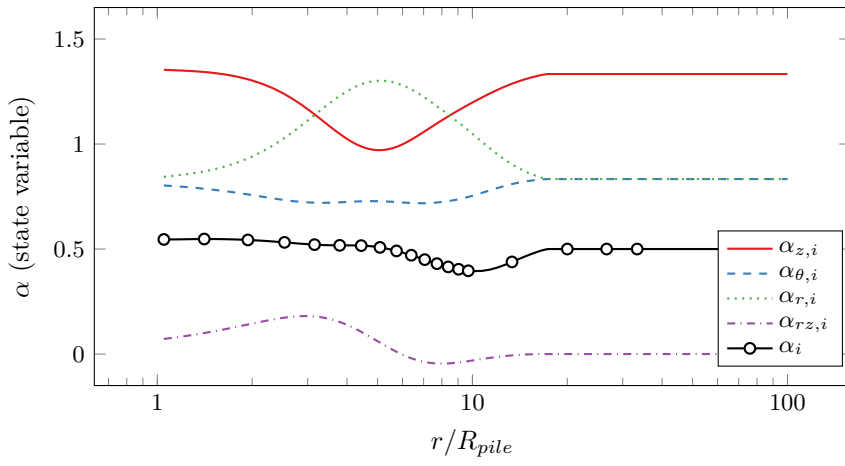


Figure 7.17: *Predicted anisotropy with SPM and SCLAY1S.*

### 7.3.3 Creep rates

The strain path method shows clearly the large distortion effects on the soil properties adjacent to the pile. Following the installation process the set-up period will take place. Some numerical issues prevented that the set-up stage is not explicitly modelled in this Thesis and it is assumed that most state variables will not change significantly near the pile shaft (with exception of the anisotropy). The initial stress condition at the pile shaft after equalisation of the installation pore water pressures was taken from the results presented by Whittle (1987) and Aubeny (1992) for Boston Blue Clay and the MIT-E3 soil model. These are given in Table 7.2 and are equivalent to a stress ratio  $\eta = q/p' = 0.6$  independent of  $K_c$  value. These assumptions can be improved upon in further research by taking the pile set-up (dissipation of pore pressures) into account in the SPM and effective stress analyses. Note that the  $K_c$  values in Table 7.2 are in good agreement with Table 2.3 and Figure 7.1.

Table 7.2: Effective stresses after set-up period from numerical models.

OCR	$K_c^1$	$K_c^2$	Stresses
1	0.38	0.42	$\sigma'_z \approx \sigma'_r \approx K_c \sigma'_{v0}$
2	0.63	0.83	$\sigma'_\theta \approx 0.5 K_c \sigma'_{v0}$

<sup>1</sup> 1D radial (Whittle 1987);

<sup>2</sup> 2D (Aubeny 1992).

The CREEP-SCLAY1S soil constitutive model is used in conjunction with the strain driver in order to calculate the creep rates for a certain applied shear load at the pile shaft. As discussed previously this is a reasonable approach as the failure on the pile interface is expected in the soil. Hence, it suffices at this stage to predict the strain rates at element level. In the analyses, the disturbed soil properties are carried over from the SPM results to start from a realistic post installation soil state. Thereafter, the soil is loaded to the final set-up stresses given in Table 7.2. Numerically this poses no problems as the CREEP-SCLAY1S model has a similar formulation for the anisotropy and destructuration.

Estimates for the deviatoric creep rate after pile installation and set-up in a disturbed soil profile are then obtained by application of a drained shear loading path similar to that of a Direct Simple Shear (DSS) test at a single stress point. The creep rates are studied for different degrees of mobilisation in respect to the undrained peak shear strength of the element test ( $\tau_{rz}^{peak}$ ). In addition, different boundary conditions for the DSS test are considered (see Figure 7.18). These boundary conditions (BC) are described below:

- BC1: no volume change is allowed in the soil element. Undrained BC.
- BC2: the radial (normal) stress perpendicular to the shear load is kept constant. The soil element will change in volume with the radial strains. Drained BC.



prescribed set-up stresses. Therefore, higher  $K_c$  values will mainly influence the shear strength magnitude and not the initial state variables of the CREEP-SCLAY1S model (i.e. the stress path follows the same  $\eta$  line). The initialisation stress path and evolution of  $\alpha$  are shown in Figure 7.19. The NCS and ICS have the same size and orientation since there is no structure ( $\chi = 0$ ).

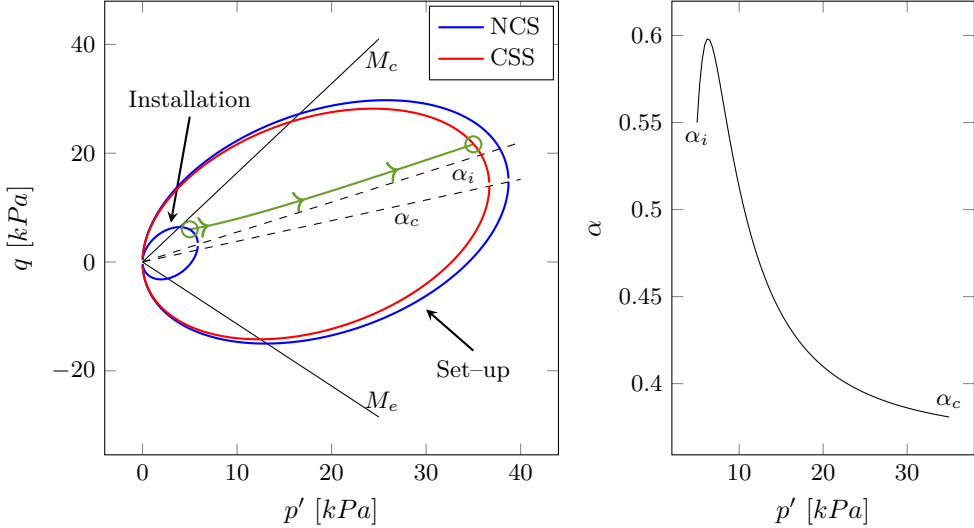


Figure 7.19: *Initialisation of set-up stresses for DSS test with  $\Delta t = 90$  days.*

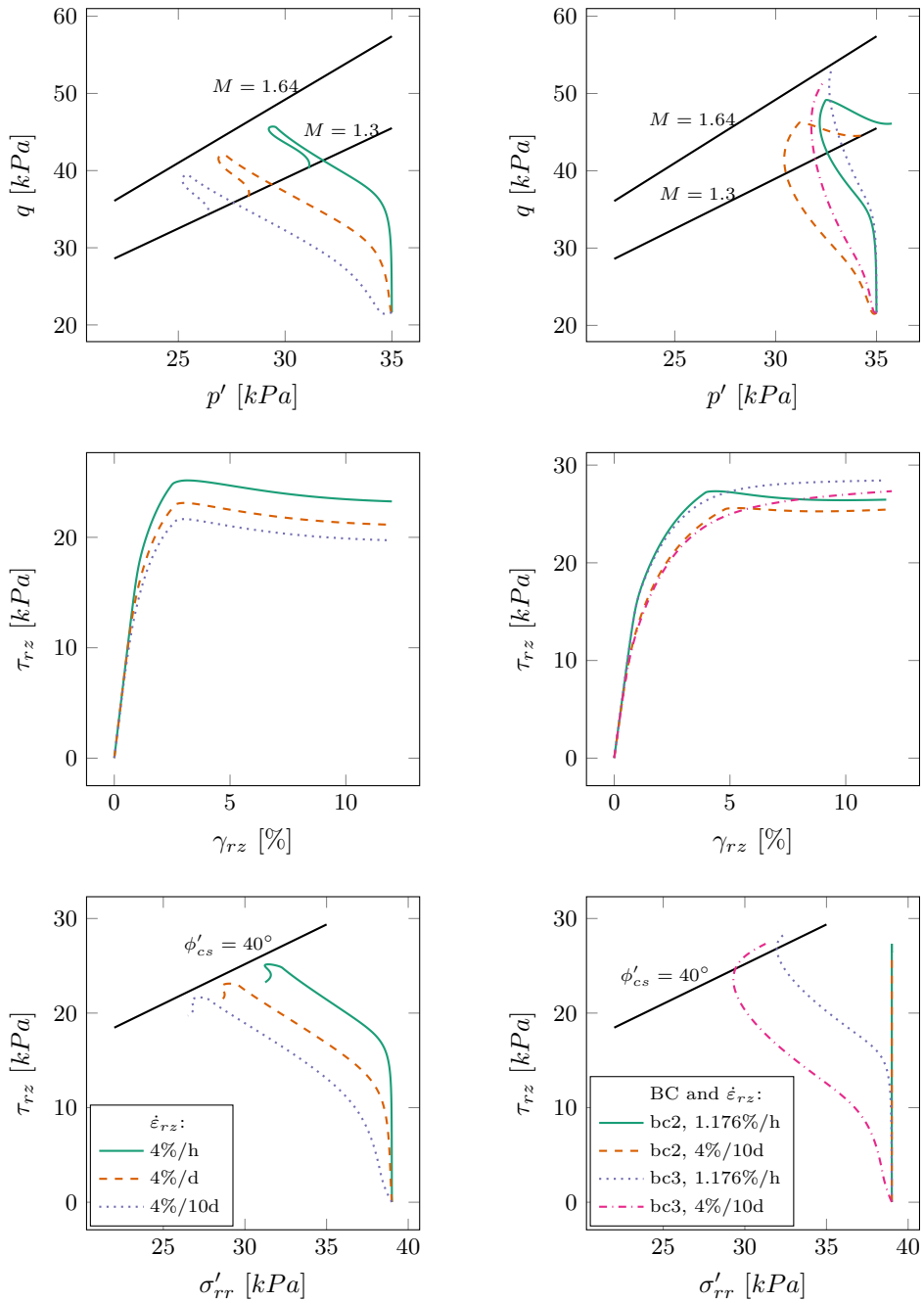
### Short-term DSS tests

The short-term undrained and drained shear strength were calculated after initialisation of the set-up stresses. For shaft bearing piles, the failure strains are very small and typical short-term pile tests are load within 1 to 2 hours, while long-term tests can take up to several days. Therefore, different rates were used in both types of tests in order to study the soil rate effects, as given in Table 7.4. The results from the undrained shear test at 4 % / h and the drained shear test at 4 % / 10 d are used as reference for the mobilisation degree of the long-term tests.

Table 7.4: Short-term DSS loading rates.

Undrained	Drained
4 % / h	1.176 % / h
4 % / d	4 % / 10 d
4 % / 10 d	–

The results from all tests is presented in Figure 7.20. Note that for the drained tests two possible boundary conditions were used, namely BC2 and BC3. The shear strength in DSS will depend on the Lode angle, with  $\theta = 0$  (Doherty and Fahey 2011). The critical state line  $M$  is calculated using Equation (3.8) for the CREEP-SCLAY1S model, giving  $M_{DSS} \approx 1.3$ , as observed for the undrained and drained test with BC2. For the reference undrained and drained (with BC2) loading rate, the peak strength was  $\tau_{rz} = 25$  and  $\tau_{rz} = 25.6$  kPa respectively. These peaks are very similar in magnitude despite the different stress paths. For the drained tests with BC3, the radial stress relaxed and failure took place at the compression critical state line  $M = 1.64$  and  $\tau_{rz} = 27.2$  kPa (slightly similar to triaxial compression). Remarkably, the stress path in the  $\tau_{rz}-\sigma'_{zz}$  plot are very similar to the trends observed by Lehane and Jardine (1994).



(a) Undrained

(b) Drained

Figure 7.20: Short-term loading of single element under DSS conditions.

## Long-term DSS tests

The creep rates for different mobilisation degrees are calculated by means of long-term holding periods in the strain driver. First the desired shear load is applied in 1 hour. Thereafter the load is kept constant and the soil is allowed to creep for 365 days. In this analysis, all boundary conditions were used in order to study the effects of stress relaxation under different kinematic constrains. The results are presented in Figure 7.21 to 7.23.

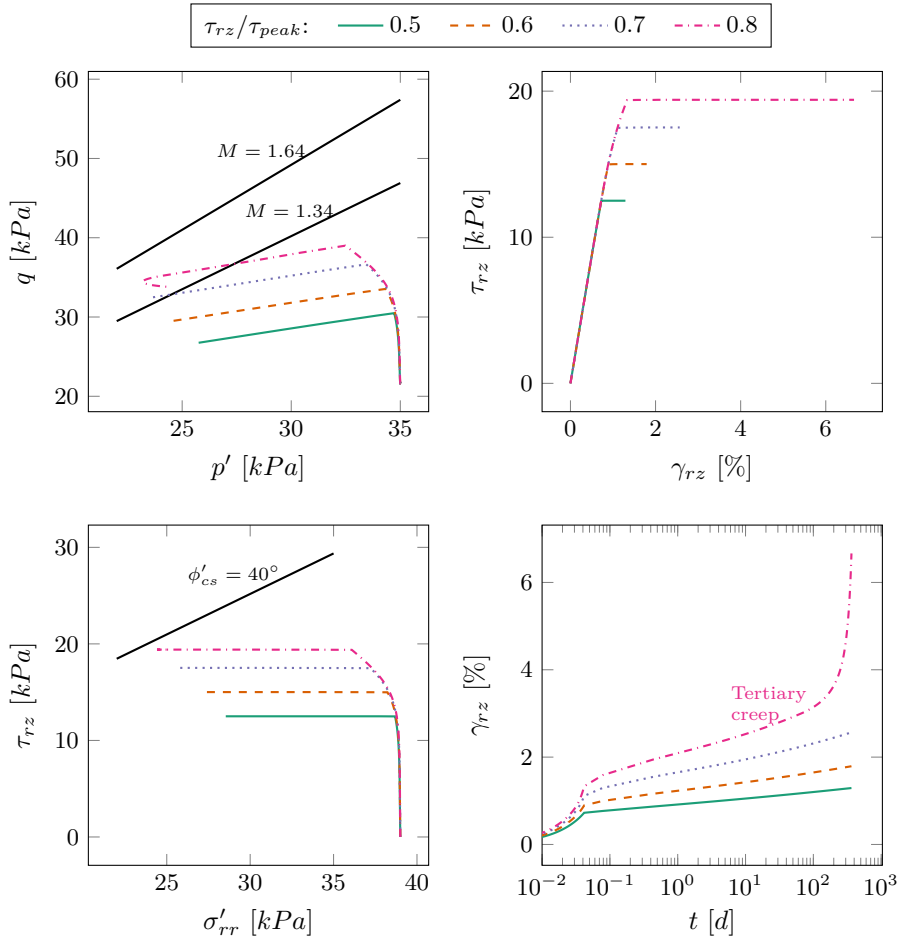


Figure 7.21: Deviatoric creep from simulated DSS tests for Undrained boundary conditions (bc1).

As can be expected during the creep stages, the accumulated shear strains increased with time and increasing shear stress magnitudes. These approximately follow a linear

trend in a semi-logarithmic plot, showing an gradually increasing slope with increasing shear stresses; similar to the results observed in the field test in this Thesis. The slightly non-linearity in the semi-logarithmic plot is caused by the evolution of  $\alpha$ ,  $M(\theta)$  and stress ratio  $\eta$  with time, as observed in equations (7.29) to (7.32).

$$\dot{\varepsilon}_v^c = \dot{\Lambda} \frac{\partial p'_{eq}}{\partial p'} = \dot{\Lambda} \frac{M^2(\theta) - (q/p')^2}{M^2(\theta) - \alpha^2} \quad (7.29)$$

$$\dot{\varepsilon}_d^c = \dot{\Lambda} \frac{\partial p'_{eq}}{\partial q} = \dot{\Lambda} \frac{2(q - \alpha p')}{p(M^2(\theta) - \alpha^2)} \quad (7.30)$$

$$\dot{\Lambda} = \frac{\mu_i^*}{\tau} \left( \frac{p'_{eq}}{p'_m} \right)^\beta \left( \frac{M_c^2 - \alpha^2 K_0^{nc}}{M_c^2 - \eta^2 K_0^{nc}} \right) \quad (7.31)$$

$$\frac{\dot{\varepsilon}_d^c}{\dot{\varepsilon}_v^c} = \frac{2(\eta - \alpha)}{M^2(\theta) - \eta^2} \quad (7.32)$$

The slope of each curve is plotted against the applied shear magnitude in Figure 7.24. Again, the creep parameter increase slightly non-linearly with respect to the applied stress magnitude, similar to the findings in this work. At mobilised ratios greater than 80%, the creep parameter becomes larger than the intrinsic value as the stress approaches the failure envelope. For BC1, BC2 and BC3 a mechanism similar to creep rupture occurred when the soil stresses approximated the maximum stress obliquity given by the critical state friction angle ( $\tau/\sigma'_n = \tan(\phi'_{cs})$ ). At this stage the creep rate accelerated and the soil could not sustain any longer the applied shear load. Especially for the drained BC2 and BC3 this is a bit unusual, perhaps indicating that also for sensitive soil in the field the “rupture” not necessarily is a totally undrained mechanism but partly material softening. The maximum mobilised shear ratio  $\tau/\tau_{rz}^{peak}$  was 0.8 for BC1 and 0.9 for BC2 and BC3. BC4 is considered a special case since the stresses are kept constant. The latter condition is not representative for a real boundary value problem and no creep rupture can be capture under this circumstance.

Given the model simplifications and the complexity of the problem this approach gives very promising results. Mechanisms similar to creep rupture were observed in the single element strain driver and was caused by stress change due to a set of given kinematic constrains. Those constraints only partly imitate the stress reduction from stress relaxation, accumulation of creep generated excess pore water pressures or softening from localisation. Nevertheless, despite some simplifications the results are in good agreement in respect to the creep rate and the trend in the creep parameter. The latter suggests that especially in soft sensitive soils other processes contribute to failure in addition to undrained tertiary creep.

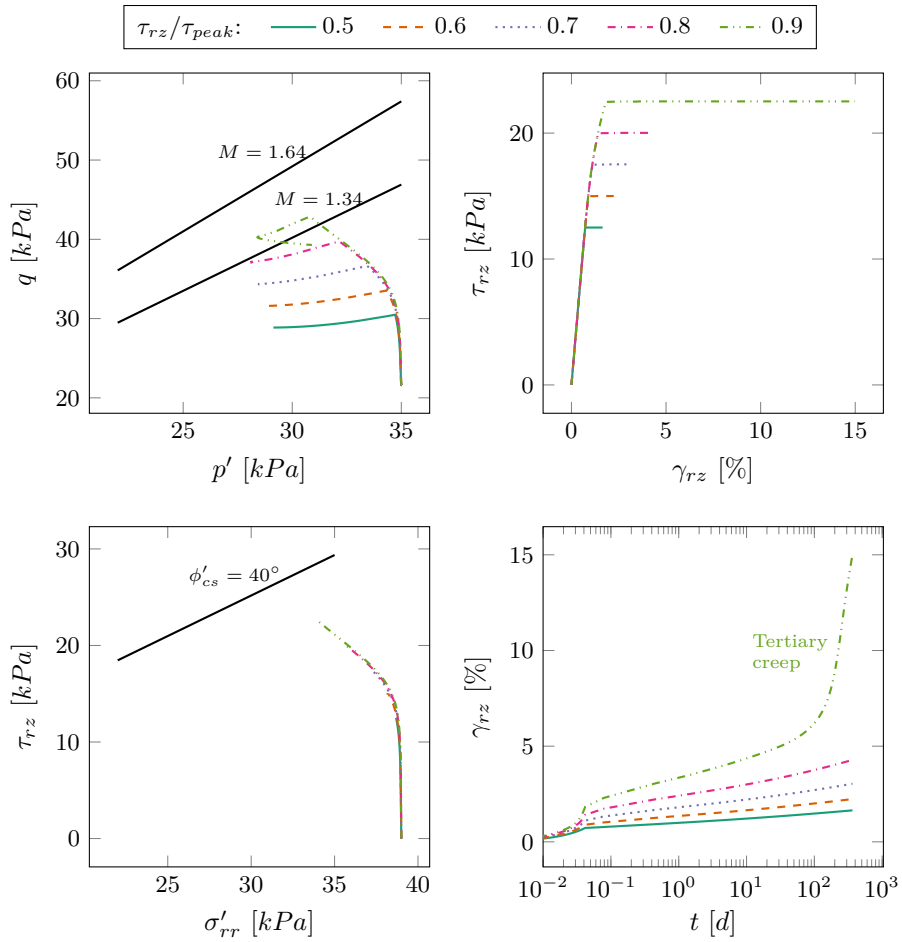


Figure 7.22: Deviatoric creep from simulated DSS tests for Drained boundary conditions (bc2).

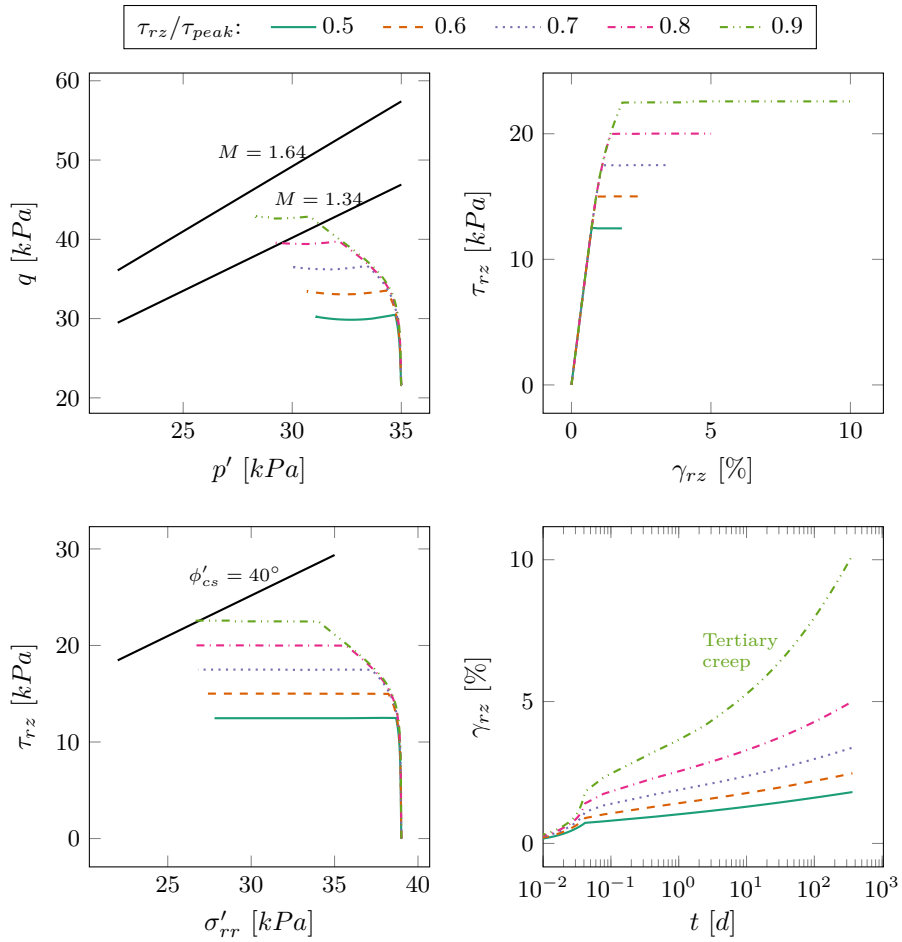


Figure 7.23: Deviatoric creep from simulated DSS tests for Drained boundary conditions (bc3).

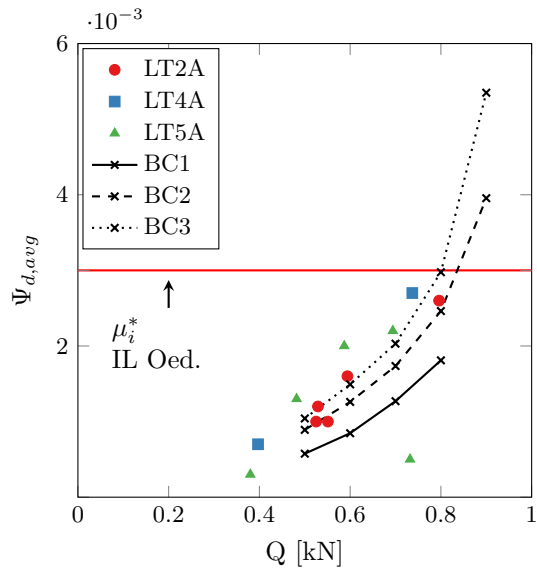


Figure 7.24: Deviatoric creep parameter from simulated DSS tests compared to field measurements.

## 8 Conclusions

This Thesis presents new findings on the long-term behaviour of tension loaded piles in natural soft clays. The results from the field tests on six pile elements are unique as they incorporate all significant stages in the pile cycle, i.e. pile installation, set-up and long-term loading, yet are short enough to link the pile response to soil behaviour. In addition to a system level interpretation of the measured pile head displacement an advanced numerical analysis that incorporates a state-of-the-art rate dependent soft soil model is performed. The measured data and simulation results are in good agreement and corroborate previous investigations, however, for the first time the physical mechanisms underpinning the measured response are generalised using an advanced rate-dependent constitutive model for soft soils.

A new non-standard mechanical loading setup has been developed for the field tests. The setup has two novel features: (1) the load was provided by pneumatic lifting bags that provide constant loads without complex control systems and (2) realistic installation effects and stresses are maintained by installing the short tension elements at large depth. This setup proves to be robust, cost-effective and easy to adapt to different loading regimes and pile head displacements. The variation of the applied load in time in the first prototype ( $\pm 10\%$ ) has been further improved ( $< \pm 2\%$ ) with the addition of a simple control system composed of solenoid valves, a portable electric air compressor and a desktop computer. With this experimental setup, new experimental data has been gathered by application of long-term sustained tension loads as well as for reference short-term quick tests.

In the reference short-term quick tests, the ultimate bearing capacity mobilises with small relative pile-soil displacements in the range of 4 to 8 mm. A sliding failure mechanism initiates at  $Q_{ult}$  which subsequently halted during further unloading to  $0.7 - 0.8Q_{ult}$ . The pile “creep” load appears to be approximately  $0.8Q_{ult}$  and represents the loading threshold from where large displacement rates start to develop in the short-term tests. The observed behaviour in these tests is similar to that previously reported in tension and compression loaded piles in soft clays (e.g. Bengtsson and Sällfors 1983; Karlsrud 2012). In addition, analysis of these results indicates that the short-term bearing capacity of single piles in tension is approximated satisfactorily with traditional total stress and effective stress based Ultimate Limit State (ULS) design methods. Load transfer methods, however, are required to accurately capture the load distribution along the pile. Here, the method proposed by Q.-q. Zhang and Z.-m. Zhang (2012) produces very good results by fitting the required displacement until the peak strength is reached. The fitted displacement magnitude falls in the middle of the range measured in the field test, i.e. 6 mm.

The long-term test results show larger pile head displacements resulting from consolidation and creep in the clay surrounding the pile, and a lower ultimate bearing capacity in tension than is obtained in the quick pile load tests ( $Q_{sls} < Q_{ult}$ ). The long-term pile response is mainly characterised by the creep deformations in the soil adjacent to the pile. In the reported tests, the pile head displacement rate is directly proportional to

the magnitude of the applied tension load, i.e. the creep rate increased with increasing pile head load (i.e. deviator stress on the pile-soil interface). There is a threshold for the load below which the creep rate tends to decrease with time and remains in the primary phase. At approximately  $0.7Q_{ult}$  this limiting load is smaller than the short-term ULS capacity. Loads above this threshold will trigger failure by creep rupture, where the creep rate accelerates with time until failure.

The reduction in the bearing capacity for the long-term pile load tests on the test site considered and within the available time, is most probably linked to the soil contraction that is triggered by the shear load next to the pile shaft. The soil contraction generates excess pore water pressures (during fast load applications) and relaxation of the horizontal effective stress due to the kinematic constraints at the pile-soil interface (Lehane and Jardine 1994). As the creep deformations develop, the stresses will relax until a final equilibrium state is reached. If the stresses in the soil are close to the failure envelope, the clay becomes unstable and creep rupture can take place. Within this unstable zone, the creep rate will accelerate and possibly generate additional excess pore water pressures. If the rate of dissipation is insufficient the generated excess pore water pressure will accumulate, reducing further the effective stresses in the soil and subsequently the available shear resistance.

Interestingly, normalisation of the measured pile head displacement rate using the pile equivalent diameter  $D_{eq}$  results in displacement rates which are in close agreement to those found in 1D oedometer tests on samples with little or no bonds (i.e. heavily remoulded state). This indicates that most of the creep deformations develop within the disturbed zone within 1 pile diameter from the pile shaft. The pile head displacement in time follow a linear trend on a semi-logarithmic plot  $\log(t) - \delta$ . Therefore, the pile head creep displacements can be extrapolated using traditional non-linear analytical creep models originally developed for 1D oedometer tests. The latter produced relatively small total pile head displacements of 6 to 14 mm when the data is extrapolated over time for a service life of 100 years. Obviously this empirical approach has no fundamental basis and should be used with care.

A more advanced numerical investigation into the expected creep rates has been performed by combining the Strain Path Method (SPM) with a single element strain driver and an advanced constitutive model for the soil that incorporates creep (CREEP-SCLAY1S). This method allows to incorporate the large deformations during pile installation and its effects on the soil properties in the subsequent analyses of the creep response. The initial results using this novel approach, show that the important features of the evolution of the creep rate as function of load magnitude and time are qualitatively captured. The expectation is that after some modifications, most notably incorporating the pile set-up stage, the results will improve further.

In conclusion, the long-term behaviour of single piles in natural soft clays is directly related to the behaviour of the soil adjacent to the pile shaft. The degree of bonds and compressibility are important properties for the long-term creep displacements of the pile element. As the applied load increases, the volume of influence becomes larger and the

soil experiences a transition from stable to unstable creep. Soil further away from the pile shaft is less affected by pile installation and therefore is more sensitive to structural changes, leading to more creep deformations, increase of excess pore water pressures and/or stress relaxation.

## 8.1 Recommendations

In long-term tests it is insufficient to only measure the radial effective contact stress after installation and the set-up period. Instead the evolution of all stress components should be known and accounted for, together with any change in soil properties, when analysing pile test results in relation to soil behaviour. By approximating the stresses in the soil before loading and having a proper soil model, the pile behaviour can be accurately captured using numerical simulations. Possible approaches to study this problem are presented below:

- Additional tests on natural and remoulded soft clays behaviour by means of advance laboratory tests that can probe stress paths similar to those under pile installation and during loading. Special focus should be given to the deviatoric creep behaviour under drained conditions and for different stress paths (that include stress rotations).
- Performing fully instrumented field tests with short element piles in homogeneous soft clays where the soil kinematics and stress changes during installation and subsequent consolidation and loading are captured. The influence area of the creep deformations and shear load need to be studied in more detail in field conditions. This is important as larger loads will mobilise a larger soil volume around the pile and perhaps will trigger more creep in the partially remoulded zone. As a consequence, the field of observation should not be limited to the pile shaft, but extend at least one pile diameter into the soil and consider all three main directions ( $z, r, \theta$ ). This requires novel field instrumentation, for example by embedding smart devices in the pile path and surrounding soil (i.e. use of MEMS accelerometers and gyroscopes and/or electromagnetic techniques to track tracers in the soil).
- Study the evolution of the soil properties by extraction of soil samples for laboratory testing of the soil next to the pile shaft by means of block sampling, at different times in the pile cycle.
- Fully coupled (i.e. material and groundwater) large deformation modelling with advanced soil models that can capture rate dependency (creep), thixotropy and allows for non-linear (small strain) stiffness.



# A APPENDIX

## A.1 Test site

Figure A.1 shows the test site location before the pile installation. Today, the area has changed substantially due to the undergoing works for the Marieholm tunnel.



Figure A.1: *Aerial view of test site. Located next to Waterloo street 100 m north-east of the Partihalls connection road.*

Figure A.2 is a blueprint of the planned construction works in the area in connection to the Marieholm tunnel project. Previous soil investigations selected in the desk study of this Thesis are surrounded by a red circle.

Figure A.3 and A.4 show the test site after installation of the 6 test piles. The container in the picture was used to store the data acquisition system and other tools required during the testing program.

### **Extensometer data**

The test site was instrumented with an vertical extensometer in order to measure the ongoing settlements. This measurements are relative to the extensometer toe, as this was considered to be fixed in time and space.





Figure A.3: *Test site after installation of the 6 test piles.*



Figure A.4: *Steel extension pile and timber mat on top of fill material.*

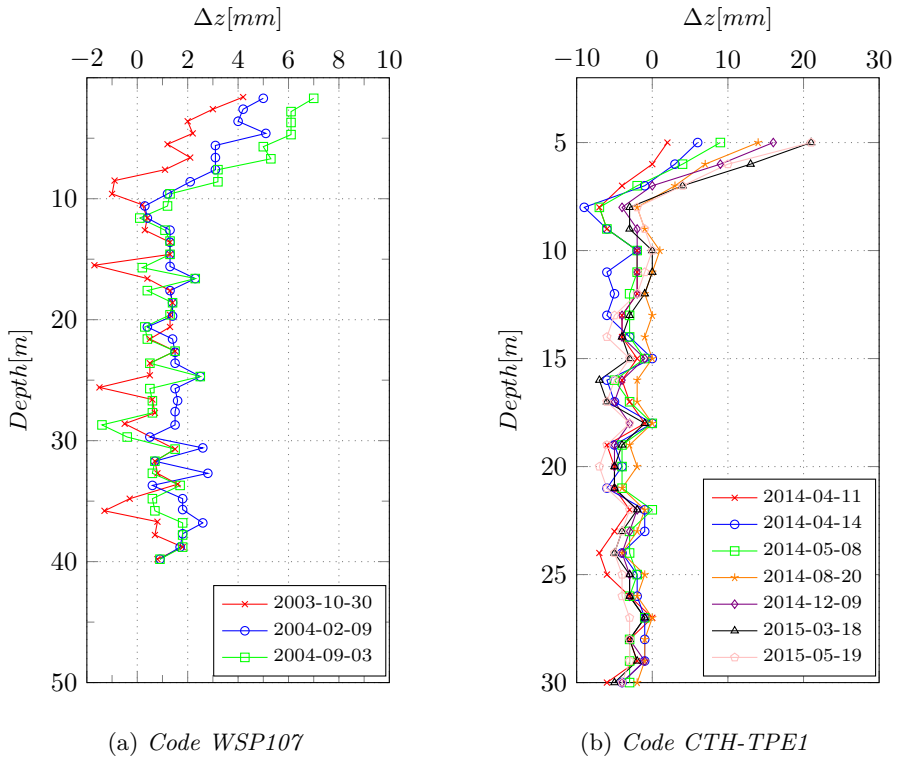


Figure A.5: Settlement measurements at the test site and from previous investigations.

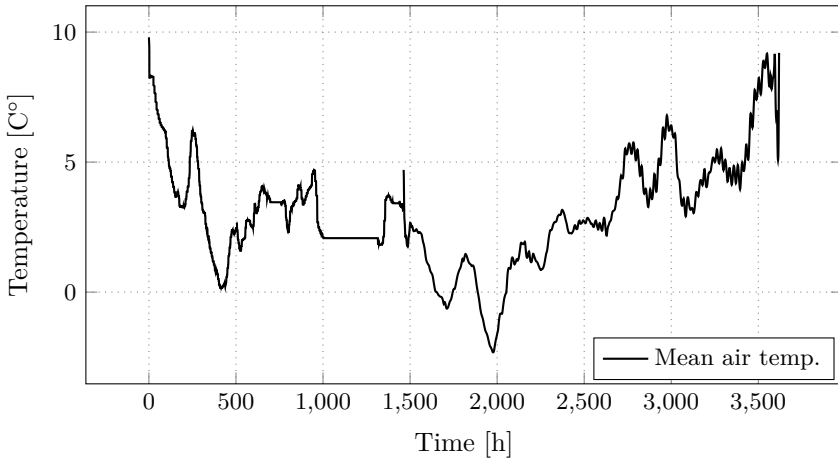


Figure A.6: Average air temperature at test site.

## A.2 Test piles

### Model pile

A model pile was used for the calibration of the strain gauges and to study the pile cross section stiffness. Figure A.7 show the 1 m long model pile with cross section 0.235x0.235 m.



Figure A.7: *Model pile used to calibrate the strain gauges (1 m long).*

### Test piles and load frame

Figure A.8 presents the equipment used for the load rig and A.9 shows the Chalmers Concrete laboratory working area together with the concrete test piles and the extension steel pile sections. Figure A.10 and A.11 show the load frame structure used for all the piles.



Figure A.8: *Equipment used for the load rig (without HEB beams). Load cell, lifting bags (white box) and portable air compressor.*



Figure A.9: *Concrete piles, steel extension piles, tell-tales and tension loading rod.*



Figure A.10: *Load frame.*



Figure A.11: *Load frame and manual pressure regulation panel.*

### A.3 Long-term measurement data

#### Pile 1 – LT1A

This pile was instrumented with a one LP, three levels of SGs, two tell-tales and two pore water pressure transducers at the shaft. The LP measurements were severely affected by tilting and movements of the reference beam, and the SG by temperature variations in the cable at ground level. Therefore, only the dial gauges measurements are presented as this were considered reliable.

The first load step aimed at 65 kN. This load was held within the tolerance limits for  $\approx 96$  days, correcting for changes under 3 occasions. The next load target was 80 kN, which is equivalent to the reference creep load  $Q_{creep}^{ref}$ . The load was held for  $\approx 55$  days, and as in previous stages, this decreased by the lifting bags self-unloading due to creep displacements. However, the load was not adjusted pass the tolerance level (72 kN). Therefore, the pile unloaded to 61 kN. The complete load and pile head displacement measurements is presented in Figure A.12 and Table A.1. Note that only the dial gauges measurements on the tell-tales are available.

Table A.1: Data from test LT1A.

Stage	t (d)	$Q_{ini}$	$Q_{end}$	$Q_{avg}$	$\delta_{ini}$	$\delta_{end}$	$\Delta\delta$
0 <sup>1</sup>	0.82	4.5	4.3	4.4	0.00	0.00	0.00
1	3.95	65.5	59.3	62.3	0.00	3.12	3.12
2	21.17	64.7	58.8	61.8	3.12	4.66	1.54
3	34.97	67.3	56.9	62.0	4.76*	5.66	0.90
4	34.81	67.4	53.9	60.2	5.77*	6.96	1.19
5	54.95	79.5	61.3	69.0	6.96	10.09	3.13

<sup>1</sup> Small load to remove slack in the loading frame.

\* Measured after load was applied.

Pile 1 was the only pile that did not failed by 2015-04-13. Following stage 5, the pile was loaded in different ways. First the pile was reloaded from 61 to 79 kN for 2 days. This load step generated significant tilting in the frame. Therefore, a quick unloading-reloading stage from 79 to 35 kN was done to verify that the tilting effect happened at the beginning of each load stage and remained permanent after that. Thereafter, the load regulation system was plugged to keep the load constant at 80 kN. However, during this time the pile experienced several unloading stages as the system was not properly configured and one of the solenoid valves failed to work. Therefore it was decided to manually regulated the load at 80 kN. This last stage lasted for approximately 87 days and the load decreased linearly with time down to 57 kN. Finally, the pile failed after 10 minutes when it was reloaded to 94.5 kN, showing large displacements and rapid unloading. This response was

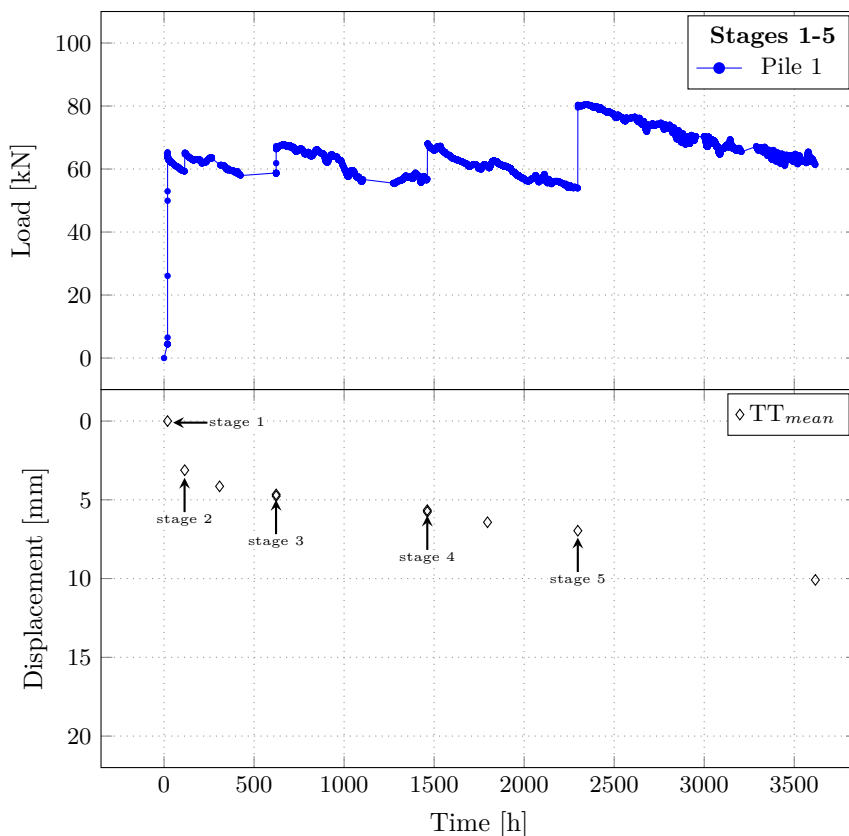


Figure A.12: *Load-displacement data for test LT1A.*

similar to that observed in the short-term tests.

Figure A.13 shows the pore pressures measurements at the pile mid section and toe. The data present some gaps due to power outage or problems with the pore pressure transducer. Similar to test LT2A, very small changes in the pore water pressure can be observed and it is hard to link these variations to the load increments. The only clear match appears to be in stage 5 when the pile was loaded to 80 kN (only toe data available). Thereafter the measurements present large variations without any further load increase. One could argue that after this load level, the soil is in an unstable state. However, one could all say that the transducer failed to work properly. Consequently, there is a lot of uncertainty in these type of measurements.

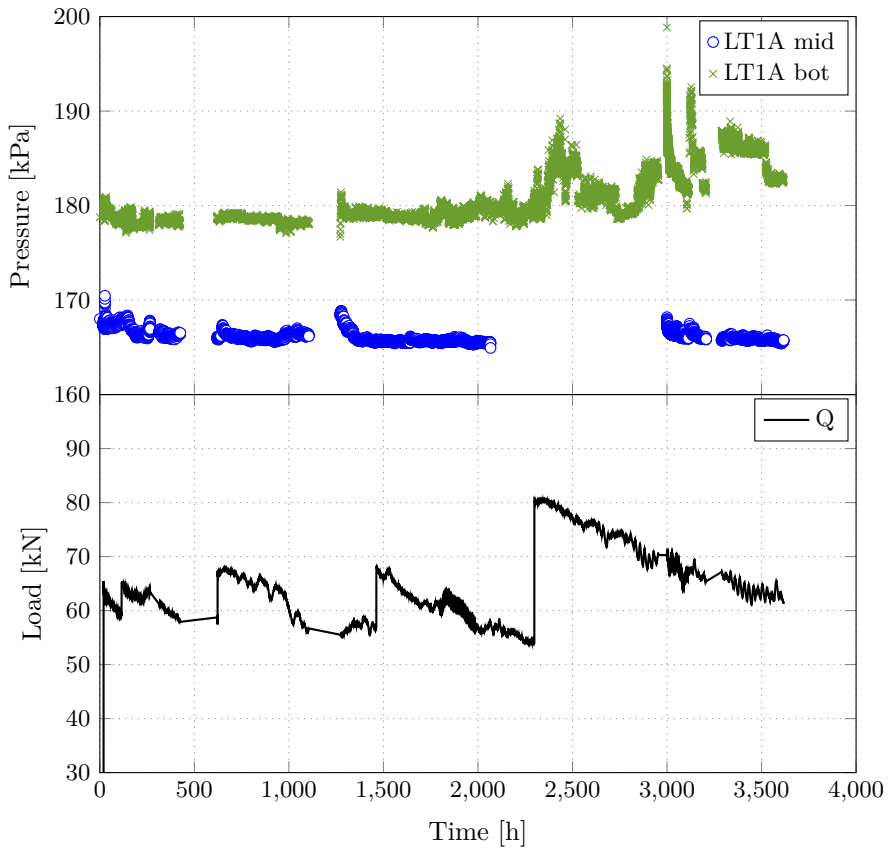


Figure A.13: Pore water pressure measurements at pile shaft for test LT1A.

### Pile 3 – LT3A

This pile was only instrumented with one LP and two tell-tales. Similar to test LT1A, the LP measurements were severely affected by tilting and movements of the reference beam. Therefore, only the manual measurements from the dial gages on the tell-tales were considered reliable. The complete load and average tell-tale measurements is presented in Figure A.14 and Table A.2. The tell-tale data is only available until the end of stage 5. Before stage 6, the pile was completely unloaded in order to fix the tilted frame by re-adjusting the lifting bag positions. Then, the pile was loaded to 84 kN. This load was held constant for approximately 2.5 hours before the pile suddenly failed with large displacements (TT could not be measured) and unloaded to a stable state around 65 kN.

Table A.2: Data from test LT3A.

Stage	t (d)	$Q_{ini}$	$Q_{end}$	$Q_{avg}$	$\delta_{ini}$	$\delta_{end}$	$\Delta\delta$
1	3.93	69.6	62.8	66.2	0.00	4.02	4.02
2	21.16	68.6	62.4	65.3	4.02	5.69	1.67
3	34.99	70.0	66.9	67.9	5.82*	7.08	1.26
4	34.82	72.1	65.7	68.4	7.15*	8.60	1.44
5	27.35	78.6	74.4	76.5	8.60	12.61	4.02
6	25.76	84.2	64.1	65.9	12.61	20.00+	7.39

\* Measured after load was applied.

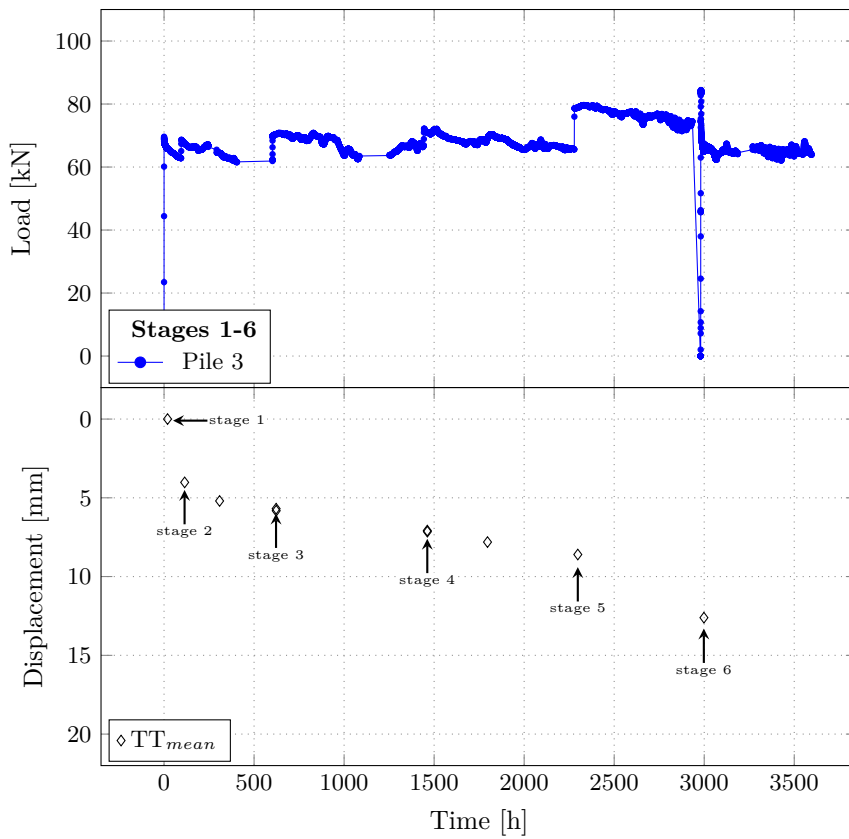


Figure A.14: Load-displacement data for test LT3A.

## Detailed measurements – LT2A

Figure A.15 to A.19 present the load–displacement curve for all stages of test LT2A in a better resolution. Average lines are presented as a guide for the load variation with time.

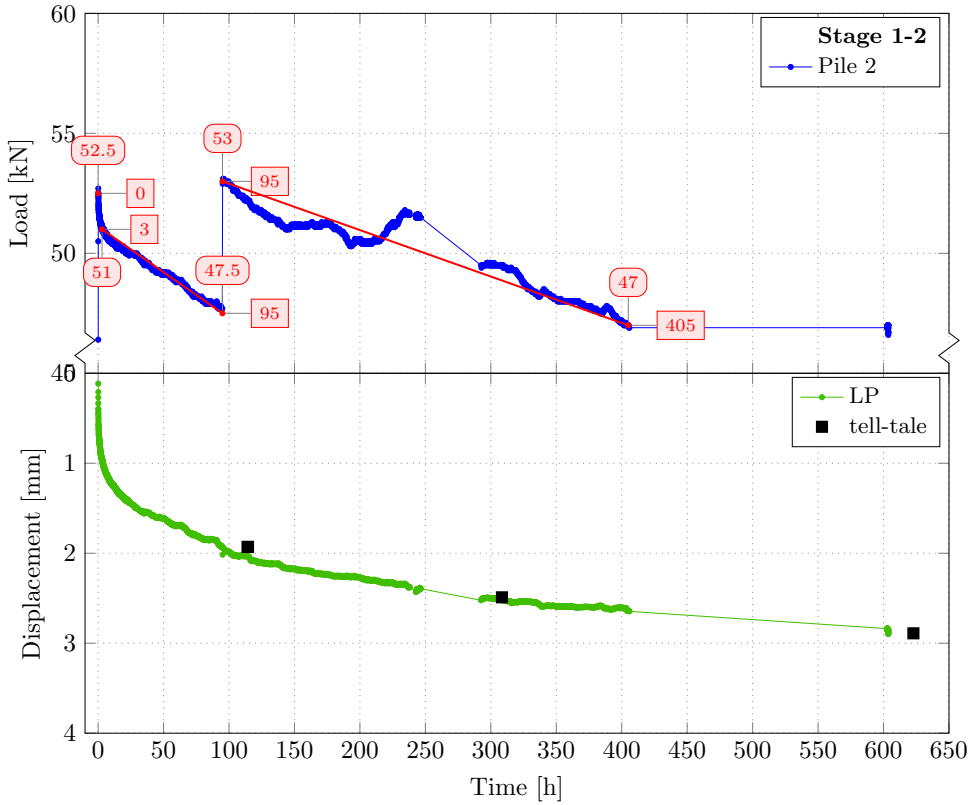


Figure A.15: Detailed data for Test LT2A, stage 1 and 2.

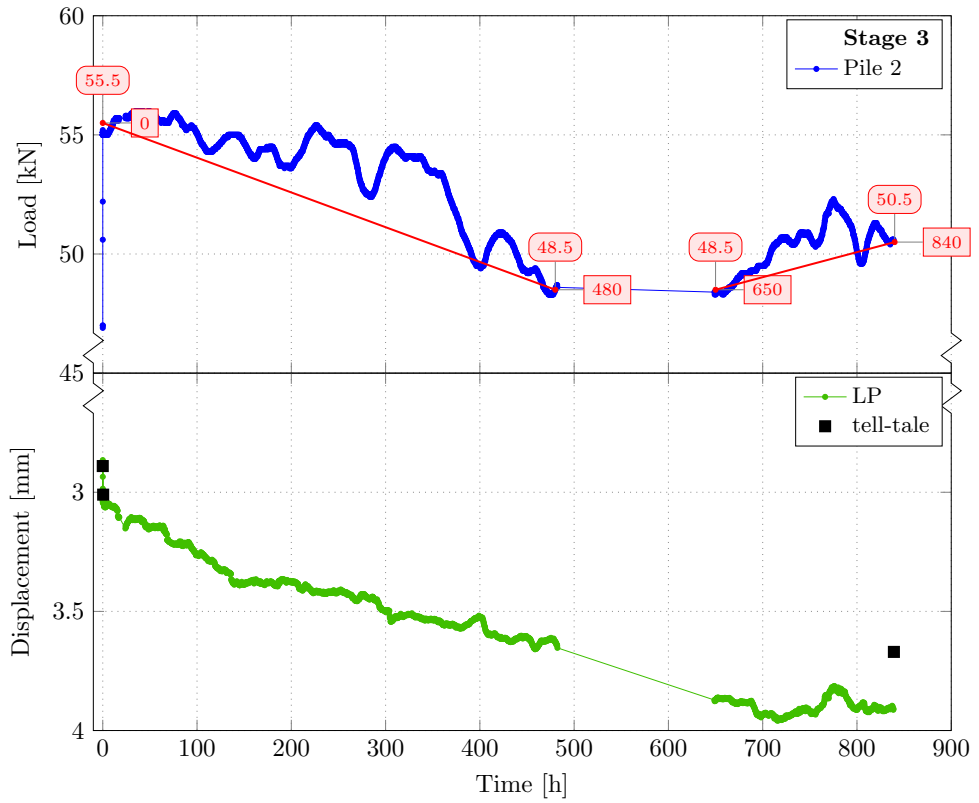


Figure A.16: Detailed data for Test LT2A, stage 3.

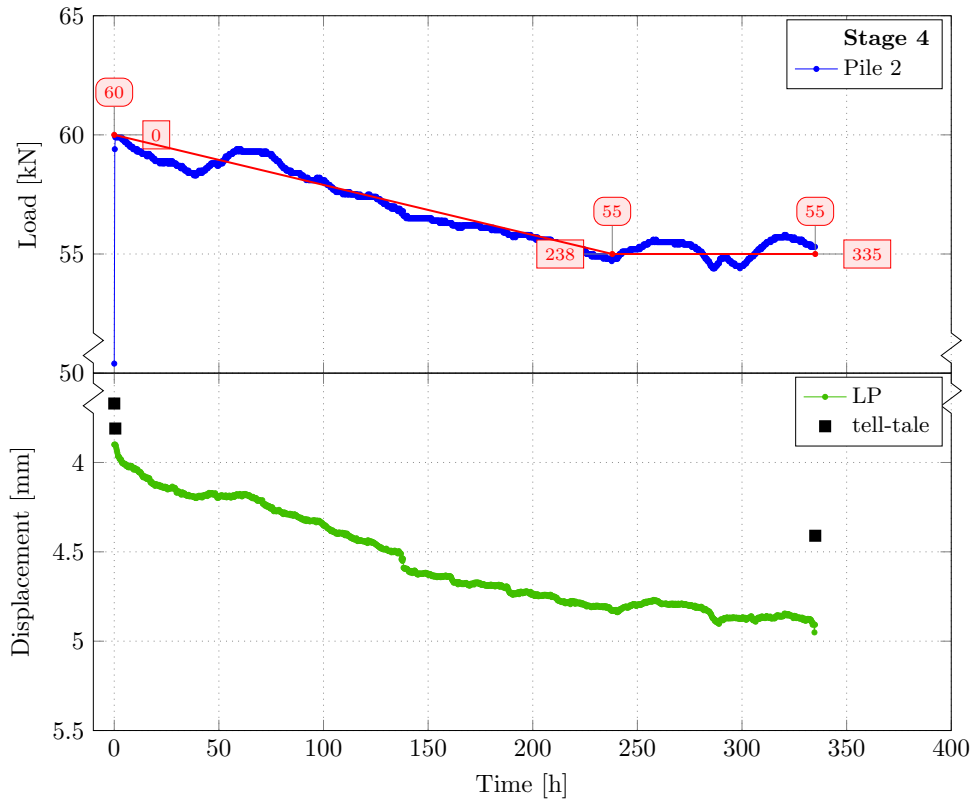


Figure A.17: Detailed data for Test LT2A, stage 4.

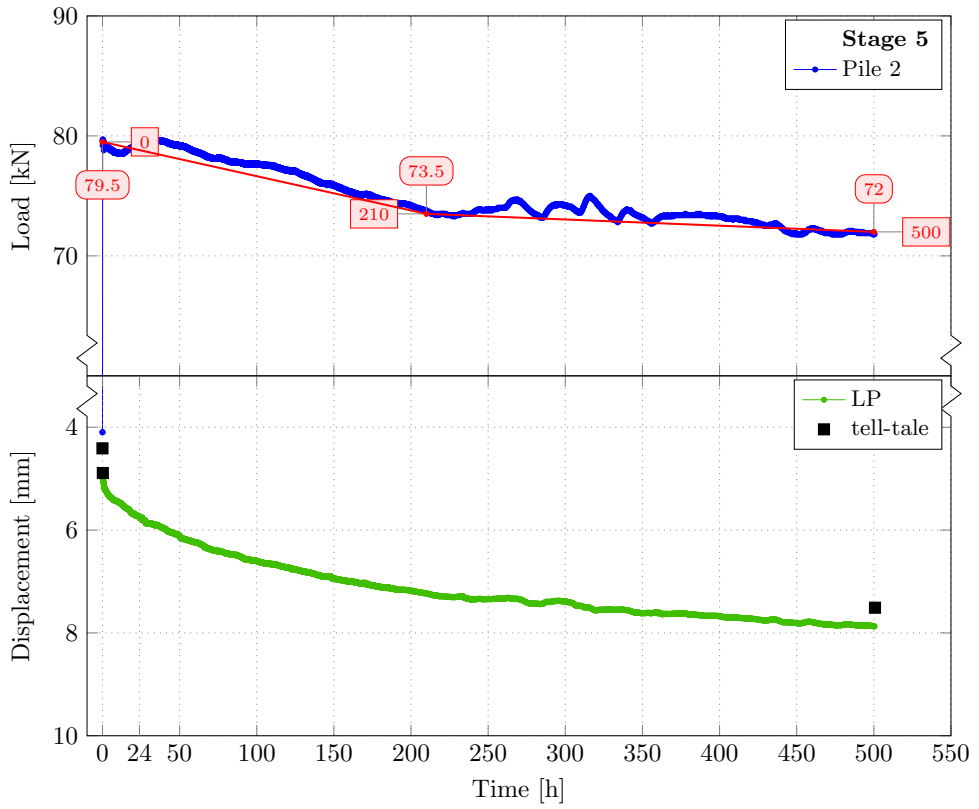


Figure A.18: Detailed data for Test LT2A, stage 5.

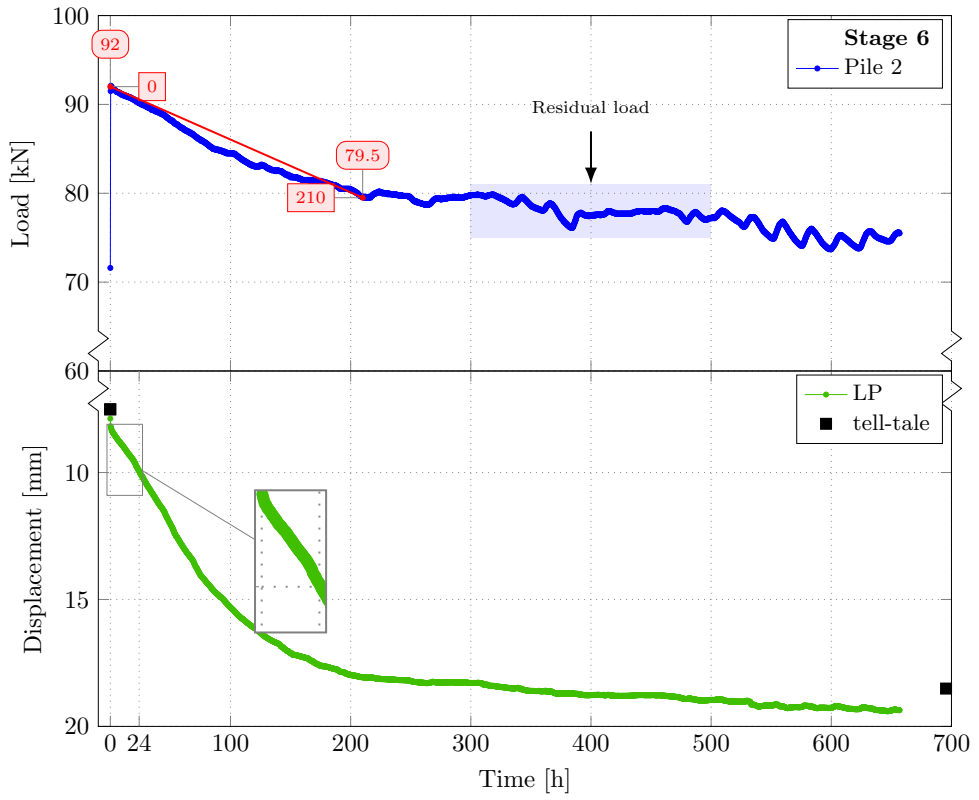


Figure A.19: Detailed data for Test LT2A, stage 6.



# References

- Alén, Claes (2015). *Krokig påle - krökt men inte rökt?* URL: <http://www.paldag.se/>.
- Allman, M. A. and J. H. Atkinson (1992). Mechanical properties of reconstituted Bothkennar soil. *Geotechnique* **42.2**, 289–301. DOI: 10.1680/geot.1992.42.2.289. eprint: <http://dx.doi.org/10.1680/geot.1992.42.2.289>. URL: <http://dx.doi.org/10.1680/geot.1992.42.2.289>.
- Aubeny, C.P. (1992). “Rational Interpretation of In-situ Tests in Cohesive Soils”. PhD thesis. MIT. URL: <http://dspace.mit.edu/handle/1721.1/13198?show=full>.
- (2016). *SPM excess pore water ppressure*. [email].
- Augustesen, Anders (2006). “The effects of time on soil behaviour and pile capacity”. PhD thesis. Aalborg University, Department of Civil Engineering.
- Augustesen, Anders, Lars Andersen, and C.S. Sørensen (2006). *Assessment of time functions for piles driven in clay*. Tech. rep. Department of Civil Engineering, Aalborg University.
- Augustesen, Anders, Morten Liingaard, and Poul V Lade (2004). Evaluation of time-dependent behavior of soils. *International Journal of Geomechanics* **4.3**, 137–156.
- Baligh, Mohsen M (1985). Strain path method. *Journal of Geotechnical Engineering* **111.9**, 1108–1136.
- Basu, Prasenjit et al. (2013). Shaft resistance and setup factors for piles jacked in clay. *Journal of Geotechnical and Geoenvironmental Engineering* **140.3**, 04013026.
- Bengtsson, Per-Evert and S. Hansbo (1979). “Settlement and bearing capacity of friction piles in soft highly plastic Clay.” *Nordic Geotechnical Meetings 79*.
- Bengtsson, Per-Evert and Göran Sällfors (1983). Floating piles in soft, highly plastic clays. *Canadian Geotechnical Journal* **20.1**, 159–168.
- Berg, Pieter van den (1994). *Analysis of soil penetration*. TU Delft, Delft University of Technology.
- Beuth, Lars (2012). “Formulation and application of a quasi-static material point method”. PhD thesis. University of Stuttgart, Germany.
- Bhat, Deepak R, NP Bhandary, and R Yatabe (2013). Residual-state creep behavior of typical clayey soils. *Natural hazards* **69.3**, 2161–2178.
- Biscontin, Giovanna and Juan M. Pestana (2001). Influence of peripheral velocity on vane shear strength of an artificial clay. *Geotechnical Testing Journal*.
- Bjerin, L (1977). *Dragloads on long concrete piles*. Tech. rep. Report 2. Swedish Geotechnical Institute.
- Bjerrum, Laurits (1973). “Problems of soil mechanics and construction on soft clays”. *8th International Conference on Soil Mechanics and Foundation Engineering*. Moscow.
- Bjerrum, Laurits and Arvid Landva (1966). Direct simple-shear tests on a Norwegian quick clay. *Geotechnique* **16.1**, 1–20.
- Bradshaw, H., R.R. Barton, and R.H. McKenzie (1984). “The Hutton TLP Foundation Design”. *Offshore Technology Conference, 7-9 May, Houston, Texas*. Offshore Technology Conference. DOI: 10.4043/4807-MS.
- Briaud, Jean-Louis and Enrique Garland (1985). Loading rate method for pile response in clay. *Journal of Geotechnical Engineering* **111.3**, 319–335.

- Brown, M.J. and John Powell (2013). Comparison of Rapid Load Test Analysis Techniques in Clay Soils. *Journal of Geotechnical and Geoenvironmental Engineering* **139**.1, 152–161. DOI: 10.1061/(ASCE)GT.1943-5606.0000733. eprint: [http://dx.doi.org/10.1061/\(ASCE\)GT.1943-5606.0000733](http://dx.doi.org/10.1061/(ASCE)GT.1943-5606.0000733). URL: [http://dx.doi.org/10.1061/\(ASCE\)GT.1943-5606.0000733](http://dx.doi.org/10.1061/(ASCE)GT.1943-5606.0000733).
- Buisman, K. A. S. (1936). “Results of Long Duration Settlement Tests”. *Proc. I ICO-SOMEF*. Vol. 1, p. 103.
- Campanella, R. G. and Y. P. Vaid (1974). Triaxial and Plane Strain Creep Rupture of an Undisturbed Clay. *Canadian Geotechnical Journal* **11**.1, 1–10. DOI: 10.1139/t74-001. eprint: <http://dx.doi.org/10.1139/t74-001>. URL: <http://dx.doi.org/10.1139/t74-001>.
- Carter, J.P., Mark Randolph, and C.P. Wroth (1979). Stress and pore pressure changes in clay during and after the expansion of a cylindrical cavity. *International Journal for Numerical and Analytical Methods in Geomechanics* **3**(4), 305–322.
- Castro, J. and Minna Karstunen (2010). Numerical simulations of stone column installation. *Canadian Geotechnical Journal* **47**(10), 1127–1138.
- Ceccato, Francesca et al. (2016). Two-phase Material Point Method applied to the study of cone penetration. *Computers and Geotechnics*. ISSN: 0266-352X. DOI: <http://dx.doi.org/10.1016/j.compgeo.2016.03.003>. URL: <http://www.sciencedirect.com/science/article/pii/S0266352X16300477>.
- Chow, F. (1997). “Investigations into the behaviour of displacement piles for offshore structures”. PhD thesis. Univ. of London (Imperial College).
- Claesson, Peter, Gunnar Holmberg, and Jan Romell (2007). *Uppföljning av kohesionspållning i mäktiga lerlager. Höghus Lilla Bommen, Göteborg*. Tech. rep. SBUF - Projekt 1034.
- Dijkstra, J., W. Broere, and O.M. Heeres (2011). Numerical simulation of pile installation. *Computers and Geotechnics* **38**.5, 612–622. ISSN: 0266-352X. DOI: <http://dx.doi.org/10.1016/j.compgeo.2011.04.004>. URL: <http://www.sciencedirect.com/science/article/pii/S0266352X11000620>.
- Doherty, James and Martin Fahey (2011). Three-dimensional finite element analysis of the direct simple shear test. *Computers and Geotechnics* **38**.7, 917–924.
- Edil, Tuncer B and Indrasurya B Mochtar (1988). Creep response of model pile in clay. *Journal of geotechnical engineering* **114**.11, 1245–1260.
- Eide, O., J.N. Hutchinson, and A. Landva (1961). “Short and long-term test loading of a friction pile in clay”. *5th International Conference on Soil Mechanics and Foundation Engineering. Paris*. Vol. 2, pp. 45–53.
- Elert, Glenn (2015). *The Physics Hypertextbook*. URL: <http://physics.info/springs/>.
- Engin, HK, RBJ Brinkgreve, and AF Tol (2015). Simplified numerical modelling of pile penetration—the press-replace technique. *International Journal for Numerical and Analytical Methods in Geomechanics* **39**.15, 1713–1734.
- Eriksson, Per et al. (2004). *Kohesionspållar rapport 100*. Rapport 100. PÅLKOMMISSIONEN.
- Fellenius, B.G. (1938). Provbekastningar av i lera nedpressade järnrör. *Teknisk Tidskrift: Väg- och Vattenbyggnadskonst* **10**, 113–118. URL: <http://runeberg.org/tektid/1938v/0117.html>.

- (1955). *Resultat från pålprovningar vid Göteborg C*. Tech. rep. 99-0836245-3 ;5. Kungl. Järnvägsstyrelsens geotekniska avdelning.
- Fellenius, B.H. (1972). Down-drag on piles in clay due to negative skin friction. *Canadian Geotechnical Journal* **9.4**, 323–337.
- (2001). From strain measurements to load in an instrumented pile. *Geotechnical News Magazine* **19.1**, 35–38.
- (2006). Results from long-term measurement in piles of drag load and downdrag. *Canadian Geotechnical Journal* **43.4**, 409–430.
- (2013). Discussion of “A simplified nonlinear approach for single pile settlement analysis”. *Canadian Geotechnical Journal* **50.6**, 685–687. DOI: 10.1139/cgj-2013-0022. eprint: <http://dx.doi.org/10.1139/cgj-2013-0022>. URL: <http://dx.doi.org/10.1139/cgj-2013-0022>.
- (2015). *Basics of Foundation Design*. 2375 Rothesay Avenue Sidney, British Columbia Canada, V8L 2B9: [www.fellenius.net](http://www.fellenius.net). URL: [www.fellenius.net](http://www.fellenius.net).
- Fleming, K. et al. (2008). *Piling Engineering, Third Edition*. Taylor & Francis. ISBN: 9780415266468. URL: [https://books.google.se/books?id=%5C\\_UE3fd5CzcUC](https://books.google.se/books?id=%5C_UE3fd5CzcUC).
- Gallagher, K. and H. St John (1980). “Field Scale Model Studies of Piles as Anchorages for Buoyant Platforms”. *Eur. Off. Pet. Conf. and Exhibit*. London.
- Graham, J, JH Crooks, and AL Bell (1983). Time effects on the stress-strain behaviour of natural soft clays. *Géotechnique* **33.3**, 327–340.
- Gras, J. P. et al. (In press). Permissible range of model parameters for natural fine grained materials [in review]. *Acta Geotechnica*.
- Gudehus, Gerd et al. (2008). The soilmodels.info project. *International Journal for Numerical and Analytical Methods in Geomechanics* **32.12**, 1571–1572. ISSN: 1096-9853. DOI: 10.1002/nag.675. URL: <http://dx.doi.org/10.1002/nag.675>.
- Guo, W.D. (2012). *Theory and Practice of Pile Foundations*. Taylor & Francis. ISBN: 9780415809337. URL: <https://books.google.se/books?id=0-XtyVK5c4EC>.
- Hansbo, S. (1984). “Foundations on friction creep piles in soft clays”. *First International Conference on Case Histories in Geotechnical Engineering*.
- Havel, Frantisek (2004). “Creep in soft soils”. PhD thesis. NTNU.
- Hicher, Pierre-Yves and Poul V Lade (1987). Rotation of principal directions in K 0-consolidated clay. *Journal of Geotechnical Engineering* **113.7**, 774–788.
- Hunt, Christopher E. (2000). “Effect of pile installation on static and dynamic soil properties”. PhD thesis. Dept. Civil and Environmental Engineering, University of California, Berkeley.
- Hunt, Christopher E. et al. (2002). Effect of pile driving on static and dynamic properties of soft clay. *Journal of geotechnical and geoenvironmental engineering* **128.1**, 13–24. DOI: 10.1061/(ASCE)1090-0241(2002)128:1(13).
- Hunter, Gavan J. and Nasser Khalili (2000). *A Simple Criterion For Creep Induced Failure Of Over-Consolidated Clays*. Ed. by International Society for Rock Mechanics.
- Jardine, R.J. and D.M. Potts (1988). Hutton tension leg platform foundations: prediction of driven pile behaviour. *Geotechnique* **38.2**, 231–252.
- Jendeby, Leif (1986). *Friction piled foundations in soft clay. A study of load transfer and settlements*. Göteborg.

- Johansson, Bo and Leif Jendebý (1998). *Portrycksökningar till följd av påslagning och dess betydelse för stabiliteten*. Tech. rep. 4. Chalmers Tekniska Högskola, Geoteknik.
- Karlsrud, K (2012). “Prediction of load-displacement behavior and capacity of axially loaded piles in clay based on interpretation of load test results”. PhD thesis. Ph. D. thesis, Norwegian Univ. of Science and Technology, Trondheim, Norway.
- (2014). Ultimate Shaft Friction and Load-Displacement Response of Axially Loaded Piles in Clay Based on Instrumented Pile Tests. *Journal of Geotechnical and Geoenvironmental Engineering* **140**.12, 04014074. DOI: 10.1061/(ASCE)GT.1943-5606.0001170. eprint: [http://dx.doi.org/10.1061/\(ASCE\)GT.1943-5606.0001170](http://dx.doi.org/10.1061/(ASCE)GT.1943-5606.0001170). URL: [http://dx.doi.org/10.1061/\(ASCE\)GT.1943-5606.0001170](http://dx.doi.org/10.1061/(ASCE)GT.1943-5606.0001170).
- Karlsrud, K and T Haugen (1985). Behaviour of piles in clay under cyclic axial loading. *Results of field model tests. 4th Int. Collf* **11**, 589–600.
- Karlsrud, K, Tor Georg Jensen, et al. (2014). “Significant ageing effects for axially loaded piles in sand and clay verified by new field load tests”. *Offshore Technology Conference*. Offshore Technology Conference.
- Karlsrud, K, F Nadim, et al. (1990). “Axial capacity of offshore piles in clay”. *Offshore Technology Conference*. Offshore Technology Conference.
- Karstunen, Minna et al. (2005). Effect of Anisotropy and Deconstruction on the Behavior of Murro Test Embankment. *International Journal of Geomechanics* **5**.2, 87–97. DOI: 10.1061/(ASCE)1532-3641(2005)5:2(87). eprint: [http://dx.doi.org/10.1061/\(ASCE\)1532-3641\(2005\)5:2\(87\)](http://dx.doi.org/10.1061/(ASCE)1532-3641(2005)5:2(87)). URL: [http://dx.doi.org/10.1061/\(ASCE\)1532-3641\(2005\)5:2\(87\)](http://dx.doi.org/10.1061/(ASCE)1532-3641(2005)5:2(87)).
- Kempfert, Hans-Georg and Berhane Gebreselassie (2006). *Excavations and Foundations in Soft Soils*. Springer Berlin Heidelberg. ISBN: 9783540328957. URL: <https://books.google.se/books?id=id1DAAAQBAJ>.
- Kimura, Tsutomu and Kunio Saitoh (1983). The influence of strain rate on pore pressures in consolidated undrained triaxial tests on cohesive soils. *Soil and Foundations: Japanese Society of Soil Mechanics and Foundation Engineering* **23**.1.
- Klingberg, Fredrik, Tore Påsse, and Jenny Levander (2006). *Bottenförhållanden och geologisk utveckling i Göta älv. Rapport k43*. Tech. rep. Sveriges geologiska undersökning.
- Kullingsjö, Anders (2007). “Effects of deep excavations in soft clay on the immediate surroundings”. ISBN 978-91-7385-002-5. PhD thesis. Chalmers University of Technology.
- Kuwabara, Fumio, Osamu Motomura, and Shinichi Yamato (1993). Long-term settlement characteristics of a friction pile. *Japanese Society of Soil Mechanics and Foundation Engineering* **33**(4), 26–35.
- Länsivaara, Tim Tapani (1999). “A study of the mechanical behavior of soft clay”. PhD thesis. Norwegian University of Science and Technology.
- Larsson, Rolf (1981). *Drained behaviour of Swedish clays*. SGI report 12. Swedish Geotechnical Institute.
- (2007). *Information 15, CPT-sondering: utrustning – utförande – utvärdering*. Tech. rep. SGI, Swedish Geotechnical Institute.
- Lefebvre, Guy and Denis LeBoeuf (1987). Rate Effects And Cyclic Loading of Sensitive Clays. *Journal of Geotechnical Engineering* **113**.5, 476–489. DOI: 10.1061/(ASCE)0733-9410(1987)113:5(476). eprint: [http://dx.doi.org/10.1061/\(ASCE\)0733-9410\(1987\)113:5\(476\)](http://dx.doi.org/10.1061/(ASCE)0733-9410(1987)113:5(476)).

- 0733-9410(1987)113:5(476). URL: [http://dx.doi.org/10.1061/\(ASCE\)0733-9410\(1987\)113:5\(476\)](http://dx.doi.org/10.1061/(ASCE)0733-9410(1987)113:5(476)).
- Lehane, B.M. and R.J. Jardine (1992). Residual strength of Bothkennar clay in soil-soil and soil-interface shear. *Géotechnique* **42.2**, 363–367.
- (1994). Displacement-pile behaviour in a soft marine clay. *Canadian Geotechnical Journal* **31.2**, 181–191.
- Liingaard, Morten, Anders Augustesen, and Poul V Lade (2004). Characterization of models for time-dependent behavior of soils. *International Journal of Geomechanics* **4.3**, 157–177.
- Liu, Hanlong, Hang Zhou, and Gangqiang Kong (2014). XCC pile installation effect in soft soil ground: A simplified analytical model. *Computers and Geotechnics* **62**, 268–282.
- Lo, KY and AG Stermac (1965). “Induced pore pressures during pile-driving operations”. *6th International Conference on Soil Mechanics and Foundation Engineering, Montreal, Canada*. Vol. 2, pp. 285–289.
- Mewis, Jan and Norman J Wagner (2009). Thixotropy. *Advances in Colloid and Interface Science* **147**, 214–227.
- Mitchell, J.K. and K. Soga (2005). *Fundamentals of soil behavior*. John Wiley & Sons. ISBN: 9780471463023. URL: [https://books.google.se/books?id=b%5C\\_dRAAAAMAAJ](https://books.google.se/books?id=b%5C_dRAAAAMAAJ).
- Mochtar, Indrasurya B and Tuncer B Edil (1988). Shaft resistance of model pile in clay. *Journal of geotechnical engineering* **114.11**, 1227–1244.
- Morrison, M.J. (1984). “In Situ Measurements on a Model Pile in Clay”. PhD thesis. Dept. of Civil Engineering MIT, Cambridge, MA.
- Müller, Rasmus (2010). *Licensiate thesis: Embankments founded on sulphide clay:-some aspects related to ground improvement by vertical drains*. KTH Royal Institute of Technology.
- Nash, D. F. T., G. C. Sills, and L. R. Davison (1992). One-dimensional consolidation testing of soft clay from Bothkennar. *Géotechnique* **42.2**, 241–256. DOI: 10.1680/geot.1992.42.2.241. eprint: <http://dx.doi.org/10.1680/geot.1992.42.2.241>. URL: <http://dx.doi.org/10.1680/geot.1992.42.2.241>.
- Nayak, G. C. and O. C. Zienkiewicz (1972). Elasto-plastic stress analysis. A generalization for various constitutive relations including strain softening. *International Journal for Numerical Methods in Engineering* **5.1**, 113–135. ISSN: 1097-0207. DOI: 10.1002/nme.1620050111. URL: <http://dx.doi.org/10.1002/nme.1620050111>.
- Olsson, Mats (2010). *Calculating long-term settlement in soft clays - with special focus on the Gothenburg region*. Lic - Department of Civil and Environmental Engineering, Chalmers University of Technology, no: 2010:3. 115. Institutionen för bygg- och miljöteknik, Geologi och geoteknik, Chalmers tekniska högskola,
- (2013). “On rate-dependency of Gothenburg clay”. ISBN 9789173859110. PhD thesis. Chalmers tekniska högskola.
- Persson, Jenny (2004). *The Unloading Modulus of Soft Clay: A field and laboratory study*. Institutionen för bygg- och miljöteknik, Geologi och geoteknik, Chalmers tekniska högskola,
- Pestana, Juan M., Christopher E Hunt, and Jonathan D Bray (2002). Soil deformation and excess pore pressure field around a closed-ended pile. *Journal of geotechnical and*

- geoenvironmental engineering* **128.1**, 1–12. DOI: 10.1061/(ASCE)1090-0241(2002)128:1(1).
- Pham, HD et al. (2010). “Modelling of installation effects of driven piles using hypoplasticity”. *Numerical Methods in Geotechnical Engineering 2010: Proceedings of the 7th European Conference on Numerical Methods in Geotechnical Engineering (Benz T and Nordal S (eds))*. CRC Press, Balkema, Leiden, the Netherlands, <http://dx.doi.org/10.4018/jgee-2010090605>, pp. 261–266.
- Poulos, HG, JP Carter, and JC Small (2002). “Foundations and retaining structures—Research and practice”. *PROCEEDINGS OF THE INTERNATIONAL CONFERENCE ON SOIL MECHANICS AND GEOTECHNICAL ENGINEERING*. Vol. 4. AA BALKEMA PUBLISHERS, pp. 2527–2606.
- Quinn, T.A.C. and M.J. Brown (2011). “Effect of strain rate on isotropically consolidated kaolin over a wide range of strain rates in the triaxial apparatus.” *Proc. Int. Symp. on Deformation Characteristics of Geomaterials, 1-3 September, Seoul*. Pp. 607–613.
- PK-R59 (1980). *Anvisningar för provpålning med efterföljande provbelastning*. Rapport 59. Pålkommissionen.
- Ramalho Ortigao, J.A. and Mark Randolph (1983). Creep effects on tension piles for the design of buoyant offshore structures. *Int Sympo on Offshore Engrg* **12**, 16.
- Randolph, Mark (2003). Science and empiricism in pile foundation design. *Geotechnique* **53.10**, 847–875.
- Randolph, Mark, J.P. Carter, and C.P. Wroth (1979). Driven piles in clay—the effects of installation and subsequent consolidation. *Geotechnique* **29.4**, 361–393.
- Randolph, Mark and S. Gourvenec (2011). *Offshore Geotechnical Engineering*. Taylor & Francis. ISBN: 9780415477444. URL: <https://books.google.se/books?id=qiI8xPQAACAAJ>.
- Randolph, Mark and C.P. Wroth (1978). Analysis of deformation of vertically loaded piles. *Journal of the Geotechnical Engineering Division* **104.12**, 1465–1488.
- (1981). Application of the failure state in undrained simple shear to the shaft capacity of driven piles. *Géotechnique* **31.1**, 143–157. DOI: 10.1680/geot.1981.31.1.143. eprint: <http://dx.doi.org/10.1680/geot.1981.31.1.143>. URL: <http://dx.doi.org/10.1680/geot.1981.31.1.143>.
- Robinson, S. and M.J. Brown (2013). “Rate effects at varying strain levels in fine grained soils.” *Proceedings of the 18th International Conference on Soil Mechanics and Geotechnical Engineering, Paris*.
- Roy, M et al. (1981). Behaviour of a sensitive clay during pile driving. *Canadian Geotechnical Journal* **18.1**, 67–85.
- Sabetamal, H. et al. (2016). Coupled analysis of dynamically penetrating anchors. *Computers and Geotechnics* **77**, 26–44. ISSN: 0266-352X. DOI: <http://dx.doi.org/10.1016/j.compgeo.2016.04.005>. URL: <http://www.sciencedirect.com/science/article/pii/S0266352X16300714>.
- Sagaseta, C, AJ Whittle, and M Santagata (1997). Deformation analysis of shallow penetration in clay. *International journal for numerical and analytical methods in geomechanics* **21.10**, 687–719.
- Sällfors, Göran and Leif Andreasson (1985). *Kompressionsegenskaper, Geotekniska laboratorieanvisningar, del 10*. Tech. rep. Swedish Geotechnical Society.

- Seng, Sochan and Hiroyuki Tanaka (2012). Properties of very soft clays: A study of thixotropic hardening and behavior under low consolidation pressure. *Soils and Foundations* **52.2**, 335–345. ISSN: 0038-0806. DOI: <http://dx.doi.org/10.1016/j.sandf.2012.02.010>. URL: <http://www.sciencedirect.com/science/article/pii/S0038080612000388>.
- SGF, Swedish Geotechnical Society (1993). *Report 2:93E, Recommended Standard for Field Vane Shear Test*. Tech. rep. Swedish Geotechnical Society.
- Sheil, Brian B et al. (2015). A practical approach for the consideration of single pile and pile group installation effects in clay: Numerical modelling. *Journal of Geo-Engineering Sciences* **2.3**, 4, 119–142.
- Sheng, Daichao, Majidreza Nazem, and John P Carter (2009). Some computational aspects for solving deep penetration problems in geomechanics. *Computational mechanics* **44.4**, 549–561.
- Sivasithamparam, Nallathamby (2011). “Development and Implementation of Advanced Soft Soil MModel in Finite Elements”. PhD thesis. University of Strathclyde.
- Sivasithamparam, Nallathamby, Minna Karstunen, and Paul Bonnier (2015). Modelling creep behaviour of anisotropic soft soils. *Computers and Geotechnics* **69**, 46–57. ISSN: 0266-352X. DOI: <http://dx.doi.org/10.1016/j.compgeo.2015.04.015>. URL: <http://www.sciencedirect.com/science/article/pii/S0266352X15000944>.
- Skempton, AW (1951). “The bearing capacity of clays”. *Selected papers on Soil Mechanics*.
- Skov, Rikard and Hans Denver (1988). “Time-dependence of bearing capacity of piles”. *Proc. Third International Conference on the Application of Stress-Wave Theory to Piles. Ottawa*, pp. 25–27.
- Standards, ISO (2016). *Geotechnical investigation and testing – Testing of geotechnical structures – Part 1: Pile load test by static axially loaded compression (under development)*. Ed. by ISO Standards. URL: [http://www.iso.org/iso/home/store/catalogue\\_tc/catalogue\\_detail.htm?csnumber=70807](http://www.iso.org/iso/home/store/catalogue_tc/catalogue_detail.htm?csnumber=70807).
- St.John, H. et al. (1983). Design of piles for tethered platforms. *DESIGN IN OFFSHORE STRUCTURES, 1983*, 61–72.
- Tavenas, F. et al. (1978). Creep behaviour of an undisturbed lightly overconsolidated clay. *Canadian Geotechnical Journal* **15.3**, 402–423. DOI: 10.1139/t78-037. eprint: <http://dx.doi.org/10.1139/t78-037>. URL: <http://dx.doi.org/10.1139/t78-037>.
- Teh, Cee-Ing (1987). “An analytical study of the cone penetration test”. PhD thesis. University of Oxford.
- Tehrani, Faraz S. et al. (2016). Comparison of Press-Replace Method and Material Point Method for analysis of jacked piles. *Computers and Geotechnics* **78**, 38–53. ISSN: 0266-352X. DOI: 10.1016/j.compgeo.2016.04.017. URL: <http://www.sciencedirect.com/science/article/pii/S0266352X16300908>.
- Ter-Stepanian, G. (1992). Mechanics of soil creep during shear. *Geomechanics and Water Engineering in Environmental Management, Balkema, Rotterdam*.
- Tian, W.-M. et al. (1994). Drained creep of undisturbed cohesive marine sediments. *Canadian Geotechnical Journal* **31.6**, 841–855. DOI: 10.1139/t94-101. eprint: <http://dx.doi.org/10.1139/t94-101>. URL: <http://dx.doi.org/10.1139/t94-101>.

- Tomlinson, M. and J. Woodward (2014). *Pile Design and Construction Practice, Sixth Edition*. Taylor & Francis. ISBN: 9781466592636. URL: <https://books.google.se/books?id=Me2sBAAAQBAJ>.
- Torpe, Guro Rosshaug (2014). “Utvikling og evaluering av prosedyrer for gjennomføring av udrenerte skjærkrypforsøk i kvikkleire”. MA thesis. NTNU.
- Torstensson, B.A. (1973). “FRICTION PILES DRIVEN IN SOFT CLAY. A FIELD STUDY”. PhD thesis. Chalmers Tekniska Högskola.
- Trafikverket (2014). *Marieholmsförbindelsen: Markteknisk undersökningsrapport MUR, Geoteknik*. Tech. rep. Trafikverket.
- Wendel, Ernst Henrik (1900). Om profbelastning på pålar med tillämpning deraf på grundläggningsförhållandena i Göteborg. *Sep. ur Tekn. samf. handlingar*.
- Wheeler, Simon J et al. (2003). An anisotropic elastoplastic model for soft clays. *Canadian Geotechnical Journal* **40.2**, 403–418. DOI: 10.1139/t02-119. eprint: <http://dx.doi.org/10.1139/t02-119>. URL: <http://dx.doi.org/10.1139/t02-119>.
- Whittle, Andrew J (1987). “A constitutive model for overconsolidated clays with application to the cyclic loading of friction piles”. PhD thesis. Massachusetts Institute of Technology.
- Wood, Tara (2016). “On the small strain stiffness of some Scandinavian soft clays and impact on deep excavation.” PhD thesis. Civil and Environmental Engineering.
- Yu, HS (2013). *Cavity expansion methods in geomechanics*. Springer Science and Business Media.
- Yu, HS, LR Herrmann, and RW Boulanger (2000). Analysis of steady cone penetration in clay. *Journal of Geotechnical and Geoenvironmental Engineering* **126.7**, 594–605.
- Zeevaert, Leonardo (1983). *Foundation engineering for difficult subsoil conditions*. 2nd ed. Van Nostrand Reinhold Company. ISBN: 0-442-20169-9.
- Zhang, Qian-qing and Zhong-miao Zhang (2012). A simplified nonlinear approach for single pile settlement analysis. *Canadian Geotechnical Journal* **49.11**, 1256–1266.